

This work is protected by copyright and other intellectual property rights and duplication or sale of all or part is not permitted, except that material may be duplicated by you for research, private study, criticism/review or educational purposes. Electronic or print copies are for your own personal, non-commercial use and shall not be passed to any other individual. No quotation may be published without proper acknowledgement. For any other use, or to quote extensively from the work, permission must be obtained from the copyright holder/s.



Simulation and characterization of the corneal limbal epithelial stem
cell niche by using new biotechnologies

Ryan Luke Dimmock

School of Pharmacy and Bioengineering

Keele University

Thesis submitted for the degree of

Doctor of Philosophy

March 2025

This thesis is dedicated in loving memory to Maurice Dimmock "Grampy"

I ACKNOWLEDGEMENTS

Firstly I want to express my deepest gratitude to my Mother, Father, Grandmother and Graham, for this PhD may not have been possible without their support and guidance.

I want to express my appreciation to Professor Yang for her support as my supervisor throughout the undertaking of my PhD and to the EPSRC for their financial sponsorship of the research. I would also like to thank the rest of our current and past research group members for their support in and outside the lab.

I would like to thank Professor Huang's lab at the University of Dundee, in particular Dr Zhang, for their support and exciting collaboration on the OCT/OCE work. Also, I wish to thank Professor Fu from Keele University, Professor El-Haj and Dr Rotherham from Birmingham University for their support in publishing aspects of this work.

Additionally, I would like to express my sincere gratitude to Dr Rauz from Birmingham Midland Eye Centre alongside Dr Joseph and Ian Mason from the NHS Blood and Transplant Services for their collective efforts in ensuring we were able to procure and work with the human tissue.

I also thank everybody who has encouraged me throughout my time on this program, especially my friends and colleagues throughout the years at the Guy Hilton Research Centre. Thank you for the laughs, camaraderie and memories.

II ABSTRACT

The limbal epithelial stem cell (LESC) niche is a vital stem cell pool which serves to replenish the cornea with competent stem cells for regrowth and repair throughout adult life. Injury and disease, such as limbal stem cell deficiency (LSCD), can damage and deplete this stem cell pool, resulting in aberrant growth across the cornea and can lead to blindness. The aims of this thesis are the investigation and replication of the LESCC niche. Investigation of the niche provided valuable insight into the combined structural and mechanical properties of the niche. Meanwhile, the replication of the niche using smart material fabrication methods enabled active manipulation of primary isolated limbal cells to model niche conditions. These aims were achieved by focusing on the mechanical characterisation of human limbal tissues by non-destructive optical coherence elastography (OCE), combined with optical coherence tomography (OCT) and anatomic replication through the development of a novel bioreactor system. The first study, using OCT/OCE characterisation, revealed the limbal undulation architecture of palisades of Vogt with alteration (in dimension and modulus) in key anatomical features with ageing. To produce a biomimetic in vitro model of the limbus, polydimethylsiloxane (PDMS) based substrates with wrinkled topography were generated by plasma treatment, acid oxidation and dual treatments using a novel stretching frame. This system enabled the PDMS substrate to flatten and wrinkle in a reversible pattern when conducting cell culture, forming the culture surface of a new type of bioreactor. The crypt-like pattern's dimensions resembled the topography of the LESCC niche. The biocompatibility of the patterned substrate was markedly improved using a Gelatin Methacrylate (GelMa) gel coating. The limbal cells cultured on the wrinkled topography proved to retain stemness through the preservation of key stem cell markers such as ABCG2 and P63, whilst indicating the induction of epithelial

change by increases in CK3 expression. It was also observed that these wrinkled PDMS surfaces were able to dictate cell growth patterns, showing alignment in motile cells and colony segregation in colony-forming cells in human and porcine limbal cells respectively. The biotechnology developed in this research has exciting potential applications as a disease model for conditions such as LSCD, ageing or injuries where substantial physical anatomical changes can be investigated for their effect on the native cell population. In translational terms, this benchtop application has the potential to reduce the dependency on patient study cases to investigate limbal and other optical surface diseases by providing an actively tuneable culture platform which has a small footprint. Additionally, this technology has scope to reduce the dependency on primary tissue isolations by providing a culture platform whose topographical features can be tailor-made to expansion conditions.

CONTENTS

I Acknowledgements	2
II Abstract.....	3
Contents.....	5
III List of Figures	13
IV list of tables.....	15
VI Publications	16
V Oral Presentations.....	17
VI Poster Presentations	18
VII Ethical Statements.....	19
VIII List of Abbreviations	20
Chapter 1: Introduction.....	21
1.1 The Generic Epithelial Stem Cell Niche	22
1.2 The Limbal Epithelial Stem Cell (LESC) Niche and the Ocular Surface.....	25
1.3 Limbal Stem Cell Pathology	34
1.3.1. Diseases of the Cornea and Limbal Stem Cell Deficiency	34
1.3.2. Overview of the Current Treatment and Intervention of Corneal Disease	40
1.4. Regenerative Approaches and Cell Therapy Using Limbal Stem Cells.....	41
1.4.1 Cell Sources.....	43
1.4.2 Maintenance of LESC Stemness in the Stem Cell Niche	45
1.4.3 Regenerative Treatment Strategies for Limbal Conditions.....	54
1.5 Viewing the Limbal Niche from Different Perspectives.....	57
1.5.1 Histological Characterisation of the Limbal Niche	57
1.5.2 3D Imaging of the LESC Niche	59
1.5.3 Mechanical Characterisation of Corneolimbal Tissue	59
1.5.4 Optical Coherence Tomography	60
1.5.6 Optical Coherence Elastography	63

1.6. Replication of the Limbal Stem Cell Niche	64
1.6.1 The Current State of Limbal Replication.....	64
1.6.2 Control of Differentiation Gradient and Migration out of The Niche	67
1.6.3 Stem Cell Culturing Technologies Employed in Ocular Surface Replication	70
1.6.4 Generation of Topography, Shape Matters	74
1.6.5 Wrinkling for the Creation of the Biomimetic Limbus	77
1.6.6 Types of Bioreactors Used in Tissue Engineering and Their Use in Limbal Replication	79
1.7 Research Summary	82
1.7.1 Clarification of the Aim for the Research	82
1.7.2 Research Questions.....	83
Chapter 2: Materials and Methods	85
2.1 Summary of Reagents	86
2.2 Principle Methods.....	88
2.2.1 Optical Coherence Tomography and Elastography.....	90
2.2.1.1 Optical Coherence Tomography (OCT) – High-Resolution	90
2.2.1.2 Optical Coherence Elastography.....	90
2.2.1.3 Optical Coherence Tomography – Standardised, Lower Resolution Screening	92
2.2.2 Production of the Bioreactor System and Design Principles Used in this Thesis	94
2.2.2.1 Use of Computer-Aided Design.....	96
2.2.3 Substrate Fabrication and the Creation of Wrinkled Surfaces.....	97
2.2.3.1 Polydimethylsiloxane Bulk/Chip Formulation and Casting.....	99
2.2.3.2 Solvent Casting of Polymer Solutions to Create Membranes and Lamination of PDMS Bulks to Create Wrinkles.....	100
2.2.3.3 Oxygen Plasma-Treatment of Thin Stretched PDMS to Create Wrinkled PDMS	101
2.2.3.4 Oxidation of Stretched PDMS Using Strong Acid to Form Wrinkles.	101
2.2.3.5 The Dual treatment Method.....	102

2.2.4 Tensile and Compression Testing for the Analysis of Mechanical Properties	103
2.2.4.1 Tension Testing	103
2.2.4.2 Compression Testing	103
2.2.5 Substrate Characterisation.....	104
2.2.5.1 Water Contact Angle	104
2.2.5.2 Raman Spectroscopy.....	104
2.2.5.3 Energy dispersive X-ray spectroscopy (EDX) from SEM	105
2.2.5.4 Atomic Force Microscopy	105
2.2.6 Imaging	106
2.2.6.1 Light Microscopy	106
2.2.6.2 Fluorescent Imaging.....	107
2.2.6.3 Live Cell Imaging.....	107
2.2.6.4 Confocal Microscopy.....	108
2.2.6.5 Scanning Electron Microscopy.....	109
2.2.7 Staining Approaches to Reveal Limbal Cell Function	109
2.2.7.1 Immunofluorescent Staining.....	109
2.2.7.2 Cytoskeleton Staining for Morphology Assessment	111
2.2.7.3 Haematoxylin and Eosin Staining and Preparation of Tissue for Histology.	111
2.2.9 Cell Culture	115
2.2.9.1 Human and Porcine Cell Limbal Cell Culture	115
2.2.9.2 Co-cultivation of Isolated Limbal Cells with 3T3-J2 Mouse Embryonic Fibroblasts	117
2.2.9.3 Wrinkled Substrate Culture	118
2.2.9.4 Human Embryonic Kidney-293 Cell culture.....	118
2.2.9.5 Rat Cardiomyoblast Culture	119
2.2.10 Statistics.....	119
Chapter 3: Characterisation of the Structure and Mechanical Properties of Limbus	121
3.1 Introduction	122
3.2 Materials and Methods.....	127

3.2.1 Summary of Methodology	127
3.2.2 Polarised Optical Microscopy	128
3.2.3 Optical Coherence Tomography	129
3.2.4 Vibrational Optical Coherence Elastography	129
3.2.5 Histology and Slice Preparation	130
3.2.6 Statistics	131
3.3 Results	131
3.3.1 Optical Microscopy of the Limbus	131
3.3.2 Optical Coherence Tomography	134
3.3.3 Optical Coherence Elastography	141
3.4 Discussion	151
3.5 Conclusion	158
Chapter 4: Fabrication and Design of a Novel Bioreactor and Generation of Wrinkled Surfaces	160
4.1 Introduction	161
4.2 Materials and Methods	167
4.2.1 Fabrication of PDMS	167
4.2.2 Fabrication of Polymer Membranes	167
4.2.3 Preparation of Laminated Blocks	168
4.2.4 Oxygen Plasma Treatment	168
4.2.5 Wet Chemical (Acid) Oxidation	168
4.2.6 Dual treatment	169
4.2.7 Mechanical Testing	170
4.2.8 Optical Coherence Tomography	170
4.2.9 Scanning Electron Microscopy	171
4.2.10 Atomic Force Microscopy	171
4.2.11 Water Contact Angle	171
4.2.12 Raman Spectroscopy	172
4.2.13 3D Printing	172

4.2.14 Bioreactor Design.....	173
4.2.14.1 Compression Frame for Laminated Blocks	173
4.2.14.2 Stretching Frame and Moulds for Chip-Based Methods.....	174
4.3 Results	175
4.3.1 Demonstration of the Bioreactor Setups	175
4.3.2 PDMS Bulk Optimisation by Compression Testing	176
4.3.3 Tension Testing of Polymer Membranes.....	178
4.3.4 Laminated Blocks.....	179
4.3.5 Oxygen Plasma Treatment	183
4.3.6 Wet Chemical Oxidation (acid-oxidation)	188
4.3.7 Dual treatment	196
4.3.8 Compositional Analysis of Materials Undergoing Treatments	202
4.3.9 Water Contact Angle Test to Predict Cytocompatibility	206
4.3.10 Preliminary Assessment of Dual treatment Wrinkled Topography Using OCE	207
4.4 Discussion.....	209
4.4.1 Bioreactor Design.....	209
4.4.2 Material Production	213
4.4.3 Material Characterisation	220
4.5. Conclusion	224
Chapter 5: Characterisation of the Cellular Response to Wrinkled Topography	226
5.1. Introduction	227
5.2 Materials and Methods.....	228
5.2.1 Limbal Cell Isolation, Expansion and Cell Culture.....	228
5.2.1.1 Limbal Cell Isolation.....	228
5.2.1.2 Co-Culture with 3T3-J2 Mouse Fibroblast.....	230
5.2.1.3 Limbal Cell Culture with Wrinkled Substrates.	231
5.2.1.4 Culture of Rat Cardiomyoblasts	232
5.2.1.5 Cultivation of HEK-293 cells.....	233

5.2.2 Coatings for surface functionalisation	234
5.2.2.1 Collagen coating for cell expansion.....	234
5.2.2.2 Polydopamine and Polydopamine + collagen coating	234
5.2.2.3 Gelatin Methacrylate Production and Coating	234
5.2.3 Tissue Assessment using Optical Coherence Tomography (OCT)	235
5.2.4 Immunofluorescence and Fluorescent Imaging.....	236
5.2.3.1 Immunofluorescent staining (primary + secondary).....	236
5.2.3.2 Cytoskeleton Staining.....	237
5.2.5 Live Cell Imaging.....	238
5.2.5.1 Automated Live Cell Imaging Using the CellCyte	238
5.2.5.2 Manual Live Cell Imaging	239
5.2.6 Image Analysis.....	240
5.2.6.1 Image-Based Counting and Morphology Analysis.....	240
5.2.6.2 Assessment of Alignment.....	240
5.2.7 3D Printing	241
5.2.7.1 CAD Design	241
5.2.7.2 3D Printing of cultureware	241
5.3 Results	242
5.3.1 Isolation and Cultivation of Human Limbal Cells	242
5.3.1.1 Immunofluorescent Staining of Human Corneolimbic Tissue.....	242
5.3.1.2 Isolation of Human Limbal Cells into Monolayer Culture	244
5.3.1.3 Characterisation and Optimisation of Isolated Human Limbal Cell Culture .	245
5.3.2 Porcine Limbal Epithelial Cell Isolation.....	249
5.3.2.1 Pre-Dissection Tissue Screening and 3T3IN Co-Culture	249
5.3.2.2 Porcine Limbal Cell Monolayer Characterisation.....	253
5.3.2.3 Optimisation of PLESC Culture – Towards Monolayer Purity.....	254
5.3.3. Cultures Performed as Part of the Substrate Developmental Process	259
5.3.3.1 Laminated Block Wrinkled Substrate Cell Culture Trial.....	259
5.3.3.2 Plasma Oxidized PDMS Topography	261

5.3.3.3 Cultivation of Cells on Acid Oxidized Topography.....	262
5.3.3.4 Cultivation of Human Limbal Cells a Matrix-Like Coating.....	264
5.3.3.5 Optimisation of GelMa Coating of Dual treatment Substrates for Cell Culture	266
5.3.4 Cultivation of Human Limbal Cells on Wrinkled Substrates	268
5.3.4.1 Immunophenotypic Assessment of Human Cells Grown on Static Wrinkled Substrates.....	268
5.3.4.2 Wrinkled Surfaces as a Contact Guiding Bio-Instructive Surface.....	271
5.3.5 Cultivation of Porcine Limbal Epithelial Stem Cells on Wrinkled Substrates ..	273
5.3.5.1 Culture of Porcine Limbal Epithelial Stem Cells on Static Wrinkled Substrates	273
5.3.5.2 Wrinkle Morphology Variation in PLESC Culture	275
5.3.5.3 Proliferation Profiling of the Growth of PLESCs on the Topographies	276
5.3.6 Limbal Cell Cultivation on Dynamized Substrates.....	279
5.3.6.1 Cultivation of Human Limbal Cells on Dynamized Substrates	279
5.3.6.2 Preliminary Cultivation of PLESCs using a 3T3IN Feeder Layer	281
5.4 Discussion.....	283
5.5 Conclusion	298
Chapter 6: Discussion and Overall Conclusion	301
6.1 Summative Discussion.....	302
6.1.1 Structural and Mechanical Characterisation of the LESC Niche	304
6.1.1.1 OCT for Tissue Structural Analysis	305
6.1.1.2 Structure-Guided ROI Identification for OCE	306
6.1.1.3 Age-Related Changes in Stiffness	308
6.1.2 Production of wrinkled substrates for the replication of the LESC niche	308
6.1.2.1 Preliminary Development: the Evolution From Laminated PDMS Blocks to PDMS Surface Treatment to Form Wrinkles	309
6.1.2.2 Characterisation of Wrinkled Substrates for Limbal Crypt Mimicry	311
6.1.2.3 Dual treatment of PDMS as an Ideal Substrate Production Method.....	312

6.1.2.4 Reversibility of Wrinkled Substrates for Dynamic Limbal Simulation in a Novel Bioreactor Setup	315
6.1.3 Preliminary Limbal Niche Model Investigation Using Primary Cells	317
6.1.3.1 Isolation of Primary Limbal Epithelial Cells from Human and Porcine Sources	317
6.1.3.2 Initial Cellular Testing and Optimisation of the Wrinkled Substrates for Use Within the Bioreactor System.....	319
6.1.3.3 Coating Selection for an Optimised Wrinkled Surface for Limbal Simulation	321
6.1.3.4 Cellular Response to the Static and Dynamic Wrinkled Topography	324
6.3 Conclusion	326
6.3.2 Research Conclusion	326
6.3.2 Future Work	331
References.....	337

III LIST OF FIGURES

Figure	Page
Figure 1.1: Diagrammatic representation of a generic epithelial stem cell niche.	24
Figure 1.2: Illustration of the anatomy of the cornea	26
Figure 1.3: Illustration of the eye, locating the limbal crypt.	27
Figure 1.4: Location of the limbus using optical coherence tomography (OCT).	28
Figure 1.5: Illustration of the corneal epithelium.	30
Figure 1.6: Comparative panels of the limbal Palisades of Vogt (POV) <i>in situ</i> demonstrating the effects of Ageing.	38
Figure 1.7: Overview of the key pathways responsible for LESC maintenance and induction of differentiation.	53
Figure 1.8: H+E stained sequential sections of the LESC niche.	58
Figure 2.1: Graphical overview of methods covered in this thesis	89
Figure 2.2: Optical Coherence Elastography setup.	92
Figure 2.3: Thorlabs spectral radar OCT setup.	94
Figure 2.4: Process flow for the design and production of bioreactor system components and cultureware.	95
Figure 2.5: Process flow diagram for material treatment to produce wrinkles.	98
Figure 2.6: Process flow diagram for the isolation and cultivation of primary limbal cells.	113
Figure 3.1: OCT images of a corneoscleral button to show the anatomy of the limbal niche.	122
Figure 3.2: Schematic overview of tissue screening, image acquisition, processing and subsequent output from the imaging analysis stages.	128
Figure 3.3: Haematoxylin and Eosin Staining of human limbal tissue used in this chapter.	132
Figure 3.4: Polarised light micrographs of cadaveric human corneoscleral tissue.	133
Figure 3.5: Examples of the limbal region demarcating process performed before OCT/OCE imaging.	134
Figure 3.6: Cross-sectional OCT images from human tissue samples.	135
Figure 3.7: Median intensity projections of volumetric OCT scans of human LESC niche regions.	136
Figure 3.8: Intensity profiles of the over 65-year-old sample group	137
Figure 3.9: Intensity profiles of the under 65-year-old sample group.	138
Figure 3.10: Quantification of the limbal POV features from projected OCT images.	140
Figure 3.11: Elastograms taken from OCE of the over 65-year-old group.	143
Figure 3.12: Elastograms taken from OCE of the over 65-year-old group.	144
Figure 3.13: Young's moduli calculated from the linear ROI method.	145
Figure 3.14: Example of drawn ROI selection for the LESC niche.	146
Figure 3.15: The over 65-year-old age group with the drawn LESC niche ROIs.	148
Figure 3.16: The under 65-year-old age group with the drawn LESC niche ROIs.	149
Figure 3.17: Young's moduli calculated from the drawn ROI method.	150
Figure 4.1: General schematic for the production of wrinkled substrates.	166
Figure 4.2: Compression frame assembly for laminated block bioreactor setup.	173
Figure 4.3: Tension arms bioreactor rig and complementary mould.	174
Figure 4.4: Photographs demonstrating the two different bioreactor setups <i>in situ</i> .	175
Figure 4.5: Young's moduli of compressed PDMS blocks at different curing agent concentrations.	177
Figure 4.6: Tension testing of PLGA and PCL membranes to determine the Young's modulus.	178
Figure 4.7: Demonstration of wrinkling using laminated blocks	180
Figure 4.8: Optical Coherence Tomography imaging of laminated blocks.	181
Figure 4.9: Bright-field micrographs of plasma-treated topographies formed using different parameters.	184
Figure 4.10: Scanning electron microscopy of plasma-treated PDMS.	186

Figure 4.11: Atomic force microscopy imaging of plasma treatment PDMS.	187
Figure 4.12: Bright-field micrographs of PDMS oxidized with sulfonitric acid to produce topography.	189
Figure 4.13: PDMS substrates which were bent to impose physical strain on the surface exposed to sulfonitric acid.	191
Figure 4.14: Variation of topography generation by PDMS stiffness.	192
Figure 4.15: Immersed PDMS chips exposed to sulfonitric acid.	193
Figure 4.16: Atomic force microscopy imaging of wet acid-oxidized PDMS.	194
Figure 4.17: Scanning electron micrograph of wet chemical oxidized PDMS.	195
Figure 4.18: Schematic representation of the dual treatment protocol.	197
Figure 4.19: OCT analysis of dual-treated PDMS chips.	198
Figure 4.20: Optical Coherence Tomography Imaging of a dual-treated PDMS chip undergoing a cyclic load using the stretching frame.	200
Figure 4.21: Scanning electron micrograph of a PDMS chip subjected to the dual treatment protocol.	201
Figure 4.22: Atomic force microscopy imaging of dual-treated PDMS.	202
Figure 4.23: Raman spectra for PDMS treatment stages.	203
Figure 4.24: Tension testing of 3.3% PDMS chips which have been exposed to the different treatment methods	205
Figure 4.25: Bar chart depicting the water contact angles for the tested materials in this chapter.	207
Figure 4.26: OCE of 3.33% dual-treated wrinkled PDMS.	208
Figure 5.1: Schematic comparison of the static and dynamic wrinkled substrate culture processes.	232
Figure 5.2: Immunofluorescent staining of corneolimbic tissue as marker validation.	243
Figure 5.3: Bright-field micrographs showing the growth of human limbal cells post-isolation.	245
Figure 5.4: Assessment and quantification of cell quality and expansion in different media growth conditions.	248
Figure 5.5: Assessment of 3T3 viability in limbal stem cell culture medium using the CCK8 kit.	250
Figure 5.6: Porcine POV location using OCT to guide limbal dissection and LESC extraction.	251
Figure 5.7: Bright-field microscopy of porcine limbal epithelial cells after isolation and the first passage.	252
Figure 5.8: Immunostaining panel of isolated PLESCs.	254
Figure 5.9: Comparison of 3T3IN co-culture and collagen-coated well culture.	256
Figure 5.10: Immunofluorescent assessment of the collagen-coated well and 3T3IN co-culture methods of expanding PLESCs	258
Figure 5.11: Generation of wrinkles on a PLGA laminated block, with demonstration of wrinkle 'decay' in culture with rat cardiomyoblasts.	260
Figure 5.12: Haematoxylin and Eosin staining of Rat cardiomyoblasts seeded on Pre-strained PDMS membrane which has been subjected to O ₂ plasma treatment.	262
Figure 5.13: HEK293 cells cultivated on acid-oxidized PDMS formulated with 5% curing agent showing random ordered wrinkled surfaces.	263
Figure 5.14: Bright-field imaging of human limbal cells cultivated in monolayer with Polydopamine or polydopamine-collagen coatings.	264
Figure 5.15: Trial of GelMa coated wrinkled PDMS for human limbal cell culture.	266
Figure 5.16: Variation in the concentration of GelMa in the coating process and the subsequent effect on cellular distribution.	267
Figure 5.17: Immunofluorescent staining of human limbal cells seeded on static wrinkled topography.	270
Figure 5.18: Analysis of alignment of human limbal cells on aligned substrates.	272
Figure 5.19: Porcine limbal epithelial cells cultivated on dual treatment wrinkled PDMS with various coatings.	274

Figure 5.20: PLESCs cultivated on substrates of different crypt widths with immunofluorescent staining for the stem cell marker p63 (red) and the epithelial marker CK3 (green).	276
Figure 5.21: Graphs displaying the CCK8 proliferation profiles of the PLESC cells grown on the wrinkled surfaces.	278
Figure 5.22: Human limbal cells cultivated on dynamized substrates with associated alignment analysis.	280
Figure 5.23: Live dead end-point of cultivation of isolated PLESCs on dynamized wrinkled substrates.	282

IV LIST OF TABLES

Table	Page
Table 1.1: Markers used in the characterisation of the limbal cells with reference to limbal stem cell differentiation.	29
Table 1.2: The matrix components of the limbal epithelial stem cell niche.	32
Table 1.3: Additional materials commonly used as coatings or laminar materials to functionalise cell culture substrates.	42
Table 1.4: Examples of studies which constitute limbal replication.	53
Table 1.5: Stem cell culturing approaches and technologies applied in limbal replication.	59
Table 2.1: Summary of reagents used across all methods summarized in this chapter.	72
Table 2.2: 3D printing parameters for both PLA and ABS.	80
Table 4.1: Tables displaying the results of the one-way ANOVA wherein Tukey's pairwise comparison post-hoc test was performed.	158
Table 4.2: Average EdX values for the detected elements in each sample.	178

VI PUBLICATIONS

- 👁 Dimmock, Ryan L., Wang, Xuyiling, Fu, Yibin, Haj, Alicia J. El and Yang, Ying (2020). Biomedical Applications of Wrinkling Polymers. *Recent Progress in Materials*, 2(1), p. 1–31, doi:10.21926/rpm.2001005.
- 👁 Dimmock, Ryan L., Rotherham, Michael, El Haj, Alicia J. and Yang, Ying (2023). Fabrication and Characterisation of Hydrogels with Reversible Wrinkled Surfaces for Limbal Study and Reconstruction. *Gels*, 9(11), p. 915, doi:10.3390/gels9110915.
- 👁 Ceylan, Seda, Dimmock, Ryan and Yang, Ying (2023). Development of Boron-Containing PVA-Based Cryogels with Controllable Boron Releasing Rate and Altered Influence on Osteoblasts. *Polymers*, 15(7), p. 1653, doi:10.3390/polym15071653
- 👁 Dimmock, Ryan, Zhang, Yilong, Butt, Gibran F., Rauz, Saaeha, Huang, Zhihong and Yang, Ying (2024). Characterizing Biomechanics of Limbal Niche Using Vibrational Optical Coherence Elastography. *Journal of Biophotonics*, n/a(n/a), p. e202400172, doi:10.1002/jbio.202400172.

V ORAL PRESENTATIONS

- 👁️ **Future Leaders Joint CDTUKSB Virtual Conference 2020:** Smart Materials Fabrication for Limbal Stem Cell Study
- 👁️ **CDT/TCES Joint Conference Birmingham 2022:** Characterisation of Limbal Mechanical Properties/Morphology and Replication of Limbal Crypt Anatomy
- 👁️ **Termis EU Krakow 2022:** Elastomer Surface Modification Technique for Corneal Limbal Epithelial Stem Cell Investigation
- 👁️ **Spie BIOS San Fransisco 2023:** Characterisation and Quantification of the Limbal Architecture and Biomechanical Properties using Optical Coherence Tomography or Elastography (Conference Presentation)

VI POSTER PRESENTATIONS

- 👁️ **Keele Institute of Liberal Arts and Sciences (ILAS) virtual conference 2021:**
Recreating the Human Limbus
- 👁️ **CDT Lifetime Joint Virtual Conference 2021:** Investigating and Replicating
the Limbal Epithelial Stem Cell Niche
- 👁️ **TCES Virtual Conference 2021:** Facile Techniques to Induce Controllable
Topographic Patterns on PDMS for Epithelial Tissue Growth
- 👁️ **Termis EU Maastricht 2021 (remote):** Smart Wrinkle Topography for Dictating
Cell Activities
- 👁️ **Keele PGR Symposium 2022:** Smart Elastomer Surface Modification For
Limbal Niche Investigation
- 👁️ **Keele Research Conference 2023:** Development of Novel Biotechnologies for
Corneal Limbal Epithelial Stem Cell Niche Investigation

VII ETHICAL STATEMENTS

All human tissue sourced and derived cells described in this thesis were subject to prior approval by the Dudley Local Research Ethics Committee (DLREC) application (06/Q2702/44). All work carried out followed the Human Tissue Authority (HTA) codes of practice.

All animal tissue used (and subsequently derived) cells described in this thesis were byproducts from animals intended for slaughter, procured commercially from a licenced abattoir.

VIII LIST OF ABBREVIATIONS

Abbreviation	Definition
2D	2-dimensional
3D	3-dimensional
ABCG2	ATP binding cassette protein G2
ABS	Acrylonitrile butadiene styrene
AFM	Atomic force microscopy
BSA	Bovine serum albumin
CAD	Computer-aided design
CK3	Cytokeratin 3
CMFDA	Chloromethyl fluorescein diacetate
DAPI	4',6-Diamidino-2-Phenylindole
DMEM	Dulbecco's modified Eagle's medium
ERP	Epithelial rete peg
FBS	Foetal bovine serum
GelMa	Gelatin methacrylate
K12	Cytokeratin/Keratin 12
LAP	Lithium phenyl-2,4,6-trimethylbenzoylphosphinate
LESC	Limbal epithelial stem cell
OCE	Optical coherence Elastography
OCT	Optical coherence tomography
P63	Tumour protein 63
PCL	Polycaprolactone
PDMS	Polydimethylsiloxane
PE	Phycoerythrin
PLESC	Porcine limbal epithelial stem cell
PFA	Paraformaldehyde
PhS-OCT	Phase-sensitive OCT
PLA	Polylactic acid
PLGA	Polylactic-co-glycolic acid
POV	Palisades of Vogt
PR	Palisade ridge
ROI	Region of interest
SD-OCT	Spectral-domain optical coherence tomography
SEM	Scanning electron microscopy
TCP	Tissue culture plastic

Chapter 1: Introduction

The investigation of the limbal epithelial stem cell niche builds upon a multidisciplinary foundation of research. Medical, biomedical, regenerative medical, material and optical imaging research are amongst the most pertinent fields of research which are the roots of this thesis. In this chapter, the established current knowledge is reviewed in the context of the wider thesis. This background review is sectioned into the key principles which underpin the project as established in the wider field and provide the basis for the work carried out. The limbal structure, function and pathology are covered alongside alternate methods of visualising the LESC niche, allowing for full appreciation of the characterisation of the niche performed in later chapters. The technologies and methods discussed in limbal replication provide the basis for comparison of the developed bioreactor and material system in later chapters in association with the cell cultivation methods employed.

1.1 THE GENERIC EPITHELIAL STEM CELL NICHE

Whilst a stem cell niche is common to all tissues within the body, there are distinct differences between morphology, physiology and lifetime presentation. For example, a stem cell pool such as the radial glial cells in the dentate gyrus possess a layered spatial arrangement concerning the fully differentiated neurons and can be considered a relatively short-lived stem cell pool due to being present only during foetal neocortical development. The radial glial cell niche differs substantially when compared to the deeply invaginated morphology of the gastric epithelial stem cell niche present throughout all adult life (*Zhou et al., 2018, Ostrem et al., 2014*).

Epithelial stem cell niches are adult somatic stem cell pools, meaning they are present throughout an individual's lifetime (*Morrison and Spradling, 2008*). The epithelial stem cell niche provides cells to epithelial tissues in which they are embedded, facilitating the epithelial tissues' function as a surface barrier for the body. The term "niche" encapsulates multiple levels including; cellular control, including

either (or synergistically together) the genetic, proteomic or intracellular signalling and can incorporate key control pathways such as the Wnt, Notch, BMP and Hedgehog pathways (*Rizvi and Wong, 2005*). At the next tier, there is the structural anatomic level: including cellular morphology, tissue architecture and matrix composition. At the outermost level is the microenvironment, at this level, the niche is the most vulnerable due to being the most accessible level. Factors of this level are cell-to-cell signalling, mechanobiological/physical cues, microenvironmental chemistry (O₂, pH, carbonate, nutrient perfusion etc.), immune cell interaction and disease state affliction – all of which can alter the niche throughout all levels. Through these levels of control, the niche maintains a high degree of self-regulation. Disruption of this critical self-regulation leads to epithelial disease including tissue degeneration, predisposition to infection and loss of capability.

When drawing comparisons between different tissues, it is important to remember that there are distinct similarities between each type of anatomic epithelial stem cell niche. These similarities manifest not only in function (to supply expanding cells to replenish and regenerate the native tissue (*Zhao et al., 2017*)), but also in terms of structure. Each form of the anatomic niche displays a common structural moiety (the presence of a crypt, bulge, ridge or pit that geographically separates the adult epithelial stem cells) and the native tissue (*Blanpain et al., 2007*). There is a common morphology, as per Figure 1.1, which can be applied to the vast majority of epithelial stem cell niches.

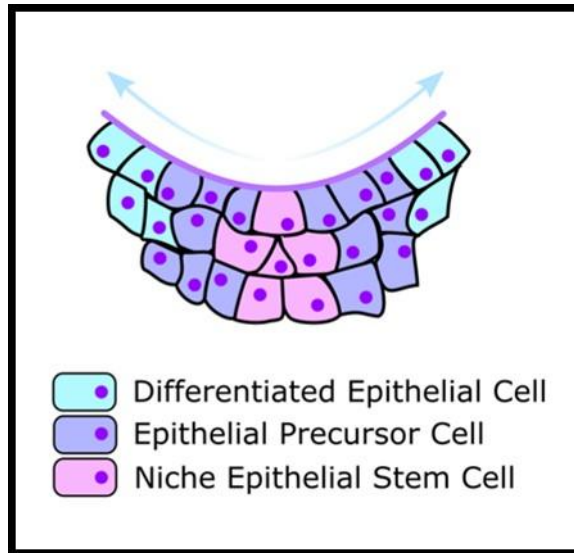


Figure 1.1: Diagrammatic representation of a generic epithelial stem cell niche. This diagram shows the differentiation and migration out from a central niche of epithelial stem cells, this basic layout is conserved between niches of different tissue types (Blanpain et al., 2007)

This type of architecture is common to most of the adult epithelial stem cell niches. In structural terms, there are a few differences in the functionality of the niches in different tissues. The shapes of the niches are presented as necessary for the organ's functionality. The skin has multiple niches in close spatial arrangement to manage keratinous growth and others facilitate epithelial expansion (Tumbar et al., 2004). Such presentation is completely different when compared to the corneal limbus which presents as a circumferential crypt which encircles the entire cornea, enabling regrowth and regeneration of the cornea (Grieve et al., 2015). All niches have the same features: an anatomically distinct population of stem cells -confined within the basal apex of the crypt or (inverted) bulge, a region in which differentiation occurs propagating away from the stem cell. These cells are identified as transient amplifying (TA) cells (Rizvi and Wong, 2005) and the commitment to the destination tissue as differentiated epithelial cells in which the niche serves.

1.2 THE LIMBAL EPITHELIAL STEM CELL (LESC) NICHE AND THE OCULAR SURFACE

The eye is an accessible region for basic visible examination, facilitating visualisation of the ocular surface and the interior of the eye. The ocular surface is the exposed component of the eye which is frontally open to the environment. Visibly, it is comprised of the sclera, conjunctiva and the cornea. The cornea is an optically clear laminar structure composed of an epithelial layer (environmentally exposed and so easily damaged), the intermediate highly ordered collagen-rich stroma bound between the Bowman's layer (epithelial side) and Descemet's membrane (endothelial side) and finally a layer of endothelium lining the inner surface of the cornea (*DeMonte and Kim, 2011*) (Figure 1.2).

The outermost epithelial layer of the cornea has a laminar structure. During the life cycle of the corneal epithelial cells, a drastic morphological change occurs. The corneal epithelium has been extensively studied in terms of its morphology and physiology. The cells change from a columnar morphology in the basal layer, which has expanded from the limbus to a flatter squamous shape. The squamous cells, at the end of their life cycle, slough off into the tear film (*Sridhar, 2018*) (Figure 1.2).

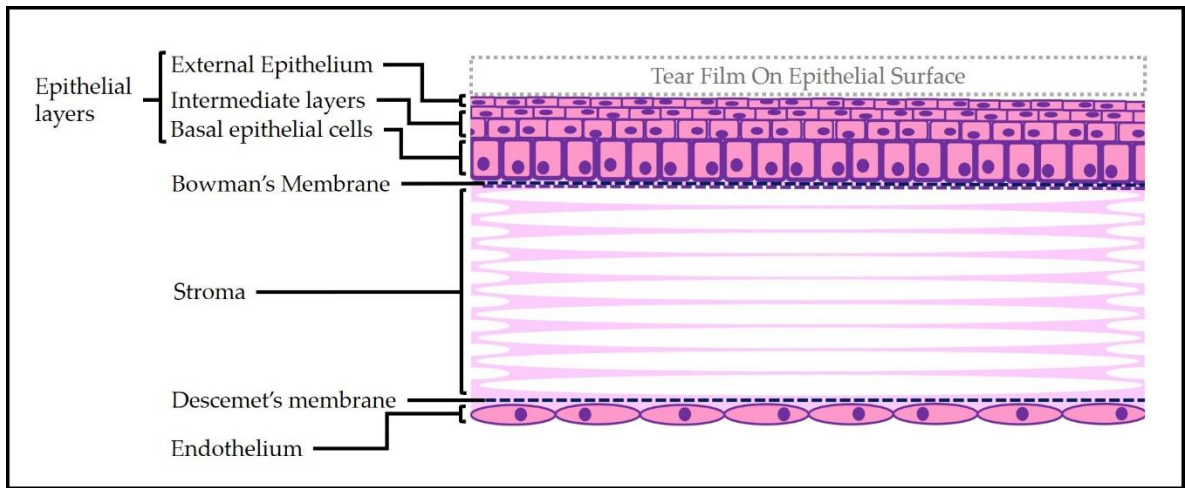


Figure 1.2: Illustration of the anatomy of the cornea. The diagram shows a section of a cross-section of the cornea. The tear film upon the external epidermal layer is the most outer-exposed layer of the cornea, with the endothelium being the innermost layer. The Stroma is highly organised with a lattice of collagen fibres making up the bulk of the structure. Image adapted from histological images and diagrammatical representations (Willoughby et al., 2010, Sridhar, 2018).

The corneal epithelial stem cell niche presents as an undulating crypt which is located at the interface between the cornea and the sclera. This structure is called the limbus and fully encircles the peripheral cornea. It is possible to easily locate the limbus due to its definitive location, although the structure itself is not visible specifically to the naked eye. Its location is peripheral (circumferentially) to the iris at the interface between the cornea and the sclera (Vemuganti et al., 2009). Figure 1.3 illustrates the location of the limbal crypt and its regional sub-divisions.

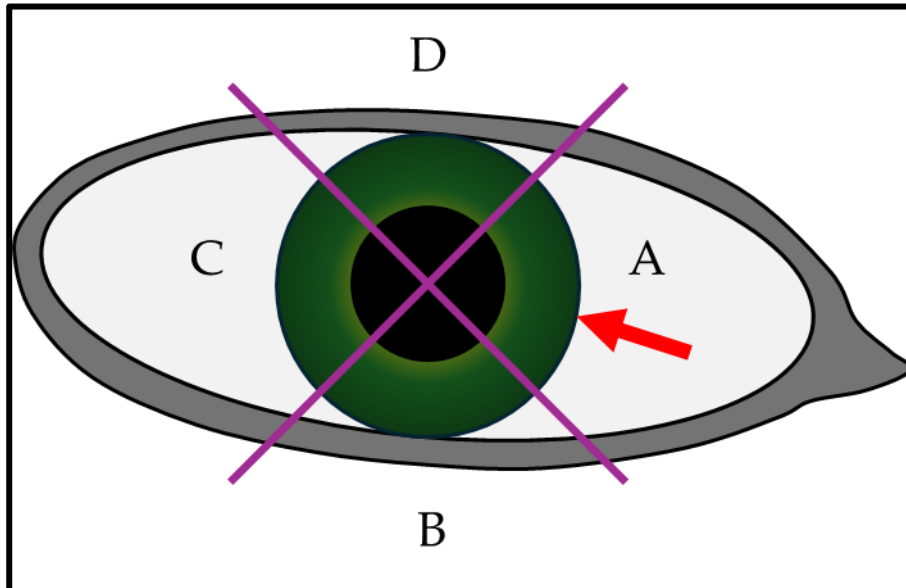


Figure 1.3: Illustration of the eye, locating the limbal crypt. The red arrow indicates the location of the limbal crypt as the circumferential feature around the border between the cornea and the sclera, visually located at the edge of the iris when observed en-face. The purple cross separates the limbus into its four anatomical regions; A) the nasal region which faces the tear duct/nose (Doğan et al., 2021), B) the inferior region which can sometimes be enclosed by the lower eyelid (Miri et al., 2012), C) the temporal region which faces the side of the head (Qiao et al., 2019) and D) the superior region, which is sometimes enclosed by the upper eyelid (Lahoti et al., 2022).

The palisades of Vogt (PV) form the crypt undulations (often resembling mountainous-like topography when viewed with OCT) (Figure 1.4), out of the optical plane with the circumferential crypt. This creates crypts-within-a-crypt, serving to segregate the limbal epithelial stem cells (LESCs), which are corneal progenitors, away from the conjunctival progenitors preventing cross-migration of these cell types (Lathrop et al., 2012). In addition to this key structure, within the limbus reside the Epithelial Rete Pegs (ERP) and Palisade Ridges (PR). The ERPs are located basally within the limbus (Shanmuganathan et al., 2007) whilst the PRs are present as the superior topographical element of the limbal palisades of Vogt. The PR is often described as the first visible feature of the palisades of Vogt during eye examinations and is used to characterise palisade presentation and frequency (Lagali et al., 2013). Measurements of these features within the niche have yielded an average limbal crypt depth of $50\mu\text{m}$ with an average depth of $50\mu\text{m}$ (Grieve et al., 2015). Examination using

OCT revealed the dimensions of the PR and ERP to be within a similar order of magnitude in terms of width (66.25 ± 12.98 and 70.28 ± 17.50 for the inferior limbus of the left and right eyes respectively and 70.77 ± 17.86 and 81.82 ± 22.86 for the superior limbus of the left and right eyes respectively) (Haagdorens et al., 2017).

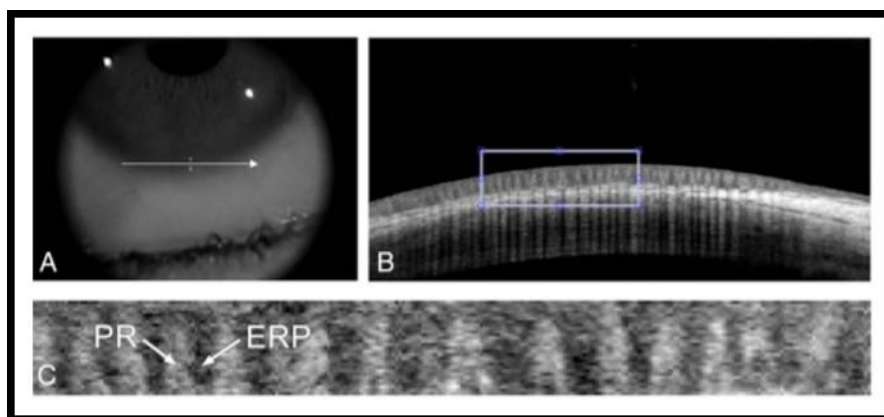


Figure 1.4: Location of the limbus using optical coherence tomography (OCT). In particular, these images focus on ocular surface anatomy viewing using the superior perspective for the Palisades of Vogt (POV). A) An en-face view at the whole eye macroscopic level: the arrow defines the location of the limbal region for the OCT scan, residing at the corneal-scleral interface where the iris visually joins the sclera. B) Cross section to locate the limbus at the ocular surface, undulating topography of the epithelium is now visible at this view. C) The delineated region, as identified in B) (rectangle), the flattened image identifies the PR and epithelial rete peg (ERP) locations. These form the undulating topography of the limbus, which houses the epithelial stem cell niche for epithelial stem cells. Image taken from Article (Haagdorens et al., 2017).

The LESC are demonstrated to reside at the base of the crypts, identifiable using immunofluorescent labelling with the stem cell marker p63 α (Grieve et al., 2015). The XYZ hypothesis, first dubbed by Thoft and Friend (1983) describes the overall direction of cellular proliferation (expansion). The initial expansion of and subsequent migration outwards of the LESC is the manifestation of the transformation of the LESC into transient amplifying cells. Subsequently, this migration and expansion out of the niche follows a convergent expansion pattern along the most basal epithelial layer (and feeds into both the stromal and the endothelial layer) of the cornea, from the limbus to the central cornea. The cells expand upwards after reaching final corneal differentiation

through the corneal epithelial layer, until finally delaminating upon quiescence at the uppermost corneal epithelial surface. This movement of cells from the limbus to the epithelial surface is illustrated in Figure 1.5. (*Thoft and Friend., 1983*).

Tracking of corneal epithelial homeostasis has been achieved in vitro by using a mouse mosaic eye model. This in part has validated the XYZ model, showing the inward expansion of the 'stripes' in the mosaic eye after wounding. However, there are observed age-related declines in limbal stem cell functionality seen through the variance in expansion patterns by both the broadening of and the swirling in the stripes over time (*Mort et al., 2009*). The XYZ hypothesis, validated with expansion tracking demonstrates how LESC and corneal homeostasis are maintained synergistically. Once the stem cells have started their path to the commitment they are collimated on an irreversible path to eventual quiescence and removal at the central corneal epithelial surface. In addition to this one-way commitment of cells out of the niche, another important regulatory mechanism is the slow cycling phenotype observed in LESC. This phenotype prevents overcrowding of the niche through high regulation of cell proliferation, ultimately meaning there is a low number of multipotent cells which are required to have a high differential capacity. This has been classically characterised in the LESC niche using a chased thymidine isomer; bromodeoxyuridine (BrdU) (*Meller et al., 2002, Song et al., 2005*) based on the early method of chasing with thymidine ([³H]TdR) (*Håskjold, 1989*) and more recently with nuclear green fluorescent protein labelling methods (*Sartaj et al., 2017*).

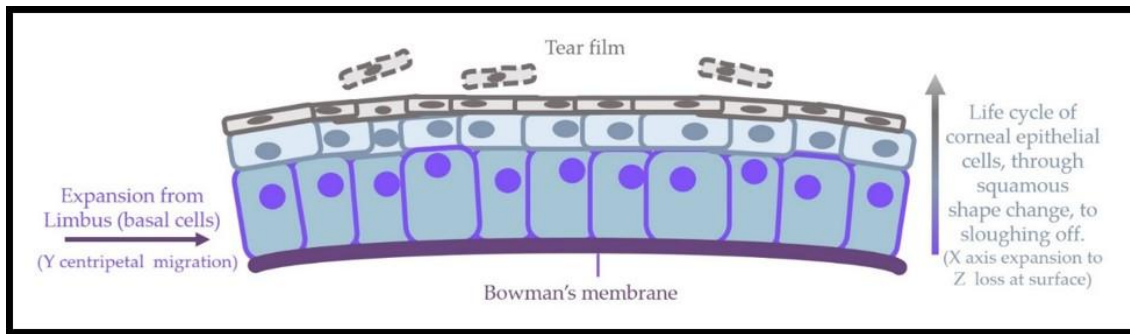


Figure 1.5: Illustration of the corneal epithelium. This diagram shows the laminar structure of the corneal epithelium and the cell expansion pattern. Expansion follows the XYZ hypothesis proposed by Thoft and Friend, the differentiated cells have expanded in from (after the transient amplification stage) from the limbus along the Y axis. As the epithelial cells age, they expand upwards through the remaining 4-6 layers, changing their morphology (becoming more flattened squamous) along the X axis before sloughing off into the tear film, as per the Z component, at the end of the life cycle upon reaching senescence (Thoft and Friend, 1983, Sridhar 2018).

Multiple markers can be used to identify the cell types within the limbus. Focusing primarily on the stem cell phenotype, ATP binding cassette transporter G2 (ABCG2) (de Paiva, 2005) and the common stem cell marker tumour protein 63 subunit α (p63 α) (Schlötzer-Schrehardt and Kruse 2005) are most commonly used to identify limbal stem cells within the niche (in histological sections or cell/tissue culture). A comprehensive list of markers used to characterise the limbus and corneal epithelium can be found in Table 1.1. Additionally, it is also important to be able to monitor differentiation towards committed corneal epithelial cells, migrating out of the stem cell niche, the commitment markers cytokeratin 12 and 3 (CK12/3) are commonly used to identify committed corneal epithelial cells (Yoshida et al., 2006, Chen et al., 2004).

Marker	Location and Presence (if applicable)	Use/Indication	References
ATP binding cassette protein G2	Limbus [+++]	Limbal Stem cell marker	<i>de Paiva et al 2005</i> <i>Dhamodaran et al., 2016</i> <i>Ghoubay-Benallaoua et al., 2017</i> <i>Chen et al., 2017</i> <i>Gouveia et al., 2019</i>
Tumour protein 63 subunit α	Limbus [+++]	General Stem cell marker	<i>Schlötzer-Schrehardt and Kruse 2005</i> <i>Dhamodaran et al., 2016</i> <i>Ghoubay-Benallaoua et al., 2017</i> <i>Stadnikova et al., 2019</i>
Integrin β 1	Limbus [+++], Basal Cornea [+/>+]	Stem cell marker	<i>Schlötzer-Schrehardt and Kruse 2005</i> <i>Chen et al., 2017</i> <i>Polisetti et al., 2017</i>
Integrin α 9	Limbus [+]	Basal	<i>Chen et al., 2004</i> <i>Gouveia et al., 2019</i>
Cytokeratin 14	Limbus [++] cornea [+]	Basal and suprabasal limbal cytoplasmic marker	<i>Schlötzer-Schrehardt and Kruse 2005</i> <i>Yoshida et al., 2006</i> <i>Ghoubay-Benallaoua et al., 2017</i> <i>Park et al., 2019</i>
Cytokeratin 15	Limbus [+++]	Limbal epithelial marker	<i>Yoshida et al., 2006</i> <i>Ghoubay-Benallaoua et al., 2017</i> <i>Dhamodaran et al., 2016</i> <i>Gouveia et al., 2019</i>
Cytokeratin 19	Limbus [++]	Basal limbal cytoplasmic marker	<i>Schlötzer-Schrehardt and Kruse 2005</i> <i>Yoshida et al., 2006</i> <i>Chen et al., 2017</i> <i>Shirzadeh et al., 2018</i>

Marker	Location and Presence (if applicable)	Use/Indication	References
Vimentin	Limbus [+++]	Basal limbal cell marker / Mesenchymal transitional marker	<i>Schlötzer-Schrehardt and Kruse 2005</i> <i>Ghoubay-Benallaoua et al., 2017</i> <i>Sanie-Jahromie et al., 2020</i> <i>Kawashima et al., 2010</i>
α -enolase	Limbus [++] cornea [+]	Basal cell marker	<i>Schlötzer-Schrehardt and Kruse 2005</i>
KGF-R bek	Limbus [+]	Not clarified	<i>Schlötzer-Schrehardt and Kruse 2005</i>
Cytokeratin 3	Corneal dominantly [++], weakly in limbus [+]	Corneal commitment marker	<i>Schlötzer-Schrehardt and Kruse 2005</i> <i>Dhamodaran et al., 2016</i> <i>Ghoubay-Benallaoua et al., 2017</i> <i>Gouveia et al., 2019</i>
Cytokeratin 12	Corneal dominantly [++] weakly in limbus [+]	Corneal commitment marker	<i>Schlötzer-Schrehardt and Kruse 2005</i> <i>Dhamodaran et al., 2016</i> <i>Chen et al., 2017</i>
Nestin	Cornea [+++]	Corneal marker	<i>Schlötzer-Schrehardt and Kruse 2005</i> <i>Ghoubay-Benallaoua et al., 2017</i> <i>Yam et al., 2018</i>
Connexin 43	Cornea [+++]	Corneal basal marker	<i>Schlötzer-Schrehardt and Kruse 2005</i> <i>Chen et al., 2017</i> <i>Dhamodaran et al., 2016</i>
Involucrin	Cornea, Limbus [++] (superficial)	Advanced tissue differentiation marker	<i>Chen et al., 2004</i> <i>Chen et al., 2017</i>

Table 1.1: Markers used in the characterisation of the limbal cells with reference to limbal stem cell differentiation. From this collation, it is possible to state that the most consistently used markers for limbal stem cell characterisation are ABCG2 and TP63, followed by CK14/15. In terms of corneal (commitment) characterisation, the well-accepted markers are CK3/12 followed by Connexin 43.

The microenvironment of the corneal epithelial niche is subject to a cycle of drying from the environment and wetting by tears. Tear fluid, like other fluids bathing different epithelia, has its unique composition. Due to this unique composition, the surface microenvironment is also unique in terms of pH and protein content as determined in human and animal studies (*Lu et al., 2018, Versura et al., 2018*). There is a limited acknowledgement of these conditions as LESC control alongside other aqueous properties including, osmolarity, charge differences and oxidative signalling; showing a restricted appreciation of the microenvironment and its effects on driving LESC differentiation. The cells within the niche are held together by the extracellular matrix. This matrix is composed of multiple collagens, laminins, fibronectin, matrilins, additionally fibrillin-1 and 2, thrombospondin, endostatin, agrin and tenascin-C, vitronectin, bamacan, chondroitin sulphate and versican, which were positively identified using immunofluorescence (*Schlötzer-Schrehardt et al., 2007*) (*Table 1.2*). From LESC isolation protocols it can be said that collagen makes up a significant structural component of the limbal extracellular matrix, as collagenase can be used to dissociate cells out of dissected ocular surface tissue sections (*Chen et al., 2011*).

Matrix component	Type	Reference
Collagens IV, VII, XV, XVII, XVIII	Collagen	<i>Schlötzer-Schrehardt et al., 2007</i>
Laminins α 1-5, β -3, γ 1-3	Glycoproteins	<i>Schlötzer-Schrehardt et al., 2007</i>
BM-40		
Nidogen		
Fibronectin		
Matrillin-2		
Fibrillin-2		
Tenascin-C		
Thrombospondin-4		
Vitronectin		
Perlecan		
Agrin		
Endostatin		

Table 1.2: The matrix components of the limbal epithelial stem cell niche. Listed is a collation of the determined matrix components, grouped by matrix protein type.

1.3 LIMBAL STEM CELL PATHOLOGY

1.3.1. Diseases of the Cornea and Limbal Stem Cell Deficiency

The driving force for the extensive investigation of the LESC niche (concurrently with corneal regeneration) is the prevalence of corneal disease which often has distressing symptoms including pain, itching and vision disturbances which can lead to permanent blindness without intervention. Whilst the cornea has a reservoir of corneal mesenchymal cells, the limbus is proposed to supply the outer epithelial layers. Therefore damage caused by disease to this outer surface affects the limbus detrimentally, resulting in a reduction in the regenerative capacity of the limbus for the cornea if not leading to limbal stem cell deficiency (LSCD). As LSCD development can be considered a multifactorial progression the acquisition of LSCD may not be due to a single cause. Therefore these precursor conditions which may include genetic, injury or immunological components can either singularly or synergistically contribute to or cause LSCD (*Moshirfar et al., 2023*).

There are multiple disorders and diseases of the cornea including but not limited to injury, corneal dystrophies/degeneration and infections. These may afflict limbal stem cell deficiency immediately or over a long time, by causing the loss of competent stem cells from the niche or through structural damage to the cornea (*Katikireddy, 2016, Liskova et al., 2018*). The need for regenerative medicine-oriented therapies is becoming more imperative due to the shortage of transplantable human corneas. However, for such therapies to work it is vital to understand how the stem cell niche changes the disease state. For example, in dystrophies which are largely inherited, there is a gradual degeneration of the cornea. For this disease state, it is appreciated that the condition originates in the stem cell niche which translates out into the destination tissue during tissue growth and regeneration.

Conditions such as dry eye and pathogenic-induced keratitis alter the microenvironment of the stem cell niche, the cell-cell interaction between limbal stem cells and mobilized immune cells, as characterized by *Polisetti et al's* study (*Polisetti et al., 2016*). This shows that LSCD can also be a downstream event derivative of a previously diagnosed state as well as being caused by a direct traumatic incident. The combined stressors of inflammatory factors secreted from incoming migratory immune cells and hyper-osmotic pressure from inflammation, the limbal stem cells lose their regenerative competency. The loss of competency can subsequently lead to stem cell loss if the stressors are of sufficient magnitude, as determined by a study into these niche microenvironment stressors (*Yang et al., 2019*). Additionally, inflammatory diseases such as Steven-Johnson syndrome (*Puangsricharem and Tseng, 1995*), chronic limbitis of non-necrotising anterior scleritis (*Khoo et al., 2018*) and superior limbic keratoconjunctivitis are significant contributors to limbal and corneal damage resulting in LSCD leading to blindness.

It has been demonstrated in vivo that the administration of rapamycin (to inhibit the mTOR pathway) exacerbated injury-induced LSCD with induced corneal inflammation and worsened opacity, thus demonstrating that inflammation is related to LSCD (*Park et al., 2019*). Chronic pathologies including chronic limbitis, scarring from thermal/chemical burns, allergies and diseases such as glaucoma (either directly or secondarily by their treatment with downstream complications), contribute to the generation of ocular inflammation (*Riccio et al., 2019, Horwitz et al., 2018, Boudoin et al., 2000, Sánchez-Avila et al., 2018*). These key physiology-changing conditions presented by limbal inflammation have yet to be fully characterised, presenting an opportunity for the use of an accurate biomimetic model which mimics the dynamic structural changes in the LESC niche (including the palisades of Vogt).

Ageing-related degeneration also factors greatly in the development of LSCD with degenerative effects manifesting similarly to hereditary disease, but presenting at much later stages in life. It was determined in a study of the effects of ageing on the limbus, that limbal-stromal vascular structure changes from fine stringy blood vessels to enlarged and shortened vessels. Additionally in the same study it was determined that the presence of the POV decreased from a positive rate of 97.5% in the youngest age group (ages 11-19) down to 40.0% in the oldest age group (60-73) with respective average limbal epithelial cell sizes of $9.89\pm 1.12\mu\text{m}$ and $12.36\pm 1.68\mu\text{m}$, (ref. Figure 1.6) (*Zheng and Xu, 2008*). During the process of ageing the POV become less defined, alluding to a loss of stem cell populations which reduces corneal regenerative capacity as ageing advances (*Zheng and Xu, 2008*). Structural degradation, characterised as a function of the reduction in the presence of focal stromal projections and visibility of the POV by SEM and confocal microscopy has also been employed in a comparison of cadaveric tissue of different ages (*Notara et al., 2013*). Alongside ageing and hereditary disease, lifestyle

choices (including contact lens wear), have been associated with the development of LSCD. This arises from the development of contact lens-induced keratopathy (by the contact of the lenses to the limbus inducing limbal hypoxia) making the LESC microenvironment not favourable for stem cell maintenance. Additionally, mechanical abrasion and potential contact lens solution toxicity contribute directly to LESC destruction and corneal damage (*Bloomfield et al., 1984 Martin, 2006*). The downstream effect of the degradation of the limbus is the observation of the conjunctivalisation of the cornea, which has been observed in patients displaying LSCD associated with contact lens wear (*Rossen et al., 2016*).

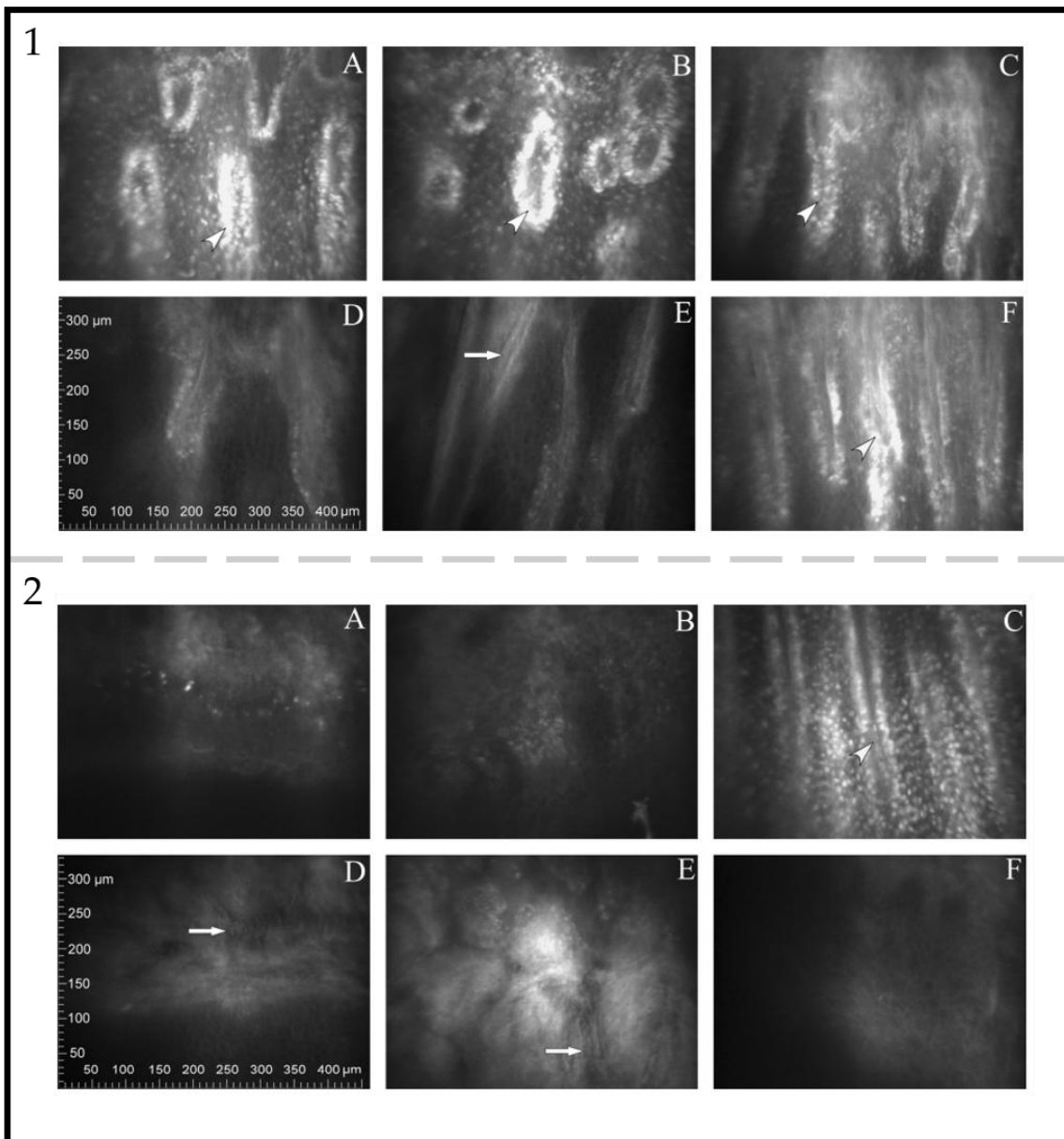


Figure 1.6: Comparative panels of the limbal Palisades of Vogt (POV) in situ demonstrating the effects of ageing. Images are obtained using in vivo confocal microscopy. Sub-panel 1) A, B, C, D, E and F are images of patients aged 11, 11, 12, 13, 17 and 19 respectively, tailed arrows denote the presence of fine blood vessels, tail-less arrows denote the presence of stromal cords. Sub-panel 2) A, B, C, D, E and F are images of patients aged 60, 61, 63, 65, 69 and 73 respectively, tailed arrows denote the presence of large blood vessels, tail-less arrows denote the presence of epithelium-stromal cords. These images show a clear difference in POV presence and morphology between age groups. Images taken from the article (Zheng and Xu, 2008).

Ocular surface neoplasia is a less commonly presenting condition compared to the others described but it can also contribute to LSCD. Tumours of the ocular surface tend to present in the reduction in clarity (and subsequent deterioration in vision) of the cornea and disturbance to the surface architecture and topography. Symptoms of the physical changes can include vision changes (leading to sight loss), bulging/inflammation and (rarely) pain; however, all of these symptoms are not necessarily present together in all patients (*NHS, 2020*). As with neoplasia in other tissues, on the ocular surface, the presentation of tumorigenesis follows a similar scale; from the benign pterygium to aggressive squamous cell carcinoma (*Sayed-Ahmed et al., 2017*). Pterygium formation is a form of ocular occlusion which is limbal-derived. These are fibrotic/fibrovascular invasions into the cornea which can originate via the limbus, whose formation is considered to be induced by ultra-violet light (*Bradley et al., 2010*). These invasive fibrotic changes have also been associated with a decrease in corneal endothelial density, also proposed to be associated with environmental UV radiation, however, this decrease in cellular density was not statistically correlated to the pathogenic presentation and symptomatic presentation of the pterygia (*Li et al., 2018*). These changes over time can be attributed to limbal disruption, as observed in cross-sectional optical coherence tomography of the limbal quadrants. Pterygium presence was specifically observed to affect the superior limbus whilst the nasal limbus was noted to change irrespective of pterygium presence (*Li et al., 2022*). These limbal changes could therefore feed into the widely associated corneal obstructions associated with pterygia, leading to restrictions in sight, due to the reduction in the provision of competent adult stem cells to replenish the corneal epithelium. It has been proposed that the use of UV-blocking contact lenses is shown to have limbal protective qualities in the short-term with the prevention of UVB-induced DNA

damage and limbal phenotypic loss with analysis of stemness markers ABCB5, P46 α and integrin β 1 (Notara et al., 2018).

1.3.2. Overview of the Current Treatment and Intervention of Corneal Disease

There are multiple interventions available for the treatment of diseases and trauma for the ocular surface (specifically the cornea) approved by the National Institute for Care Excellence (NICE). The approved treatments can be ailment-specific, for example; photochemical corneal collagen cross-linking used in the treatment of keratoconus. This procedure is used to strengthen the cornea to mitigate the progression of the disease (NICE, 2020). Additionally, there are treatments which may be a general purpose solution such as the cornea transplant (NICE, 2020). Within the remit of corneal transplant, there are three subtypes of procedure; penetrating keratoplasty (full thickness), deep anterior lamellar keratoplasty (the outer and intermediate corneal layers) and endothelial keratoplasty (the innermost corneal layer) (NHS, 2020). Keratoprosthetics is the use of biomaterials in place of donor tissue to replace damaged cornea. This approach is used when donor tissue is not appropriate for the condition or the patient, however (similarly to the regenerative approaches) this requires special consent and permission to be performed on a patient due to limited safety and efficacy data (NICE, 2020).

1.4. REGENERATIVE APPROACHES AND CELL THERAPY USING LIMBAL STEM CELLS

Regenerative medicine provides exciting avenues for a plethora of diseases that traditionally would have otherwise been thought incurable or something to be tolerated. In other tissues and organ systems, regenerative approaches are making breakthroughs e.g. autologous chondrocyte therapy being a NICE approved therapy which is gaining traction (*NICE, 2020*).

However, despite the ease of accessibility to the limbus by the front of the eye, the regenerative approach has yet to take its place amongst the standard interventions currently used. It is proposed that the severely debilitating nature of side effects and treatment failures (vision impairment/loss) may significantly contribute to this lack of adoption but the availability of donor tissue for research, treatment manufacture and administration also presents major challenges to overcome.

Multiple studies have been carried out on the implantation of limbal stem cells for the potential treatment of diseases caused by limbal stem cell deficiency. Early studies date back to the late 1990s, including the application of allografted limbal stem cells into patients with reported limbal stem cell deficiency. Findings indicated that patients transplanted with limbal stem cells displayed epithelization and corneal recovery. Furthermore, few patients received side effects from these studies indicating a potential avenue for corneal regenerative research and medicine (*Tseng et al., 1998, Dua et al., 1999*). A later example of this successful regenerative approach is the transplantation of ex vivo expanded LESC, which garnered popularity with the media and brought positive attention to the field (*Kolli et al., 2009*). Despite these promising results, however, this particular approach is not yet

fully approved to be used in clinics without special dispensation to perform the procedure or research.

It is the view of NICE that limbal cell allografts are not adequate in terms of safety and efficacy (*NICE, 2020*). However, in a retrospective study of ophthalmological cases, one alternative called autologous simple limbal epithelial transplant (SLET) has proven a successful and potentially safer alternative. With the use of patient-derived limbal cells, this circumvents the immunological challenges and risk of outright rejection of allografts (*Sangwan et al., 2012, Vazirani et al., 2016*).

Within regenerative approaches, 3D culture technologies have seen prevalence in other tissue types. These applications range from in vitro creation of cell-laden structures with expanding cells which are transplanted into an injury to regenerate a wound. An example is the use of a 3D printed staggered lattice pattern gel laden with dental papilla cells and Hertwig's epithelial root sheath cells to begin the regeneration of rat dental fossae within 8 weeks (*Tang et al., 2022*). This approach describes the use of a "pre-fabricated tissue" of cells shaped to fit a structural feature, which over a healing period thereafter integrates into the wound and begins to regenerate the entire anatomical superstructure. An alternative approach, still using a 3D technique, describes the expansion of cells in a 3D spheroid culture to achieve a specific cellular function before transplantation. The use of Mesenchymal stem cells/Human umbilical vein endothelial cell spheroids in ischemic stroke therapy development is an example of this approach. In this study, the generation and implantation of these spheroids demonstrated pro-neurogenic/neuroprotective qualities in both neurite outgrowth assays and in transplantation into rats with ischaemic brain injury (*Hsu et al., 2021*). These approaches can be translated in the regeneration of the cornea and adaptations of

these approaches are in various stages of development. In the vein of pre-expanded 3D culture, excised and seeded human lenticles are an example of a transplantable biologically derived construct seeded with corneolimbic epithelial cells. This study was a proof of concept of the successful transplantation of these scaffolds in a live host (*Park et al., 2023*). Similarly, material-based methods have been used to a similar end where a semi-synthetic material membrane of silk-fibroin and polyethylene glycol successfully supported sheets of LESC cells of a few layers in culture. These sheets were transplanted into a rabbit LSCD model and presented a significantly lower neovascularisation score 60 days after transplant compared to silk fibroin grafts alone (~1 for silk fibroin-LESC grafts compared to >3 for silk fibroin alone). Additionally, the clarity score was significantly greater in the silk fibroin-LESC grafts (with a clarity score of >3 compared to a score of <1 for the silk fibroin grafts alone (*Li et al., 2017*)). These promising examples of 3D cultured LESC transplant technologies highlight the emergence of transplantable ex vivo cultured 3D constructs containing LESC with restorative potential for conditions such as LSCD and other corneal diseases.

1.4.1 Cell Sources

In the investigation and treatment of limbal epithelial stem cell niche and limbal conditions, there are a variety of cell sources that are considered. For research, typically animal model tissue is used; many studies have employed rabbit models in the study of limbal structure, cell cycle proliferation and cell culture studies (*Park et al., 2006, Góes et al., 2008, Yeh et al., 2016*). Whilst highly accessible, small animal species are not truly translatable models to the human limbus, to remedy this, the porcine limbus was characterised and found to be close to the human limbus in both structure and phenotypic function. Therefore the use of

porcine tissue is an effective animal model for human limbal tissue investigation (Notara et al., 2011). Regardless of how effective animal models and animal-derived models may become, currently, the use of animal cells and animal-derived products is not permitted unless under specific conditions outlined by guidance EMEA/CHMP/CPWP83508/2009: the guideline on xenogenic cell-based medicinal products. This guideline concerns the production of advanced therapeutic medicinal products (ATMPs) by the EMA (EMA, 2024). Therefore, in the treatment of disease in humans, cells are currently sourced from humans, from allogeneic sources which are cultured in vitro before transplant or autologous (sourced from the recipient patient) (Paulkin et al., 2010). These expanded cell transplants have the advantage of providing a regenerative therapeutic course of treatment however, there are considerations to the preparation and implementation of these cultures clinically. The principal consideration is the requirement for xeno-free or ATMP regulatory approved culture conditions (EMA, 2024). This extends not only to the cell type used as aforementioned but also to the medium components, culture substrates (if a specialist culture surface such as an amniotic membrane is to be used) and matrix simulating coating components (Cite). The pipeline for producing the limbal cell transplants falls under the category of “point of care manufacture” (Hourd et al., 2014). This classification comes primarily owing to the challenges of storing the limbal stem cells, where it has been found that even relatively short-term storage (up to 7 days at 4°C) can reduce the proliferative capacity and reduction in limbal stem cell markers such as P63 and CK19 (Liu et al., 2012). Therefore with these considerations in mind, limbal stem cell transplant cultures are typically isolated, expanded and transplanted within the shortest amount of time to maximise the stemness of the transplanted cells and maximise the success rate as discussed in section 1.4.3.

1.4.2 Maintenance of LESC Stemness in the Stem Cell Niche

Maintenance of stemness is the critical function of the niche, this is carried out at all levels of consideration of the niche previously described. At the anatomic level, it may be said that the crypt morphology of stem cell niches conserves the stemness of the epithelial stem cells in that particular niche. This statement can be attributed to the observation that the stem cells for an epithelial stem cell niche are located in the basal apex of the crypt. This observation is not only made in the limbal niche but other tissues such as the intestine and skin (*Carulli et al., 2014, Gonzales and Fuchs 2017*). Crypt morphology and basal localization relate to both the slow-cycling proliferative and high differential capacity properties of the limbal stem cells, this localization serves as a highly regulatory segregation mechanism. Put simply, the crypt serves as a 'pouch' in which the stem cells are held until they are required (by being drawn out of the niche following the XYZ hypothesis).

In parallel to the anatomical features of the niche, the correct culture conditions drive the maintenance of the tissues and stem cell characteristics. When culturing ocular epithelial tissue, it is important to remember that keeping a monolayer on tissue culture plastic bathed in media, is not representative of the nature of the ocular surface (both in terms of anatomical structure and physiology) (*Grieve et al., 2015, Haagdorens et al., 2017*). The limbus is a matrix-dense tissue with heavy levels of keratinisation at the corneal leading face: where corneal differentiation out of the limbus arises (*Pathak et al., 2016; Shi et al., 2020*). Therefore when culturing limbal epithelial cells in a monolayer with a low-viscosity aqueous solution they will not maintain their true limbal stem cell properties. Hence engineering the correct microenvironment is of vital importance. This can be effectively combatted using hydrogels to suspend the cells in 3D culture, allowing

the cells to orientate, expand and signal in 3 dimensions (which is more representative of tissue). Examples of such studies include compressed collagen gels for LESC culture (*Mi et al., 2010*), Xeno-free hydrogels such as the Hy-stem-c hydrogel (*Chen et al., 2017*) and biomaterial scaffolds including electrospun PCL (*Sanie-Jahromie et al., 2020*). In these examples the seeding mechanism and therefore the direction of cell propagation were different. For example, the keratinocyte-encapsulated compressed collagen gel was purely a surface alternative to the amniotic membrane for the limbal epithelial cells to grow upon. However, these epithelial sheets developed stratification and presented positivity for Ck3 and Ck14, demonstrating the maintenance of a limbal epithelial with a capacity to differentiate the cells towards a corneal fate (*Mi et al., 2010*). Whilst not vastly different in terms of being a surface-seeded construct the electrospun PCL allowed the limbal stem cells to penetrate the pores of the nanofibre scaffolds to small depths (as visualised by scanning electron microscopy), therefore, whilst being a surface-seeded scaffold, they possess a degree of porosity to facilitate a deeper 3D culture (*Sanie-Jahromie et al., 2020*). Finally, the Hy-stem-c hydrogel was used as a growth surface to extract cells from limbal explants placed on the surface and grow epithelial cell layers up to 5-7 cell layers thick after 21 days. These expanded tissues showed positivity (by immunofluorescence) for ABCG2, Involucrin, K12, connexin 43, K19 and integrin β 1. Co-expression of these markers together demonstrated an ability to isolate and expand from explants a 'tissue' that possessed limbal progenitor phenotypes but also showed commitment towards the corneal epithelial fate through the full thickness.

Topography, as a physiological micro/nanostructure aids in the establishment of the necessary microenvironment. This is achieved by facilitating native matrix protein expression and deposition. The topographic profile has an

entrapping effect, amplifying the effects of material absorptive/adsorptive properties or functionalising components (as further discussed), by exploiting the principle of increasing surface area and roughness to achieve this increase in matrix deposition. Topography has demonstrated the ability to self-assemble a large corneal construct through its influence over matrix deposition spatial arrangement of cells and matrix adherence, using corneal stromal cells (*Guillemette et al., 2009*). Studies with non-limbal stem cell types, at the cellular level, such as corneal stromal stem cells demonstrate how the influence of surface topography enhances matrix deposition and ordered self-assembly (*Karamichos et al., 2014*). In later studies, this effect was defined more clearly with a grooved substrate achieving both cellular alignment and significant matrix organisation, whilst allowing for the maintenance of construct integrity after removal from the substrate (*Syed-Picard, 2018*). There is a lack of characterisation of limbal matrix deposition, however, from the perspective of the limbal cell-to-matrix interaction, there is some progress. The presentation of focal adhesions between limbal epithelial cells and silk fibroin/silicon wafer substrates which were topography-dependent illustrates this effect well (*Lawrence et al., 2012*).

In addition to topography, functionalisation of the biomaterials used will aid in the achievement of increased matrix expression/deposition or use as a substitute for the native matrix, as reviewed by Rahmany and Van Dyke (*Wang et al., 2015, Chen et al., 2017, Rahmany and Van Dyke, 2013*). This commonly used term (functionalisation) refers to the enhancement of the material interactivity biocompatibility. Such features include: reducing cytotoxic properties, enhancing hydrophilicity and promoting a more biomimetic bonding pattern/type adopted during cell adhesion to the material (*Rana 2017; Carmagnola et al., 2018*). *Table 1.3* lists common surface functionalisations and native matrix components often used in cell culture. Such enhancements are generally achieved by applying a

coating or subjecting the surface to a modification process such as laser radiation treatment applied to poly(2-hydroxyethyl methacrylate) to improve the attachment of limbal epithelial cells (*Zainuddin et al., 2011*). Additionally, physical surface treatments such as plasma oxidation may be employed to improve the culturing viability of the surface. For materials such as Polydimethylsiloxane (PDMS), oxidative plasma can be used not only to generate topography (as later discussed) but to also enhance cell adhesion (in conjunction with other components) as observed with LESC (*Kang et al., 2012*) and as also noted with the treatment of poly(lactide-co-glycolide) with oxygen plasma (*Wan et al., 2004*)

Surface functionalising component	Application	Cell type	Reference
Matrigel	Expansion of Limbus-derived (Human) LESC	ABCG2 ⁺ and ABCG5 ⁺ cells	<i>Kim et al., 2017</i>
Fibronectin Laminin Collagen IV	Expansion of corneal epithelial cells on processed fish scales as a novel substrate for potential transplantable substrate	Immortalised Human Corneal Epithelial Cells	<i>Hsueh et al., 2019</i>
Laminin 1 and 5	Coating of glass for the transdifferentiation of hair follicle stem cells into corneal epithelial-like cells.	Murine vibrissa follicular epithelial cells	<i>Blazejewska et al., 2009</i>
Acrylic-modified contact lens	Limbal Explant Culture, Progenitor maintenance	Limbal explant	<i>Zhang et al., 2014</i>
<i>B. mori</i> cocoon silk	Expansion of limbal epithelial/stromal cells as a potential transplantable scaffold	Human limbal epithelial and stromal cells	<i>Bray et al., 2013</i>
Chitosan Gelatin	Expansion of limbal epithelial cells and corneal cells for the assessment of the biocompatibility of these materials as culturing substrates	Human limbal epithelial cells and human corneal epithelial cells.	<i>De la Mata et al., 2013</i>
Laser treatment	Laser treatment of poly(2-hydroxymethyl methacrylate) for improved cell adhesion	Limbal epithelial cell culture	<i>Zainuddin et al., 2011</i>

Table 1.3: Additional materials commonly used as coatings or laminar materials to functionalise cell culture substrates. The use of these materials is considered commonplace in tissue engineering and cell culture, the above examples selected are for limbal and corneal applications exclusively.

At the signalling level, the Hippo signalling pathway, via the Yes-associated protein (YAP) (*Mahoney et al., 2014*) is recognized as an epithelial developmental pathway which is implemented during the morula stage, activating the Sox2 gene transcription. Control of Sox2 gene products and their downstream effectors contribute to the maintenance of stemness and increase the proliferative capacity of stem cells, (*Bhattacharya et al., 2019* *Rossant and Tam, 2017*, *Wicklow et al., 2014*).

Of significant interest to limbal engineering, the Yes-associated Protein 1 (YAP1) is one of these effectors. YAP1 has been detected in both corneal basal epithelial cells and limbal epithelial cells and is proposed to have a regulatory effect on the limbal differentiation into corneal tissue. YAP1 knock-out prevented corneal epithelial expansion (*Kasetti et al., 2016*). Furthermore, it has been demonstrated that YAP in addition to Np63 and β -catenin (a pro-proliferative pathway), all regulate the stem cell phenotype and can be modulated by substrate stiffness. It is reported that with a softer substrate, greater YAP inhibition is observed alongside greater Np63 expression and β -catenin activation, resulting in greater LESC expansion. Stiffer substrates resulted in LESC proliferation inhibition indicating mechanobiologically controlled differentiation (*Gouveia et al., 2019*). β -catenin is part of the Wnt/ β -catenin pathway. Substrate stiffness relates to native matrix stiffness where these models have demonstrated to some precision the relationship between stiffness and LESC behaviour, in native tissue it has been observed that changes in tissue stiffness are related to ageing and disease. This effect was demonstrated by the conjunction of findings that firstly, the cornea and corneoscleral axis stiffened with age (*Elsheikh et al., 2010*, *Geraghty et al., 2014*). Secondly, there is significant limbal niche structural degradation coupled with a significant reduction in key LESC marker expressions such as CK16, P63 and ABCG2 showing a

reduction in stem cell presence in the elderly limbal niche (*Notara et al., 2013*), this structural degradation presented in a loss of limbal crypt visibility and definition, meaning that the anatomical structure required to house the limbal stem cells was diminishing as alluded to by the reduction in stem cell marker expression. Appreciating these relationships together, the corneoscleral axis stiffens with age and there is a visible age-related degradation in the limbal niche anatomy which corresponds to a loss in stem cell presence, it is plausible to correlate these relationships. The effect of actively softening the corneal matrix has been explored (using collagenase directly) and has demonstrated that a region live cornea, after treatment with collagenase to soften the matrix, presents evidence of a much greater capacity to maintain epithelial progenitor populations (by presenting limbal markers such as p63, ABCG2 and CK15) whilst showing a marked decrease in the epithelial markers (CK3 and $\alpha3\beta1$). This demonstrated an active stiffness-dependent reversal of phenotype in vivo. However, for a medically relevant model to determine the effect of substrate stiffness on limbal stem cell fate actively, the integration of niche anatomical structure changes is needed in future models to fully model age-related and pathological changes in the limbus.

This pathway maintains stemness through the prevention of β -catenin degradation by the binding of Wnt to the Frizzled receptor and its coreceptor LRP5/6 (*González et al., 2019*). BMP signalling additionally complements Wnt signalling as this pathway is integrated with the Wnt pathway. The BMP/Wnt pathway in the limbal niche regulates SMAD (mothers against decapentaplegic family transcription factor signalling) in addition to β -catenin as part of the Wnt/ β -catenin pathway (*Theerakittayakorn et al., 2020, Zhang et al., 2015*). The regulatory function of this pathway chiefly maintains the quiescence of LSCs within the niche. The BMP pathway is maintained as a crosstalk between the niche cells and the limbal

epithelial progenitor cells (those beginning commitment in the transient amplification stage). Knockout of this regulatory function results in the loss of maintenance of stemness (*Chen et al., 2015*). The Notch pathway plays a role in the regulation of corneal wound healing. Notch signalling follows the scheme of ligand-to-notch receptor binding to gene transcription, which includes: the hairy and enhancer of split1, hairy and enhancer of split-5 and hairy/enhancer-of-split related with YRPW motif protein 1 (HES1, HES5 and HEY1 respectively). However, despite being observed and measured in studies, this pathway has not been characterised fully in the corneal/limbal regulatory context. Inhibition of this pathway completely prevents the differentiation of LESC into corneal tissue, but not the ability to stratify when it is air-lifted (*González et al., 2019*). Notch-1 has been detected in the basal corneal epithelium, suggesting this, alongside the limbus to be a regulatory zone for cell proliferation and differentiation (*Thomas et al., 2007*).

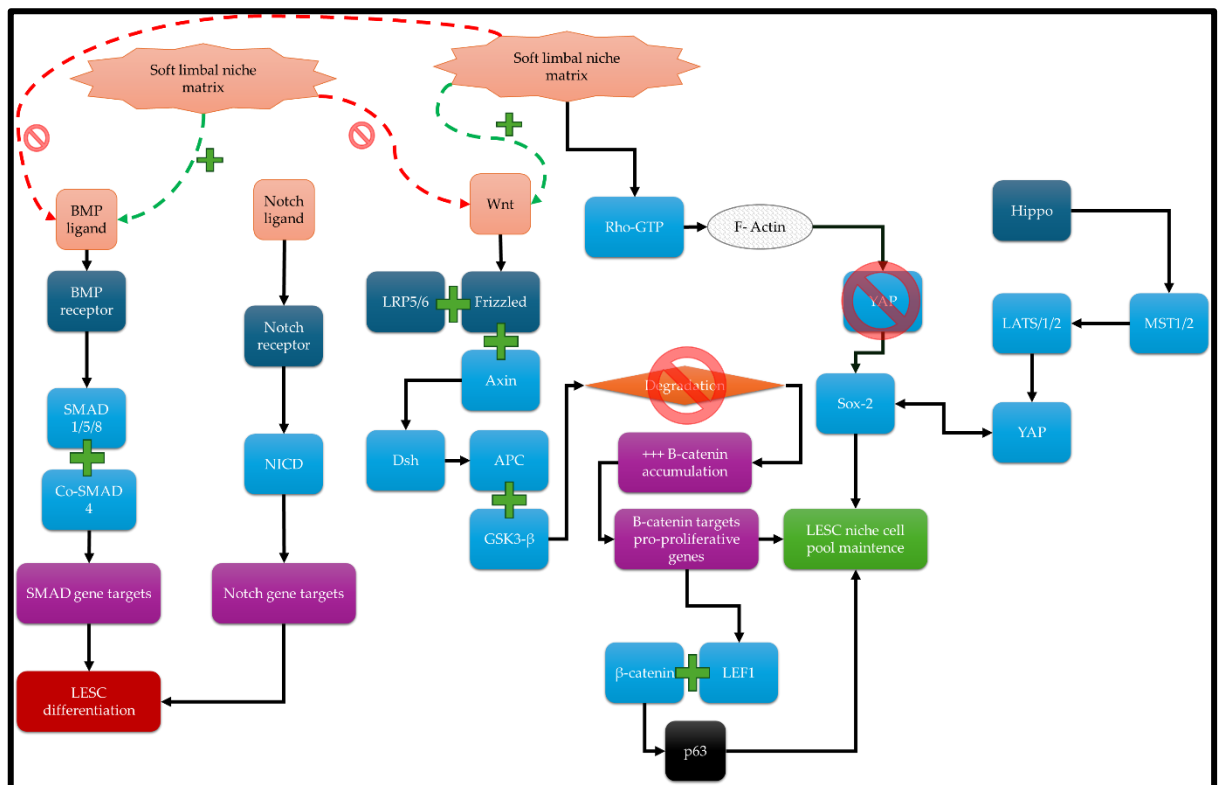


Figure 1.7: Overview of the key pathways responsible for LESC maintenance and induction of differentiation. The pathway scheme outlined includes mechanobiological dependent signalling, a crucial determiner of LESC fate within the niche (Reya and Clevers 2005, Mahoney et al, 2014 Zhang et al., 2020 Xie et al., 2020 Gouveia et al., 2019 Fisher et al., 2020 Robertson et al., 2021).

The sonic hedgehog signalling pathway (often shortened to hedgehog or Shh) in development is involved in the decision of limb patterning, left-right asymmetry, the anterior-posterior axis and hair follicle formation. However, in adult life, this pathway is yet another internal stem cell maintenance regulatory pathway employed by the LESC niche regulating the cell cycle and critical to corneal wound healing (Saika et al., 2004). Following the same signalling format, the ligands including pigment epithelium-derived factor (PEDF) bind to their corresponding receptor, transduce down the hedgehog (Shh) pathway and initiate the transcription of the Gli3 gene which regulates LESC proliferation and migration (Fan et al., 2019).

The use of epidermal growth factor as a media additive (biochemical stimulus) for maintaining the stemness of limbal stem cells is considered a more conventional way for maintaining stem cell qualities in culture with this approach

being a widespread staple not only in this field (*Fernandéz-Péres et al., 2017, Meller et al., 2002*) but in wider stem cell science such as embryonic culture, iPSC culture and neural progenitor culture. In addition to the use of growth factor, feeder cell cultures such as the 3T3 fibroblast secondary culture can be also implemented to maintain the stemness of cultured limbal epithelial cells by reducing stress-induced cellular damage. Such a protocol was used to expand limbal epithelial cells ex vivo for human limbal epithelium with a human-derived 3T3 feeder layer which is a viable xenobiotic-free alternative to murine 3T3 layers used for therapeutic expansion (*Sharma et al., 2012*). Additionally, a study which employed murine 3T3 in its evaluation of a selection of human-derived feeder layers on LESC expansion for the same purpose, however, this study found its limitation in the use of rabbit limbal cells instead of human cells (*Wang et al., 2017*).

1.4.3 Regenerative Treatment Strategies for Limbal Conditions

These therapies are specifically designed to facilitate tissue regeneration towards original or near-original tissue functionality using transplanted stem cells. These cells are typically taken from a donor source, either the same patient or a compatible donor, and transplanted after a culture or processing phase. *In situ*, these cells differentiate into the target tissue and self-regulate in the same manner the original missing stem cells should (*Kumar et al., 2022*).

In limbal disease, typically simple limbal epithelial transplant (SLET), where LESC are transplanted from the patient's healthy eye into the affected eye, is indicated for LSCD. However, SLET is contraindicated for dry eyes, blindness, disorganized anterior segments untreated adnexal pathologies (*Moshirfdar et al, 2023*). Alternatively, cultured limbal epithelial transplants (CLET), a procedure

where cells from a donor are cultured externally before transplantation into the patient's eye(s), has demonstrated prospective indications for burns, chronic injuries, ulcers, congenital defects and surgical applications which require specialist-controlled epithelial regrowth (*Dhar et al., 2023*). In a registry consolidating cultured epithelial autograft surgery outcomes in burn patients, success rates were good. Out of 68 patients, overall survival was recorded at 87% (94% paediatric/ 84% adult) whilst the percentage mean engraftment was recorded to be 81% percentage in adults and 84% in paediatric patients. It is interesting to note that the paediatric statistics are more favourable towards higher rates of engraftment and survival (*Fagan et al, 2024*). Currently the regenerative approach of corneolimbal transplantation by way of limbal transplantation has demonstrated good long-term outcomes through the reduction of the return of LSCD symptoms in allograft techniques. However, autograft techniques proved to be much less ineffective. This was assessed by evaluating the survival of transplants, using four different techniques across a 60 month post-operative period (*Borderie., 2019*).

Technique	Implant success rate	Maximum assessment period	N _{total} Patients	Source
Cultured limbal epithelial transplant	81% adult 84% paediatric	Average 109.2 adult Average 111.1 paediatric	68	Fagan et al., 2024
	77%	1 year	112	Rama et al., 2010
	41.6% at 2.1 years 23.1% at 6.7 years	Average 6.7 years	9	Behaegal et al., 2019
Autologous Cultured limbal stem cell Transplant	100% (3 years) 71% (5 years)	5 years	7	Borderie et al., 2019
Allogeneic cultured limbal stem cell transplant	29% (3 years) 0% (5 years)	5 years	7	Borderie et al., 2019
Autologous limbal tissue transplant	75% (3 years) 75% (5 years)	5 years	8	Borderie et al., 2019
Allogeneic limbal tissue transplant	50% (3 years) 33% (5 years)	5 years	8	Borderie et al., 2019
Conjunctival limbal autograft	77.8%	Average 4.15 years	27	Elsani et al., 2019

Table 1.4: Summary of limbal epithelial surgical interventions and their success rates. This summary includes the maximum assessment period and some key assessment time points. Implant success rate is defined in each particular study however the key definitions relate to ocular surface integrity, clarity and pain.

A review of the current options for the treatment of LSCD outlines a strategic approach to the identification and management, firstly the inflammation is controlled then either LSCD is identified as either partial or total LSCD. CLET, as an allogeneic stem cell transplant procedure (with a 70-77% long-term success rate with an 81% adult engraftment rate) (Rama et al., 2010, Borderie et al., 2019, Fagan et al., 2024) has both unilateral and bilateral application, which contrasts with SLET which is unilateral only with a 50-100% success rate (Vazirani et al., 2016, Borderie et al.,

2019, Elhusseiny et al., 2022). An initially earlier developed method, but still largely successful (77.8% success), is the conjunctival limbal autograft (CLAU) transplant method, where a larger portion of tissue compared to SLET is transplanted into the LESC-deprived limbal niches to instigate regeneration (Elsani., 2019, Elhusseiny et al., 2022) In addition to limbal transplant procedures, methods including the application of human amniotic membrane to the deficient limbus has shown promise in corneal applications through its use in the treatment and recovery of corneal ulcers (up to 93% closure rates) (Sheurech et al., 2021). Although mesenchymal stem cells (MSC) have exciting applications in the scientific research field, there is currently limited pre-clinical or clinical trial data to support the safety or adoption of MSCs clinically until there is further information with the animal/stimulatory models to support the safe use in humans. An example of a potential MSC application which may be suitable is the En^+/En^- Human limbal MSC tested in a rabbit transplant model which showed they did not have a deleterious effect on the host and may be safe for human indication (Damala et al., 2023).

1.5 VIEWING THE LIMBAL NICHE FROM DIFFERENT PERSPECTIVES

1.5.1 Histological Characterisation of the Limbal Niche

Histology is a widespread tool for visualising tissues functionally and structurally, typically the tissue is sliced into very thin sections after being embedded either in wax or cryo-sectioned as frozen mounted sections. As part of the revelation of tissue structure and cellular function, various stains can be applied to sectioned tissue. Such stains can range from the commonly used combination of haematoxylin and eosin (H+E), used to stain nuclei (haematoxylin, purplish blue) and the

extracellular matrix (eosin, pink). An example of this stain being used to affect limbal characterisation is in the sequential slicing and staining of the limbal structure using H+E to reveal the undulations within the LESC niche, through the POV, as exemplified in Figure 1.6 (*Dua et al., 2005*).

In addition to the use of structural revealing stains such as H+E, immunohistochemistry, exemplified by Figure 1.8, can be used to look for markers of interest in a given sample, alluding to the tissue and their constituent cell functions. In the characterisation of the LESC niche, epithelial markers such as the cytokeratins 13, 14, 15 and 19 were shown to be localised throughout the limbal epithelium, identifying these cells as epithelial (*Dua et al., 2005, Pathak et al., 2016*). The limbal epithelial stem cell markers ABCG2 and P63 have been used to identify basally located LSCs (*De Paiva et al., 2005, Shanmuganathan et al., 2007*).

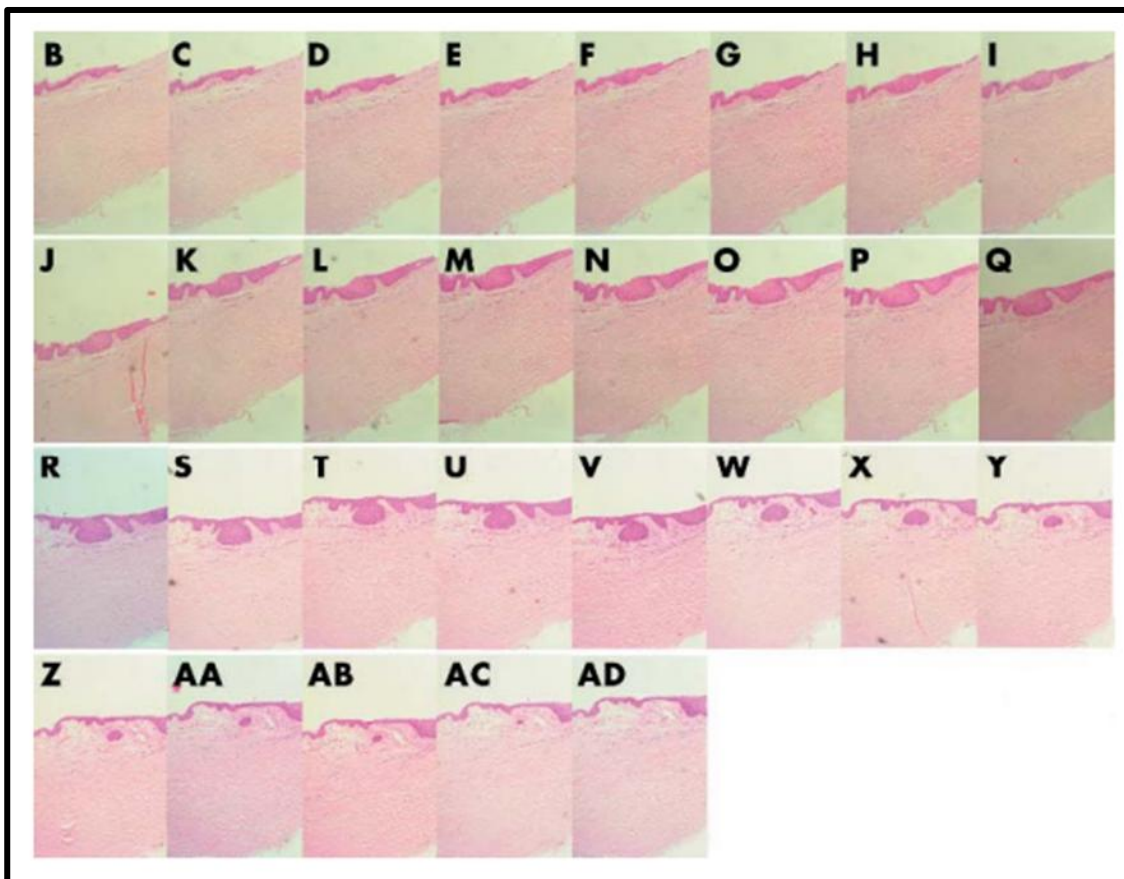


Figure 1.8: H+E stained sequential sections of the LESC niche. B-AD shows how the niche propagates through the POV, interspersed by undulations. Magnification is 100X, image taken from (Dua et al., 2005).

1.5.2 3D Imaging of the LESC Niche

In association with the sliced methodologies of collating imaging information about the LESC niche, there are alternative imaging modalities to view the LESC niche. These modes of imaging, including variants of confocal microscopy, can reduce the destructive impact that slicing tissue can impart on the tissue structure. A notable study by (Grieve et al., 2015) characterised the mammalian LESC niche using confocal microscopy, revealing the undulating structure around the entire limbal crypt. Additionally (Notara et al., 2011) using confocal microscopy with immunostaining in conjunction with scanning electron microscopy to reveal structure, determined the functional and phenotypical similarity of the porcine limbus to humans. In a similar vein, (Massie et al., 2015) outline a protocol for resin embedding whole limbal tissue for high-resolution scanning electron microscopic imaging.

1.5.3 Mechanical Characterisation of Corneolimbal Tissue

The characterisation of corneolimbal tissue pre-OCE has been restricted to traditional compression-based methodologies. A prime example of a compression methodology would be the use of nanoindentation to derive Young's modulus for the corneoscleral rim, wherein the limbal region was found to be 10Kpa by this method (Eberwein et al., 2014). Concerning surface compression methods, a method of the analysis of anatomical mechanical properties at high resolution was the use of atomic force microscopy to measure the Bowman's layer, Descemet's

layer and the anterior layer which yielded Young's moduli ranging between 2-123Kpa (*Last et al., 2009, Last et al., 2012*). However, an application which could be considered a precursor to OCE would be the derived optical image-based analysis based on set intra-ocular pressures. Here image sets were acquired across cadaveric donor corneas, and then the regional stiffnesses were calculated based on the strain measured when the tissues were subjected to a defined intraocular pressure (*Hjørtaal et al., 1996*).

1.5.4 Optical Coherence Tomography

Optical coherence tomography (OCT) is an imaging modality which utilises long wavelength light (typically towards the infrared end of the spectrum) to be able to penetrate shallow depths in certain media, particularly soft tissue. Although there is a large growing variety of OCT technologies, commercially and within research, the governing principle behind OCT is the same. The near-infrared light is split into separate paths by an interferometer, the scanning beam is directed to the sample while a reference beam is directed via a separate arm to a mirror. The scanning beam, typically a linear scan across a b-line, is scattered and reflected by the sample back towards the device. The reflected scan beam superposes with the reference beam and the coherence is recorded by a photodetector and processed into an image by a computer (*Aumann et al., 2019*). In non-mechanical dependent methods of A-scan generation (for example Fourier domain OCT and spectral domain OCT), the A-scan component is computed, not scanned mechanically across the optical path. During this computation, the acquired spectrum is processed using a Fourier transform to generate the computed A-scans which can be computed into visible images. (*Zhang et al., 2016*).

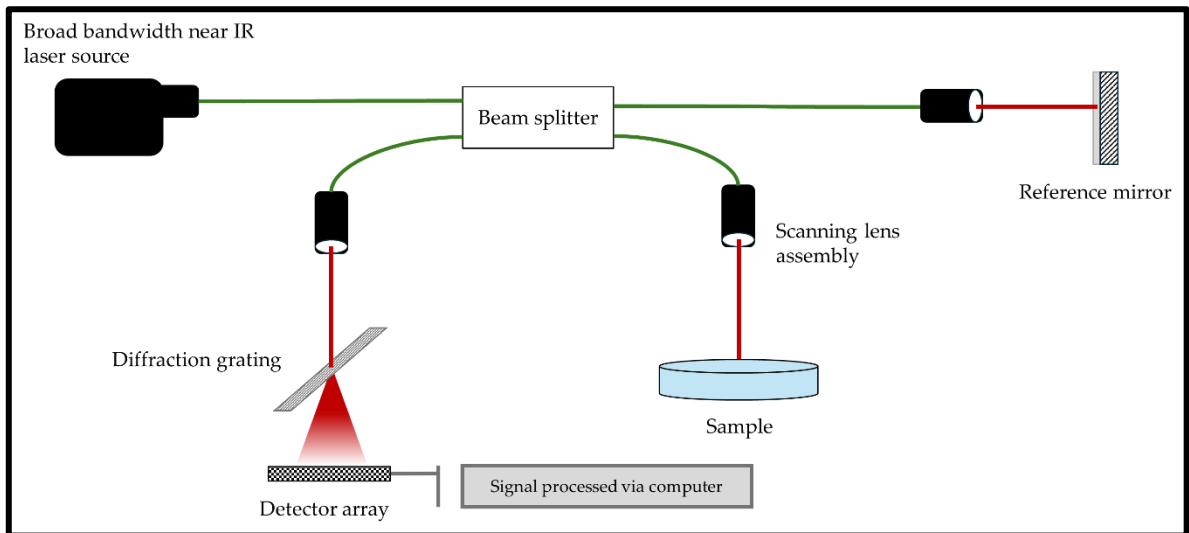


Figure 1.9: Schematic representation of a spectral domain OCT (SD-OCT) system. SD-OCT records the diffracted scan beam (which splits the beam into spatially separated wavelengths) using a high-speed line camera (Li et al., 2012, Aumann et al., 2019).

Optical coherence tomography is a clinically utilised technology that is typically used in clinics and by optometrists to measure the thickness and quality of the retina. In retinal diagnostics, it is typically used to screen for macular degeneration and diabetic retinopathy. However, OCT is becoming an emerging imaging technology in other tissue applications and is seeing translation in epithelial studies. Of interest is its application in ocular surface study. Currently, high-resolution images are restricted to relatively wide-view structural imaging (where the structural imaging encompasses several millimetres of width) often over a large radial cross-section over part of the sclera, the limbal crypt and a substantial part of the central cornea. This is advantageous in the diagnosis of wider corneal disease, for example, the diagnosis of pterygium and keratoconus (Soliman and Mohamed, 2010, Rocha et al., 2013) It is still however limited by structural resolution for niche imaging.

OCT has also been used in the diagnosis of limbal stem cell deficiency, however, like the aforementioned examples the resolution of the limbal structure

was low and restricted to broad regional resolution due to the wide imaging window. However, it is of valuable note that macrostructural changes, including fibrosis, were detected to allow the diagnosis of LSCD (Mehtani et al., 2017). As these developments move forward, it is becoming increasingly possible to use high-resolution OCT to resolve limbal crypt microstructure. Such advancements in the increase of imaging resolution can be attributed to the refinements of the bipartite nature of OCT resolution; the transverse resolution and the axial resolution (Drexler 2004). Optimisation of the axial resolution is mainly found in the improvements in technical specifications of setup components. For example, a laser with a specific near-infrared wavelength such as 800nm (Werkmeister et al., 2017) will yield a greater structural resolution, by having a smaller axial resolution, compared to a device using a longer spectral laser wavelength (Ishida and Nishizawa, 2012). In terms of transverse resolution, optimisation of this property can be improved in the same manner as other optical systems as it is related to the focal point of imaging. Transverse resolution is governed by the focused transverse spot size, given as $\frac{1}{e^2}$ of the radius of a Gaussian beam, where the beam is defined by:

$$\Delta x = \left(\frac{4\lambda}{\pi}\right)\left(\frac{f}{d}\right)$$

Where d = the spot size and f = the focal length. In lieu of this, the transverse resolution is also relatable to the double Rayleigh length of the objective, defined as:

$$2z_r = \frac{\pi\Delta x^2}{2\lambda}$$

This means that to optimise the transverse resolution, the aperture size can be reduced at the cost of diminishing focal depth (thus reducing the depth of penetration and working distance) (Drexler, 2004). The use of computed profiling

from Fourier domain OCT shows the possibility of quantifying the epithelial rete peg and palisade ridges within the palisades of Vogt using this technique (Haagdorens et al., 2017).

1.5.6 Optical Coherence Elastography

Optical coherence elastography (OCE) is an advancement of OCT. In this modality, an OCT system is used as the camera capture system whilst a mode of agitation (whether sample or camera-based) is imparted to induce an intentional displacement in the sample. The differences in the tracked displacements in the sample are compared to relative regions within the sample or standards of known stiffness (*Kennedy et al., 2014*). Currently, investigation into the limbal niche is fairly restricted, with ophthalmologists focusing mainly on the central cornea (*Lan et al., 2021*) or the determination of intraocular pressure (*Ma et al., 2023*). Whilst these parameters have extensive clinical use i.e. the monitoring of corneal quality and the diagnosis/monitoring of diabetes, there is little focus on the LESC niche. However, there have been studies performed on the limbus in comparison to neighbouring structures, including the cornea and the sclera (*Zietcovitch et al., 2020, Zhou et al., 2019*). Whilst these studies provided valuable information on the limbal anatomic stiffness as a macrostructure in comparison to neighbouring features, there was no high-resolution insight into the finer POV microstructure of the LESC niche. As there are OCT modalities that can reveal these structures it was hypothesised there is a capacity to mechanically characterise these features together moving forwards as part of the scope of this research.

1.6. REPLICATION OF THE LIMBAL STEM CELL NICHE

1.6.1 The Current State of Limbal Replication

In terms of true limbal replication, there are limited studies on full replication. This is due to the complexity of the internal topography innate to this epithelial stem cell niche. This challenge is manifested through the limbal compound crypt architecture. Therefore the existing limbal replication studies focus on the generation of singular crypts, such studies include those such as the generation of biomimetic limbal crypts in RAFT (Real Architecture for 3D Tissues) constructs (*Levis et al., 2013*). More novel applications such as microfabricated pockets in poly(lactic-co-glycolic acid) to aid in limbal epithelial cell outgrowth in an ex vivo culture model for a regenerative application can constitute limbal replication studies (*Ortega et al., 2014*). However, these can present significant pitfalls when considering the true architectural replication of the limbal stem cell niche, in particular the complex crypt-within-a-crypt presentation, is brought into question. However, the generation of biomimetic limbal stem cell populations, with regenerative therapeutic capacity, holds promise for eventual clinical implementation.

In addition to structural replication, microenvironmental replication has been achieved through the employment of bioreactor technology. Perfusion technology in this field is better known for being employed to preserve whole cornea and decellularized cornea samples (*Guindolet et al., 2017, Garcin et al., 2019*). However, perfusion technology has also been applied to the study of flow shear stress on limbal epithelial expansion (*Kang et al., 2014*). This study highlights the effect of micro-scale mechano-stimulation administered to the cells topically,

therefore demonstrating the prevailing need for the expansion of bioreactor development and investigation in this field, especially from a mechanical perspective.

Though the challenge of true limbus replication is far from being achieved, current studies demonstrate the ability to isolate and maintain the limbal stem cell phenotype and subsequent manipulation thereof. The main purpose behind limbal replication is to create a biomimetic stem cell niche in vitro to have therapeutic potential in corneal regenerative medicine. In addition to studies which intend to structurally replicate the limbus, targeted central corneal regenerative studies (through the use of corneal progenitors (including dissociated limbal-derived stem cells)) have qualities attributable to limbal replication (*Table 1.4*).

Study/Purpose	Type of study	Cells	Primary result	Reference
Long-term culture of corneal explants	Structural/Architectural tissue engineering	Human cornea limbal explants	The outgrowth of organised corneal tissue has the potential for corneal regenerative medicine	<i>Szabó et al., 2015</i>
Compressed Collagen Gels as scaffolds for Limbal Epithelial Cells		Bovine LESC	The Plastically compressed collagen gel was demonstrated to be a superior LESC culture substrate with the LESC presenting more biomimetic corneal epithelial structures with more biologically representative cell morphology/stratification	<i>Mi et al., 2010</i>
Induction of Hair follicle – corneal epithelial (like) cell transdifferentiation using limbal microenvironment	Microenvironmental study	Murine vibrissa hair follicle stem cells	Achievement of HF – CE (like) differentiation, demonstrating a promising source of inducible (through the limbal micro environment) pluripotent cells for corneal tissue engineering	<i>Blazejewska et al., 2009</i>
Limbal niche cells to reduce angiogenesis in cultivated oral mucosal epithelial cells		Rat oral mucosal epithelial cells (COMECs), rat limbal niche cells (LNC) and 3T3 cells	Significantly lesser angiogenic potential co-culturing COMECs with LNCs compared to conditioned medium or a 3T3 layer, showing a more promising avenue for limbal COMEC transplantation as a developing LSCD therapeutic option.	<i>Duan et al., 2019</i>

Table 1.5: Examples of studies which constitute limbal replication. This collation of examples provides insight into the broad definition of limbal replication. Replicating the niche and niche properties does not have to be restricted to full architectural., physiological replication or complete biomimicry, though as a field it has limbal replication has yet to achieve either of these goals.

1.6.2 Control of Differentiation Gradient and Migration out of The Niche

In addition to direct biochemical which generally maintains stemness, cellular mechanobiology, which is tied to tissue dynamics and architecture, is now widely demonstrated to affect cell fate and maintenance. Recent studies seek to elucidate the precise mechanism of mechanotransduction and its subsequent effect on tissue growth, regeneration and development. Such studies are essential to the development of regenerative medicine and have vital value when applied to stress epithelial organs such as skin, intestine and vasculature. These principles can also be applied to limbal engineering, particularly when concepts such as the XYZ hypothesis of corneal expansion and its subsequent effect on limbal stem cell differentiation are considered (*Thoft and Friend, 1983, Joon et al., 2014*). The drawing effect of epithelial expansion, as outlined by this XYZ hypothesis (also regulated by the crypt shape) is proposed to be a driving force in the causation of differentiation by mechanical means, mediated by mechanotransduction signalling. The stiffness of the crypt, at the cellular and tissue level can be attributed to the matrix stiffness which serves not only as the supporting substructure but also as the key physical effector in translating mechanotransduction signalling. Matrix stiffness has been demonstrated to influence LESC differentiation with a pro-corneal tendency, as seen in a comparison between uncompressed and compressed collagen gels which reported moduli for each of ~3Pa and ~2.9 KPa respectively (*Jones et al., 2012*).

Through in vitro cultures and subsequent manipulations, it is observed that changing the shape of the epithelial stem cell niche can determine stem cell fate in terms of stem cell commitment. Such alterations include the modification of niche shape through changes in topography and alterations in crypt stiffness. Current

studies into topographical alterations use nanopatterning of culturing surfaces or membrane base approaches. The membrane-based approach by (Helling *et al.*, 2018) introduced a dynamic method of altering the skin epithelial stem cell niche (Helling *et al.*, 2018). From this it is observed that the imposed undulation caused clustering in human neonatal keratinocytes, which exhibited high expression of beta-1 integrin, E-cadherin and nuclear YAP, thus indicating a potential mechanism in the mechanobiological determination of the fate of stem cells in the epithelial niche. This clustering behaviour also highlights a preference by LESC which tightly localises within a crypt environment. It is proposed that this shape-based-localisation enhances all regulatory mechanisms, including biological and physical methods to both maintain stemness and induce differentiation.

Another study also implicates YAP in fate determination through the YAP-TAZ and Notch signalling pathways via mechanotransduction signalling. Such determination was achieved through the observation of high-volume differentiation and cell cycle termination in YAP/TAZ depleted cells (depletion by short interfering RNA) (Totaro *et al.*, 2017).

Therefore it is plausible to propose that the crypt shape in terms of steepness and curvature affects stem cell maintenance by having a physically additive effect (through the effects of cellular mechanobiology) on the stem cell maintenance pathways within the crypt. Additionally, it may be proposed that the crypt slope at different gradients affects LESC proliferation and differentiation. This is in line with the XYZ hypothesis (Thoft and Friend, 1983, Joon *et al.*, 2014) and other in silico crypt-based growth models. Which although being intestinal tissue-based has strong relatability in terms of crypt niche function (Sei *et al.*, 2019). Furthermore, in-depth characterisation of the effect of limbal crypt morphology on stem cell fate will elucidate the downstream effects of optical surface inflammatory disorders on

LSCD, transplant efficacy and predictive capacity. There is a current deficit in the capacity to predict whether an individual is liable to develop corneal abnormalities arising from LSCD later on in life due to a pre-existing condition and/or pathology. If this shortfall is addressed, a working LSCD, limbal degeneration or injury model could prove an invaluable tool for healthcare services.

From these in vitro investigations it is becoming increasingly possible to characterise the mechanism by which the alterations to the epithelial stem cell niche translate into niche disruption through the progression of the disease state. It is apparent that compressive or tensile loaded systems have not been used for limbal niche research, It is proposed that manipulation of crypt shape/depth, using such principles can exert the mechanobiological cues and influence limbal differentiation through limbal crypt physical mimicry. A similar effect has been observed with the control of epidermal stem cell differentiation in response to crypt depth change (*Helling et al., 2018*).

Pressurised fluid flow can induce mechanobiological cues through the application of force by shear stress along the cells as demonstrated in mouse osteocyte culture. This particular system shows the induction of calcium oscillations through the Wnt/ β -catenin pathway which is proposed to be induced by the increase in intramedullary pressure generated by the fluid flow (*Hu et al., 2015*). Such systems have cross translatability in ocular studies where the alteration of the pressure of the aqueous humour similar to the high-pressure conditions as observed in glaucoma (*Selbach et al., 2005*) can be studied to assess the effect of such conditions on differentiation in and outward of the limbus. Mechanical characterisation of the limbal tissue using compressive methods however has been conducted, to determine the soft tissue properties, nanoindentation of a cornea maintained in culture (including the limbus) determined the creep profile (in terms of

penetration depth of the limbus) and a limbal modulus of 10.4 KPa (*Philipp et al., 2014*). Compression characterisation contrasts to tensile measurements (as a secant determination of observed regional stress) of limbal tissue; Young's modulus for meridional measurements of the limbus yielded between 3.4 MPa and 13.1 MPa dependent on intraocular pressure (ranging from 2 mmHg to 100 mmHg) and 5.92 MPa – 27.5 MPa for circumferential surface tissue Young's modulus determination (for the same pressure range) (*Hjørtdal., 1996*).

1.6.3 Stem Cell Culturing Technologies Employed in Ocular Surface Replication

There are many varied applications and cross-applications of stem cell culturing technologies, with very little in the way of standardisation, particularly when methodologies for LESC cultures are considered. Many of the technologies being applied have been seen in embryonic, induced pluripotent stem cell (iPSC) and cardiac stem cell culture, eg, Matrigel as applied in cardiac stem cell culture (*Bakunts et al., 2008, Lam et al., 2017*) and 3T3 fibroblast feeder in iPSC and embryonic culture (*Knoebel et al., 2009, Fang et al., 2018, Almenario et al., 2020*). However between these culturing technologies, there are significant commonalities, for example, there has to be a native matrix component mimicry, as seen with the amniotic membrane, Matrigel and fibrin approaches (*Table 1.5*). Having the correct matrix composition influences stem cell fate both in terms of maintenance and guidance of differentiation.

Culturing Approach	Purpose of the culture	Reference	Notes
3T3 fibroblast feeder	Analysis of the effect of Bevacizumab on K3 and VEGFA expression in human limbal epithelial cells in culture	Notara et al., 2019	
	3T3 was used as a control for the development of a human-derived feeder system	<i>Shirzadeh et al., 2018</i>	Novel human-derived umbilical cord-derived feeder cells used
	Culture of LESC on contact lenses	<i>Tóth et al., 2017</i>	
	Used as a control against bone marrow stromal cell feeder culture	González et al., 2016	Novel bone marrow stromal feeder cells used
Explant	Expansion of limbal cells before seeding onto transplant scaffold	Sanie-Jahromie et al., 2020	
	Long-term expansion of limbal explants	<i>Szabó et al., 2015</i>	
	Limbal-derived progenitor maintenance	<i>Zhang et al., 2014</i>	
	Development of serum and feeder-free culture of human corneal epithelial stem cells	<i>Lekhanont et al., 2009</i>	Explants on Amniotic membrane with serum free medium
Digested Monolayer	Cells digested for monolayer seeding on Matrigel.		Collagenase A and Trypsin EDTA
	Isolation and expansion of comparative controls	Yam et al., 2018	Dispase II and Collagenase I
	Cells digested for monolayer culture on feeder layer/3D layered system	González et al., 2016	Dispase II and Trypsin EDTA
Amniotic membrane	Control for the collagen-like peptide layer	Haagdorens et al., 2019	
	Expansion of potential novel stem cell source for corneal regeneration	Yam et al., 2018	
	Expansion of limbal cells into corneal lineage	Dhamodaran et al., 2016	Additionally conjunctival and oral mucosal epithelial cells

Amniotic membrane	Development of serum and feeder-free culture of human corneal epithelial stem cells	<i>Lekhanont et al., 2009</i>	Explants on Amniotic membrane with serum free medium
	Matrigel constructs for the comparison of the effect of different matrix component substitutes on limbal explant growth	<i>Ahmadiankia et al., 2009</i>	AM used for Control
	Expansion of Human LESC	<i>Meller et al., 2002</i>	
	AM, for transplant with and without allograft for corneal regeneration	<i>Tseng et al., 1998</i>	
Xeno-free culture	Development of xeno-free LESC expansion	<i>Ghoubay-Benallaoua et al., 2017</i>	Additionally limbal stromal stem cells
	Xeno-free hydrogel system for corneal epithelial cells	<i>Chen et al., 2017</i>	Hy-stem-c hydrogel
	Development of human umbilical derived feeder culture for xeno-free feeder system for limbal culture	<i>Shirzadeh et al., 2018</i>	
Feeder-free culture	Feeder-free expansion of immortalised human corneal epithelial cells	<i>Haagdorens et al., 2019</i>	Collagen-like peptide hydrogel layer
	Development of feeder-free LESC expansion	<i>Ghoubay-Benallaoua et al., 2017</i>	Additionally limbal stromal stem cells
	Development of serum and feeder-free culture of human corneal epithelial stem cells	<i>Lekhanont et al., 2009</i>	Explants on Amniotic membrane with serum free medium
3D Scaffolds	Scaffold for transplanted cells for corneal transplant	<i>Sanie-Jahromie et al., 2020</i>	Electrospun PCL
	Expansion of LESC for mechanobiological analysis	<i>Gouveia et al., 2019</i>	Compressed collagen gel
	Expansion of bovine LESC	<i>Mi et al., 2010</i>	Compressed collagen Gel

3D Scaffolds	Matrigel constructs for the comparison of the effect of different matrix component substitutes on limbal explant growth	Ahmadiankia et al., 2009	Collagen type I
2D Substrates	Limbal Epithelial expansion	Tóth et al., 2017	Contact lenses
	Limbal-derived progenitor maintenance	Zhang et al., 2014	Surface-modified contact lenses
Matrigel Matrix	Gene expression analysis of Limbal niche cells and bone marrow stem cells	Wang et al., 2020	
	Differentiation of limbal fibroblasts/bone marrow mesenchymal stem cells into corneal epithelial cells	Katikreddy et al., 2013	
	Matrigel constructs for the comparison of the effect of different matrix component substitutes on limbal explant growth	Ahmadiankia et al., 2009	
Fibrin Matrix	Expansion of Limbal epithelial progenitors	Riestra et al., 2017	Fibrin is human-derived from adult plasma
	Expansion of LESC using novel 3D feeder layer system with fibrin gel intermediate layer	González et al., 2016	
	Fibrin construct for expansion of rabbit limbal epithelial cells for autologous transplant	Talbot et al., 2006	

Table 1.6: Stem cell culturing approaches and technologies applied in limbal replication. Some of these methods have been cross-applied from previous stem cell applications with other stem cell types. Other approaches, such as novel scaffold applications have been derived from other means. This collation demonstrates the approaches most popularly used in the field of limbal replication for regenerative medicine.

1.6.4 Generation of Topography, Shape Matters

In wider regenerative medicine, there is a significant reliance on biomaterials and substantial investment in their development and study. The evolution of these materials has taken the course from mere bio-tolerance (examples such as materials employed in total hip replacement (*Boutin et al., 1988*)) to full bio-integration such as that observed in bioglass (*Cohrs et al., 2019*). In the fields of regenerative medicine and tissue engineering, biomaterials are employed to simulate in vivo environments within a table-top in vitro setting, thus circumventing the ethical complications that are associated with performing human and animal in vivo studies (*McLaren, 2001, Lo and Parham, 2009, Bart van der Worp et al., 2010*). These materials can be used to study the effect of changing topography concerning the stem cell niche (*Helling et al., 2018*) and additionally the limbal epithelial stem cell niche (*Haagdorens et al., 2019, Dimmock et al., 2023*). These biomaterials can also be incorporated into bioreactor systems to stimulate mechanical, chemical and electrical effects on the stem cell niche (*Burdick and Vunjak-Novakovic, 2009, Mahadik et al., 2015, Pires et al., 2015, Rödling et al., 2017, Seo et al., 2018*). These approaches have been translated into epithelial tissue engineering and subsequently formed part of the foundation of limbal niche engineering.

A case applied to epithelial tissue engineering is the membrane bioreactor utilised in guiding the differentiation of hepatic stem cells (*Piscioneri et al., 2018*). The membrane approach can be applied to all types of epithelial stem cell cultures in conjunction with environmental manipulations. This approach facilitates the exploration of near biological mimicry of the native tissue environment and its relation to disease state (loss of elasticity/surface tension, change in media microenvironment). Such

changes will allow further in-depth characterisation of the epithelial stem cell niche internal mechanisms and its interaction with native committed tissue, immune cells and incoming mesenchymal cells. Bringing together the concepts of tissue mimicry and co-culture are vital concepts are vital considerations for the creation of true tissue-like in vitro models. These should be considered when a growth/expansion system or a disease modelling system is being designed. An example of a limbal cell expansion system following a similar epithelial tissue expansion system is the use of an amniotic membrane for cell expansion. For regenerative applications such as potential regenerative graft applications, mesenchymal stem cells (MSC) can be expanded on the surface for the membrane+cell layer to be applied as a “patch” for skin regeneration (*Aghayan et al., 2022*). This use of surface biomimicry can be directly compared to its application in LESC cultivation where suturing of the amniotic membrane was performed to create crypts to increase the number of limbal progenitor cells (as determined by an increase of >20% p63 α expression in sutured membranes compared to flat) (*Bisevac et al., 2023*). Here the subtle differences in the same expansion technology (amniotic membrane) between the tissue types is the end point application, where in the case of the MSC culture the expanded patch was ready for graft application, the LESC expanded amniotic membranes required an additional topographical consideration for the preservation of the desired stem cell type.

To further understand how it may be possible to apply the techniques being discussed, especially in the context of limbal epithelial stem cell niche engineering, the responses of the stem cells in all states must be assessed. Understanding all of the tissue properties, particularly soft tissue in the context of corneal replication grants the best insight into the possible tissue/tissue constructs in all environments. Soft tissue dynamics has been investigated since the 1960s and reviewed multiple times. A recent

review explores the capacities of structural modelling of soft tissues, and the relation of the matrix and its components to the mechanical performance, which translates to the downstream physiological impact on the mechanobiology of the soft tissue that can be assessed through modelling (*Lanir, 2017*). This research highlights the importance of the consideration of cell adhesion and matrix composition when generating tissue constructs or material-dependent cell studies such as topography-induced differentiation/alignment. Consideration of tissue mechanics features heavily in the selection of appropriate biomaterials for tissue replication. For example, bone tissue engineering requires the use of stiff, strong materials to mimic or indeed take on the structural role of the implanted bone a notable example being the use of a 3D printed Polyetheretherketone (PEEK) calcium hydroxyapatite composite as a potential implantable material (*Olodapo et al., 2020*). In contrast, soft tissues such as skin require drastically softer materials for tissue replication, such as the fibrin agarose gels evaluated for use as a skin replicating biomaterial (*Ionescu et al., 2020*). Due to similarities in tissue elastic modulus between the limbus and skin (~8MPa for skin and 1.6MPa for the limbal ring) (*Asejczyk-Widlicka et al., 2007, Ionescu et al., 2020*) a soft gel based material such as the skin replicating fibrin agarose gel should be considered for limbal engineering.

Patterning of culturing substrates has been observed to have a significant impact on the localization, arrangement, differentiation and cellular function of cells. Substrate topography encompasses an enormous scope of different surfaces, ranging from variants of micropillar arrays to rough-etched nano topographies, to wrinkled polymer substrates. In the replication of the limbus, few topographies can match the native architecture of the limbus in vivo including grooved and ridged topographies. An early example of such is the creation of bioengineered limbal crypts which have been

grown on moulded micro ridges on a RAFT construct. This process demonstrated a high proportion yield of LESCes with the p63 α marker (*Levis et al., 2013, Levis et al., 2015*). Though maintaining a pure stem cell pool is good with such a construct, it is limited by its lack of ability to be mechanically manipulated in culture to create a dynamic crypt model.

Static systems as established, maintain stemness, however, what is not well defined is the use of dynamic systems in ocular applications. Dynamization holds great value for disease state modelling, with cross applications for the prediction and correlation of glaucoma to limbal degradation (*Mastropasqua, 2015*). However for a system to become dynamic the structure and the method for the creation of the topography (upon which the cells are seeded) must facilitate movement and manifest a biologically relevant change. Given this consideration, it may be said that surface wrinkling, specifically polymer surface wrinkling (as recently reviewed in the Biomedical Applications of Wrinkling Polymers) constitutes a suitable candidate for limbal replication (*Dimmock et al., 2020*).

1.6.5 Wrinkling for the Creation of the Biomimetic Limbus

Wrinkled topography may hold the greatest potential for the creation of biologically relevant limbal crypts. Wrinkling presents as sinusoidal-like waveforms which propagate across the surface of a material when the bulk and surface experience stress. The generation of wrinkles as a physical phenomenon in natural occurrences such as skin has been extensively reviewed (*Cerda and Mahadevan, 2003, Miller, 2007, Genzer and Groenwold, 2006*). As a basal requirement for wrinkle formation, particularly in the context of the creation of crypt topography on 'chip devices', the surface (can also be referred to as 'skin' or 'film') must be stiffer than the bulk (*Genzer*

and Groenwold, 2006). Often discussed in terms of modulus, the formation of the wrinkles can be predicted. A simplistic model, as proposed by Allen in 1969, can be used to predict wrinkle formation within an ideal system. Expressed in terms of the critical wavelength (λ), layer thickness (h), plane strain moduli for both the surface and bulk (\bar{E}_s and \bar{E}_f) where $\bar{E}_s = E_s/(1/\nu_s^2)$ and $\bar{E}_f = E_f/(1/\nu_f^2)$ with the Poisson's ratio for each (ν_s and ν_f). The equation:

$$\lambda = 2\pi h \left(\frac{E_s}{3E_f} \right)^{1/3}$$

This work (Allen, 1969) does present some flaws however as it does not take into account certain real material properties such as non-linearity and excessive strain imparted in the system (Dimmock et al., 2020). There are more sophisticated models which have been more recently generated, these incorporate the non-linear aspects of wrinkling, earlier work used the non-linear elasticity theory (Cai and Fu, 1999) and later work using the Gent material model, which provides a more representative model of material wrinkling (Cai and Fu, 2019). Wrinkled have been previously used in other cell culture applications including the investigation of antibiotic properties of wrinkles topographies and the control of the cell's activities, including alignment, migration, morphology and phenotypic expression markers of differentiation (Dimmock et al., 2020).

Current methods for the generation of biocompatible/biologically representative wrinkles have a heavy focus on the use of polydimethylsiloxane (PDMS) as a bulk material (Tong et al., 2016, Osmani et al., 2017, Yu et al., 2018). PDMS has a Young's modulus in the KPa to MPa range, making it highly deformable; therefore an ideal candidate as bulk material for the formation of wrinkled topography (Yan et al., 2019). In addition to this core mechanical property, the biocompatibility of this material is also

attractive. Traditionally this material is regarded as bio-tolerant with long-standing use in medical devices and implants. A more recent application is the fabrication of anti-bacterial PDMS films using silver nanoparticles which demonstrated bio-safe qualities for an implantable medical device surface technology (*Kim et al., 2017*). This biotolerance can be enhanced towards full integrative biocompatibility. To generate the wrinkles, this bulk material must be modified to achieve the discussed stiffness differential; the surface to be wrinkled must be made stiffer. There are already multiple methods established for creating wrinkles on PDMS, ranging from early protocols using thin film metal deposition of gold (*Bowden, 1998*) to biocompatible coating such as graphene (*Wang et al., 2016*) and oxidative plasma treatment (*Bowden et al., 1999, Glatz and Fery, 2018*). Replicating the LESC niche in a biomimetic manner will not only rely on the underlying principles for basal wrinkle generation and biocompatibility but also require the application of further techniques if the architectural and functional complexity of the LESC niche is to be replicated. An example of such an application is the generation of hierarchical wrinkled poly(urethane acrylate) substrate for the modulation of cell physiology (*Seonwoo et al., 2016*).

1.6.6 Types of Bioreactors Used in Tissue Engineering and Their Use in Limbal Replication

It is appreciated that in addition to the limbal-specific examples of replication studies described in this research, there is a plethora of bioreactor technology being employed in other tissue engineering fields which has strong application potential to this field. The following examples serve to highlight such applications: the creation of an in vitro intestine system to represent the human intestine using a 3D epithelial cell-seeded silk perfusion tube system (*Zhou et al., 2018*), the engineering of skin epithelial

stem cell crypts using moulded microwell (pit) topography (*Abaci et al., 2018*) and the use of microscale bioreactor technology for the investigation of Caco-2 cell physiological function in a biomimetic villus-like structure with fluid perfusion dynamics (*Costello et al., 2017*).

For direct limbal applications, there is very little bioreactor technology being specifically developed for microscale applications. That said, there is an investment in material-based applications. An example of this is the development of sandwich co-culture wherein limbal stem cells are cultured in the same vessel as the feeder cells, but separated by a porous membrane and/or fibrin layer with differentiation controlled by air-lifting (*Deng et al., 2016*). Additionally, concepts utilised in whole corneal and corneoscleral rim preservation technology rely heavily on bioreactor technology. These principles and studies (in the pursuit to preserve the entire cornea) can have the potential for significant cross translatability to limbus preservation and investigation, should limbus expansion and characterisation with this technology be investigated. Examples of such technology include the perfusion bioreactor developed for cornea storage, tested with porcine corneas, where the dynamic culture of the corneas demonstrated an improvement in corneal clarity (therefore preservation). Within this bioreactor, multiple physiological characteristics were controlled including; intraocular pressure and the use of airlifting and perfusion. Improved corneoscleral preservation was observed in porcine tissue, maintaining physiological quality for nearly 1 week, preserving both the limbus and the epithelium (*Guindolet et al., 2017*).

In addition to these ophthalmological transplant-specific innovations, applications such as dynamic substrate-based mechanobiology studies for guided epithelial stem cell differentiation can also be considered to be bioreactor studies as

these are defined, controlled conditions for determining desired cell growth, with strong cross translation to limbal crypt research (*Helling et al., 2018*).

In addition to the requirement for further study into the epithelial stem cell niche reaction to environmental cue changes, it is important to maintain the physiological and anatomical likeness of both simulations in bioreactors, experimental culture and potential tissue-engineered treatments. Maintaining such a likeness will enable the accurate prediction and anticipation of niche reactions to transplantation and the target disease state, facilitating optimized renewal and regeneration. Current approaches are steering towards this end goal of physiological mimicry however there is a requirement for multi-factor testing to characterize multiple cue effects simultaneously and their possible interactions. Thus furthering understanding of both cue downstream effects and enabling genuine optimization of niche activity for both therapeutic purposes and physiological homeostasis after transplantation.

1.7 RESEARCH SUMMARY

1.7.1 Clarification of the Aim for the Research

The research aims to *develop a biomimetic system which replicates the Limbal Epithelial Stem Cell Niche (LESC), not only in a static form as seminally established but also in a novel dynamic form to model the anatomical homeostasis of the niche.*

This aim is further refined by the three practical aspects of the project:

- (i) Characterize the LESc Niche using non-destructive modalities including (but not limited to) optical coherence tomography (OCT) and optical coherence elastography (OCE).
- (ii) Validate the concept of using elastomeric substrates featuring surface-engineered wrinkled properties to generate an actively tunable topography that will enable effective limbus replication.
- (iii) Design and fabricate a bioreactor capable of sustainable reproduction of the artificial constructs which mimic the LESc Niche to create a model which has translatability towards modelling such as LSCD.

The objectives are to contribute to the effectiveness of Corneal LESc Niche simulation and characterization by:

- Investigating and developing the use of non-destructive modes of analysis of the limbal anatomy at the niche level. Principally by using optical coherence tomography (OCT) to explore structure and optical coherence elastography (OCE) to explore the mechanical properties of the tissue.
- Designing and fabricating new substrate systems to replicate the limbal stem cell anatomic niche.

- Investigating the effect of the physical change in the anatomic niche, by substrate dynamization and curvature, on limbal stem cell fate as predicted to be a factor in age-related deterioration and diseases such as LSCD. These fate changes are to be assessed as a function of both physical control and the maintenance of stemness within each substrate type.

1.7.2 Research Questions

- 1.
2. Can the non-destructive imaging modalities OCT and OCE be utilized to effectively characterise (structurally and mechanically) the limbal stem cell niche?
3. Through novel use of smart material substrate modification, bioreactor design principles and the culturing principles from established stem cell technologies, can an effective dynamic biomimetic system be produced that facilitates cell growth?
4. Can the surface engineering process method produce surface wrinkles which enable:
 - (i) Characterization of these artificial constructs and analysis of the effect of these generated topographies on limbal stem cell behaviour and effective limbus replication.
 - (ii) Enhanced understanding of how alterations in the anatomic niche change the fate of LESC and the linkage with Limbal Stem Cell Deficiency (LSCD).
 - (iii) Progression towards a model which can simulate the natural ageing process and/or diseased states.

5. 4. What benefits can be gained from the development of a dynamic model replicating the LESC niche, above those witnessed using static form replication?
6. 5. To what extent can the method be seen to facilitate a practical application in the discipline?

Chapter 2: Materials and Methods

2.1 SUMMARY OF REAGENTS

Table 2.1 is a compilation of all reagents used in the undertaking of the research within this thesis. Each item is categorised by application type and the supplier catalogue (Cat. No.) is included for reference.

Type	Item	Cat. No.	Brand/supplier
Basal medium	DMEM-F12	11320033	Gibco
Basal medium	DMEM high glucose	11965092	Gibco
Complete medium	CNT-Prime	CNT-PR	CellnTec
Supplement	Isoproterenol	420355-100MG	Sigma
Supplement	Insulin-transferrin-selenium (ITS)	41400045	Gibco
Supplement	Penicillin-streptomycin	17-602	Lonza
Supplement	B27 supplement	17504044	Gibco
Supplement	Adenine	A2786-5G	Merck
Supplement	Hydrocortisone	H0888-1G	Merck
Supplement	Calf serum	30-2031	ATCC
Supplement	Foetal Bovine Serum	35-016-CV	Corning/SLS
Bio-Reagent	Phosphate buffered saline (PBS)	21-040-CV	Corning/SLS
Bio-reagent	Trypsin-EDTA	15090046	Gibco
Bio-reagent	Gentamicin	15710064	Gibco
Bio-reagent	Amphotericin-B	15290018	Gibco
Bio-reagent	Dispase-II	D4693-1G	Merck
Bio-reagent	Collagenase-A	101035780 01	Roche/Merck
Print filament	Flashforge PLA blue	PLA1KG	Flashforge
Print filament	Flashforge ABS green	ABS1KG	Flashforge
Assembly parts	A2 stainless M3 x30 mm socket head bolt	SSCF-M3-30-A2	Accu
Assembly parts	A2 stainless M3 nut	HPN-M3-A2	Accu
Assembly parts	316L Stretch bioreactor arms	custom order	Kloekner metals
Stain	Haematoxylin	GHS216-500ML	Sigma
Stain	Eosin	Lamb/100 D	Raymond A Lamb Ltd
Stain	CellTracker Green CMFDA	C2925	Thermofisher Scientific

Stain	4',6-Diamidino-2-Phenylindole, Dihydrochloride (DAPI)	D1306	Thermofisher Scientific
Stain	Phalloidin-Texas Red	T7471	Thermofisher Scientific
Reagent	Triton X-100	9036-19-5	Merck
Bio-reagent	Bovine serum albumin		Merck
Bio-reagent	Human serum	H4522-100ML	Corning/SLS
Antibody	Anti-P63	ab124762	Abcam
Antibody	Anti-CK3	ab77869	Abcam
Antibody	Anti-ABCG2	ab229193	Abcam
Antibody	AlexaFluor 488 conjugated Anti-K12	ab22216	Abcam
Antibody	Anti-vimentin	MAB2105	Bio-technie/R&D Biosystems
Antibody	PE-conjugated Anti-ABCG2	FAB995P	Bio-technie/R&D Biosystems
Antibody	PE-conjugated Anti-Vimentin	IC2105P	Bio-technie/R&D Biosystems
Antibody	PE-conjugated Anti-Nestin	IC1259P	Bio-technie/R&D Biosystems
Antibody	NL637 conjugated Donkey-Anti-rabbit	NL005	Bio-technie/R&D Biosystems
Antibody	NL493 conjugated Donkey-Anti-mouse	NL009	Bio-technie/R&D Biosystems
Reagent	Ethanol-denatured for IMS 70%	3221-M	Merck
Material Kit	Polydimethylsiloxane: Sylgard-184	2646340	Dow Corning
Reagent	Nitric acid	438073-100ML	Merck
Reagent	Sulphuric acid	258105-1L-PC	Merck
Reagent	Dopamine Hydrochloride	H8502-25G	Merck
Reagent	Tris base (powder)	648310-500GM	Merck
Reagent	Hydrochloric acid	258148-2.5L	Merck
Reagent	Gelatin from bovine skin gel strength 225g Bloom	G9382	Merck
Reagent	Methacrylic anhydride	276685-100ML	Merck
Reagent	Lithium phenyl-2,4,6-trimethylbenzoylphosphinate (LAP)	900889-1G	Merck
Reagent	Vitronectin	SRP3186	Sigma
Reagent	Rat tail collagen (low)	11563550	Fisher Scientific
Material	Polylactic-co-glycolic acid	untraceable	Group stocks
Material	Polycaprolactone – medium molecular mass	704105-100G	Merck

Solvent	Chloroform	366927-2.5L	Merck
Adhesive	Silicone rubber compound (liquid flowable)	187-3460	RS Components
Mounting	Histomount	008030	Thermofisher Scientific
Fixative	Paraformaldehyde	158127-3KG	Merck

Table 2.1: Summary of reagents used across all methods summarized in this chapter.

2.2 PRINCIPLE METHODS

Figure 2.1 Introduces all of the methods used in this thesis, categorising each method into their area of interest and highlighting which chapter they were utilised in graphically.

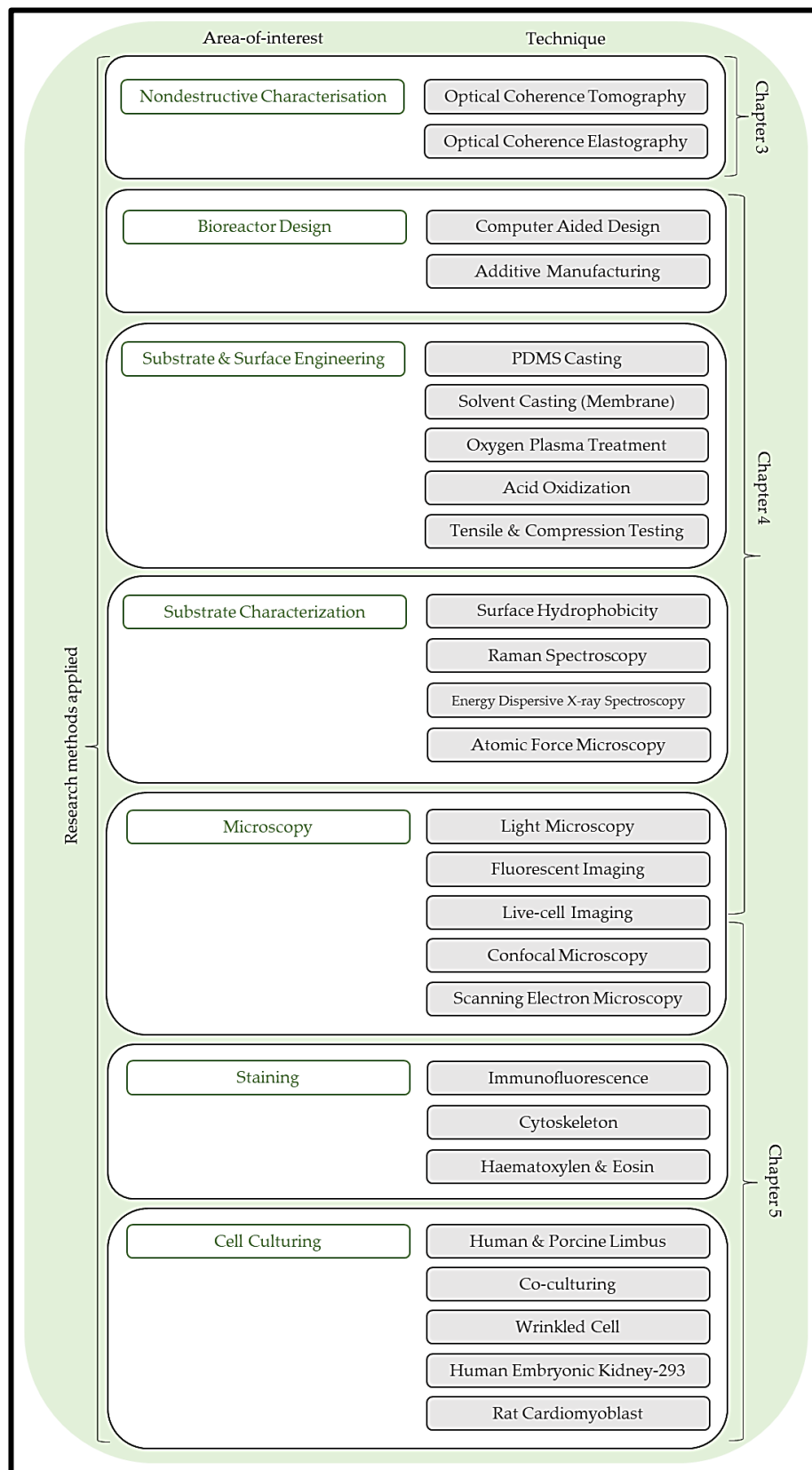


Figure 2.1: Graphical overview of methods covered in this thesis. Each of the methods used is segregated by the area of interest and their implementation in the thesis.

2.2.1 Optical Coherence Tomography and Elastography

2.2.1.1 Optical Coherence Tomography (OCT) – High-Resolution

The OCT imaging system used to obtain en-face images was a lab-built spectral domain OCT system (SD-OCT), utilised at a research collaborator's facility at the University of Dundee. The system comprised a broadband laser with a centre wavelength of 1310nm and bandwidth of 110nm, a reflecting mirror array, a X10 LSM02 objective lens (Thorlabs, USA) and a high-speed InGaAs linear array, of maximum sampling frequency 91,912 Hz (SUI, USA).

Image data was initially captured using a customised LabView program (National Instruments, USA) and then processed into viewable images using a custom script in Matlab (MathWorks, USA). The OCT setup was operated, and data was acquired following the previous study (*Song et al., 2013*). The volumetric data stacks were converted into en-face images using median average projection and intensity profiles were extrapolated using ImageJ using the plot profile function. The quantification was also performed using ImageJ where the x-axis was plotted in micrometres and represented the true lateral scale for epithelial rete peg and palisade ridge measurement.

2.2.1.2 Optical Coherence Elastography

The OCE procedure was performed utilizing the same OCT camera setup with an x10 magnification lens as aforementioned. However, in the OCE acquisition, the external vibration system (shaker) was employed to impart a vertical oscillating displacement on the sample, which was detectable by the phase-sensitive (PhS-OCT).

Thus the depth-resolved elasticity was resolved non-destructively by the detection and differentiation of regional stiffnesses by the changes in vertical amplitude (once the imparted vibration was accounted for by the software) (*Zhang et al., 2020*).

Vibrational OCE image captures were taken as a 12s time series across a 3.65 mm B-scan line. During recording, the sample was placed on top of a vibrational shaker (Brüel & Kjær Sound & Vibration Measurement A/S, Denmark), controlled and driven by a signal generator to produce vibrations with a frequency of 850 Hz and an amplitude of mVpp (Keysight Technologies Inc., USA). The setup of the system is depicted in Figure 2.2. These time series' depth-resolved elasticity information in limbal tissue with axial and lateral resolutions of 6.9 μm and 12.4 μm respectively. The SNR was 53 dB and displacement sensitivity was 2 nm. The OCE data was recorded through the customised LabView program (National Instruments, USA) and the elastograms were processed and output using the dedicated Matlab script (MathWorks, USA).

A 1% agar reference phantom containing 0.006% Titanium dioxide w./v. was applied to the surface of the tissue, which was mounted on a bed of agar of the same composition. Agar was used as a reference phantom due to its elastic modulus being within a similar range to soft tissue. Additionally, the agar was substantially softer than the tissue, ensuring a distinct reference was established. Using a softer reference was advantageous for elastogram resolution as softer regions were darker (less intense) than the stiffer regions (*Li et al., 2015*). When orientating the tissue on the agar, 1-2 large droplets of liquid agar were dropped onto the agar bed then the tissue piece was placed on the solidified droplet, ensuring the tissue piece assumed anatomical orientation and conformation. Similarly, the ImageJ was used to extrapolate intensity values from the elastogram images which were subsequently used to calculate the

stiffnesses of the anatomical regions investigated. These calculations were done by averaging the ROI for the anatomical region and comparing these averages to the average of the agar reference regions (which were of known stiffness; 14.6 ± 0.8 KPa which, as determined by compression testing and validated against literature (*Li et al., 2015*)).

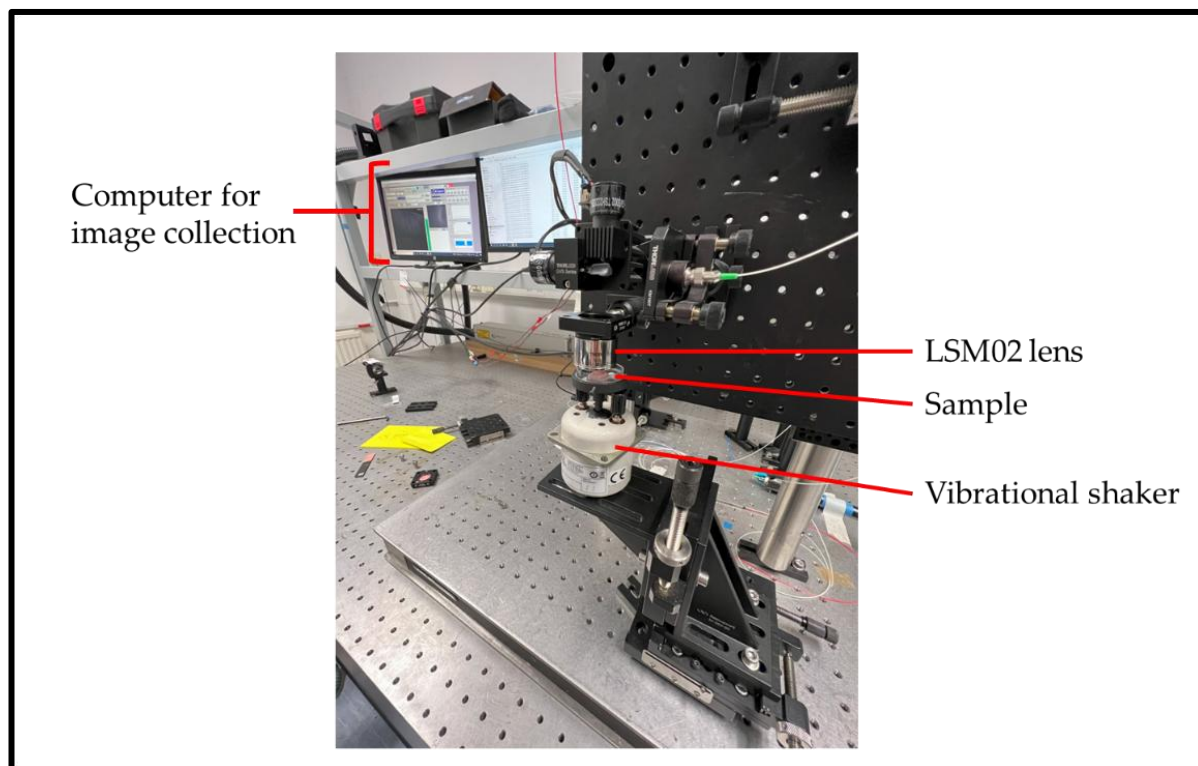


Figure 2.2: Optical Coherence Elastography setup. This is showing an example OCE setup where the sample is placed on top of the vibrational shaker which is in turn placed under the custom-built PhS-OCT device fitted with an LSM02 (x10) lens. For accessibility in this instance, the wires to the signal generator are not connected to the vibrational shaker.

2.2.1.3 Optical Coherence Tomography – Standardised, Lower Resolution Screening

For material observations and porcine tissue screening, a commercially obtained OCT system at the Keele laboratory was used (*Thorlabs, Germany*), which was fitted with the LSM03 lens kit. This equipment differs principally from the lab-built

system due to the lower lateral resolution resulting in the more appropriate use of this equipment as a screening device. However, the detection principle is similar with this system being a type of spectral domain OCT. B-scans were obtained using the Thorlabs spectral radar Telectro-II device. Image acquisition was controlled by the dedicated Thor-labs OCT software with pixel-averaging windows set to 1x1 to obtain the highest fidelity images possible. Image field correction was applied to flatten the edges of the image to compensate for the lens distortion. The 3D mode was used to acquire multiple B-scans throughout a 6 x 6 mm acquisition area to create volumetric images. Depending on the sample being imaged, any resulting surface shine which caused reflective artefacts on the b-scan images could be mitigated by immersion in aqueous media. A Schott cap, used to prevent lateral reflective artefacts (which are almost always observed) when using well plates with transparent sides, was employed as the vessel. Either distilled water (for material), PBS (for fixed or non-viable specimens) or culture medium (for live tissues) was used for immersed samples. In the case of live tissues, the Schott caps were autoclaved and a sterile internal environment was maintained by transferring the tissues into the cap in a biological safety cabinet and then sealing the cap with a sterile 35 mm petri dish lid with either autoclave tape or parafilm. An example of a non-sterile immersed sample is demonstrated in Figure 2.3.

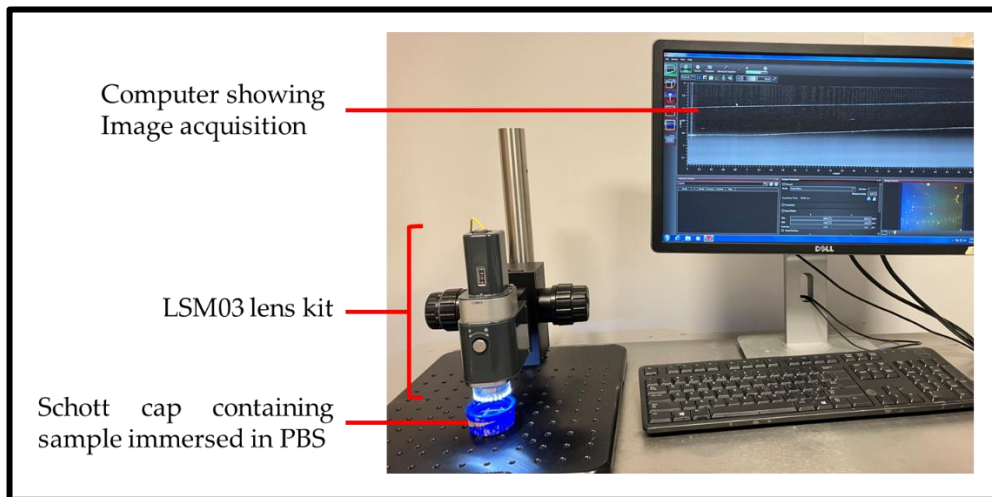


Figure 2.3: Thorlabs spectral radar OCT setup. Here is an example of wrinkled material in a stretching frame being imaged whilst immersed in PBS, a Schott cap is used to prevent lateral reflective artefacts from being introduced into the final image render. The Telectro II unit, on which this OCT system is based, is situated out of frame under the bench.

2.2.2 Production of the Bioreactor System and Design Principles Used in this Thesis

Figure 2.4 outlines the design and assembly processes which were employed in the production of the bioreactor systems developed in this thesis. The workflow outlined covers both compression and stretch frame systems.

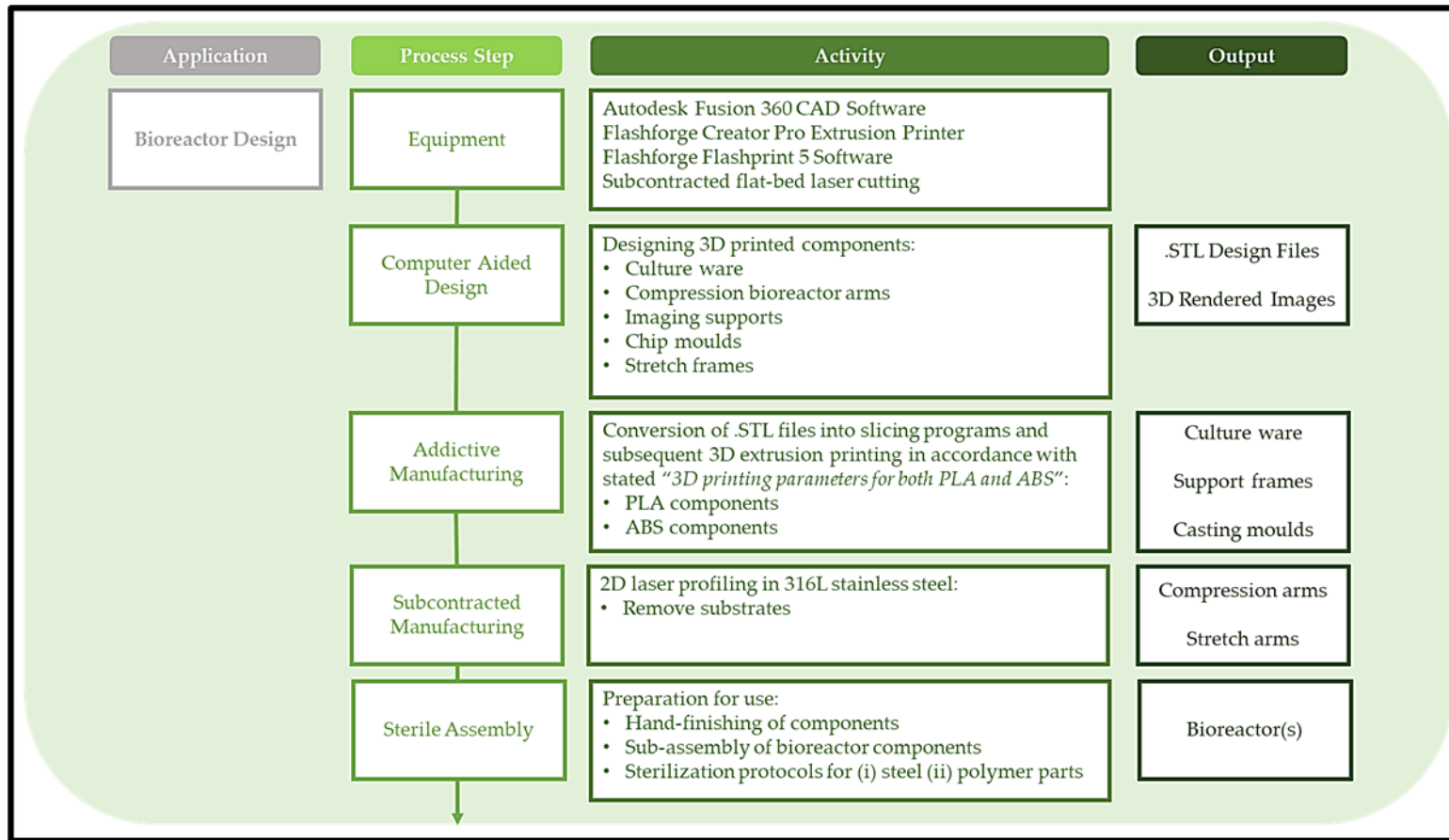


Figure 2.4: Process flow for the design and production of bioreactor system components and cultureware. Here the processes for the design, manufacture and assembly of the bioreactors, their components parts and 3D-printed cultureware are visually summarized.

2.2.2.1 Use of Computer-Aided Design

Fusion 360 (Autodesk, USA) was used to design and export the 3D models for all 3D printed cultureware, compression bioreactor arms and imaging supports produced by additive manufacturing. The models for each were exported in the .STL format. Fusion 360 was also used for 3D renderings of designed models for illustrative purposes, in particular the PDMS chip mould and the stretch frame models. The CAD functionality of this program was utilized in the design of the stretch frame arms which were subsequently laser cut from 316L stainless steel (Kloekner Metals, UK).2.2.2.2 3D Printing.

The STLs were sliced into the .x3g format for printing using the Flashforge FlashPrint 5 (Flashforge, China) utilizing the fast settings. The print parameters were automatically set to as per Table 2.2. The printing for most parts was performed using the Flashforge Creator Pro extrusion printer in polylactic acid (PLA).

For culture, the retainer rings and printed bioreactor frames were sanitised in 70% ethanol or industrial methylated spirits for 40 minutes and dried in the biological safety cabinet immediately before use. The PDMS chip mould needed to be heat resistant to 70 °C without warping during PDMS curing, therefore Acrylonitrile butadiene styrene (ABS) was ideal due to having a higher glass transition (100°C) temperature than PLA (56 °C) (Rosli *et al.*, 2020, Barassa *et al.*, 2021). To create a smooth mould surface, the ABS mould was vapour smoothed. In a fume hood, a lidded large glass petri dish of acetone was brought to boiling point (56 °C). When vapour was visible, the moulds were placed face down in the vapour layer on metal supports, above the acetone layer and the glass lid was replaced. After the vapour layer re-establishes the parts were

incubated for 60s before being removed. The parts were initially aired in the fume hood for 30 minutes and left for at least 24 hours before being used. Smoothing was repeated if there were any significant surface aberrations.

<u>Parameter</u>	<u>Value PLA</u>	<u>Value ABS</u>
Nozzle size	0.4 mm	0.4 mm
Extruder temperature	200 °C	220 °C
Bed temperature	50 °C	105 °C
Layer height (average)	0.3 mm	0.3 mm
Fill density and patterning	10% Hexagonal	15% Hexagonal
Print speed average	70 mm/s	60 mm/s
Shell count	2	2

Table 2.2: 3D printing parameters for both PLA and ABS. The parameters are based on the “Fast” settings used in the FlashPrint 5 slicing program for PLA and the “Fine” settings used for ABS.

2.2.3 Substrate Fabrication and the Creation of Wrinkled Surfaces

Figure 2.5 introduces the processes involved in producing the various wrinkled surfaces employed throughout this research. All method types used throughout are included.

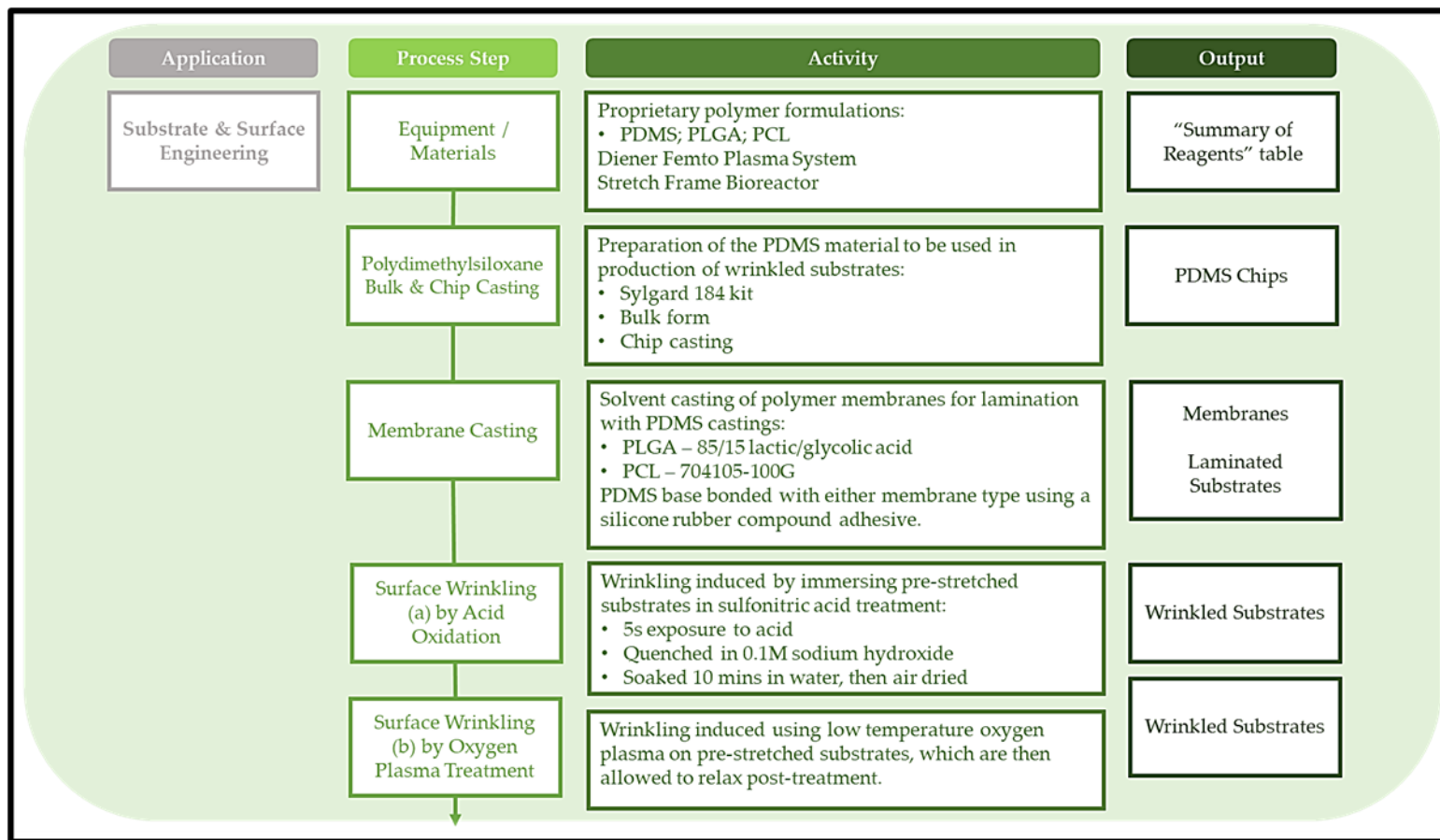


Figure 2.5: Process flow diagram for material treatment to produce wrinkles. This diagram summarizes the workflow to produce wrinkled substrates, the acid oxidation (a) and plasma treatment (b) can be performed sequentially to produce dual-treated substrates.

2.2.3.1 Polydimethylsiloxane Bulk/Chip Formulation and Casting

Polydimethylsiloxane was used as the base material for the generation of wrinkled substrates in all applications, both investigative and for cell culture. The fabrication of this base material utilized the Sylgard 184 kit (*Dow Corning, USA*). The kit comprises two parts, an elastomer base, and a curing agent. These components are proprietary reagents of Dow Corning, therefore the complete composition/formulation is not completely disclosed. Both kit components were combined at the recommended 1:10 ratio of curing agent to elastomer. The elastomer liquid component was dispensed using a syringe, in the required quantity for the mould, minus the curing agent volume into a universal and the curing agent was subsequently pipetted into the universal. To ensure homogenous mixing, a mechanical mixer was used to stir the elastomer for at least 1 minute until the mixture had become turbid with fine bubbles and these had a uniform distribution throughout. The prepared moulds were thermocured at 70 °C in an oven for 2h to yield solid gelated PDMS.

The stiffness of the resultant PDMS gel could be varied through the alteration of the ratio of the curing agent to the elastomer. This temperature and time were chosen as the balance between a workable incubation time between mixing and use. This is based on the scale of lowering the curing temperature of a PDMS mixture resulting in requiring a longer cure time to fully cure the PDMS (*Prabowo et al., 2015*). At the lowest PDMS formulation utilised (2.5% curing agent) it was necessary to allow curing to occur overnight to ensure full curing of PDMS chips before wrinkle formation or material testing. Increasing the curing agent increases the amount of net elastomer

cross-links able to be formed, whilst inversely, reducing the curing agent increases softness by allowing saturation of maximum cross-links thus allowing for a more elastic PDMS silicone gel (*Sales et al., 2022*).

2.2.3.2 Solvent Casting of Polymer Solutions to Create Membranes and Lamination of PDMS Bulks to Create Wrinkles

PLGA was obtained as 85/15 lactic/glycolic acid granules (from group stocks), whilst PCL (*Merck-Aldrich, UK*) was obtained in polymer pellets. The polymer granules/pellets were dissolved in 99% Chloroform (Merck Aldrich UK) at the proportion of 0.25% w.v. Dissolution was achieved over 24 hours using a magnetic stirrer in a sealed glass bottle. After dissolution, the solution was poured into a 150mm glass petri dish which was immediately sealed using tape in a flow hood. To control the rate of chloroform evaporation an 18ga blunt-tipped needle was inserted into the sealing tape, luerLock aperture facing downwards. The purpose of this needle was to facilitate chloroform vapour escape, at a slow rate when exposed to the moving airflow of the fume hood. An additional consideration to the development of this method was the positioning of the restricted vapour vent to the rear of the fume hood to improve fume extraction, to the benefit of other lab users.

The laminated blocks were produced by the adhesion of the PLGA or PCL membranes to the moulded PDMS blocks using a silicone rubber compound adhesive. The adhesive was spread in a very fine layer using a coverslip as a spreader and a 5x magnifying glass to ensure homogenous spreading was achieved. To create the wrinkled topography using this method, the blocks were compressed laterally, using specially designed compression frames, typically achieving up to 20% compression.

2.2.3.3 Oxygen Plasma-Treatment of Thin Stretched PDMS to Create Wrinkled PDMS

To induce wrinkling on the surface of PDMS, the substrate material is required to be pre-stretched then oxidized and allowed to relax to form the wrinkles across the upper surface (*Glatz and Fery, 2018*). This was performed using low-temperature oxygen plasma, generated by the Diener Femto device.

The PDMS substrates subjected to oxygen plasma were placed surface-up in the chamber with the applied pre-stretch either as membranes between fixed points or in the later stages of the research, as PDMS chips on stretching frames. The chamber was evacuated to a near-total vacuum of 0.3 mbar. The standard parameters for treatment were; 1.5mbar O₂ pressure for 10-minute exposure at 50W power. Power variance was achieved through the amendment of parameters via the integrated computer controller into the Diener Femto plasma machine. After treatment, the substrates were only able to be removed from the chamber after the flush and vent sequences were run to release the vacuum and safety maglock.

2.2.3.4 Oxidation of Stretched PDMS Using Strong Acid to Form Wrinkles.

The sulfonitric acid was prepared by first carefully introducing sulfuric acid into nitric acid dropwise into a glass beaker immersed in an ice bath in a fume hood. Once both acids were safely mixed to the 3:1 ratio of sulfuric to nitric acid, the sulfonitric acid was heated to 80°C and stirred (with a magnetic stirrer) in a fume hood for 2 hours. This step follows principles from the method used by (*Watanabe et al.*,) with a twofold purpose; firstly increases the user safety of this aggressive mixture and secondly allows better control over material oxidation as the acid is weakened (*Watanabe et al.*,

2015). After thermal attenuation, the acid was allowed to cool before being transferred to the nalgene® storage bottle.

PDMS substrates were stretched using the stainless stretching frames to 20% elongation. These pre-strained substrates were then exposed to the sulfonitric acid, the standard exposure time being 5 seconds. Immediately after exposure, the substrates were quenched in 0.1M sodium hydroxide and then transferred to a large water bath for 10 minutes. After oxidation, substrates were air-dried.

2.2.3.5 The Dual treatment Method

For dual treatment, specially moulded PDMS chips designed for the steel stretching frames were used. These chips were pre-stretched to 20% elongation and immersed in sulphonic acid (the same used in acid oxidation) for 5s. The oxidized substrates were air-dried after a two-stage quenching. The first quench was for 15 seconds in 0.1M sodium hydroxide solution, followed by a 10-minute soak in a large distilled water bath. After ensuring both the substrates and the stretching frames were dry, the frames with the attached substrates were transferred to the Diener Femto plasma treatment machine. The chips were then exposed to the oxygen plasma with the power set to 50W, oxygen pressure set to 1.5 mbar and an exposure time of 10 minutes. To form the wrinkles on the surface, the chips were removed from frames at this stage to relax the elongation and allow the topography to propagate across the surface.

2.2.4 Tensile and Compression Testing for the Analysis of Mechanical Properties

2.2.4.1 Tension Testing

Tensile testing was performed on the testometric mechanical testing machine, configured for the tensile arrangement, with the 250 Kgf load cell fitted. The sample polymer membranes were pre-cut into 5mm x 35mm strips, with tabs of autoclave tape at each end to ease handling of the membrane samples and were fitted into the jaws. The tests were manually stopped when the membranes reached or surpassed their yield points. The test speed for the tensile tests was 0.1mms⁻¹.

2.2.4.2 Compression Testing

The machine used for compression testing was the BOSE electroforce 2300 series (Bose). Due to practical limitations, only the 22 N load cell was employed for the compression analyses. For purposes of PDMS selection by modulus, only the initial linear region was required, hence the employment of the 22 N load cell was appropriate. Initial safety parameters were set up in the machine software to ensure the protection of the load cell, the ramp was set to not exceed 0.05mm (this is in terms of the machine's registered displacement) and the load cell force maximum was set to 20 N in both positive and negative directions. The rate of compression application was set to 0.01 mms⁻¹.

Interpretation of the mechanical load test data in both compression and tension testing was a multi-stage process. 1) The output was converted from .CSV format by Excel (Microsoft). 2) Following extraction and calculation of the actual displacement (zeroed value) with positive converted values. 3) They were plotted in a separate

software capable of handling the large volume of data points (exceeding 2-4000 per series) (Graph).

2.2.5 Substrate Characterisation

2.2.5.1 Water Contact Angle

The water contact angle method for surface hydrophobicity was used as a predictive measure for a substrate's cytocompatibility. It is appreciated in biomaterial science that an increased hydrophilicity in a material is correlated to a greater cellular compatibility in culture, provided the surface is not cytotoxic (*Ferrari et al., 2019*). The measurements were undertaken on the Attention One water contact angle instrument, controlled using the associated software. Acquisition was taken over 10 seconds at a frame rate of 15 frames per second. The baseline was manually drawn underneath the droplet using the substrate as the parallel guide. The software calculated the contact angle of the droplets between the edges of the meniscus and the baseline on both sides of the image.

2.2.5.2 Raman Spectroscopy

The Raman spectra were acquired using the DXR Raman microscope machine (ThermoFisher Scientific) with the acquisition being controlled through the Omnic software (ThermoFisher Scientific). The collected sample was set up in the bench to collect 6 acquisitions per point, subject to averaging to produce a final x6 average spectrum per point. It was decided to use a custom point map acquisition due to the inability to directly import MAP files into the spectra processing program (Quasar). These collection points however followed an even grid distribution over the visible

surface to reduce bias. Post-collection, the spectra were saved in .CSV format and analysed further using Quasar software through the “post-processing” functions to improve the quality of the output. The parameters of pre-processing were as follows. Firstly the spectrum had been ‘cut to keep’ between 243 and 3000 cm⁻¹, secondly, a rubber band baseline correction was applied and finally, a Savitzky-Golay filter with a window of 15 and polynomial order of 2 was applied.

It was decided to maintain a simplistic approach to process the spectra, using only a minimal smoothing function for post-processed PDMS spectra, where the Savitzky-Golay filter was commonly used to smooth spectra (*Zhang et al., 2017, Sheehy et al., 2023*).

2.2.5.3 Energy dispersive X-ray spectroscopy (EDX) from SEM

EDX is a spectrographic technique used to analyse the electron backscatter from scanning electron microscopy. The Hitachi TM4000 scanning electron microscope (*Hitachi, Japan*) was used to acquire the scans and the EDX spectra coupled with the Oxford Instruments Xplore detector (*Oxford Instruments, UK*). For each surface, 4 spectral acquisitions from 5 regions were collected and averaged from each sample surface. Due to limitations in sample preparation, replicates were regional replicates, not sample replicates.

2.2.5.4 Atomic Force Microscopy

Samples of wrinkled PDMS were outsourced to the Sheffield Surface Analysis Centre at the University of Sheffield for Atomic Force Microscopy and surface analysis by the peak force tapping method. From this analysis surface maps of the wrinkled

topography and quantification of the roughness quotient were obtained for the acid-oxidized, plasma-treated and the dual treatment PDMS wrinkled surfaces.

2.2.6 Imaging

All images, as captured by their respective devices were processed and scaled using the open-source software package FIJI (ImageJ). Quantification functions were performed using their appropriate plugins. Alignment analysis was performed on fluorescent images using the OrientationJ plugin which produced histograms of the alignment of cells against a vertical axis. Image-based cell counting and basic morphology analysis were performed using fluorescent images which were first thresholded to create binary images. Smoothing was applied to reduce small particle contamination and the watershed function separated adjoining particles (cells). The processed binary image was subjected to the particle analysis function to count the total particle number and measure the average circularity of all particles in each image. Regions of interest (ROI) were defined contextually, for cellular images, the ROIs were typically the full field of view images, typically at x10 magnification unless otherwise specified. For linear or boxed ROI, these were defined in ImageJ for analysis and are specified on each image used. Replicates for imaging and analysis were typically $n = 3$ unless otherwise specified.

2.2.6.1 Light Microscopy

Bright-field microscopy for cell culture was performed using an inverted bright-field microscope (Leica) and digitised using a digital camera controlled with the associated software.

For pre-screening of human tissue the Leica MZ10F fluorescent dissecting microscope (*Leica*) was used, in the Bright-field setting with a polarised camera filter arranged underneath the objective lens (*Nikon, Japan*). The purpose of the filtering lens was to sufficiently remove any reflective glare from the tissue during imaging in a low-cost manner, to reveal the POV structures not visible using unfiltered Bright-field camera images alone.

2.2.6.2 Fluorescent Imaging

Fluorescent imaging at low to medium power was acquired using the Leica MZ10F fluorescent dissecting microscope controlled with the dedicated Leica Application Suite X program (*Leica, Germany*).

2.2.6.3 Live Cell Imaging

Automated live cell imaging was performed using the CellCyte live cell imaging system. Confluence-based analysis used the Bright-field mode (enhanced contrast). The cells were seeded following experimental parameters and following individual cell protocols. The well plate was seated on the CellCyte machine and the acquisition parameters for the experimental duration were set up in the software. Each experimental acquisition exceeded no longer than a single inter-passage cultivation period. Enhanced contrast is an automatically adjusting feature, thus manual adjustment was not necessary. Exposure frequency and images per well varied with well plate sizes, machine availability, and experimental constraints.

Cell counting analysis followed a fluorescence-dependent program, therefore the cells were stained using CellTracker green CMFDA dye (Thermofisher Scientific,

UK) (a live cell tracking dye) during the passage. After centrifugation and counting, the cells were resuspended in 1 ml medium with 2µl of the live tracking dye and incubated at 37°C for 30 min. After incubation, the cells were centrifuged to remove the dye solution. After staining, the cells were seeded as required and the CellCyte was set up similarly to the enhanced contrast program, with additional optimisation of the green fluorescent channel.

The alternate method of live cell imaging utilised the Leica MZ10F fluorescent dissecting microscope. During the passage, the cell pellet was resuspended in 1-2 ml of medium (dependent on cell number/dispersion requirements) containing 2-4 µl of the CellTracker Green CMFDA (Thermofisher Scientific, UK). The suspension was incubated in the dark for 30 minutes before re-centrifugation to remove the dye solution. The substrates/wells were then seeded as required and tracked. Manual tracking was typically performed when wrinkled substrates were employed (due to the difficulty of visualising cells through the material) using a transmission setup. Fluorescent images were captured using the green (FITC) filter.

2.2.6.4 Confocal Microscopy

3-Dimensional z-stacks were acquired using the Olympus FL2100 series confocal microscope (Olympus, Japan) controlled using the linked proprietary software. Typically resolution was limited to 800x800 to balance the number of slices per acquisition against memory usage, allowing an optimised maximum stack depth and multi-cellular depth imaging. Stacks were then projected through the Z-projection to create a 2D projected image from the 3D acquisition. Additionally, the stacks could be cropped, rotated (transform rotate function) and 3D-projected to achieve cross-sectional reconstructions.

2.2.6.5 Scanning Electron Microscopy

High-resolution imaging of material surfaces was attained using the Hitachi TM4000 scanning electron microscope. The scanning parameters were as follows; an accelerating voltage of 15 kV, medium vacuum conditions and utility of the secondary electron (SE) detector. Before scanning, samples were air-dried for at least 24 hours before coating. The samples were sputter coated with gold, with a thickness of approximately 10 nm shortly before imaging.

2.2.7 Staining Approaches to Reveal Limbal Cell Function

2.2.7.1 Immunofluorescent Staining

Before staining, cultures were fixed in 4% paraformaldehyde in PBS at room temperature within a fume hood (20 minutes for monolayer culture or 45 minutes for wrinkled substrate culture). All fixed cultures, substrates, and vessels were washed twice with PBS to remove traces of fixative, before staining. Wash steps in staining differed between standard monolayer culture and material culture due to the sensitivity of the cells on substrates.

In monolayer culture, all PBS washes were performed once as a pipetted action with a swirl, whereas for wrinkled substrates, a gentler single PBS immersion was employed to ensure maximum cellular retention. Cells were permeabilized and simultaneously blocked in a solution of 0.3% Triton-X (Merck, UK) with 5% bovine serum albumin (BSA) (Merck, UK) as blocking buffer or 5% human serum (Lonza, UK) for 10 min in monolayer or 15 min on wrinkled substrates. Human serum was used as a blocking solution as it was observed there were fewer background and fluorescent

artefacts in human samples compared to using BSA. The combined permeabilization and blocking solution was washed off with PBS. The primary antibody was mixed at a working concentration of 1:100 in 1% BSA/human serum in PBS for mouse monoclonal anti-Cytokeratin 3, rabbit monoclonal anti-P63, rabbit monoclonal anti-ABCG2 and rabbit monoclonal Alexa Fluor 488 conjugated anti-K12 (Abcam, UK).

The rat monoclonal anti-vimentin primary antibody (R&D biosystems, UK) was mixed to a working concentration of 8 µg/ml in 1% BSA/human serum PBS. The primary antibodies were incubated at 40C in the dark overnight and subsequently washed off with PBS. The secondary antibodies were applied immediately after washing. Donkey anti-mouse conjugated with NL493 and donkey anti-rabbit conjugated with NL637 antibodies were mixed in 1% BSA/human serum PBS to the same dilution ratio in correspondence to their related primary antibody. Secondary antibodies were incubated for 2 hours at room temperature in the dark before being washed in PBS. Cells were counterstained with the nuclear stain 4',6-diamidino-2-phenylindole (DAPI) (Thermofisher Scientific, UK) at the working concentration of 1 µg/ml in PBS and incubated in a monolayer in the dark at room temperature for 10 minutes or 15 minutes for substrates. The DAPI dye is subsequently washed off with PBS. Stained monolayers/substrates were maintained in the dark in PBS after staining.

Phycoerythrin (PE) directly conjugated antibodies were also used as a stinge-step immunostain for the isolated limbal cells. Mouse anti-hNestin, rat anti-hVimentin, and mouse anti-hABCG2 (R&D Biosystems, UK) were applied to monolayer cultures 1:100 dilution (same as the primary-secondary method) and incubated at 4°C in the dark overnight. The PE-conjugated antibodies were washed off twice with PBS and the stained wells were maintained in the dark in PBS.

2.2.7.2 Cytoskeleton Staining for Morphology Assessment

For cytoskeletal staining cultures were specially fixed in 10% formalin, as this was a manufacturer-recommended fixative for the actin stain used. Following fixation the cells were permeabilised using 0.3% Triton-X for 15min. The cells were washed with PBS following the procedures adopted for immunostaining. Phalloidin Texas Red was diluted to a working dilution of 330nM (5µl stock of a 33µM stock per 500 µl aliquot working solution) and applied in sufficient amounts to just cover the surface containing the cultured cells. The stain was incubated in the dark for 45 minutes at room temperature, washed twice gently then stored in the dark in PBS.

2.2.7.3 Haematoxylin and Eosin Staining and Preparation of Tissue for Histology

Both whole tissue and cells were preserved in 4% PFA, cells following the preservation protocol outlined in section 2.2.7.1 and whole tissue after infiltration with 4% PFA at 4°C for a minimum of 48h.

Monolayer and substrate cultured cells were washed with PBS to remove the fixative then the culturing surface was flooded with Haematoxylin solution with a dropping pipette for 3 minutes. The haematoxylin solution was removed by washing with tap water and irrigated using a dropping pipette. Eosin Y solution was pipetted onto the surface and incubated for 1min 30s. The surface was gently washed in excess tap water until the stain fully evolved. Monolayers/substrates were stored in PBS.

Fixed tissue pieces were dehydrated first by an ethanol gradient from 70% through to 100%. The dehydrated tissue was cleared using xylene twice then immersed in molten paraffin wax and allowed to infiltrate for 1hr, then refreshed in clean wax and re-infiltrated. Wax-infiltrated tissue pieces were orientated in wax

cassettes and immobilised for slicing using a microtome. The tissue was sectioned into 10µm slices and captured onto polylysine-coated microscope slides (SLS Scientific, UK). Wax-embedded slices were de-waxed firstly using xylene and then rehydrated by an ethanol gradient from 100% ethanol to washing with distilled water. Once hydrated the tissue was stained as per monolayer cells. After staining and washing the stained tissue was preserved by the application of histomount resin (to the tissue) and careful placement of a clean coverslip over the resin/tissue bead. Imaging was performed 24 hours later once the resin was cured.

2.2.8 Cell Isolation

Figure 2.6 introduces an overview of the limbal cell isolation and cultivation processes in this research.

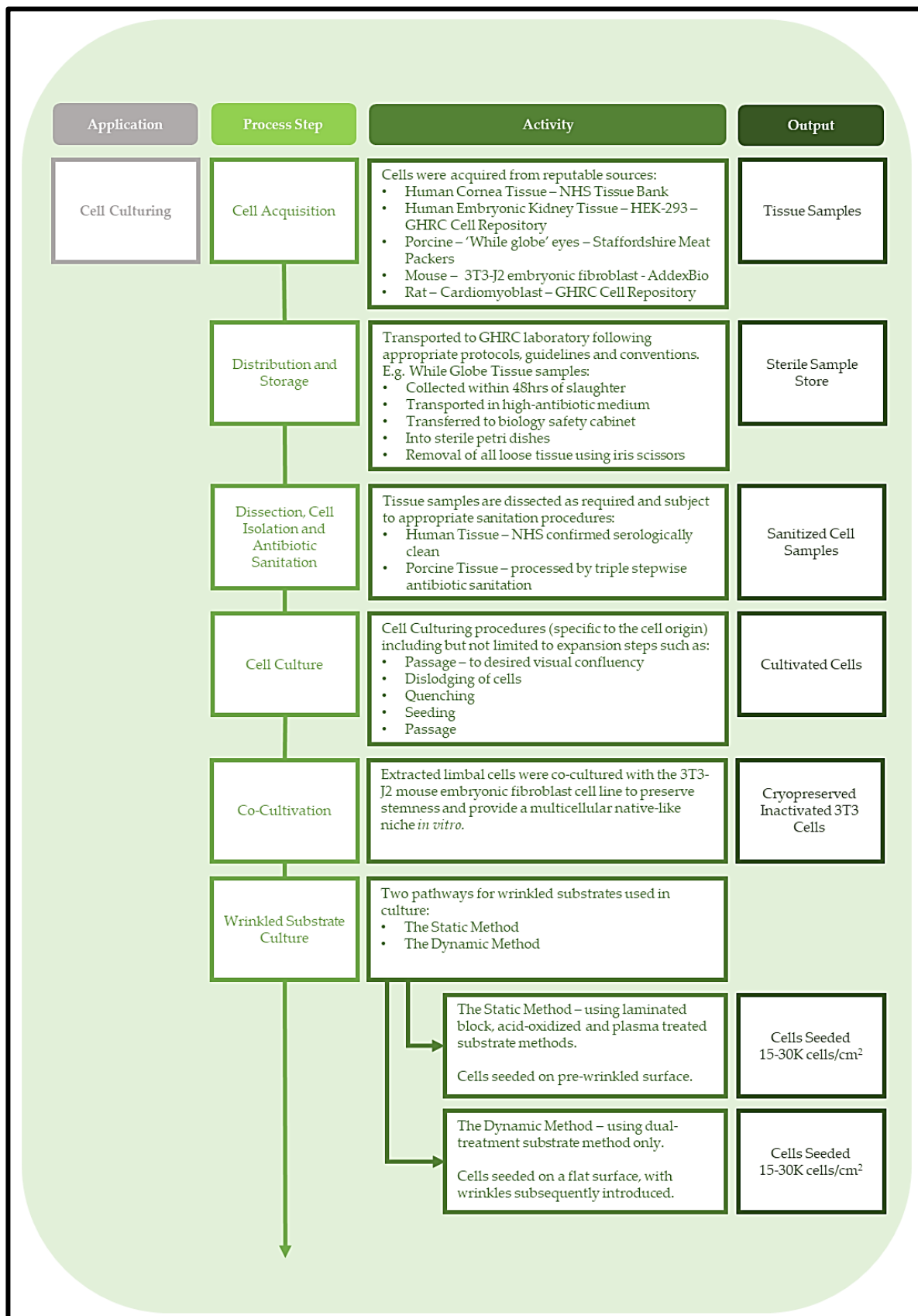


Figure 2.6: Process flow diagram for the isolation and cultivation of primary limbal cells. This diagram visualises the process of cell isolation from primary tissue to cultivation on wrinkled substrates.

For both species, the tissue was dissected into corneoscleral button quarters to present the limbus for isolation. In the human tissue, this was simply done by identification of the POV using polarised microscopy (human tissue) or by using the Thorlabs OCT device for the porcine tissue. OCT was used for the porcine tissue due to the thicker porcine epithelium causing greater glare, therefore the polarised microscopy was not suitable to see the POV.

For porcine tissue, the tissue was supplied as whole globes from the abattoir (Staffordshire Meat Packers) within a maximum of 48 hours of slaughter. The globes were transferred to a biological safety cabinet and dissected in 95mm sterile petri dishes. All loose tissue including attached eyelid(s), trailing optic nerves, and rectus muscle was removed using iris scissors or a scalpel. The globes were perforated and once the button was isolated the lens, iris and all the easily debrided dark tissue were removed using forceps. The dissected buttons were thoroughly washed in and then transferred into the dedicated sealed sterile Schott cap for OCT screening. Subsequently, the tissue was cut into quarters using a scalpel, and the pieces containing the identified and demarcated LESC niches were set aside for cell isolation and sanitized with antibiotics (porcine only).

Human tissue supplied from the NHS tissue bank was confirmed serologically clean (after being tested before delivery by the NHS) and, therefore did not need antibiotic treatment. The porcine tissue was subjected to a triple stepwise antibiotic sanitization using 125 µg/ml Amphotericin B (Gibco), 500 µg/ml Gentamicin (Gibco) and 500 units/ml (5%) Penicillin Streptomycin (Lonza) for 1 min per wash, interspersed with 1 min PBS washes to remove the antibiotic, transferring to a clean well, exchanging to fresh forceps each time.

The tissue pieces selected for isolation were subjected to a 2-step enzyme digestion. The first step utilized Dispase II (Merck) at 1.2 IU/ml, incubated at 37°C for 2h, to loosen the limbal epithelial tissue which eased debridement by using forceps and no. 15 scalpel blades. The debrided epithelium was subsequently incubated in 1 mg/ml Collagenase A in culture medium at 37°C for 14-18h. Tissue digestion into single cells or small cell clusters was verified microscopically over the last 4h of the digestion period. After the second digestion, the suspension was diluted in excess culture medium and centrifuged at 250 g for 5 min then resuspended in fresh culture medium after the enzyme-laden medium was aspirated. The cells were transferred to a collagen-coated 6-well plate for passage 0 expansion. Isolation was tracked visually, success was determined when colonies formed and proliferation by colonial expansion was observed.

2.2.9 Cell Culture

2.2.9.1 Human and Porcine Cell Limbal Cell Culture

Established cells, both human and porcine, were grown to 75-90% visible confluency, both typically taking 6-8 days to reach the desired confluency. Once desired growth was attained, the culture medium was aspirated and the monolayer was washed once in sterile PBS followed by incubation in 1X trypsin (Gibco) for 3 -6 min at 37°C. Either light tapping (human cells) or the application of a cell scraper (porcine limbal epithelial stem cells) was used to completely dislodge cells. The digestion was quenched using an equal volume of culture medium to the volume of trypsin used. The suspended cells were centrifuged at 250 g for 5 min, the cell pellet resuspended in 1 ml to enable counting after the supernatant was aspirated, and then

the cells were transferred into a T25. Typically limbal cells were passaged at a density of 8K cells/cm². For immunophenotyping in well plates, cells were passaged and seeded at 30 K cells/cm², for both isolated species.

The cells were cultivated in DMEM-F12 (Gibco, UK), supplemented with 10% foetal bovine serum (FBS), 100 U/ml penicillin/streptomycin (Lonza, UK), 20mM L-Glutamine (Gibco, UK), 0.1X insulin transferrin selenium (ITS) supplement (Gibco, UK), 1 µg/ml isoproterenol (Merck, UK), 0.4 µg/ml hydrocortisone (Merck, UK) and 2.43 µg/ml adenine (Merck, UK).

Originally, this formulation arose out of an in-house protocol, however, it is heavily based on existing LESC medium formulations which require the key components of hydrocortisone and adenine to retain LESC proliferative capacity and cell size maintenance (*Yu et al., 2016*). Whilst ITS is known to be a necessary component in ocular media (*Bueno et al., 2009*). Cholera toxin is classically used as a cyclic AMP (cAMP) accelerator to boost cell cycle entry rate, however, it is expensive and a bacterial product, therefore a pharmaceutical alternative was used. A β-adrenergic receptor agonist, isoproterenol, was used as this molecule has demonstrated similar cAMP stimulation in limbal cell culture (*Ghoubay-Benellaoua et al., 2021, Yu et al., 2016*). In addition to performing the same function as cholera toxin, Isoproterenol is safer to handle (as it is labelled as mostly irritant compared to the much more harmful cholera toxin) and far more cost-effective as a medium additive, making it a more suitable choice for this formulation.

2.2.9.2 Co-cultivation of Isolated Limbal Cells with 3T3-J2 Mouse Embryonic Fibroblasts

Extracted limbal cells were co-cultured with the 3T3-J2 mouse embryonic fibroblast cell line as a means to preserve stemness and provide a multicellular native-like niche in vitro. "Active 3T3" cultures were passaged by trypsinization with 0.5x trypsin for 3 minutes at 37°C with 10x repeated pipetting down the culture surface to dislodge the cells. The digestion solution was quenched with an equal volume of culture medium to trypsin used and the suspension was centrifuged at 1200 rpm. The re-suspended cells were re-seeded at a ratio of 1:6 in T75 flasks (for expansion and inactivation). 3T3 cells were inactivated when they reached 70-90% confluency using mitomycin-C at a working concentration of 10 µg/ml in culture medium for 2 hours. After the inactivation period, the cells were washed 3 times with PBS and then trypsinized as per regular passage. Cells were counted and seeded in the destination vessel at 20K 3T3 cells/cm² 24 hours before the limbal cells were passaged/isolated onto the 3T3 layer. The lower density of inactivated cells allows the isolated porcine limbal cells to form colonies without inducing premature confluence within a short amount of time. If not immediately used at the point of inactivation, inactivated 3T3 cells were cryopreserved in 10% DMSO/culture medium and placed into -80°C storage (before being transferred to liquid nitrogen for long-term storage). Porcine limbal cells were typically seeded at 4K cells/cm² in co-culture and passaged every 6-8 days. The 3T3-J2 cells were cultivated in high glucose DMEM (Gibco, UK) containing 10% calf serum (ATCC, UK), 100 U/ml penicillin-streptomycin and 2mM L-glutamine. Medium formulation followed the supplier's recommended protocols. In co-culture, the 3T3 cultivation medium was exchanged out of the cultivation vessel immediately before the

introduction of the limbal cells, at this point all the cells were subsequently cultivated in the limbal cell culture medium as prescribed in section 2.2.9.1.

2.2.9.3 Wrinkled Substrate Culture

There are two ways wrinkled substrates were used in culture, the static method and the dynamic method. When investigated, the laminated block, acid-oxidized and plasma methods followed the static method only whereas only the dual treatment facilitated legitimate dynamization. The static method is a pure contact-guidance method whereby the cells were seeded on a pre-wrinkled topography compared to the dynamic method where the cells were seeded on a flat surface and then the wrinkles were introduced. Subsequently, the wrinkles were altered *in situ* to be flattened by the application of tension. These changes in the topography state, (while the cells were attached) are a source of mechanical stimulus at the cellular/"anatomy" interface level. Cells were seeded on the substrates at numbers between 20-60K cells/substrate, equivalent to 15-30 K cells/cm².

2.2.9.4 Human Embryonic Kidney-293 Cell culture

Human embryonic kidney-293 (HEK-293) cells were acquired from the research group cell repository. For expansion, the cells were cultivated in standard T25 and T75 flasks depending on the required cell number. The cells were passaged at 60-90% confluence following the same trypsinisation process as the limbal cell. These cells however were centrifuged at 1200 rpm for 3 minutes. The flasks were seeded at 250K cells/flask after passage. The basal medium used was DMEM (Gibco, UK)

containing: 10% FBS (Corning, UK), 100 U/ml penicillin/streptomycin (Lonza, UK), 20mM L-glutamine (Gibco, UK) and 2% B27 supplement (Thermofisher Scientific, UK).

2.2.9.5 Rat Cardiomyoblast Culture

Rat cardiomyoblasts were kindly donated from the Dr George research group within the Guy Hilton Research Centre at Keele University. For expansion, the cells were cultivated in T25 flasks. The basal medium was DMEM (Gibco, USA) which was supplemented with 10% FBS (Corning, UK), 100 U/ml penicillin/streptomycin (Lonza, UK), 20mM L-glutamine (Gibco, UK) and 2% B27 supplement (Thermofisher Scientific, UK). The cells were passaged at 60-90% confluence by trypsinization in 1x trypsin for 3 minutes at 37°C, cells were dislodged by tapping the flask. The digest was quenched with an equal volume culture medium before centrifugation at 1200 rpm for 3 minutes. The flasks were seeded at 250K cells/flask after counting and passaged every 4-6 days. Rat cardiomyoblasts were typically seeded onto vitronectin-coated substrates at 20 K cells/cm². Vitronectin (Sigma, UK) was made up to a working dilution of 1:5000 in PBS and incubated on the substrates overnight at 37 °C before culture.

2.2.10 Statistics

Statistical testing was performed using the open-source R-based package Jamovi (*Jamovi*). Two principal tests were performed. For comparisons of two populations, an independent samples T-test was employed. The Student's variant was employed in all cases, under the assumption the populations are normally distributed and are found to have equal variances as assessed in the integrated Levene's test.

One-way analysis of variance was used where three or more groups were being compared. This was coupled with a pairwise post-hoc analysis, either the Tukey or Games-Howell pairwise comparison. The decision to apply either test hinged on the outcome of the integrated Levene's test. If the populations were found to possess unequal variances then the Games -Howell was applied, otherwise, the Tukey pairwise comparison was applied for populations with equal variances. For all tests $\alpha = 0.05$.

Chapter 3: Characterisation of the Structure and Mechanical Properties of Limbus

Experimental work in this chapter was performed

in collaboration with the University of Dundee

Content from this chapter features in the publication: Characterizing Biomechanics of Limbal Niche Using Vibrational Optical Coherence Elastography (Dimmock et al., 2024)

3.1 INTRODUCTION

The limbus is a unique anatomical structure located circumferentially around the central cornea. This feature is presented as a wide epithelial crypt which encircles the cornea (*Shanmuganathan et al., 2001*). Within this large crypt, a series of undulations known as the palisades of Vogt (POV) reside. Within this undulating region, the crests of the POV are known as the palisade ridges (PR), and the troughs are known as the epithelial rete pegs (ERP) (*Haagdorens et al., 2017*). Prominent examples of these micro-scale undulations, typically within the order of 50-150 μm (*Grieve et al., 2015*), have previously been observed by slit lamp examination (*Townsend., 1991, Haagdorens., 2017*). In this chapter, the structure, and mechanics of the LESC niche are explored and characterised. Figure 3.1 provides reference OCT images of the key anatomical structures discussed throughout this chapter, from both the en-face and cross-sectional perspectives.

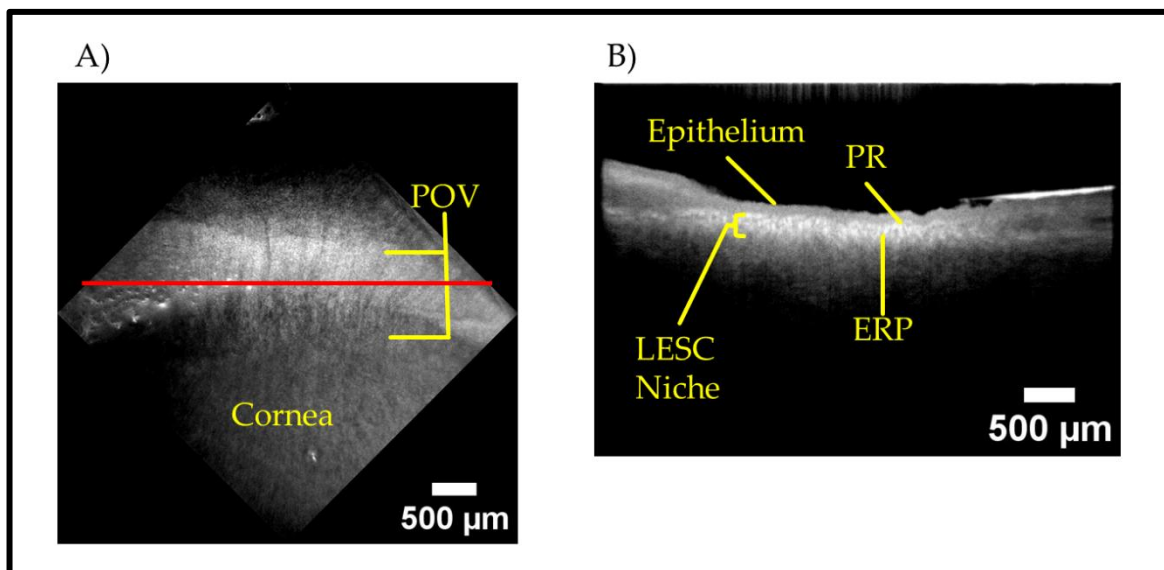


Figure 3.1: OCT images of a corneoscleral button to show the anatomy of the limbal niche. A) En-face perspective, showing the palisades of Vogt relative to the cornea, the red line marks the ROI for the cross-section. B) Cross-section, as taken across the red line in A), the cross-section shows the epithelial and the niche layers whilst also revealing the PR and the ERPs. The scale bars = 500 μm

In the en-face view, the striations of the POV, propagate radially to the rim of the cornea (the location of the limbal crypt) ((*Shanmuganathan et al., 2001*). In the cross-sectional view, these striations are revealed to be the aforementioned undulating features with the PR and ERP labelled as part of the LESC niche layer, which underlies the uppermost epithelial layer.

The limbal epithelial stem cell (LESC) niche is anatomically unique. It resides within the uppermost layer of the eye – the cornea and serves two major functions: maintaining sight and maintaining a barrier to the ocular internal environment (particularly the retina). The former function is attributed more to the nature of the stem cell pool, where this constant self-replenishing pool of limbal stem cells provides a source of corneal epithelia throughout adult life. LESCs facilitate constant regeneration of the cornea, combatting ageing: injury and infection contribute to maintaining central corneal clarity – vital to maintaining sight. This point has been retroactively proven when degraded corneas (suffering from limbal stem cell deficiency) have received limbal stem cell implants to induce corneal healing and recovery (*Shortt et al., 2007, Shen et al., 2015, Sagga et al., 2018, Le et al., 2020*). The second function of the limbus is to act as a barrier with a two-fold function. Primarily, the LESC niche is a functioning component of the epithelial layers including the cornea which constantly supplies cells. Thus the limbus can be considered as part of the outward-to-inward barrier that all epithelium, including the cornea serve (*Bashir et al., 2017*). Secondly, but not less important, the lateral barrier function of the limbus is also vital in maintaining sight. Without the presence of a structurally integral limbus around the entire cornea, or LESC niches in the superior/inferior regions, the cornea is observed to opacify through the process of conjunctivalisation (*Townsend, 1991*). This process is described as the invasion of neo-vasculature and conjunctival cells into the cornea,

which would have ordinarily been kept at bay by the limbal structures (*Lim et al., 2009, Jirvosa et al., 2011*). Conjunctivalisation is a continuous process which contributes to the degradation of the cornea and is a feature of multiple ocular conditions, including LESD and pterygium and is associated (by consequence) with injuries to the cornea and the conjunctiva. This is exemplified by the study into the post-operative outcomes of conjunctivalisation progression in patients after receiving cultured corneal epithelial transplants. It was observed in this study that 62.5% of patients did not present post-operative neovascularisation into the central cornea, limiting sight. However, a limitation of this study is that the limbal margins in near totality were affected by the procedure and subsequent neovascularisation (*Dobrowolski et al., 2021*). These progressive changes, namely the invasion of neovasculature and goblet cells have been demonstrated to be VEGF dependent, where systemic inhibition of VEGF expression prevented neovascularisation and goblet cell invasion in a mouse conjunctivalisation model (*Joussen et al., 2003*). The formation of pterygium is considered to be similar in nature to conjunctivalisation associated with LSCD or other disease. The formation of these fibrotic lesions presents similar pro-inflammatory features (including stromal neovascularisation), invasion of goblet cells and physical disruption to the physical structure of the corneal and limbal matrices (*Reda et al., 2018, Shrahraki et al., 2021*). Pterygium differs slightly from conjunctivalisation in the sense that the pterygium origins can be attributed to defunct limbal cells which proliferate outwards, showing positivity for limbal markers including P63 and CK15, these cells were found on the leading surface of the lesion, demonstrating that the formation of these fibrotic lesions is not only due to the breach of the limbal structure but due to an over-proliferation of these cell types (*Bai et al., 2010 Shrahraki et al., 2021*).

In this chapter, the non-destructive methodology of optical coherence tomography (OCT), then subsequent optical coherence elastography (OCE) have been employed to quantify the limbal epithelial stem cell niche. The advantage of this imaging approach is that no dissection is required to obtain 3-dimensional depth-resolved images from tissue specimens or live patients. In this chapter, cadaveric corneoscleral tissue was investigated to structurally (and subsequently mechanically) characterise the LESC niche.

OCT is an interferometric imaging method which typically employs a near-infrared scanning laser and can penetrate a limited depth in tissue. The light from the scanning laser is reflected and collected, with the changes in the signal coherence analysed by the signal processor (typically employing an interferometer), facilitating imaging dependent on the changes of tissue density which alters the coherence of the probe beam (*Aumann et al., 2019*).

Currently, OCT sees active clinical use in retinal applications in optometry and ophthalmology. It is used for the diagnosis of conditions such as glaucoma (*NICE, 2023*) and in surgical procedures such as percutaneous coronary intervention (PCI) (*NICE, 2023*). In these clinical applications, the larger scale organ and tissue structure is of more interest, therefore the imaging tends to be in scales of several millimetres or even reconstructed with scales of centimetres (*Brandao et al., 2016, Longobardo et al., 2019*). Whilst these scales are suitable for medical imaging they are too broad to capture the microscale details of tissue microstructures.

However, in epithelial surface imaging, there have been strides forward in this field; particularly in the corneal surface. There have been efforts to structurally characterise the corneal and the limbus together, beginning to show the microstructures of the corneolimbal surface with investigative and diagnostic

applications (*Herber et al., 2022*). Relevant studies have used OCT to quantify structures in the limbal niche, revealing micro-scale structures in high resolution, in particular the POV – the undulating structure which is of interest in this thesis (*Haagdorens et al., 2017, Varma et al., 2021*).

Advancing from OCT, optical coherence elastography (OCE) is an emerging non-destructive tissue testing method applied in this research to tissue. The core principle behind this methodology is the specimen being agitated and the phase difference tracked and computed into elastographic (mechanical) information (*Kennedy et al., 2013*). This method acts similar in principle to acoustic methods of elastography such as ultrasound elastography (*Sporea et al., 2011*) and magnetic resonance elastography (utilizing an acoustic driver) (*Mariappan et al., 2009*).

However, in contrast to more macroscale elastography techniques like these, OCE can resolve fine structures mechanically due to smaller imaging windows at higher magnification. Alternate OCE methods have revealed mechanical information from visual information and have been applied in corneal applications, eg. an air pulse variant of OCE was able to detect age-related changes in vivo in mice (*Li et al., 2014*). In humans, there has been an *in-vivo* probe developed to measure corneal, limbal and scleral regions using OCE by generating Rayleigh waves (undulating surface propagating waveforms) with a contact acoustic probe (*Ramier et al., 2020*). A method has been developed in a porcine ex vivo model that simulates a heartbeat in a move towards a non-contact method of OCE (*Nair et al., 2020*). These described methods move towards refining diagnostic modalities with applications for the diagnosis of corneal disease where the stiffness of the cornea can be used as a marker for diseases such as keratoconus (*De Stefano and Dupps, 2018*).

This chapter describes the process developed to characterise and quantify the limbus in greater detail, amalgamating the refined detail of high resolution of the limbal epithelial stem cell niche (*Haagdorens et al., 2017*) and the mechanical property characterisation enabled through OCE (*Kennedy et al., 2013*). Consequently, the relationship between the microstructure of the LESC niche and the directly correlated mechanical properties was analysed. Additionally, the correlation of donor age to the limbal structure and its corresponding mechanical properties was investigated. Finally, the efficacy of image processing methods was evaluated, facilitating future improvements.

3.2 MATERIALS AND METHODS

3.2.1 Summary of Methodology

In this chapter, the tissue was processed and analysed following a specific workflow. As per Figure 3.2, this workflow was applied to all tissue samples undergoing OCT volumetric imaging and OCE mechanical analysis. The LESC niche was first located and marked in all tissues. The samples were then subjected to OCT imaging and subsequently OCE analysis, with additional equipment being required to perform the vibrational OCE. Histology was performed post-OCT/OCE analysis. For OCT and OCE analysis the tissue samples remained un-fixed (not fixed in any fixative) to preserve tissue mechanical properties. Tissues were subsequently fixed in 4% paraformaldehyde for histology and storage after structural and mechanical studies were completed on the samples.

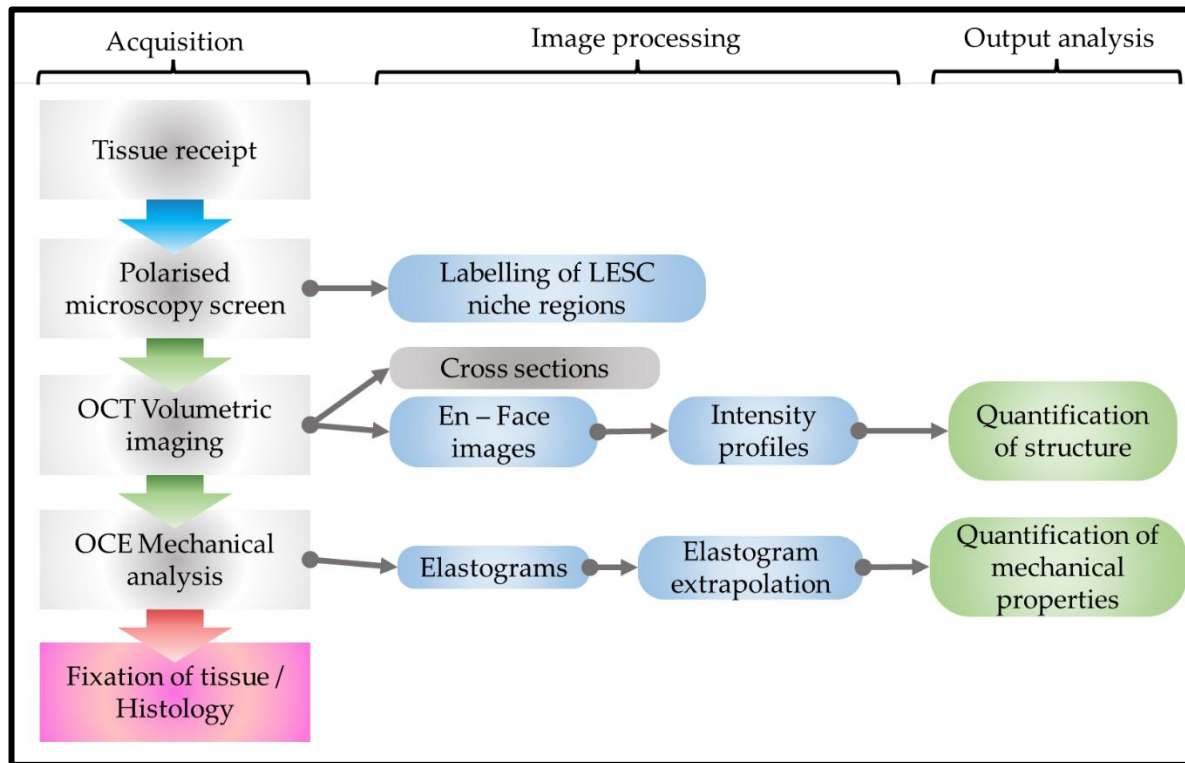


Figure 3.2: Schematic overview of tissue screening, image acquisition, processing and subsequent output from the imaging analysis stages. Here the workflow is broken down and split into its processes based on the modality being used to examine the tissue.

3.2.2 Polarised Optical Microscopy

The Leica FL dissecting microscope was used to visualise the corneoscleral tissue in the Bright-field mode. High contrast was achieved using a high gamma setting across all tissue samples. To remove glare, a digital camera polarising lens filter (Nikon, UK) was oriented under the objective lens and above the LED lighting array. The images were recorded using the Leica proprietary software and processed with ImageJ.

3.2.3 Optical Coherence Tomography

A collaboration was established with the University of Dundee to use their lab-built OCT/OCE equipment and the spectral domain OCT system (SD-OCT) was used to collect en-face images. The imaging system was set up as per section 2.2.1.1, the collected 3D data was processed into viewable images using a custom script in Matlab (MathWorks, USA). The OCT setup was operated, and data was acquired following a previous study methodology (Song *et al.*, 2013). The volumetric data stacks were converted into en-face images using median average projection and intensity profiles were extrapolated using ImageJ. Using this custom-built technology was much more favourable than using the commercial Thorlabs kit due to the direct integration of the lab-built OCT camera into the optical coherence elastography system. Therefore consistency between structural imaging and localisation of regions of interest for the structural and mechanical study could directly be maintained *in situ* on the same machine.

3.2.4 Vibrational Optical Coherence Elastography

The OCE procedure was performed using the SD-OCT system to record the images over an approximate 12s time series across a 3.65mm B-scan line. To induce oscillating vertical displacements in tissue, (which could be tracked used to differentiate regions of different stiffnesses by the PhS-OCT (Phase-sensitive OCT)) a vibrational shaker was situated underneath the sample (Brüel & Kjær Sound & Vibration Measurement A/S, Denmark). This was controlled and driven by a signal generator to create vibrations with a frequency of 850 Hz and an amplitude of 150mVpp (Keysight Technologies Inc., USA). The control of the input frequency and the

amplitude of the applied vibrations honed the clarity of the output elastogram, these values were considered the optimal values for these tissue samples as they produced the optimal signal-to-noise ratio and facilitated equal force distribution during “loading”. For other tissues of different stiffnesses, these values would be optimised accordingly. These time series depth-resolved elasticity information in limbal tissue with axial and lateral resolutions of 6.9 μm and 12.4 μm respectively, an SNR of 53 dB and displacement sensitivity of 2mm. As per OCT, the data was recorded through the customised LabView program (National Instruments, USA) and the elastograms were processed and output using the Matlab script (MathWorks, USA).

A 1% agar reference phantom containing 0.006% Titanium dioxide w./v. was applied to the surface of the tissue, which was mounted on a bed of agar of the same composition, ensuring the tissue assumed a shape approximating normal anatomical conformation by laying the tissue on a partially cured large droplet of agar phantom. ImageJ was used to extrapolate intensity values from the elastogram images which were subsequently used to calculate the stiffnesses of the anatomical regions investigated by comparing each region of interest to the average of reference regions which were of known stiffness; 14.6 ± 0.8 KPa which was confirmed by compression testing (and validated against literature) (*Li et al., 2015*).

3.2.5 Histology and Slice Preparation

The tissue was fixed in 4% paraformaldehyde for 24 hours before slice processing. An ethanol gradient from 70-100% was used to exclude water from the tissue pieces (including the POV) which were dissected from the corneoscleral rims. Subsequently, these sections were infiltrated with paraffin wax, sectioned into 10 μm thick slices and mounted on polysine slides for microscopy. The tissue slices were

cleared with xylene and the ethanol gradient was reversed (using water) to rehydrate the slices before staining. Haematoxylin and Eosin were used to stain the tissue slices. Images were processed using ImageJ.

3.2.6 Statistics

Testing for statistical significance was performed using the R-based software package Jamovi. Student's T-tests were performed between variables of interest. For age analysis, the sample population was split into even group sizes of $n = 5$ with the median age of 65-year-old being the divisive age. Comparisons of anatomical stiffness (epithelium vs. niche) in OCE were tested as $n = 5$ per anatomical region per age group and $n = 10$ when all

3.3 RESULTS

3.3.1 Optical Microscopy of the Limbus

Optical microscopy is the fundamental biological technique for cellular and tissue and tissue assessment. In this section, optical techniques are used to visualise the limbus from the enface and the cross-sectional perspectives to validate the OCT structural imaging and provide guidance of the ideal scanning location during acquisition for both OCT/OCE for human cadaveric tissue. Figure 3.3 presents examples of the human tissues used in the non-destructive testing study, sliced and stained with haematoxylin and eosin as prepared histological sections to reveal the limbal niche anatomy in samples from each age group. It was found in all samples that there was some tissue damage observed due to storage and handling to varying extents, however, there were some valuable qualitative observations to make. In the

younger tissue (CSR11 and CSR16) the crypt architecture, containing an intact limbal niche structure was better observed. Whereas in older tissues (CSR07 and CSR10) it was much rarer to find intact crypts, containing cells with POV undulations. These observations also indicate that in the future histology may be more beneficially performed before OCE/OCT analysis or performed on dedicated histology samples.

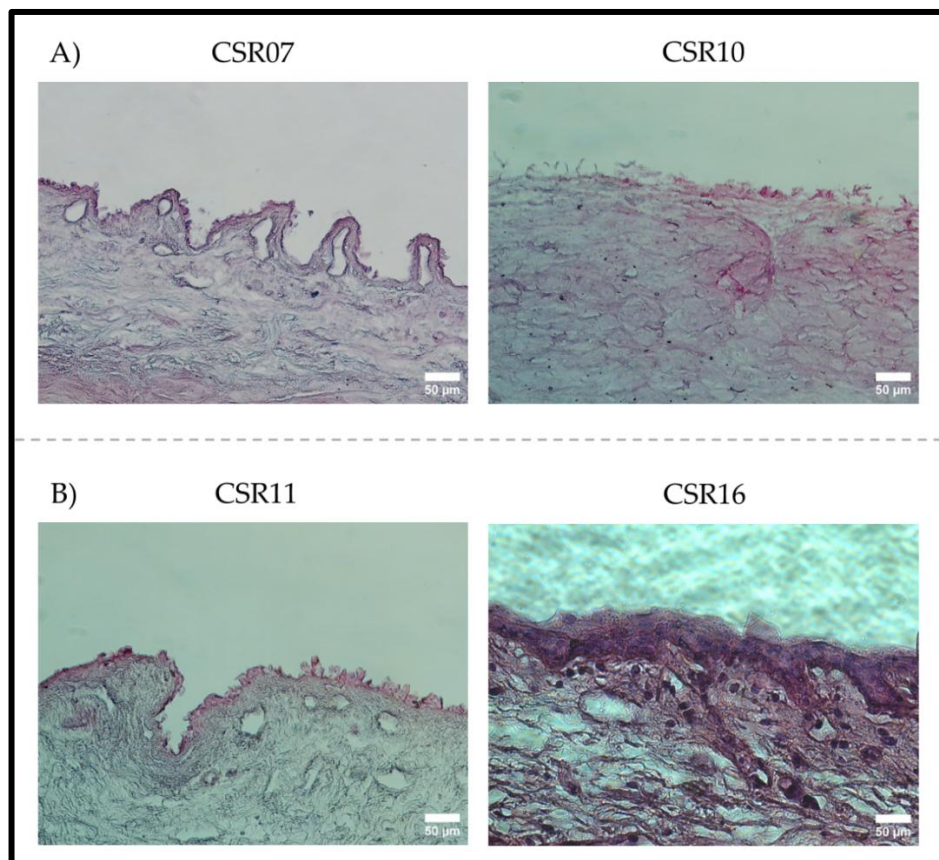


Figure 3.3: Haematoxylin and Eosin Staining of human limbal tissue used in this chapter. Row A) shows example samples from the over 65-year-old age group whilst row B) presents examples from the under 65-year-old age group. N=2 samples successfully visualised for each age group.

Before use in OCE/OCT examination, the human tissue was observed under the Leica dissecting microscope as shown in Figure 3.4. To aid in the visualisation of the finer architectural features, the glare from the microscope LED illumination array was compensated for using a separately mounted polarising lens

oriented under the objective lens. This filter lens facilitated the visualisation of some of the limbal features not normally resolvable using a non-polarised setup.

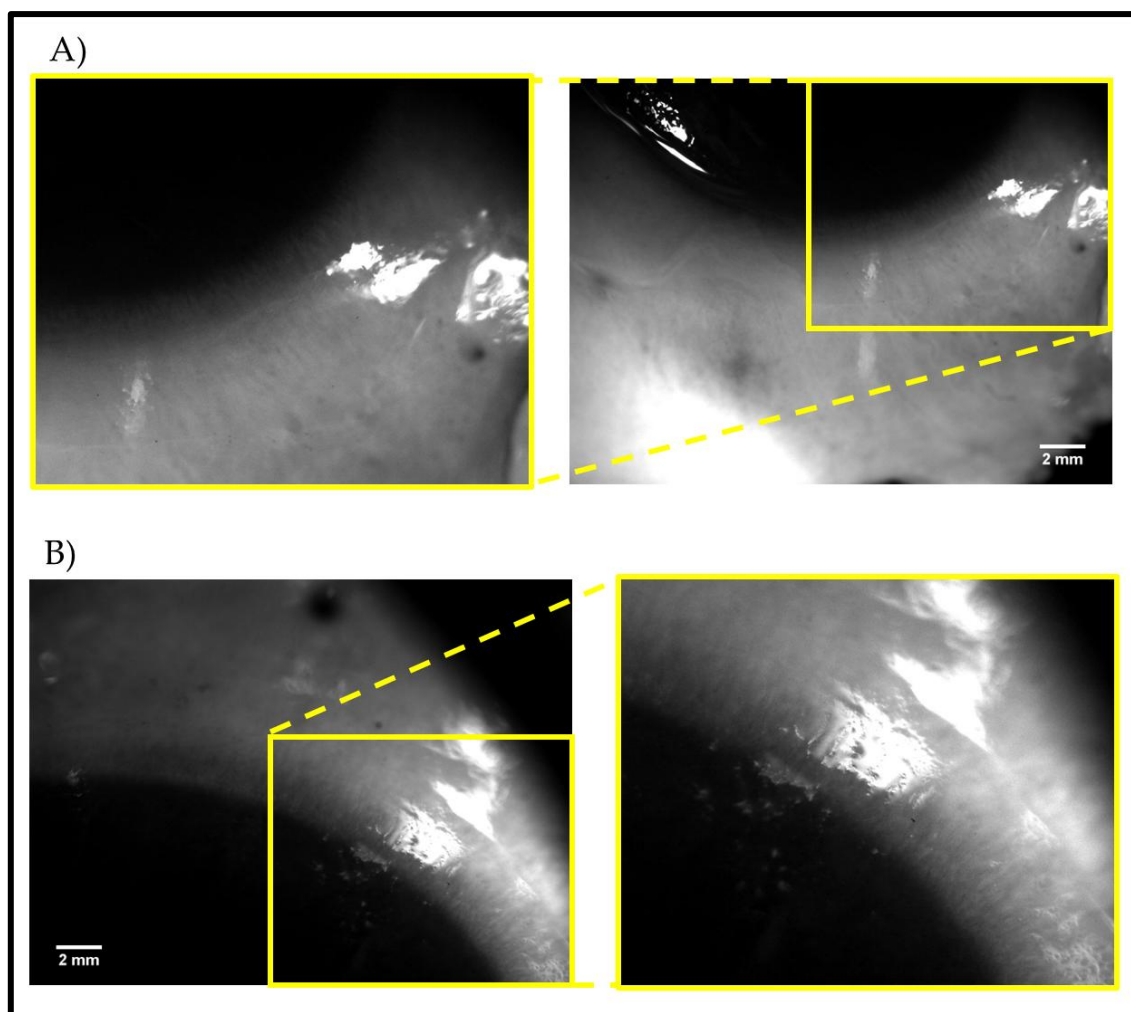


Figure 3.4: Polarised light micrographs of cadaveric human corneoscleral tissue. A) Example of a sample from the under 65-year-old group. B) An example from the over 65-year-old group. Scale bars = 2mm and are applied to the original image, magnified images are simple enlargements of the original image.

The polarized optical microscopy method was used to screen the tissue samples and locate the POV, to aid effective OCT/OCE imaging of the correct anatomical regions. Before the samples were imaged, they were marked with a small locating “tattoo” in the sclera as exemplified in Figure 3.5, at the midpoint of the located LESC niche region, using a 27ga. hypodermic needle and black ink. On the well plate

lid, brackets mark the edges of the niche regions for imaging. An example of such marking is also demonstrated in Figure 3.5. During OCT analysis the tissue remained unembedded (resting on the sample platform) and rested upon domes made of agar to recreate the natural curvature of the corneoscleral buttons. The tissue samples were hydrated using droplets of physiological phosphate buffered saline (PBS).

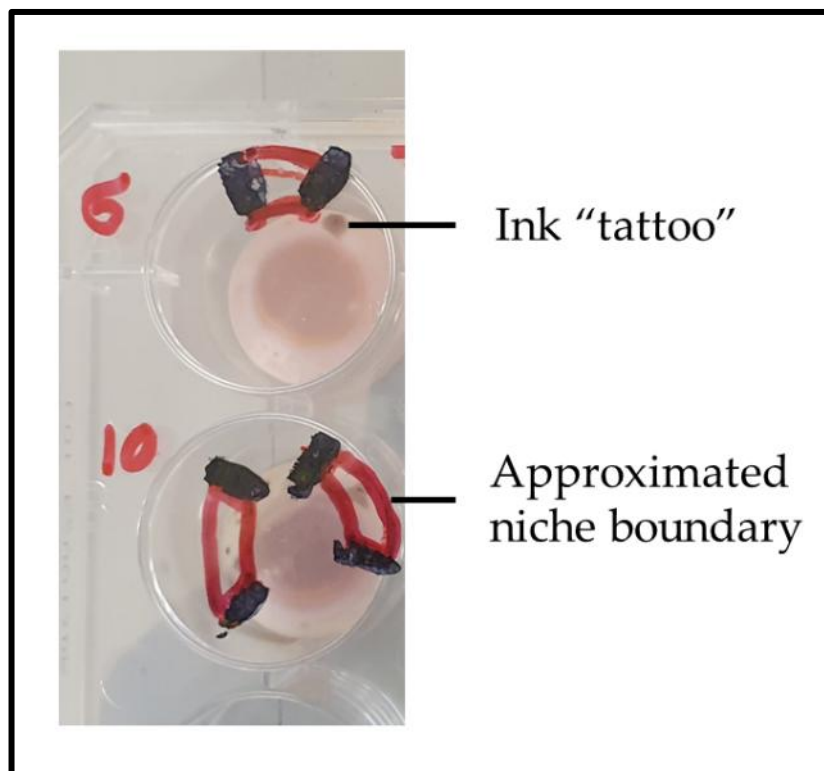


Figure 3.5: Examples of the limbal region demarcating process performed before OCT/OCE imaging. The ink dot tattoos are aligned to the centre of the brackets to show the approximated boundaries of the most prominent identified LESC niche regions.

3.3.2 Optical Coherence Tomography

Optical coherence tomography was utilised to produce high-resolution projected structural images of the limbal epithelial stem cell niche. On first inspection of the volumetric OCT, it was possible to view the tissue as cross-sectional views in Figure 3.6, here the undulations of the limbal epithelial niche, consisting of the limbal palisades of Vogt, underneath the epithelium are easily observed.

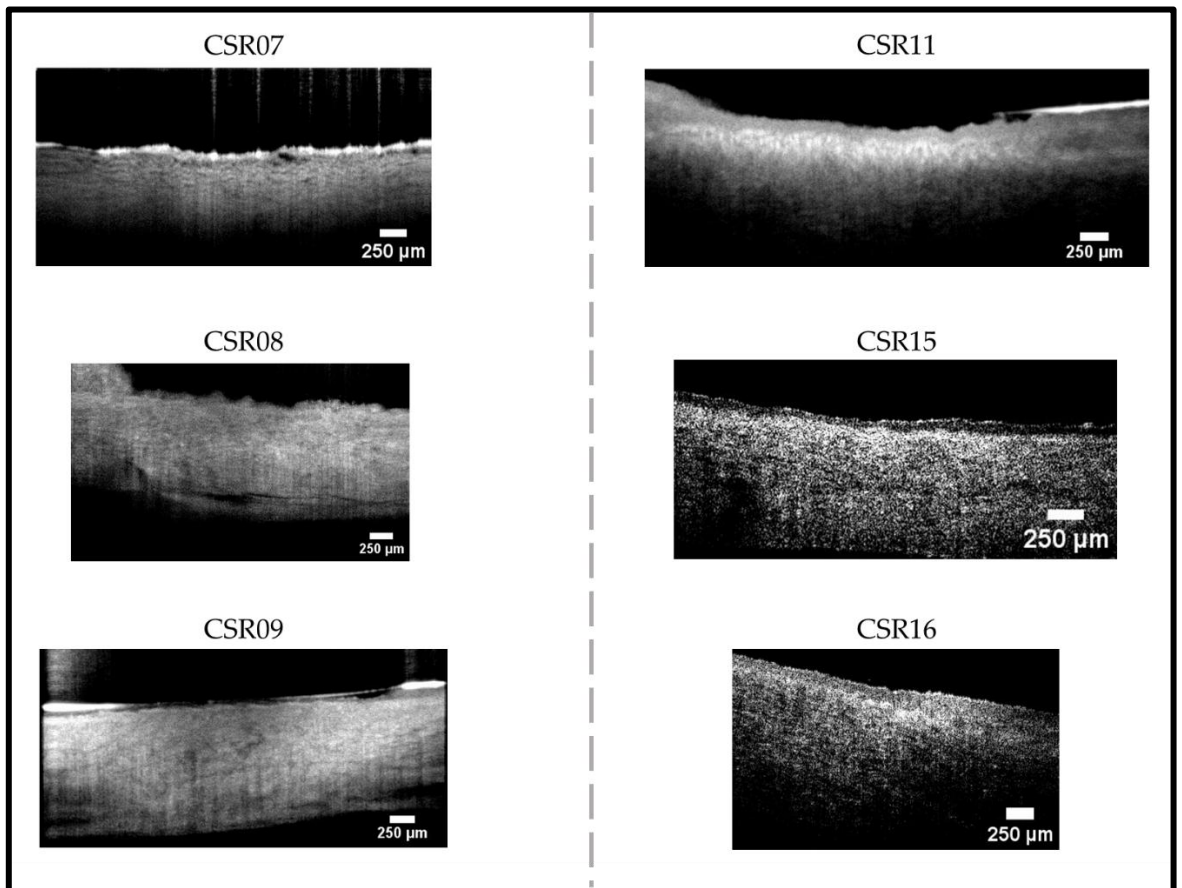


Figure 3.6: Cross-sectional OCT images from human tissue samples. Left-hand side: examples from the over 65-year-old age group. Right-hand side: examples from the under 65-year-old age group. All scale bars = 250 μm . N=3 cross-sectional reconstructions from each age group are shown.

From these structural images, it was possible to extrapolate quantitative information about the architecture of the niche. The method employed here was the intensity profiling method, where the grey value of each pixel across a region of interest of known distance is plotted, Figure 3.7 presents these ROIs for each of the samples. This allowed a crypt profile to be plotted for each POV region in each age group.

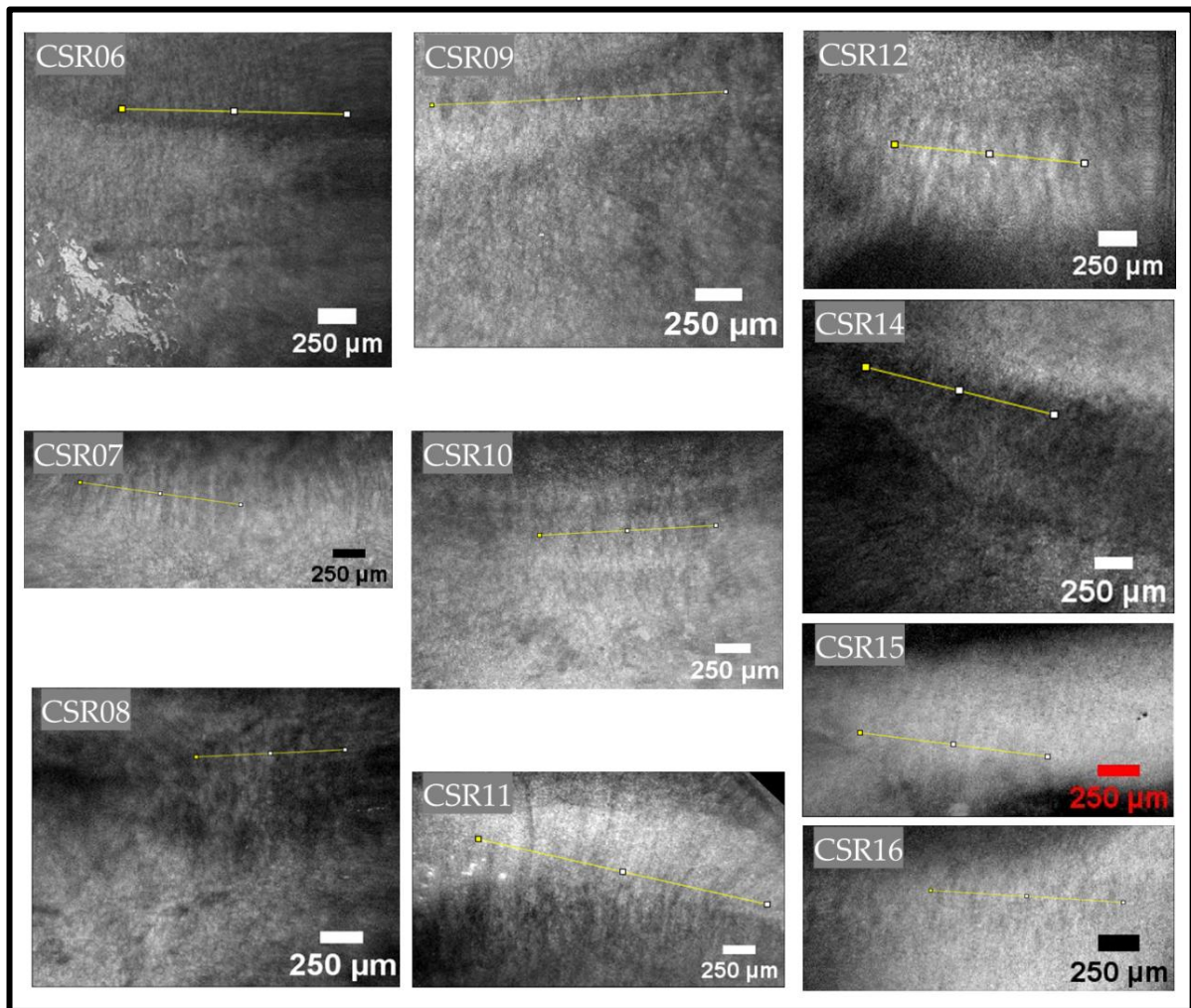


Figure 3.7: Median intensity projections of volumetric OCT scans of human LESC niche regions. Yellow lines demarcate corresponding ROIs for crypt intensity profiling. Scale bars are equal to 250 μm in length. All sample ROIs are shown.

The intensity profiles provided a pseudo-cross-sectional view of the LESC niche and facilitated the quantification of the POV. The first step in this process was the drawing of the profiles to gain a distance against the grey value (intensity) for each specimen. The curves presented in Figures 3.8 and 3.9 were smoothed by subjecting the intensities to a 2-step moving average down the entire plot, effectively de-noising the plots.

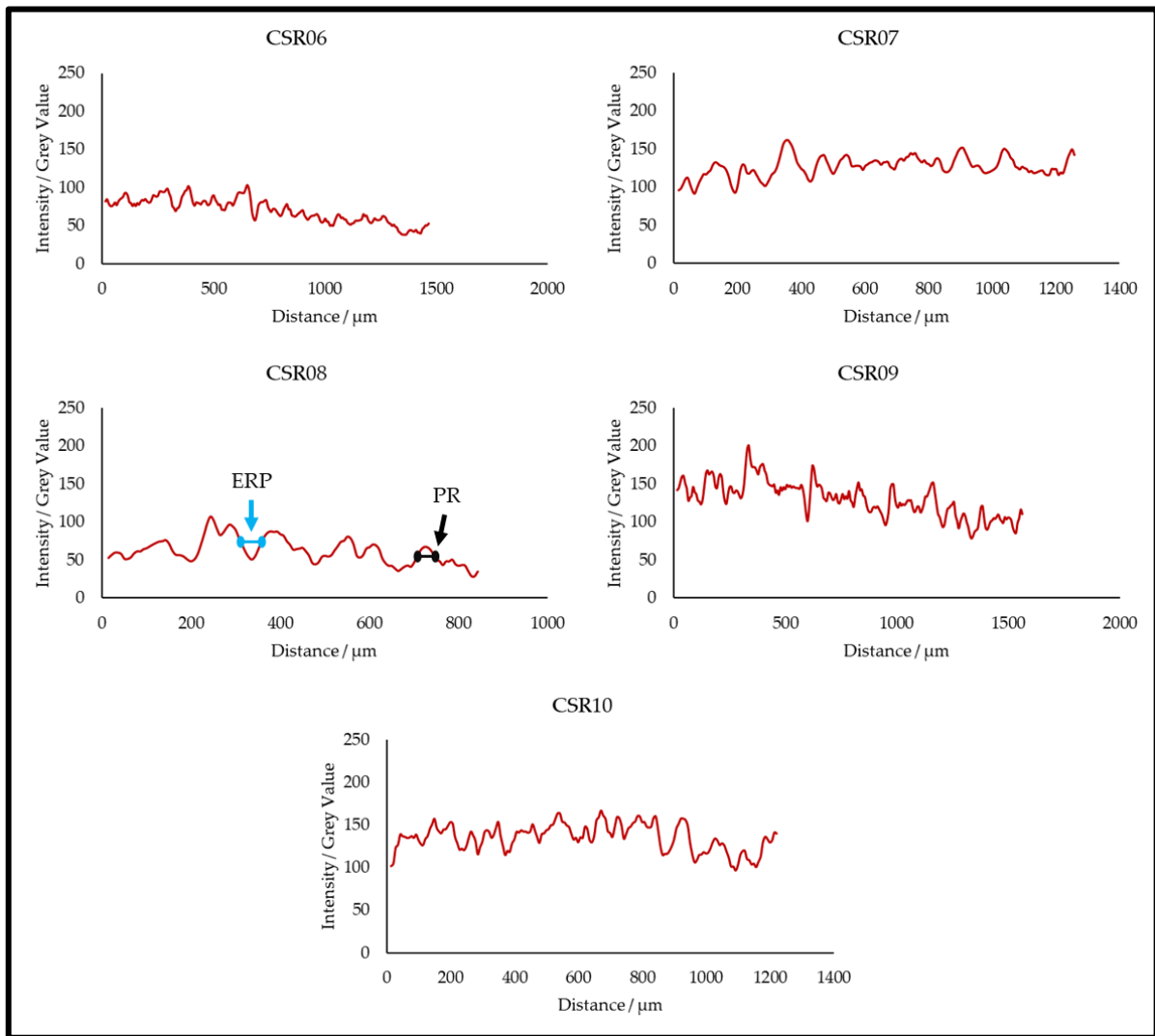


Figure 3.8: Intensity profiles of the over 65-year-old sample group. Profiles were drawn from the corresponding regions of interest marked in Figure 3.7. Examples of the measured width regions are as demarcated on the CSR08 profile. The ERP width measurement points example is represented by the blue bar and the PR width measurement points example is represented by the black bar. Lateral distance is scaled by each X-axis.

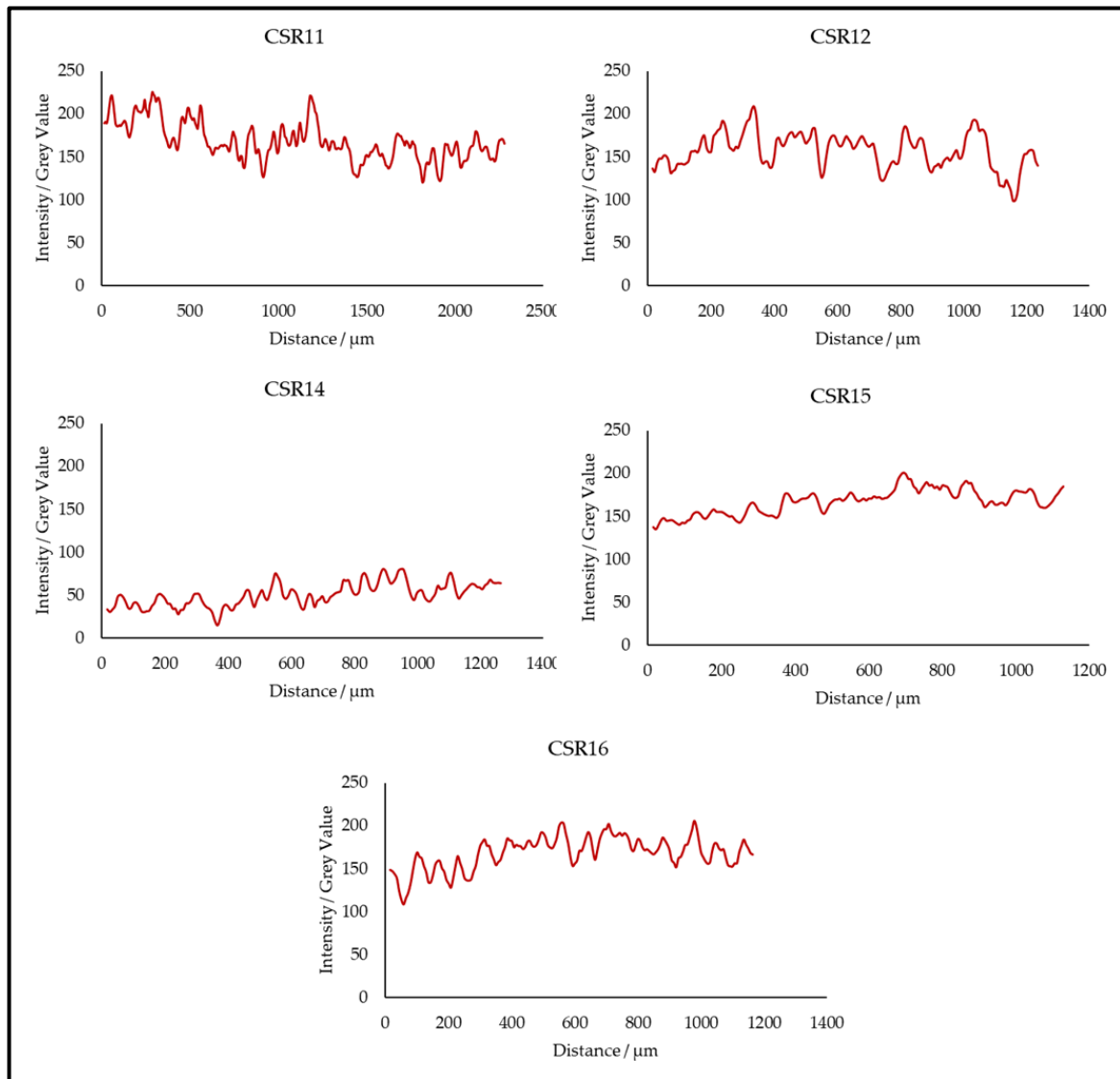


Figure 3.9: Intensity profiles of the under 65-year-old sample group. Profiles were drawn from the corresponding regions of interest marked in Figure 3.7. Lateral distance is scaled by each X-axis.

From these intensity profiles the distance in micrometres was used to calculate the ERP and the PR widths, this was performed by measuring the distance between trough segments (for ERP width) and the crest segments (for PR width) across the profiles using ImageJ. These anatomical measurements were chosen because the intensity profiles directly represent the dimensions of the anatomical features due to being exactly scaled laterally. Therefore the main advantage of analysing these profiles

is that the lateral length measurements are accurate as distance in μm . However, the limitation of using this image-based analysis method is that the scaling for feature dimensions is only available for the lateral axis, revealing only the ERP and PR. If this method was translated to material studies (a potential focus of future work) these measures would correlate to crypt width. The direction of measurement which could not be scaled was depth, which was expressed as intensity/grey value as extracted from the image, the brighter the points are in the image, the closer to the objective the feature is. However, in the acquisition and generation of the images, each depth point was not quantified, resulting in the depth component of the intensity profile being an arbitrary scale. Future work could look into the incorporation of quantified depth, acquired through OCT, into the intensity profiling method specifically by being able to correlate specific tissue depths to the grey values output in imageJ and plot this scale on the Y-axis. Therefore the relief of the plotted line as a function of grey value against distance in μm (provided the LUT (lookup table) for the image or the scale of the image remains unchanged before plotting) is a reliable scaled visualisation of the ROI topography as long as the LUTs are unchanged. From these measurements, it was ascertained that there were subtle observable changes in the niche structure when measured using this method as summarised in the charts in Figure 3.10. For the under 65-year-old group the PR width was found to be $43.4 \pm 4.57 \mu\text{m}$ with an ERP of $33.3 \pm 4.56 \mu\text{m}$. For the over 65-year-old group, the ERP was measured at $42.8 \pm 7.8 \mu\text{m}$ whilst the PR was calculated to be $29.9 \pm 3.22 \mu\text{m}$. Whilst there were observed differences, they were not found to be statistically significant between age groups, for either PR or ERP measurements, when tested using Students' T-tests. $P = 0.254$ for the ERP T-test and $P = 0.875$ for the PR T-test. These measurements were used.

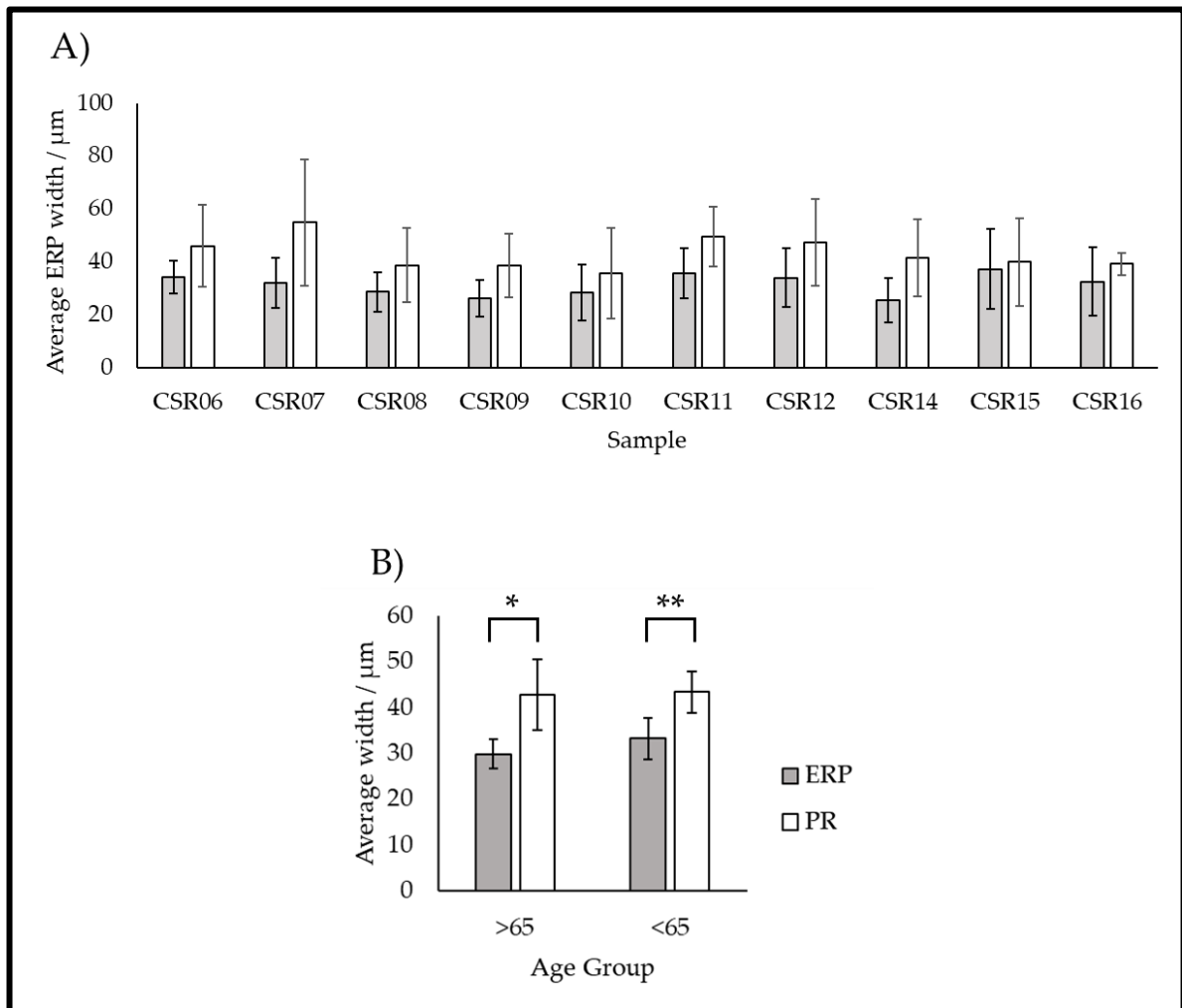


Figure 3.10: Quantification of the limbal POV features from projected OCT images. A) Average PR and ERP widths for each investigated sample and B) shows the average ERP and PR widths across the samples within the allocated age groups (n = 5 for each age group). Statistical significance is denoted by * (P = 0.009) and ** (P = 0.007) as determined by the Students' T-Test.

To determine if there was statistical significance between age and the measured anatomical features, Students' T-tests were performed between: each age group PR (P = 0.875), each age group ERP (P = 0.254) and within each age group: ERP vs PR >65 (P = 0.009) and ERP vs PR <65 (P = 0.007). From these comparisons, it is plausible to say that between age groups there is no significant difference in the width

of either the PR or ERP. However, in both age groups, the widths of PR and ERP are statistically significantly different, with the PR tending to be wider than the ERP.

3.3.3 Optical Coherence Elastography

After OCT was performed to structurally visualize and characterize the LESC niche, the same imaging system was employed, in conjunction with the vibrating stimulation device, to produce the OCE elastograms. The main difference in the acquisition is that the OCE was acquired as a 2D b-scan over an approximate 12s time series to collect the vibrational data required to calculate regional modulus. The subsequently produced elastograms are illustrated in the scale of the reciprocal of strain ($\frac{1}{Strain}$), a relative measure of substance stiffness as acquired by the OCE device. The displayed elastograms (Figures 3.11, 3.12, 3.14, 3.15 and 3.16) were produced using the greyscale LUT, therefore the images can be interpreted as the greater the intensity (brightness) of the region, the greater the relative stiffness of that region. Analysis of these images was performed in ImageJ to overcome software accessibility (Matlab) and machine hardware limitations.

Each layer of the analysed samples was able to be easily identified and then marked using linear ROIs as shown in Figures 3.11 and 3.12. Except for CSR14, which was limited to region length, consistent straight-line ROIs of 350 pixels for each line were used. These ROIs were then used to calculate the Young's modulus for the epithelial and LESC niche. To calculate the modulus, the epithelial and LESC niche layer intensity (Grey) values were plotted across the respective ROIs and the values were extrapolated. These values were averaged and compared to the average intensity value for the agar reference layer for each image. The agar used had a known

Young's modulus of 14.6 ± 0.8 KPa, thus directly comparing the averaged epithelial/limbal ROIs (2/3) to the averaged agar ROI (1) in each image produces Young's modulus for each anatomical region which are summarised for comparison in Figure 3.13.

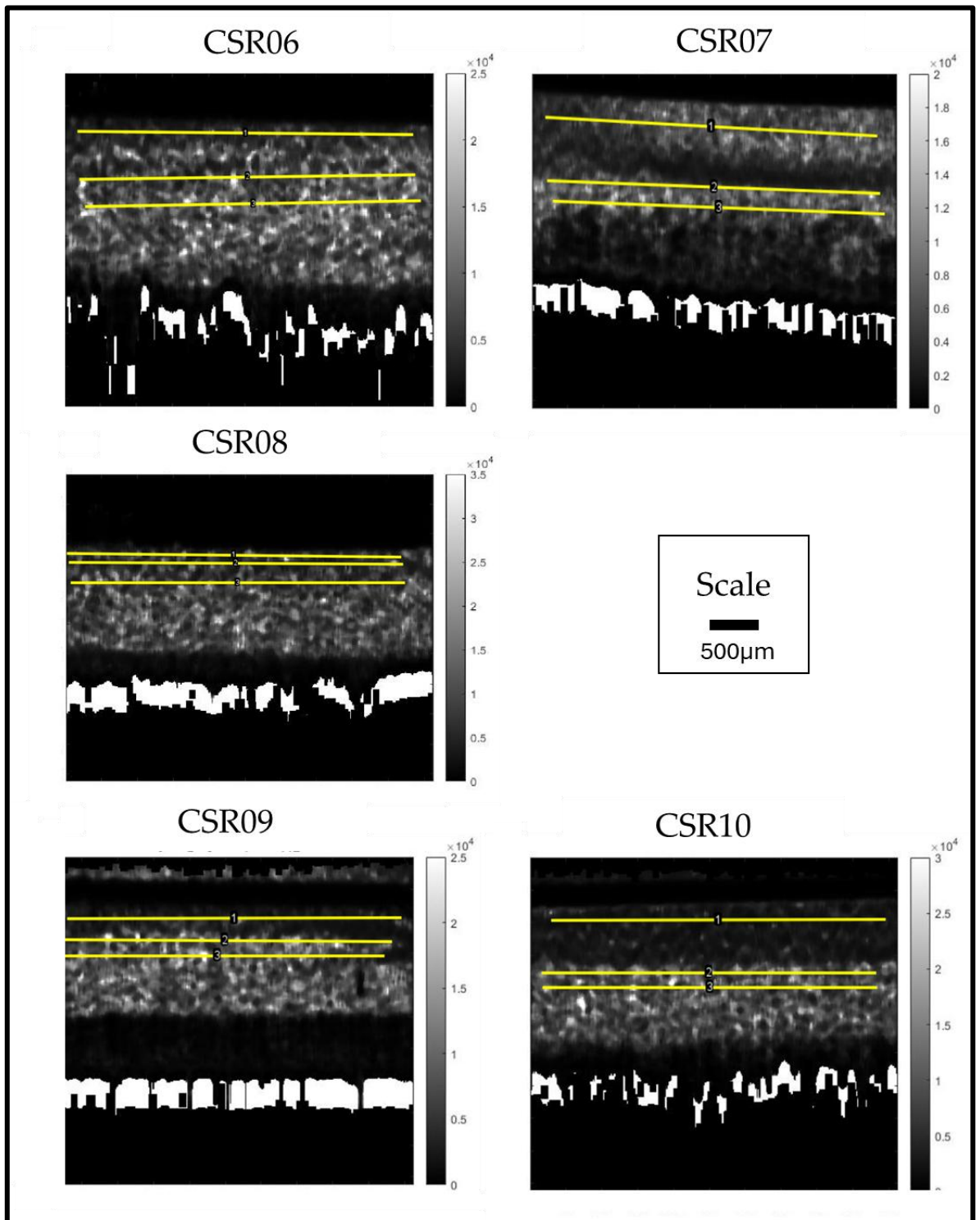


Figure 3.11: Elastograms taken from OCE of the over 65-year-old group. Linear ROIs used for the linear method of averaging each layer's elasticity are marked as yellow lines on each elastogram. 1) is drawn across the agar reference layer, 2) is drawn across the epithelial layer and 3) is drawn across the LESC niche layer. The elastogram gradient scales represent elasticity as $\times 10^4 \frac{1}{Strain}$, darker regions are softer and lighter are stiffer. The scale bar = 500 μ m and applies to all elastograms.

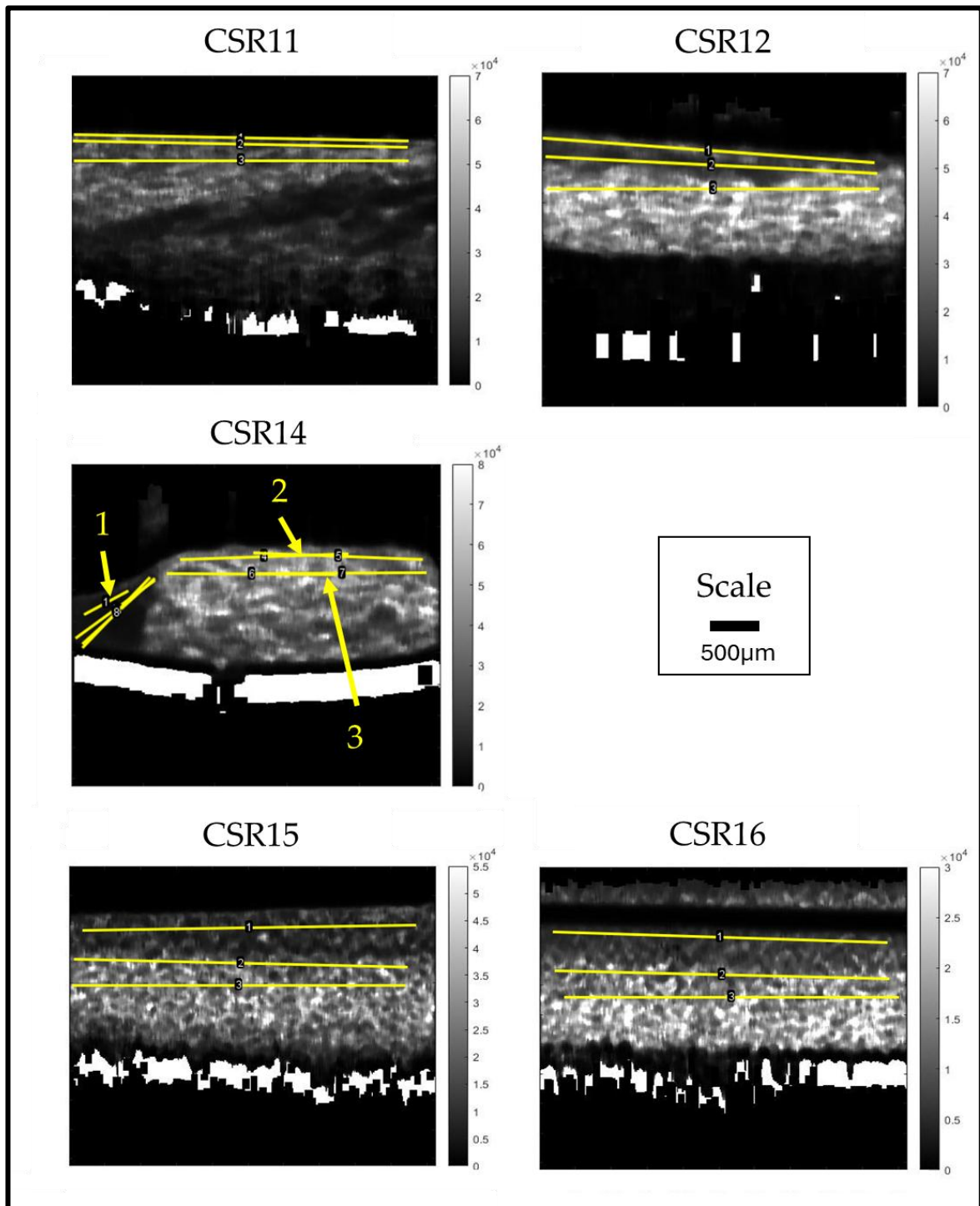


Figure 3.12: Elastograms taken from OCE of the over 65-year-old group. Linear ROIs used for the linear method of averaging each layer's elasticity are marked as yellow lines on each elastogram. 1) is drawn across the agar reference layer, 2) is drawn across the epithelial layer and 3) is drawn across the LESC niche layer. The exception is CSR14 which has these regions separately enumerated and marked, following the same ROI identifiers. The elastogram gradient scales represent elasticity as $\times 10^4 \frac{1}{\text{Strain}}$, darker regions are softer, and lighter are stiffer. The scale bar = 500 μm and applies to all elastograms.

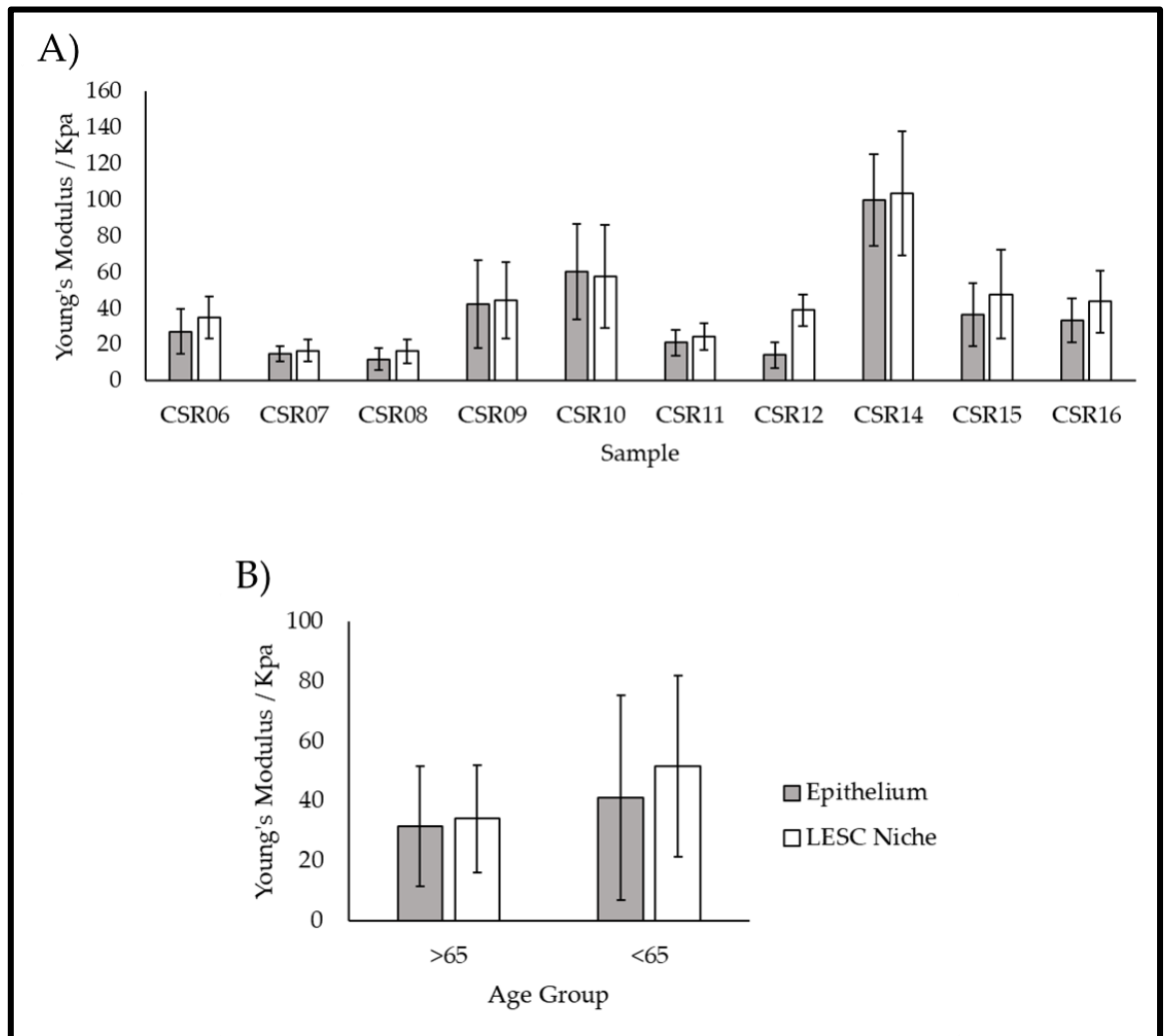


Figure 3.13: Young's moduli calculated from the linear ROI method. A) Shows the average Young's modulus for the epithelium and the LESC niche regions for each investigated sample. B) Compares the average Young's modulus for the epithelium and LESC niche in all the samples within each age group (N = 5 for each age group).

Students' T-tests were performed between: each age group epithelium ($P = 0.601$), each age group LESC niche ($P = 0.294$) and within each age group: epithelium vs LESC niche >65 ($P = 0.834$) and epithelium vs LESC niche <65 ($P = 0.617$). By the current analysis method (using ImageJ), there was no significant difference between age groups. However, there was a distinct mean decrease in epithelial stiffness by 23.5% and a limbal stiffness decrease of 34.1% between the >65 and <65 -year-old groups.

The linear ROI method of extracting stiffness information was able to extract stiffness averages from both anatomical regions of interest in all samples and the agar reference layer. The linear approach was ideal for the agar reference and the epithelial layers however, due to the undulating nature of the LESC niche, it was considered a tailored drawn approach (as defined below) may be required to increase the accuracy of the LESC stiffness measurements. Therefore, the analysis as exemplified in Figure 3.14, relies on drawing the undulating LESC niche ROI based on the structural imaging (which was acquired simultaneously with the elastograms) then superposing the drawn ROI and extracting the intensity values as per the linear method.

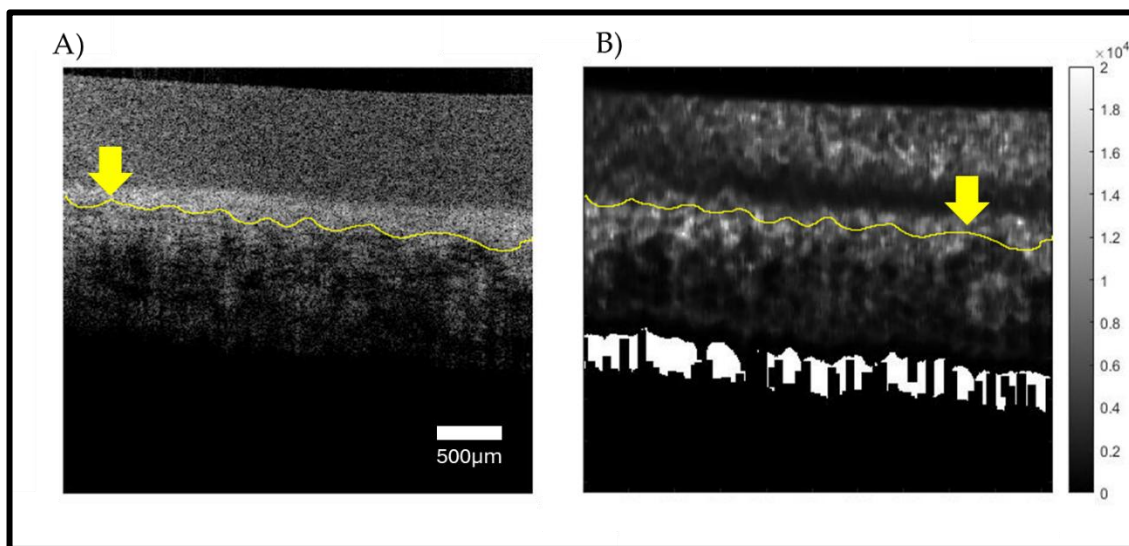


Figure 3.14: Example of drawn ROI selection for the LESC niche. This Figure uses the sample CSR07 as an example. A) Structural image taken from the OCE acquisition. B) Elastogram with the gradient scale ranging from 0-2 x10⁴ $\frac{1}{Strain}$. A and B) The yellow lines show the drawn ROI whilst the yellow arrows indicate the ROI positioning, following the niche microstructure. The scale bar = 500 µm and applies to both the structural image and the elastogram. N=5 for each age group using the drawn method.

The following elastograms contain the drawn LESC niche ROIs utilised in the drawn LESC niche method of calculating niche modulus as presented in Figures 3.15 and 3.16. The epithelial ROIs are not included as they remain the same linear ROIs as utilised in Figures 3.11 and 3.12. The agar reference (including ROIs used to calculate

the ratios used to calculate Young's modulus) remained unchanged in Figures 3.11 and 3.12 and were directly applicable to Figures 3.15 and 3.16 as only the method of drawing the limbal ROI was changed to reflect the limbal conformation. The value for the reference agar was determined by our collaborator in Dundee using nanoindentation specifically as a comparative standard for use with this OCE equipment and elastogram interpretation to generate Young's modulus values, (ref. section 3.2.4).

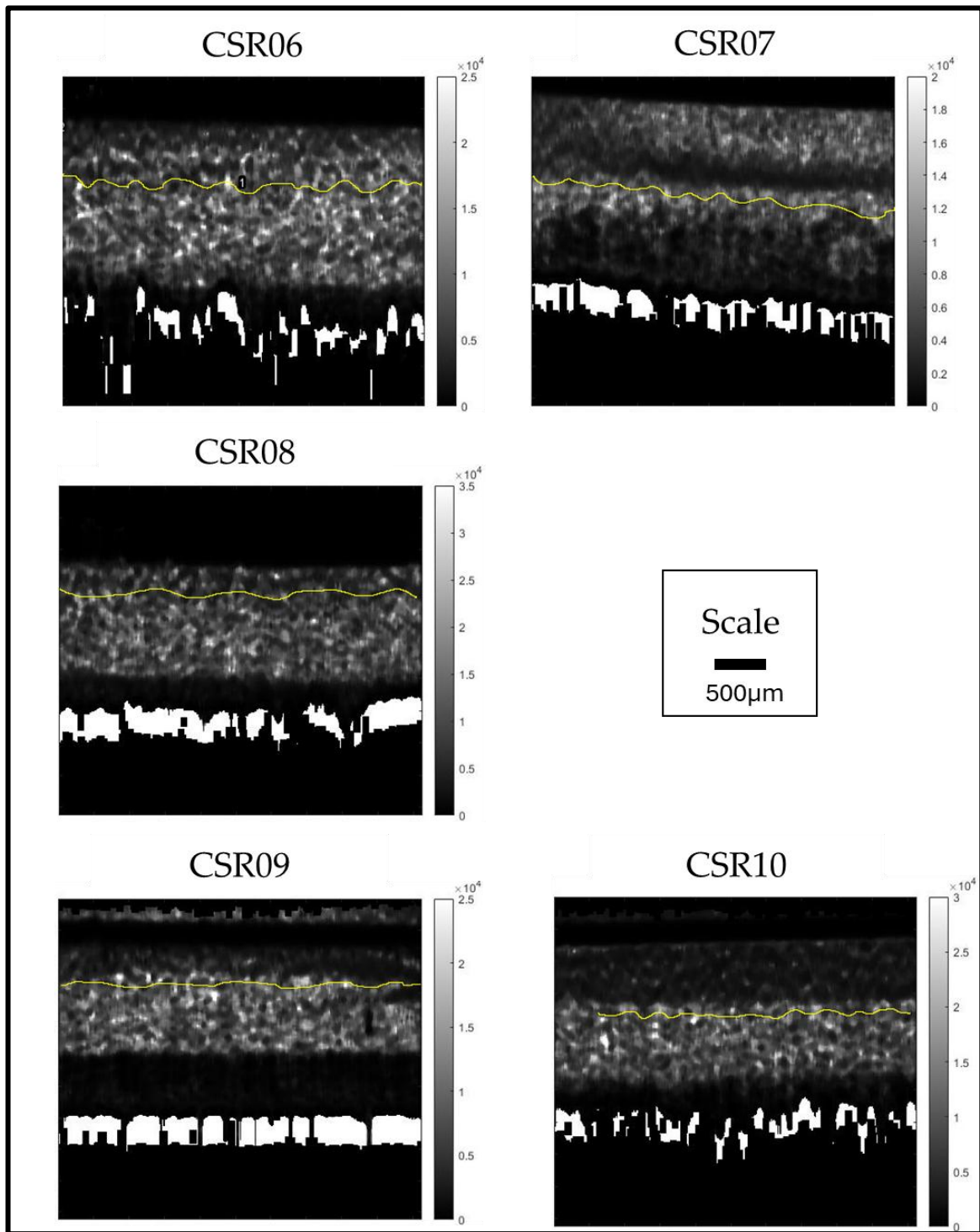


Figure 3.15: The over 65-year-old age group with the drawn LESC niche ROIs. The yellow lines drawn across the undulations of the LESC niche are the drawn ROIs used to calculate Young's modulus for the drawn LESC niche ROI method. The scale bar = 500 μm and applies to all elastograms.

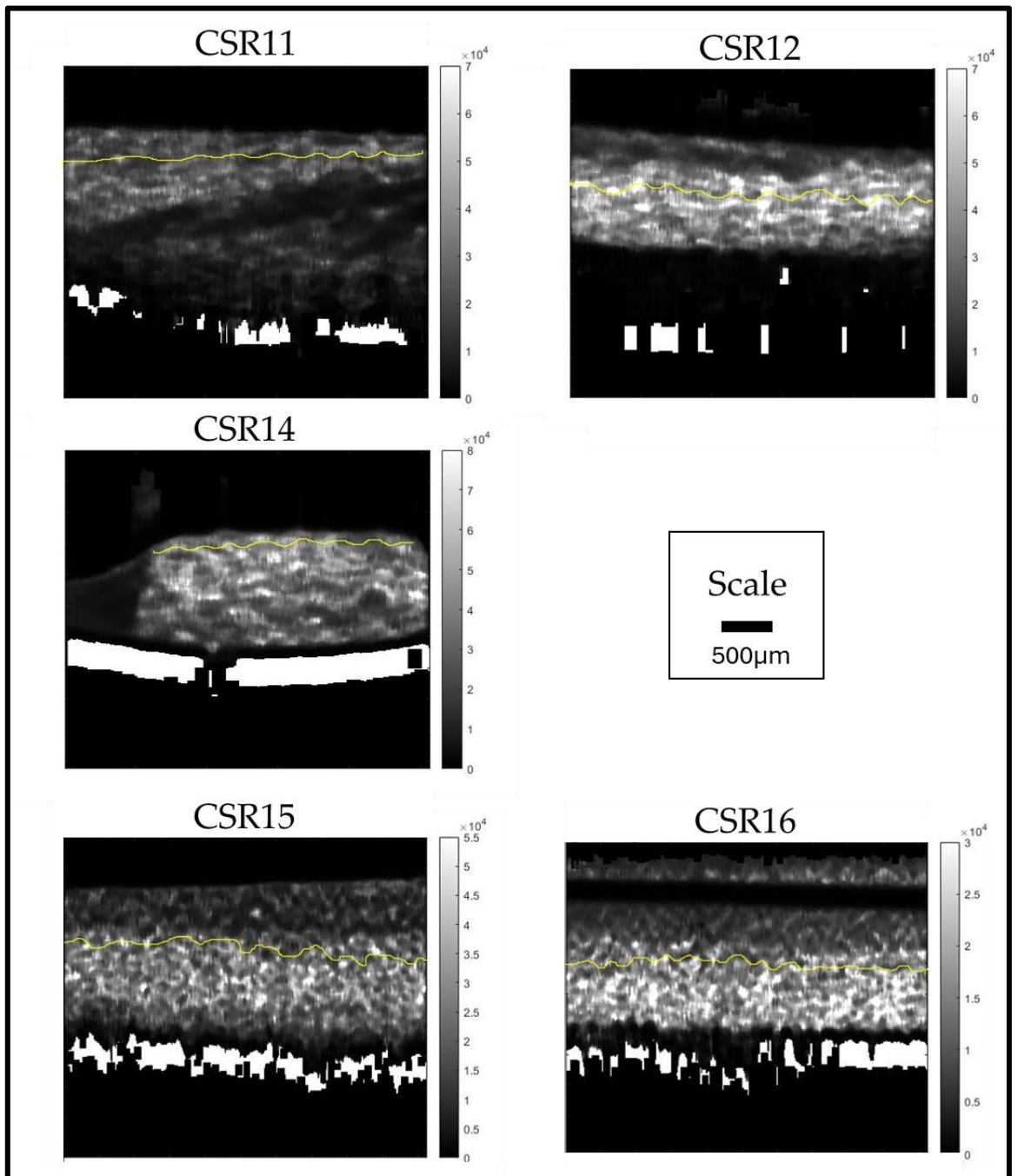


Figure 3.16: The under 65-year-old age group with the drawn LESC niche ROIs. The yellow lines drawn across the undulations of the LESC niche are the drawn ROIs used to calculate Young's modulus for the drawn LESC niche ROI method. The scale bar = 500 μm and applies to all elastograms.

As previously described, the extrapolated grey values from along these drawn ROIs were taken and compared to the average value obtained for the agar reference to obtain the ratio required to calculate Young's modulus. The results from the subsequent Young's modulus calculations (derived from the agar reference value of known stiffness of 14.6 ± 0.8 KPa) are presented below in Figure 3.17.

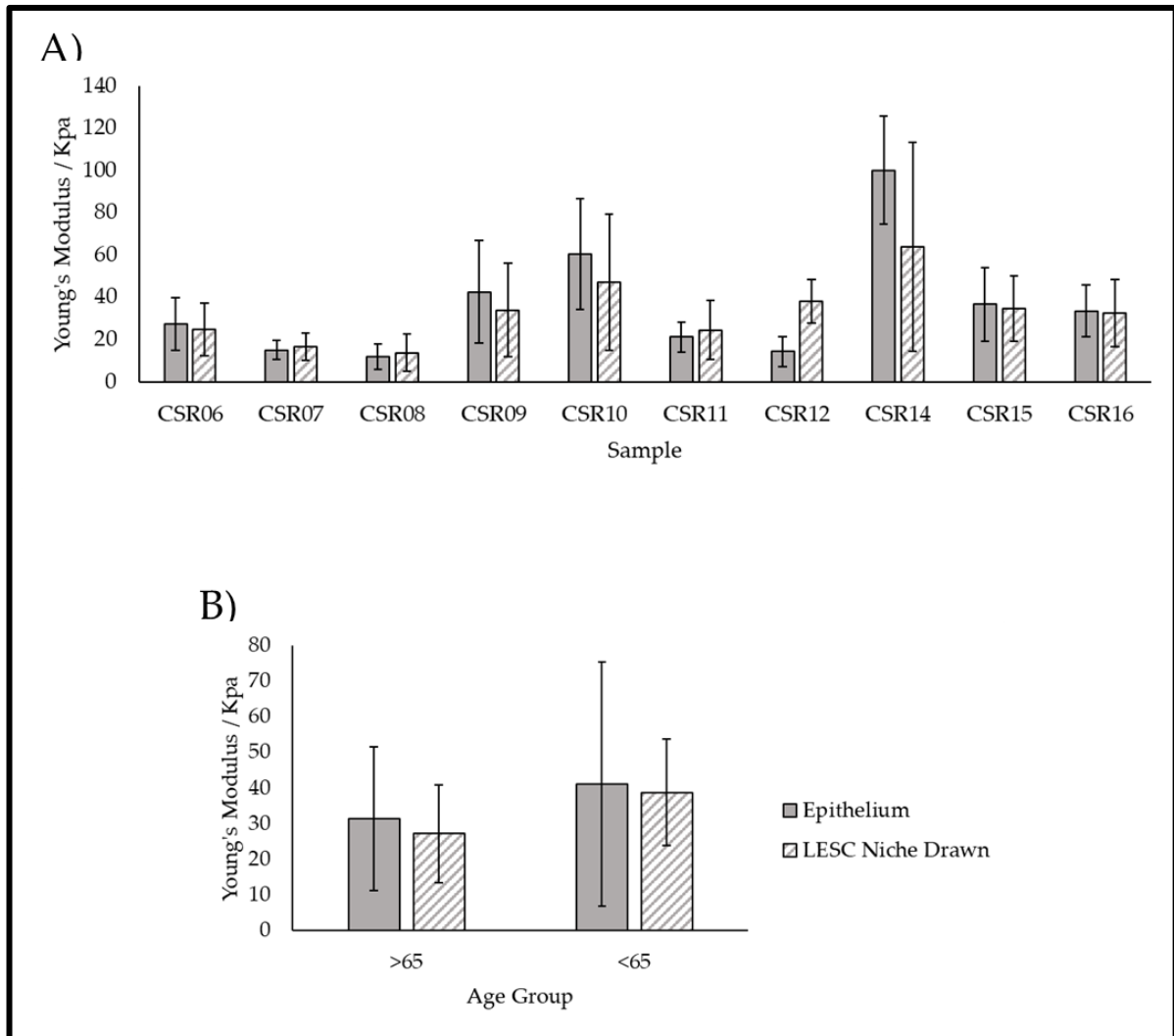


Figure 3.17: Young's moduli calculated from the drawn ROI method. A) Shows the average Young's modulus for the epithelium and the LESC niche (drawn ROI) regions for each investigated sample. B) Compares the average Young's modulus for the epithelium and LESC niche (drawn ROI) in all the samples within each age group (N = 5 for each age group).

The linear and drawn ROI methods of Young's modulus calculation of the LESC niche were compared. It was noted that the average modulus is lower in the drawn group 32.9 ± 14.8 KPa compared to the linear group 42.9 ± 25.2 KPa. Additionally, it was also observed that the error was markedly lower in the drawn ROI method overall compared to the linear method, showing the drawn method had less variation and is therefore more specific.

The T-tests for the age comparison showed that $P = 0.238$ between the over 65-year-old group and the under 65-year-old group. As before, the current analysis using ImageJ showed no significant difference between age groups. However, there was a clear mean decrease in LESC niche stiffness (as found by the drawn method) to decrease by 29.8% between the younger and the elder group. The average modulus for the over 65-year-old group was found to be 27.2 ± 13.7 , whereas the under 65-year-old group was 38.7 ± 14.9 .

3.4 DISCUSSION

In this chapter, the architecture and corresponding mechanical properties of the limbal epithelial stem cell niche were explored using a non-destructive imaging modality. These methods used the same platform, spectral domain optical coherence tomography (SD-OCT) as the base imaging platform with the addition of the vibrational component to enable the elastographical analysis of the cadaveric tissue. In this proof of concept work, cadaveric human tissue enabled the structural and mechanical property analysis of the tissue at the micro-scale against an age scale. The tissue samples ($n = 10$ total) were segregated into two age groups; the under 65-year-old group ($n = 5$) and the over 65-year-old group ($n = 5$).

The SD-OCT method workflow was established to provide a unified output of structural and mechanical information about the tissues. This output comprised two key images, the en-face images acquired from OCT to provide structural quantification and the elastograms acquired from OCE to provide mechanical information about the tissue.

Derived from the imaging outputs were the analytical outputs, which in both cases, were calculated from pixel intensity values obtained using a manual ROI-based processing method. This method facilitated the calculation of anatomical feature width (ERP and PR widths) by direct measurement of the profiles and the calculation of the regional Young's modulus across an ROI by comparison to the agar reference.

A secondary output from the OCT, which enabled the direct comparison to “traditional” tissue analysis methods such as paraffin wax embedded histology was the cross-sectional perspective images of the OCT scans. These were simply resolved by virtually revolving, and re-slicing the volumetric images within the ImageJ. These cross-sectional images, as seen in Figure 3.6 were able to reveal limbal microstructures such as the (i) undulations created by the PR and the ERP, (ii) the difference in optical densities imparted by the epithelial and (iii) LESC niche layers. The epithelium typically tends to appear less intense, with a more “ghostly” appearance in comparison to the more intense and brighter LESC niche layer. These optical characteristics can be visually compared to the observations in the histology of the niche, eg. in Figure 3.3. In ophthalmological research, high-resolution OCT has been used to image the limbal niche (*Haagdorens et al., 2017*) which, in addition to this SD-OCT modality conforms to the long established limbal niche reconstruction based on histology and modelling (*Dua et al., 2005*).

The en-face projections of the SD-OCT scans were able to yield intensity profiles for each tissue. These profiles were plots of lateral distance against pixel intensity across the ROIs. The darker the intensity, the deeper that pixel is (in arbitrary terms) concerning the known lateral scale in micrometres. From these plots, it was possible to measure the ERP as $33.3 \pm 4.56 \mu\text{m}$ for the under 65-year-old group and $29.9 \pm 3.22 \mu\text{m}$ for the over 65-year-old group whilst the PRs were measured at $43.4 \pm 4.57 \mu\text{m}$ and $42.8 \pm 7.8 \mu\text{m}$ respectively. The average ERP width across the entire set was $31.4 \pm 4.1 \mu\text{m}$ whilst the PR was $43.1 \pm 6.0 \mu\text{m}$. Overall, these values, in magnitude, are consistent with limbal microstructure measurements made using other techniques such as confocal microscopy and histology (*Dua et al., 2005, Grieve et al., 2015*). Although the age-related changes were found to be statistically insignificant through T-testing, the cause may be accounted for by the large inter-sample variation observed between the samples within the age groups. In turn, this created a large observable deviation (variation) within the age groups which in turn reduces the power of the testing over an $N = 5$ sample group. Due to the lack of availability of cadaveric tissues, it was not possible to test more samples, restricting the ability to increase the power of statistical testing. However, by looking at the difference in averages, it is possible to discern differences between age groups in terms of anatomical feature dimensions and infer age-related changes. In these samples, as shown in the summary of POV profile measurement in Figure 3.10 there was an observed 10.2% reduction in ERP width in the over 65-year-old group in comparison to the under 65-year-old group. Additionally, in terms of changes in the PR, there is a 1.4% reduction in the elder age group compared to the younger group. These acquired values for the ERP width for the under 65 years old group and over 65 years old group fall within the lower range of the target range of the design crypt width criteria for material production (further discussed in chapter 4) of width 15-150 μm . Therefore the primary values

attained in this OCT study of the tissue further refine the limits of acceptability to this range, thus guiding the design criteria of the wrinkled material production. With further work to gather a wider range of elder/diseased tissue limbal POV dimension values, it may be possible to use these ERP widths to specify wrinkled material deformation limits to mimic ageing dynamically, given the appropriate online imaging could be used to measure the materials sterile.

Together these observations, in conjunction with the conformational observations in Figure 3.6, demonstrate a tangible loss of significant crypt structure with advancing age. These conformational changes would also suggest a weakening in LESC niche capacity in the elder group compared to the younger group. These findings are concordant with wider literature where age-attributed changes in limbal anatomical conformation were assessed using alternative methods such as confocal microscopy (*Zheng and Xu, 2008, Notara et al., 2012*). These studies also demonstrate a loss of LESC niche structure, manifesting in a loss of POV presence.

At the OCE stage of the workflow, the mechanical properties of the epithelial and the LESC niches were scrutinised. In a similar manner to how the OCT images were processed for quantification, it was possible to extrapolate and calculate regional stiffnesses using ROI-based pixel intensity profiling of the elastograms. The analysis was performed using ImageJ in this research due to accessibility to MATLAB and limitations in processing large image files. However, as outlined, this workflow facilitates the ability to extract compressed elastography information from JPEG format elastograms and assess limbal niche changes with age.

The calculations were performed by direct comparison of the regional intensities on the elastograms (which are scaled proportionally to stiffness) to the 1% agar reference of a known (and validated) Young's modulus of 14.6 ± 0.8 KPa (*Li et al.,*

2015). This analysis was broken down into two methods, the linear ROI method and the drawn ROI method. From the linear ROI method, the epithelial Young's modulus was found to be 31.5 ± 20.2 KPa and 41.1 ± 34.2 KPa for the over 65-year-old and the under 65-year-old groups respectively. Additionally, the LESC niche layer was found to be 31.8 ± 17.9 KPa and 51.8 ± 30.3 KPa for the over 65-year-old for the under 65-year-old groups. Although statistical significance wasn't found when comparisons were drawn between the age groups for both the epithelium and the LESC niche layer, there was a 23.4% decrease in average epithelial stiffness in the elder group compared to the younger group. The niche layer was also observed to decrease in stiffness, with a 38.6% decrease in LESC niche layer stiffness.

The values obtained from these methods are in line with those obtained from corneal tissue analysed using atomic force microscopy (*Last et al., 2009, Last et al., 2012*). However, these values are contradicted by limbal elasticity studies which employed finite element modelling (an in silico modelling method) and phase-sensitive optical coherence elastography, where the determined limbal elasticities were an order of magnitude greater in stiffness compared to the values reported and discussed in this chapter (*Asejczyk-Widlicka et al., 2007, Zvietcovich et al., 2020*). Despite this apparent disparity, phase-sensitive OCE presents much greater advantages over 'classical' methods such as AFM and nanoindentation. First and foremost is the fact that the method, by principle, is non-destructive and has the potential to be translated and engineered into a clinically useable format, whereas AFM and indentation techniques are invasive and require tissue isolation. Secondly, OCE allows for the analysis of multi-dimensional mechanical measurements (including depth, which is unique to this technique) with the simultaneous support of structural imaging provided by the OCT camera capture used to record the OCE measurements (*Dimmock et al.,*

2024). The imaging advantage is only conferred in 2-dimensions (restricted to surface only) in AFM whilst in indentation techniques there is no structural image support, only mechanical characterisation.

Given the disparity between elasticity studies, future work in refining this analytical methodology would prove beneficial as correlated structural/mechanical characterisation in this anatomical region develops. Further mechanical property validation may include direct testing methods, such as nanoindentation to regionally validate discrete regional elastic properties. Such validation experiments would have value in the confirmation of agreement of the attained mechanical property values for both the tissue samples and reference material by OCE and those attained by other studies. Considering the epithelial layer, in structural terms, was found to be continuous in the structural imaging it was deemed appropriate to keep the output for the linear epithelial ROIs and only re-sample the LESC niche. As per the example in Figure 3.14, the undulations of the niche were mapped using a drawn ROI which was subsequently transferred to the elastograms to extrapolate the regional elasticity data across the undulations as shown in Figures 3.15 and 3.16. Using this alternative approach, the stiffness of the limbal niche was found to be 27.2 ± 13.8 KPa in the over 65-year-old group and 38.7 ± 14.9 KPa in the under 65-year-old group. There is a 29.7% reduction in stiffness in the younger group in comparison to the elder group, a trend that is consistent with the linear ROI approach to calculating LESC niche stiffness. However, it is noted the error in the drawn method for both age groups was observed to be lesser than the error observed in the linear ROI method, with a 20.2% decrease in the drawn ROI method determined stiffness compared to the linear ROI method in the over 65-year-old group. In the under 65-year-old group the decrease in

stiffness was found to be greater at a 25.3% decrease in the drawn ROI method compared to the linear ROI method.

A further comparison can be drawn between the anatomical regions and the ROI-based methods of elasticity extrapolation. In the over 65-year-old group, the linear ROI method of measuring the LESC niche elasticity was observed to be 8.3% stiffer than the epithelium, (compared to the drawn method which was observed to be 13.7% softer than the epithelium). For the under 65-year-old group the linear ROI measured niche elasticity was found to be 26% stiffer than the epithelium (whereas the drawn method was found to be 5.8% softer). From these comparisons, it is apparent that the regional specificity of the ROI matters.

In this case, where the ROIs match the undulations of the tissues (as defined by the structure) it is revealed that the niche is softer than the more averaged (linear) approach, which in other studies looks at the limbus in a more macro scale would be inclined to suggest the limbus is stiffer (*Asejczyk-Widlicka et al., 2007, Zvietcovich et al., 2020*). The more specific approach applied in this research has revealed a softer microstructure and reduced inherent error, more in line with work that suggests a limbus of a softer Young's modulus as measured using precision methods such as AFM and nanoindentation (*Last et al., 2012, Eberwein et al., 2014*). Therefore a valid compromise would be to amalgamate the linear ROI approach for epithelium measurement and the drawn ROI for the LESC measurement as it is demonstrated that these are structurally relevant ROIs and have mechanical properties measurements that are concordant with other precision measurements.

3.5 CONCLUSION

This chapter has described a workflow with the capability to virtually dissect the corneal limbal epithelial stem cell niche in a manner that yields images comparable to histological sections. These images can be volumetrically manipulated, reprojected and then quantified to yield structural information about the LESC niche. Using the same imaging equipment (with mechanical additions) this workflow then allows the mechanical characterisation of the LESC niche. These results have facilitated the complementary characterisation of the structural and mechanical properties (and the interplay), illustrating the age-related effects. It has been demonstrated that with increasing age there was a loss in crypt structure and a softening of the tissue structure, this would suggest that the limbal crypts (the EPR) would have degraded in integrity and a loss of stem cell pool competence. This was observed mechanically by a mean decrease in epithelial stiffness by 23.5% and a limbal stiffness decrease of 34.1% between the >65 and < 65-year-old groups using the linear ROI method. The drawn method of LESC niche stiffness determination was compared to the linear method and found that there was a 23.3% decrease in stiffness (across the whole population) observed. In the findings of age-related changes in the niche, it was found that the average modulus for the over 65-year-old group was found to be 27.2 ± 13.7 Kpa, whereas the under 65-year-old group was 38.7 ± 14.9 Kpa (a 29.8% change from the younger to older groups). The tissues reported upon in this chapter had been stored in organ culture for a significant time, with the potential for both cellular and niche changes whilst in storage. Therefore it would prove interesting if future work could be applied to fresh tissue. Future work would seek to maximise the efficiency of extracting the raw elastographic data out of the OCE files using MATLAB

software to reduce errors introduced through compression, thus increasing mechanical data resolution.

Chapter 4: Fabrication and Design of a Novel Bioreactor and Generation of Wrinkled Surfaces

4.1 INTRODUCTION

This research aimed to establish proof-of-concept employed in the production of a bioreactor system featuring wrinkled substrate surfaces. Two methods were employed to achieve substrate wrinkling: 1) the compression of a bilayer substrate and 2) oxygen plasma treatment/wet chemical oxidation of uniaxially stretched elastomer. To achieve the former method, a compression frame was designed. To achieve the latter, the treatment process parameters were optimised and a sturdy stretching frame was fabricated to perform successful topography fabrication using both treatment methodologies.

Once wrinkled materials were produced, bioreactor assemblies were set up in 6-well plates to trial suitability for culture, testing the accessibility to the substrates and the adjustability of the frames *in situ*. The term “bioreactor” as used in the context of this research encompasses the compression/stretching frame (with the corresponding wrinkling substrate) contained within a 6-well plate with culture medium. Once it was determined that a viable bioreactor system was established, quantification of the topography and visualisation of the topography shape was required. This analysis sought to ascertain the structural biomimicry of the generated surfaces in comparison to the human LESC limbal anatomic niche. As discussed previously (Ref. Chapters 1 and 3) the LESC anatomic niche has a specific undulating crypt shape and dimensions as determined by OCT imaging. These dimensions are an average of 50 μ m depth (range = 35-120 μ m) and an average of 50 μ m width (range = 15-150 μ m). Therefore developing the ability to visualise the created topography in these dimensions was critical to assessing the current methods of material production. This in turn facilitated further optimisation giving rise to the generation of more biomimetic topographies.

The development of the associated material fabrication procedures and the design of a compression bioreactor to facilitate substrate compression were the priorities. These properties translated well into the stretched approach due to the elasticity of the bulk material and its ability to be surface-modified by various processes. In the design process, there was an imperative to ensure cytocompatibility, therefore the selection of materials was restricted to materials which are considered biocompatible. First and foremost, the materials evolved in the production process must not be contact-toxic and have sufficient stability so that they do not degrade into toxic degradation products (*Biswal et al., 2020*). An example of a study using engineered polymer constructs (which were optimised with biocompatibility and cellular bioactive effects in mind) was the development of boron-containing PVA-based cryogels (*Ceylan et al., 2023*). In this particular study, a polymer composite scaffold was designed to structurally mimic cortical tissue but maintain cell cytocompatibility at an interface level in the base design of the material. A bioactive molecule (Boron) was incorporated into the scaffold to induce changes to cellular behaviour.

Similarly, this research seeks to describe the development of a bioreactor design which meets the biocompatible needs of the target limbal epithelial cells, through material selection and treatment protocol design, coupled with a physical method of cellular control through the formation of topography.

Thus for this research application, the bulk material was selected as Polydimethylsiloxane (PDMS), specifically Sylgard 184, a thermo-cured PDMS compound. This material, in its native and freshly cured state, is well known for its chemically inert nature and therefore *prima facie* biocompatibility. PDMS is unable to degrade into harmful degradation products or present harmful functional chemical groups which would directly harm cells upon contact (*Gómez-Varela et al ., 2021*).

PDMS has been extensively used in microfluidic devices and advanced surface applications (*Akther et al., 2020, Tang et al., 2021, Majhy et al., 2021*) due to its acknowledged biocompatibility, ability to be physically deformed/manipulated and surface functionalised. The highly pliable nature of cured PDMS, which has previously been demonstrated to be modifiable through altering ratios of crosslinker, plasticiser and binder as characterised by using mechanical means, makes this material a highly desirable choice for a bulk material choice for wrinkling in the physical sense (*Kosta et al., 2020*).

The compression bioreactor was designed as a simple per-sample device to fulfil the requirement to generate wrinkled topography in polylactic-co-glycolic (PLGA) and polycaprolactone PCL polymer film laminated to PDMS blocks (laminated blocks). In these laminated blocks, the surface film had a significantly greater Young's modulus compared to the PDMS bulk (*Luk et al., 2013, Shirazi et al., 2014, Wang et al., 2014*). The frame allowed varied amounts of compression to be applied either continuously or dynamically (by manual alteration of the amount of compression). When experimental pitfalls were found with the compression-based laminated block system, a tension-based frame with a specially moulded PDMS chip bioreactor system and material treatment workflow was designed to generate more ideal culture substrates.

The use of oxygen plasma treatment on an elastomer surface has previously been established to generate a wrinkled topography. Owing to the ability of this method to both generate topography and a biocompatible surface in a single treatment, it was considered that this method was worthy of pursuit to generate control surfaces which could enable comparison of cell growth/behaviour on a static, pre-wrinkled surface. Like the compressed laminated block method, this method required a novel design element to facilitate treatment. To create the topography the elastomer must be

uniaxially stretched before treatment with this stretch being maintained through the plasma treatment cycle. After treatment the substrate was relaxed, and the silicate-like layer which formed on the upper surface (arising from O₂ plasma-mediated cross-linking) had a greater modulus compared to the bulk. During relaxation, wrinkling was observed. This phenomenon could only be achieved through the careful balance of plasma treatment parameters in terms of exposure time, O₂ pressure and plasma generation power. To provide the uniaxial strain, a dual-purpose stretching device was designed and constructed to apply simple uniaxial stretch of the elastomer within the treatment chamber. Co-opting the designed frame employed in the plasma treatment process, the wet chemical oxidation of pre-stretched PDMS was explored. In principle, wet chemical (acid) oxidation works in the same way as oxygen plasma wherein the elastomer surface is stretched and oxidized to form and stiffen the exposed surface, leaving the bulk sufficiently elastic to satisfy the simple wrinkling formula requirements (*Dimmock et al., 2022*). Static examples of the generation of wrinkled PDMS include the randomly ordered surfaces produced in the creation of microspheres (*Yin et al., 2014*). However, it has also been demonstrated that it is possible to achieve more linear ordered wrinkling using this approach (*Watanabe and Mizukami, 2012, Watanabe and Hashimoto, 2015*).

The developments in wrinkling PDMS explored in this chapter were capable of producing undulating topographies which can be maintained in either a static state (constant presence of topography) or with an ability to be dynamized, where the shape of the crypt was able to be altered from an undulating shape to a flattened surface. Within the purview of this project, the term “dynamic” is applied to the topography due to the ability to actively change the morphology of the surface during culture. These changes can be effected without removing the cells, re-starting the culture or using

new material for a different undulating surface. Static systems have previously been used in the replication of LESC niche features, ranging from the use of collagen gel channels (*Haagdoresn et al., 2019*), to fibre-based scaffold niche reconstructions (*Tan et al., 2022*) and membranous/fibre cell transplant techniques which have niche mimicry (*Li et al., 2017, Sanie-Jahromie et al., 2020*). Whilst these static systems have proven ability to preserve LESC stemness (thus revealing some insight into niche function) a dynamic system is considered more favourable in a stem cell niche modelling capacity, as tissue is very rarely static. Tissue movement comes through natural body movements such as blinking and eye movements, inflammation from disease and tissue architectural alterations from injury and ageing. It is proposed that all of these could potentially either individually (or synergistically) mechanically alter stem cell function through the alteration of LESC crypt morphology. Additionally, being able to modulate topography shape in depth, width and steepness (to both extremes) and homeostatic biomimicry has positive future implications for modelling limbal disease. The substrates produced by the dual treatment method demonstrated the greatest dynamic capacity by retaining their shape and returnability after a total of 4x cyclic loading during cellular testing (section 5.3.6.1).

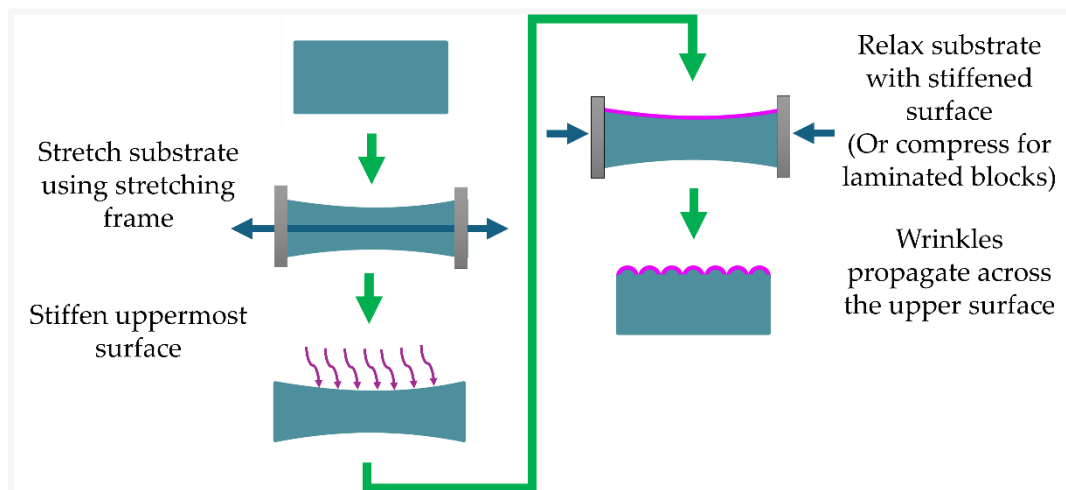


Figure 4.1: General schematic for the production of wrinkled substrates. This schematic describes the process of producing wrinkles on an elastomer surface using both a stretching frame (for acid oxidation and dual treatment) or a compression frame (for the laminated block method).

This chapter describes how the generation of wrinkled topography is achieved by merging smart-material fabrication with physical phenomena (*Dimmock et al, 2020*) to replicate the LESC niche undulating topography (*Grieve et al., 2015, Shanmuganathan et al., 2007, Dimmock et al., 2023*). To this end, a compression bioreactor system using simple components which allowed control over the formation of wrinkled topography was initially designed and fabricated. The ability to fine-tune substrate material (polydimethylsiloxane), which was integral for both methods of wrinkle generation, was attained through compression testing. However, due to flaws in the laminated block method, alternative methods of wrinkling were explored. The principle methods of O₂ plasma treatment and wet chemical oxidation of PDMS were able to generate the wrinkled surface phenomena. These core methods formed the foundation for producing a material model of the LESC anatomic niche.

4.2 MATERIALS AND METHODS

4.2.1 Fabrication of PDMS

Throughout this chapter, PDMS (polydimethylsiloxane) is defined as the base bulk material from which wrinkled topography was created. The final solid PDMS was produced by the mixing of the two liquid components, the elastomer and the curing agent in the desired curing agent concentration, expressed in percentages ranging from 2.5-10%. Once correctly mixed, the pre-cured PDMS was dispensed using a 1ml syringe into the desired mould(s). These moulds were incubated overnight at 50°C. Once fully cured, the PDMS was carefully removed from its mould and overflowed edges scored by a razor if necessary to aid in the removal of the moulding without damage.

4.2.2 Fabrication of Polymer Membranes

PLGA and PCL were sourced in the granule form. The polymer granules were dissolved in 99% Chloroform at the proportion of 0.25% polymer concentration (by mass). Each granule type was dissolved in chloroform with stirring for 24 hours. A taped closed 150mm glass petri dish was used for solvent casting of the polymer solution in a fume hood. To control the rate of chloroform evaporation, an 18ga blunt-tipped needle was inserted into the sealing tape, LuerLock aperture facing downwards. This needle vent ensured the vital slow rate of evaporation needed to solvent-cast the thin polymer membrane.

4.2.3 Preparation of Laminated Blocks

The laminated blocks were produced by the adhesion of the PLGA or PCL membranes to the moulded PDMS blocks using a silicone rubber compound adhesive. The adhesive was spread in a very fine layer using a coverslip as a spreader, utilising a 5x magnifying glass to ensure homogenous spreading was achieved. To create the wrinkled topography using this method, the blocks were compressed in the lateral direction, using specially designed compression frames.

4.2.4 Oxygen Plasma Treatment

The method used for oxygen plasma treatment was low-temperature oxygen plasma, employing the Diener Femto device. The PDMS substrates subjected to oxygen plasma were placed surface-up in the chamber and a near total vacuum of 0.3 mbar is imparted upon the chamber. The standard parameters for treatment were; 1.5mbar O₂ pressure and 10 minute exposure. Power variance was achieved by changing the parameters using the touchscreen interface of the onboard computer controller integrated into the Diener Femto plasma machine. After treatment, the substrates were only able to be removed from the chamber after the flush and vent sequences were run to release the vacuum and safety maglock.

4.2.5 Wet Chemical (Acid) Oxidation

The sulfonitric acid was prepared by first carefully introducing sulfuric acid into nitric acid dropwise into a glass beaker immersed in an ice bath in a fume hood. Once the acids were safely mixed to the 3:1 ratio of sulfuric to nitric acid, the sulfonitric acid was heated to 80°C and stirred with a magnetic stirrer within a fume hood for 2 hours.

After thermal attenuation, the acid was allowed to cool before being transferred to the nalgene® storage bottle. PDMS substrates were stretched using dedicated stretching rigs to defined elongations. These pre-strained substrates were then exposed to the sulfonitric acid for the specified time. The standard exposure time was 5 seconds, however, during optimization this exposure time was varied. Immediately after exposure, the substrates were quenched in a 2-step sequence: (1) using 1M sodium hydroxide and then (2) transferred into a large water bath for 10 minutes. After oxidation, substrates were air-dried.

4.2.6 Dual treatment

In the dual treatment method, PDMS chips (0.5mm thick x 10mm wide x 20mm long overall) were produced using 3D printed moulds, where pin holes corresponding to the stretching frame pillars (positioned at zero stretch) were moulded in place. Once pre-stretched to 20% elongation, the substrates were first subjected to wet chemical oxidation, following the procedure in section 4.3.5 with an exposure time of 5 seconds. The oxidized substrates were dried in the air after quenching. After ensuring both the substrates and the stretching frames were dry (and without removing the chips), the frames with the substrates attached were transferred to the Diener Femto plasma treatment machine. The chips were then exposed to the oxygen plasma using the standard program as outlined in section 4.2.4 with the power set to 50W, oxygen pressure set to 1.5 mbar and an exposure time of 10 minutes. To form the wrinkles on the surface, the chips were removed from frames at this stage to relax the elongation and allow the topography to propagate along the surface.

4.2.7 Mechanical Testing

The machine used for compression testing was the BOSE electroforce 2300 series (*Bose*). The initial linear region was extrapolated from the acquired data, using the 22 N load cell. The rate of compression application was set to 0.01 mms⁻¹. To construct a profile of bulk material properties, PDMS of curing agent concentrations of 2.5%-10% curing agent concentration were fabricated and compressed. PDMS blocks were compressed as 10mm x 10mm x 10mm cubes, samples were tested at n = 3.

Tensile testing was performed on the testometric mechanical testing machine, with the 250 Kgf load cell fitted. The sample polymer membranes were pre-cut into strips (with tabs of autoclave tape at each end to ease handling of the membrane samples and these were fitted into the jaws). The test speed for the tensile tests was 0.1mms⁻¹. PDMS samples were tested as treated chips with dimensions 0.5mm thick x 10mm wide x 20mm long, n = 3 for each type of substrate tested.

4.2.8 Optical Coherence Tomography

B-scans were obtained of the materials using the Thor-labs spectral radar Telestro-II device. In the acquisition of the images, (controlled through the dedicated Thor-labs OCT software) pixel averaging windows were set to 1x1, meaning the highest resolution images by pixel were attained. Image field correction was applied to flatten the edges of the image to compensate for the lens distortion. For volumetric images, the 3D mode was applied to acquire multiple B-scans throughout a 6 x 6 mm acquisition area.

4.2.9 Scanning Electron Microscopy

High-resolution imaging of material surfaces was attained using the Hitachi TM4000 scanning electron microscope. The scanning parameters were as follows; an accelerating voltage of 15 kV, medium vacuum conditions and utility of the secondary electron (SE) detector. Before scanning, samples were air-dried for at least 24 hours before coating. The samples were sputter coated with gold, with a thickness of approximately 10 nm shortly before imaging.

4.2.10 Atomic Force Microscopy

Samples of wrinkled PDMS were outsourced to the University of Sheffield for atomic force microscopy (AFM) for surface analysis by the peak force tapping method. From this outsourced analysis surface maps of the wrinkled topography and quantification of the roughness quotient were obtained for the acid-oxidized, plasma-treated and dual treatment evolved wrinkled PDMS surfaces. Due to the cost of outsourcing, only preliminary data was acquired with n=1 samples of each treatment type being sent for AFM analysis.

4.2.11 Water Contact Angle

The method used for the assessment of surface hydrophobicity was water contact angle. Measurements were taken using the Attention One water contact angle, controlled using the associated software. Data acquisition was taken over 10 seconds at a frame rate of 15 frames per second. The baseline was manually drawn underneath the droplet and the software calculated the contact angle of the droplets between the edges of the meniscus and the baseline on both sides of the image. The contact angle

was calculated as an average of all frames taken per sample to determine how hydrophobic or hydrophilic each sample was.

4.2.12 Raman Spectroscopy

The Raman spectra were acquired using the DXR Raman microscope machine (*ThermoFisher Scientific*) with the acquisition being controlled through Omnic software. The collected sample was set up in the bench (in the software) to collect 6 acquisitions per point and produce a final x6 average spectrum per point. Post collection, the spectra were saved in .CSV format and analysed (post-processing and averaging) using Quasar, a spectroscopy-optimized package of Orange (which is a Python-based workflow package). The parameters of pre-processing were as follows: Firstly the spectrum had been 'cut to keep' between 243 and 3000 cm^{-1} , secondly, a rubber band baseline correction was applied and finally a Savitsky-Golay filter with a window of 15 and polynomial order of 2 was applied.

4.2.13 3D Printing

Custom-designed parts were designed using Fusion 360 (Autodesk) computer-aided design program and exported in the .stl format. The .stl part files were sliced using Flash Print 5 to create G-codes specific to the relevant material type being printed (refer to section 2.2.2.2 for print parameters). The generated .gcode files were utilised by the Flashforge FDM printer wherein the parts were printed. Prototype and non-reuseable parts were printed in polylactic acid (PLA) whereas thermal-resistant or reusable parts were printed with Acrylonitrile butadiene (ABS).

4.2.14 Bioreactor Design

4.2.14.1 Compression Frame for Laminated Blocks

In this setup, the arms of the frame were 3D printed with a biocompatible material (ABS). The frames were assembled using A2 grade M2 25mm bolts and A2 grade M2 nuts to facilitate sterilisation using 70% IMS before implementation in a sterile environment. Using a pair of forceps, the bolts were able to be simply tightened or released sequentially to facilitate both assembly and tuning of the compressed substrate (to initiate the generation of the wrinkles). To prevent slippage of materials a U-shape groove was incorporated along the inside of the arms, any upwards slippage of PDMS blocks. Sterilisation was performed using 70% IMS for a minimum of 40 minutes during frame assembly (in the biological safety cabinet). Assembly of the compression frame and parts dimensions are presented in Figure 4.2.

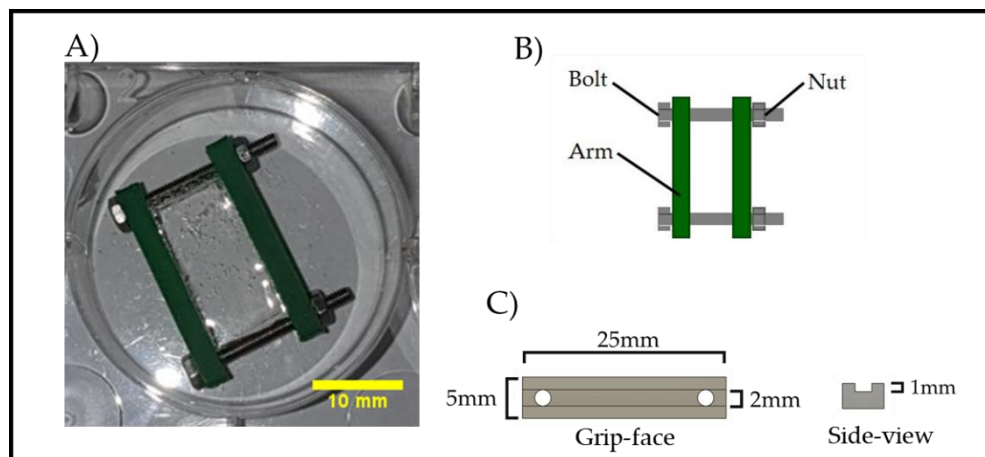


Figure 4.2: Compression frame assembly for laminated block bioreactor setup. A) In-situ with a PDMS test piece inside a 6-well plate well. B) An illustration showing the component assembly of the frame. C) Scaled rendering of the compression frame grip arm from the CAD software.

4.2.14.2 Stretching Frame and Moulds for Chip-Based Methods

The stretching frame, as presented in Figure 4.3, had to serve a two-fold purpose as both complex cultureware and as an implement vital for the preparation of the substrates following the lessons learned in the compression frame.

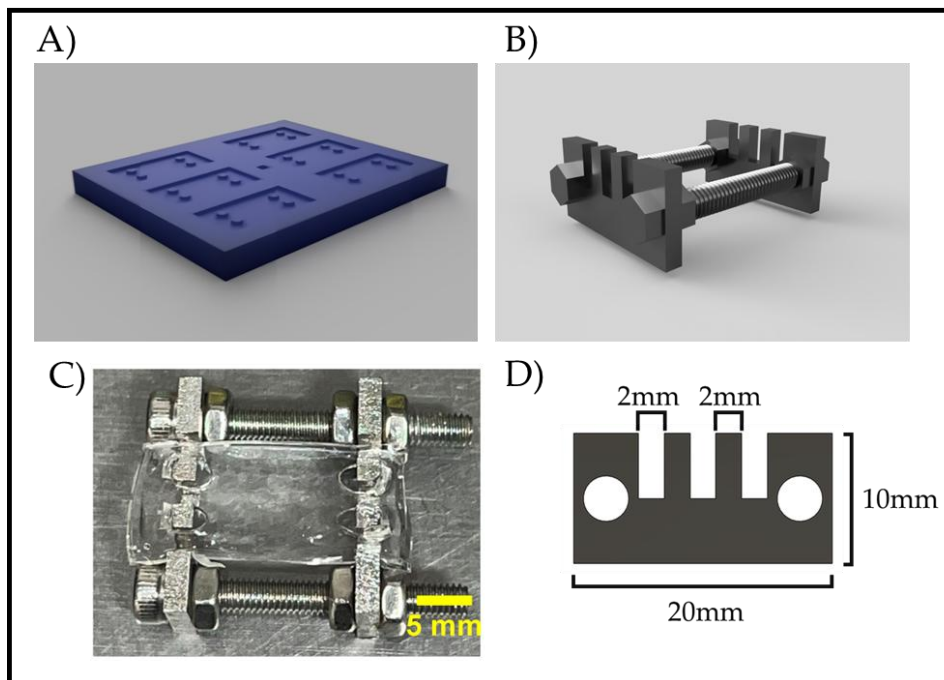


Figure 4.3: Tension arms bioreactor rig and complementary mould. A) 3D render of a mould, B) 3D render of assembled stretching arms, C) photograph of assembled bioreactor setup with an untreated PDMS substrate chip (moulded from a mould (as illustrated in A) stretched to 20% strain as if in use. D) Scaled rendering of the compression frame grip arm from the CAD software.

These stretching frames had to be durable, therefore the decision was made to make the arms out of 316L stainless steel. This grade of steel is widely used in liquid handling/tolerating environments from food processing to medical device applications. It is commonly used for its balance of high strength and corrosion resistance, albeit requiring specialist tools to machine/fabricate (Abbas et al., 2021).

The arms were designed using CAD (Fusion 360) (Autodesk, USA) and laser cut (Kloeckner Metals UK). The nuts and bolts used were 304 stainless steel (grade A2) with the bolts being 30mm socket head M3 bolts and nuts being M3 sized (Accu, UK), with similar metallurgical composition and properties to 316L.

4.3 RESULTS

4.3.1 Demonstration of the Bioreactor Setups

Shown in Figure 4.4, are examples of each type of bioreactor frame *in situ* as intended in the 6-well plates. In these exemplar setups, it is possible to see the wrinkles propagating across the surface of the compressed laminated blocks. It is observed even when hydrated in PBS that the wrinkles had begun to degrade and the membrane started to peel away. In the stretch bioreactor setup, the culture medium was used to visualise how the stretched (to flatten) suspended substrate is covered by the medium. Due to the optical properties of PDMS (even after surface treatment) and the coloured medium being similar, it is difficult to see the PDMS and its surface without using a dissecting microscope or OCT imaging.

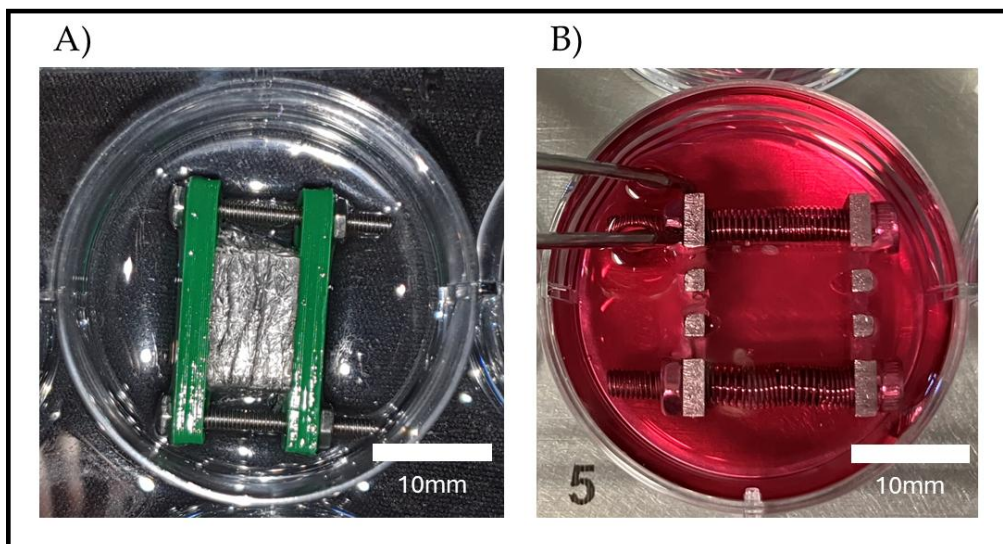


Figure 4.4: Photographs demonstrating the two different bioreactor setups *in situ*. A) The compression bioreactor setup with a PCL laminated PDMS block compressed to 20% compression, originally immersed in PBS with some removed to visualise the obvious surface wrinkles and delamination. B) The stretch frame configuration, with the specially moulded substrate chip immersed in culture medium, stretched to 20% stretch to remove wrinkles from the surface, forceps show the ease of accessibility. Both scale bars = 10mm.

4.3.2 PDMS Bulk Optimisation by Compression Testing

The compression testing of PDMS was used to (i) determine Young's modulus for each of the formulations and (ii) to demonstrate the ability to control the modulus through the composition ratio of PDMS elastomer to curing agent. The average Young's modulus increased concurrently with the increased percentage of curing agent in the composition, with the softest composition 2.5% reporting a modulus of 0.24 ± 0.515 KPa and the stiffest composition of 10% presenting a modulus of 3.51 ± 0.601 KPa, as summarized in Figure 4.5. Overall there is a nearly 15-fold increase in PDMS stiffness when the curing agent concentration is increased from 2.5% to 10%. Additionally, it was noted that variability in the data (as shown in Figure 4.5) increased with the increase of the curing agent. After the performance of a one-way analysis of variance (ANOVA), it was determined that most fractions are significantly different from

each other with $P > 0.05$, however, 2.5% and 3.33% were not found to be significantly different. This test contributed towards the selection of the PDMS formulation most suitable for each wrinkling application. This is to ensure that sufficient difference between the bulk (as tested here) and the surface can be achieved. This profile does not follow a linear trend, but the increase in Young's modulus with an increase in curing agent relationship does provide a guide for PDMS formulation selection. On stretching frames, only 3.33% and 2.5% can be used without the PDMS snapping during plasma and/or acid exposure. 10% PDMS, the manufacturer's recommended fraction cannot even be applied to the stretch frames without damage to the substrate in the first instance.

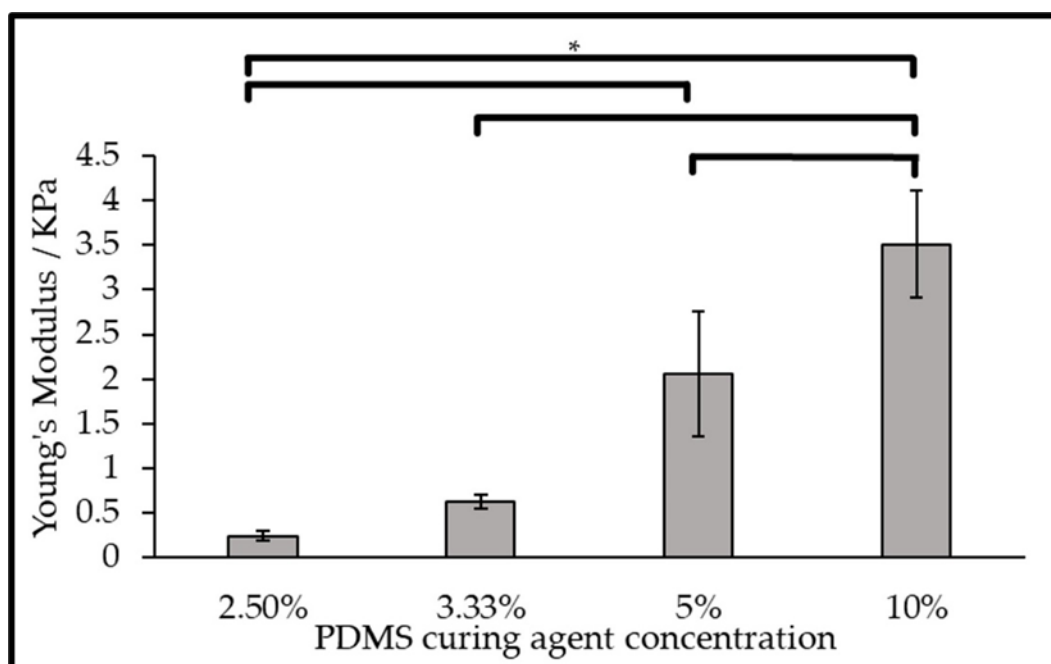


Figure 4.5: Young's moduli of compressed PDMS blocks at different curing agent concentrations. A significant difference between the groups was determined using a one-way ANOVA Tukey post-hoc test, where $P > 0.05$, $n=3$.

4.3.3 Tension Testing of Polymer Membranes

The membranes were subjected to mechanical testing alone, to ensure that they were mechanically appropriate materials to use in the generation of wrinkles. To ensure suitability, at a minimum they must have attained Young's modulus 10-fold greater than the PDMS bulk material measured through compression testing. Having this in mind, the observation that the membranes attained moduli of 195 ± 52.4 KPa for PLGA and 75.6 ± 40.0 KPa for PCL, was established that satisfied the requisite stiffnesses as demonstrated in Figure 4.6. It should also be noted that the PCL membrane was observed to be significantly more elastic than the PLGA membrane. This significance was determined by the Student's T-test where $\alpha = 0.05$ and the P value = 0.035.

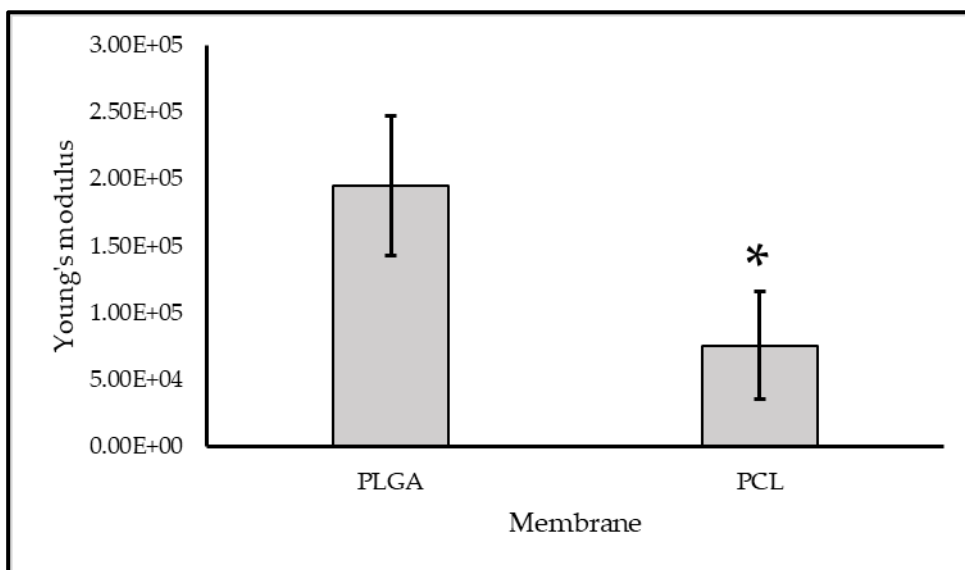


Figure 4.6: Tension testing of PLGA and PCL membranes to determine the Young's modulus. Statistical significance is signified by the "*" icon and determined by the Student's T-test, $n=3$.

4.3.4 Laminated Blocks

Polydimethylsiloxane blocks were laminated with two types of membranes, polylactic-co-glycolic acid (PLGA) and polycaprolactone (PCL). These blocks were first coated with a fine layer of silicone glue then the membranes were applied and weighed down applying even pressure for the duration of the glue curing. The principle of using the membrane laminated PDMS satisfied the simple model for wrinkling (*Dimmock et al., 2021*), by way of using an additive method to provide the surface (membrane) with higher Young's modulus compared to the lower modulus bulk (the block). In these instances the prerequisite conditions for surface wrinkling were achieved, facilitating a mode of wrinkling comparable to the formation of wrinkles visible upon unilateral compression of skin. To achieve wrinkling the laminated substrate blocks were compressed from opposing sides using a compression frame, (whose design is described in section 4.3.1.1). Upon the application of the compressive force, the wrinkles were immediately visible across the laminated surface.

This method of wrinkle generation produced comparatively giant wrinkles in comparison to the other methods discussed, the crypts possessed defined morphology visible to the naked eye. This feature, in addition to the mode of generation through compression, sets this method apart significantly from the other approaches to generating topographies discussed in this chapter. The morphology of these wrinkles was (very) the typical form associated with the term wrinkling, Figure 4.7 demonstrates these compression-formed wrinkles.

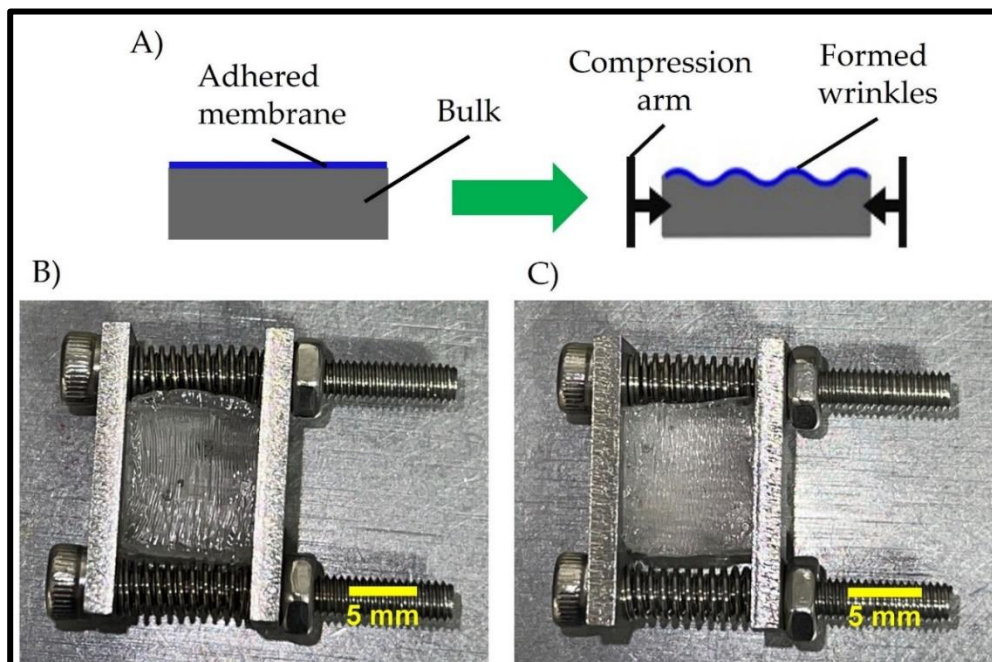


Figure 4.7: Demonstration of wrinkling using laminated blocks. A) a representative diagram demonstrating wrinkle formation, B) a laminated PCL block compressed to 10% and C) a laminated PLGA block compressed to 10%. B) and C) are scaled to the presented scale bars of 5 mm.

Examples of such classical soft matter wrinkling are discussed in (Lee et al., 2023) wherein the wrinkling of the skin and its implications for cosmetic surgery is investigated and (Chavoshnejad et al., 2021) where the age-related degradation of collagen, resulting in skin wrinkling is discussed. Therefore it can be confidently stated that this topography is macro-scaled (and the largest scale-generated topography discussed in this chapter) with crypt to crypt width of $194.8 \pm 43.4 \mu\text{m}$ and a height of $39.5 \pm 5.1 \mu\text{m}$ for PLGA laminated blocks and a width of $72.4 \pm 22.2 \mu\text{m}$ and a height of $14.2 \pm 2.4 \mu\text{m}$ for PCL laminated blocks. These dimensions were proposed to enable multicellular cultivation within the crypts, to create a sinusoid crypt culture akin to the observed limbal palisade of Vogt structure (Patel et al., 2006) (Dua et al., 2005).

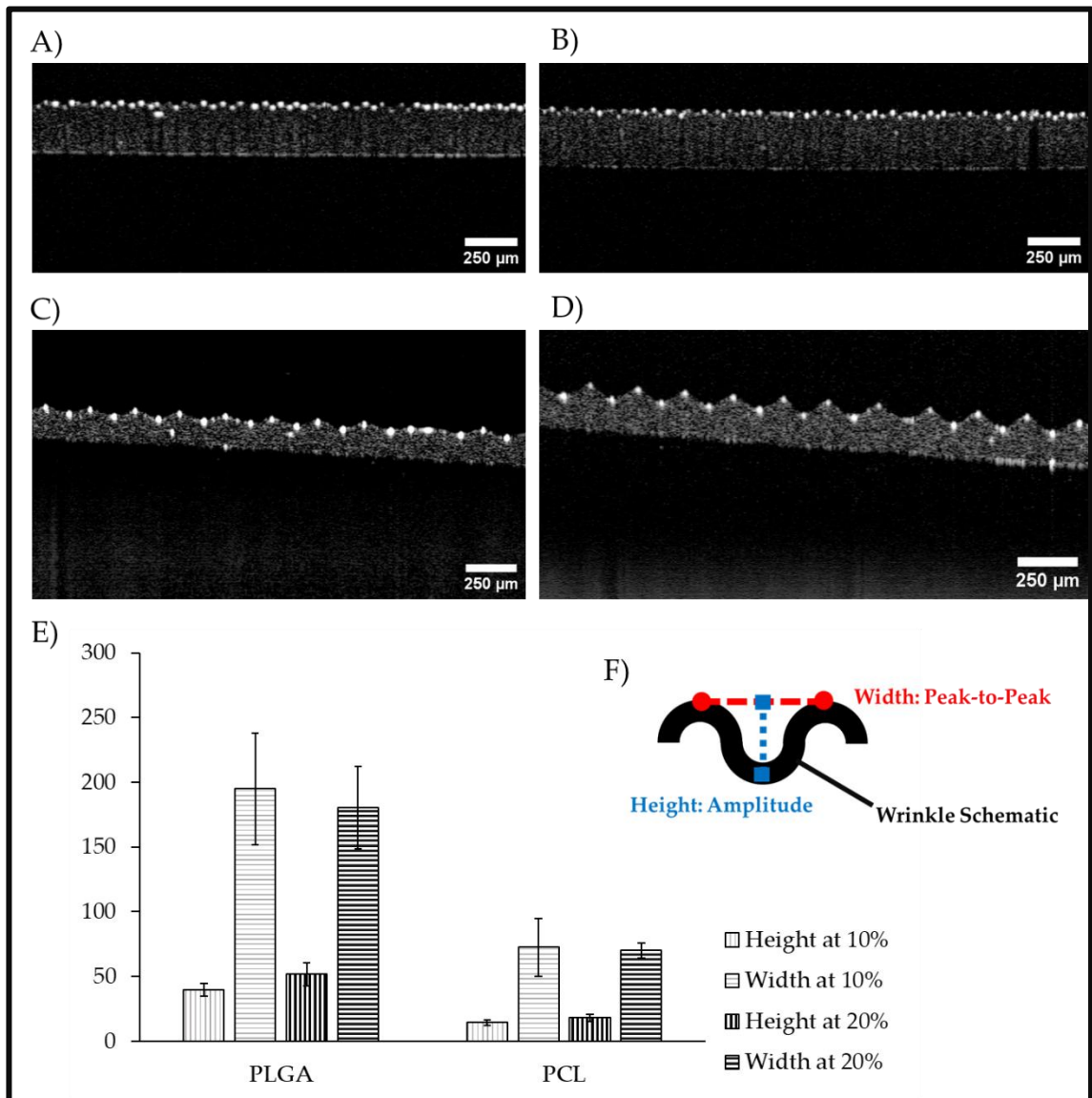


Figure 4.8: Optical Coherence Tomography imaging of laminated blocks. A) OCT B-scan of PCL laminated block at 10% compression, B) OCT B-scan of PCL laminated block at 20% compression, C) OCT B-scan of PLGA laminated block at 10% compression and D) OCT B-scan of PLGA laminated block at 20% compression. E) quantification of crypt shape from OCT B-scans, showing the comparison between the levels of compression and change in dimensions. F) Illustration of a wrinkle undulation demonstrating how OCT measurements of wrinkled materials were taken, 3 blocks of each composition were measured at both levels of compression with averages taken of $n=10$ measurements of crypt height and width.

It was hypothesised that the amount of pressure applied to the blocks could effectively control the crypt dimensions of the laminated blocks. Whilst the crypt shape

was demonstrated to have changed, as shown in Figure 4.8 the increase of bilateral compression from 10% to 20% strain caused the peak-peak width to narrow and the crypts to deepen. However when compared using a statistical method (one-way ANOVA with Tukey’s pairwise comparison), it was ascertained that intra-material comparisons yielded no statistically significant difference. However inter-material comparisons did demonstrate that there is a significant difference between the crypt dimensions offered by the different materials, refer to Table 4.1 for relevant P-values below.

Tukey Post-Hoc Test – Width				
	PLGA 10%	PCL 10%	PLGA 20%	PCL 20%
PLGA 10%	—	0.004*	0.928	0.003*
PCL 10%		—	0.008*	1
PLGA 20%			—	0.007*
PCL 20%				—

Tukey Post-Hoc Test – Depth				
	PLGA 10%	PCL 10%	PLGA 20%	PCL 20%
PLGA 10%	—	0.004*	0.135	0.009*
PCL 10%		—	< .001*	0.87
PLGA 20%			—	< .001*
PCL 20%				—

Table 4.1: Tables displaying the results of the one-way ANOVA wherein Tukey’s pairwise comparison post-hoc test was performed. The P-values are listed for each comparison and pairs which were found to be statistically significantly different are listed with a ‘*’ where $\alpha = 0.05$

Though the morphology of the laminated blocks showed great promise, there was a significant drawback, an observed delamination of the membrane under prolonged compression in cell culture. The delamination was observed through the loss of wrinkle shape over time during incubation. Critically, due to this delamination, it was deemed that the laminated block method of wrinkling was unreliable, despite

extensive efforts to find an appropriate biocompatible and compressible adhesive that does not delaminate upon wetting.

4.3.5 Oxygen Plasma Treatment

Whilst the laminated block method presented initial promising features for use in the bioreactor system, the observed delamination (and subsequent uncontrolled loss of topography) was problematic. The solution therefore was to develop the bioreactor substrate with an elastomer wrinkling method which directly modified the bulk and could offer topographical permanence. Oxygen plasma treatment, as demonstrated in other studies such as the method presented by Glatz and Fery offered a promising avenue of development (*Glatz and Fery, 2018*). Oxygen plasma treatment is an alternative method to achieve the desired topography compared to the adhesion of membranes to the PDMS bulk. In essence, the overall principle is the same, exploiting the use of a formed 'film' on the surface which is significantly stiffer than the bulk underneath. Following the simple wrinkling model (*Dimmock et al., 2022*) the wrinkles form when the lateral force is exerted upon the system. However, this is where the similarities end. The first major difference is there was no addition of material to the system, only the bulk material was required at the start of the process. The O₂ plasma treatment generated a stiffer surface film by introducing oxygen-mediated cross-linkages between the cured PDMS elastomer chains. Plasma treatment could even be used to cross-link liquid PDMS by this mechanism. This is a well characterised process and results in the formation of a silicate-like layer which is in the order of up to ~100nm thick (*Glatz and Fery, 2019, Ismail et al., 2020*). The second major difference is the mechanism by which the lateral force is applied to form the wrinkled topography. In this method, the substrates are pre-stretched before exposure to the plasma. After the

surface is subsequently stiffened by plasma treatment, the substrate is considered to be in a flat 'neutral' state. When the stretch was released, the entire surface contracted inwards from both lateral directions simultaneously, this imparted a lateral force through the surface to induce topography formation.

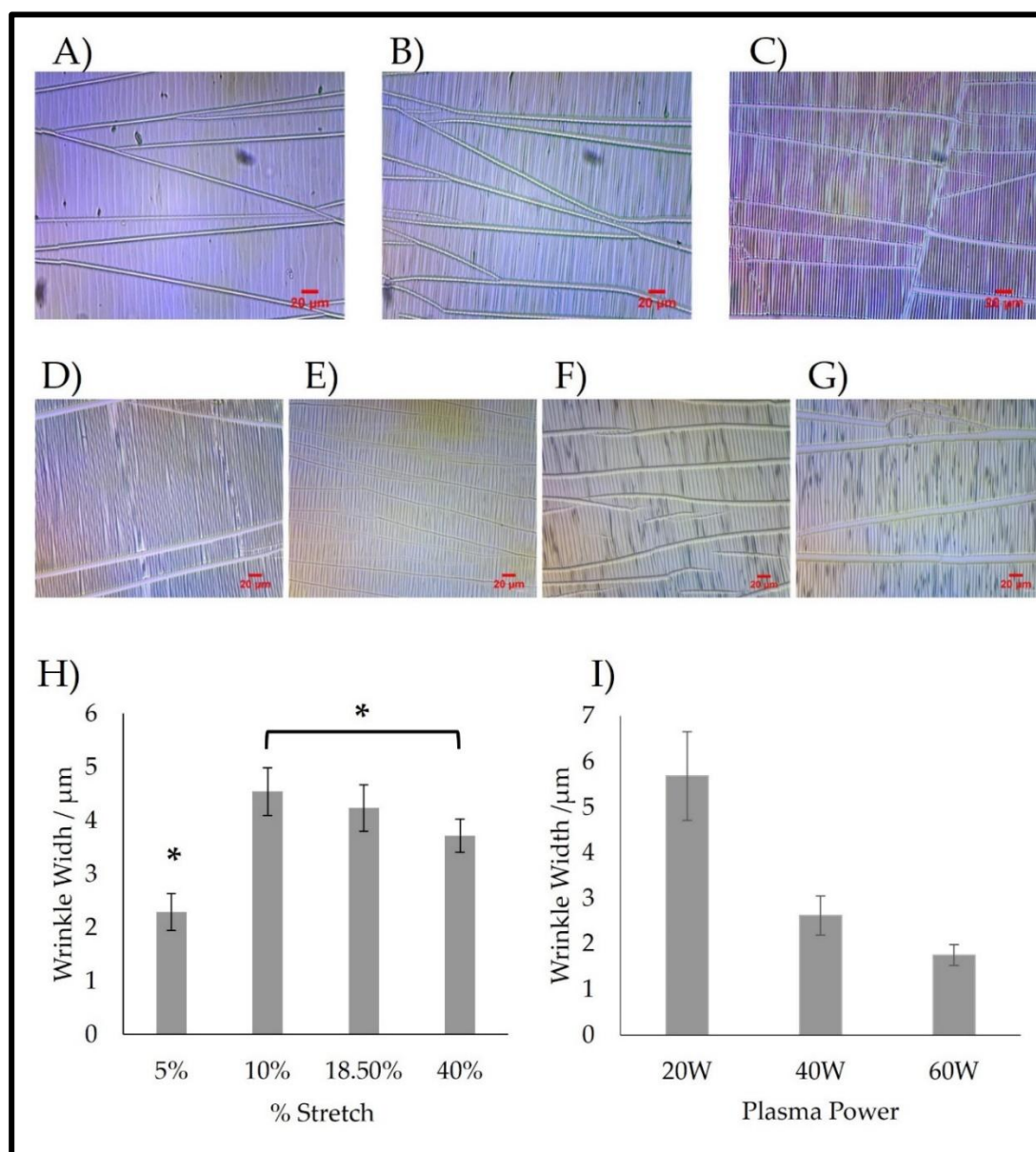


Figure 4.9: Bright-field micrographs of plasma-treated topographies formed using different parameters. A-C) variation by treatment power and D-G) variation by stretch application. Scale bars are 20 μm length for all images. H) Bar chart presenting quantification of wrinkle width (crest-to-crest) in terms of percentage stretch applied and I) bar chart presenting quantification of wrinkle width in terms of plasma power applied to the substrates. Statistic significance is marked with * on charts where $P < 0.05$, $n=5$ substrates were measured with averages of 5 measurements per substrate taken.

Figure 4.9 serves to demonstrate the capability of using low-temperature oxygen plasma in the generation of topography. The first row presents variation in applied power of A) 20W, B) 40W and C) 60W with respective wrinkle widths of $5.68 \mu\text{m} \pm 3.07 \mu\text{m}$, $2.62 \mu\text{m} \pm 1.37 \mu\text{m}$ and $1.75 \mu\text{m} \pm 0.71 \mu\text{m}$. Stretch was maintained constant at 10%. The second row of images presents applied stretches of A) 5% stretch, B) 10% stretch, C), 18.5% stretch and D) 40% stretch., with respective wrinkle widths of $2.28 \mu\text{m} \pm 1.09 \mu\text{m}$, $4.54 \mu\text{m} \pm 1.41 \mu\text{m}$, $4.23 \mu\text{m} \pm 1.38 \mu\text{m}$ and $3.72 \mu\text{m} \pm 0.98 \mu\text{m}$. Plasma power was maintained constant at a power of 50W. For both tests oxygen pressure was maintained at 1.5mbar and the duration of exposure was unchanged from 10 minutes. All measures are $n = 10$ from a sample group of $n = 4$. One-way ANOVA, with a Games – Howell post-hoc test (due to unequal variances) indicated that wrinkle widths resultant from the lowest stretch applied (5%) were statistically significant from the others, whilst 10% was also significantly different from 40% stretch, where $P < 0.05$. The same statistical method was used for the power test. It was evaluated that wrinkle widths generated by all power application conditions were statistically significant from each other, where $P < 0.05$.

Depth analysis by optical methods proved to be unsatisfactory due to the small scale of the wrinkles, however, an inspection of the plasma-treated surface by scanning electron microscopy revealed the nature of the wrinkles in much greater detail. The wrinkle curvature was more obviously resolved, and the topographies taken for electron microscopy were subjected to the 'standard' plasma treatment program, which was 50W power, 1.5 mBar Oxygen pressure and 10 minutes exposure time formed under a 20% stretch. The average wrinkle width for these substrates was

measured to be $4.12 \mu\text{m} \pm 1.1 \mu\text{m}$, measurement $n = 5$ sample $n = 3$. This is consistent with the power and stretch variability testing. However, still being a 2-dimensional method of imaging, the capacity for depth-resolved imaging and thus the accurate mapping of the crypt morphology was not possible using the electron microscopy method shown in Figure 4.10.

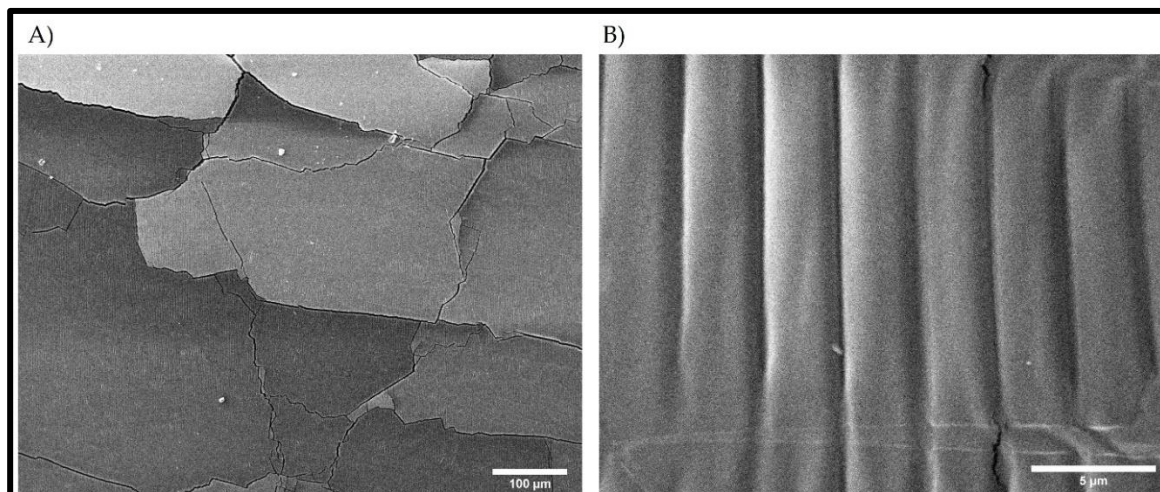


Figure 4.10: Scanning electron microscopy of plasma-treated PDMS. A) Acquisition at low power showing wrinkles at low power and surface cracking (X150) with a scale bar representing $100 \mu\text{m}$. B) Acquisition at high power showing individual wrinkles (X5000) with a scale bar representing $5 \mu\text{m}$.

Atomic force microscopy facilitated 3-dimensional mapping of the plasma-generated topography due to the ultra-high resolution of the equipment. A drawback of this is that these results were obtained as a commercially outsourced service (Sheffield University) due to equipment availability, therefore due to cost and labour considerations replicates were limited to $n = 1$ as a preliminary analysis of the chip format substrates. There is potential to investigate these substrates further using AFM, particularly in the comparison of substrate surface roughness. However there are limitations to measuring crypt depth with the substrates of crypt dimensions exceeding

the acquisition window at the highest magnification, but at the lower presented magnification, it would be feasible to look at both depth and roughness. However, given the uniqueness of this method (to accurately map the topography vertically within nanometer accuracy) it is possible to calculate the depth from crypt trough to crest. The measurement calculated from the highest resolution rendering, as visualized in Figure 4.11, was 722 nm.

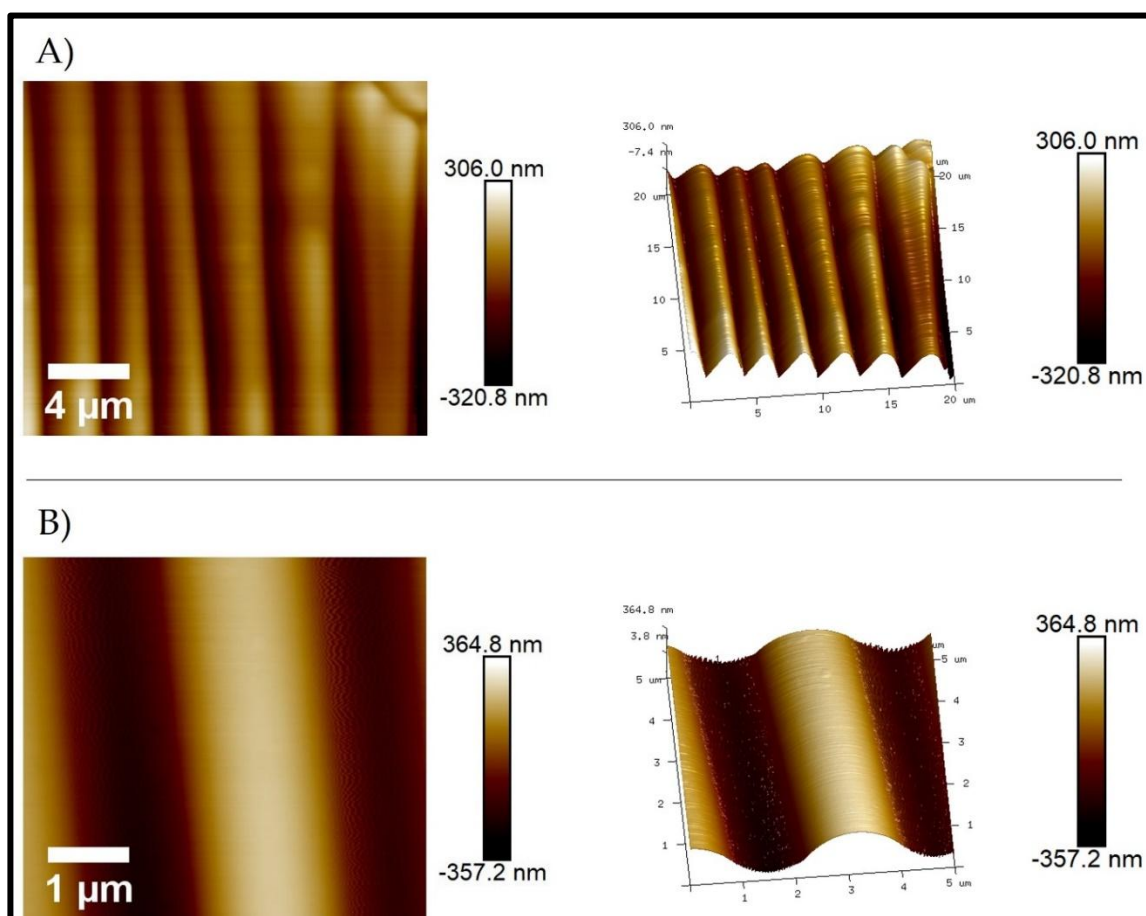


Figure 4.11: Atomic force microscopy imaging of plasma treatment PDMS. A) en-face and 3D spatial rendering of AFM 20 μm x 20 μm window and B) en-face and 3D spatial rendering of AFM 20 μm x 20 μm window. The En-face image (left) is scaled to the nominated scale bar, whilst the 3D rendered image (right) is scaled to the associated XY grid.

4.3.6 Wet Chemical Oxidation (acid-oxidation)

Wet chemical oxidation was introduced at a later stage in the substrate development process once the laminated block method was considered obsolete. This avenue of development was considered a necessity due to the limited size of wrinkles being produced by oxygen plasma treatment. Therefore a method with the same quality of topographical permeance as associated with the oxygen plasma treatment but with larger topographical features was needed. The size of topographical features should mimic the native limbal niche architecture in healthy tissue, therefore using the Grieve et al. study, a crypt depth of up to 50 μ m and crypt width range of 15-150 μ m was used as a literature-based target range (Grieve et al., 2015). However, as determined by OCT, the native interpalsade crypt (ERP) width could be ~30 μ m, therefore wrinkles of this order, provided they can house at least single cells were acceptable initially. Acid oxidation of PDMS shares a similarity to the oxygen plasma treatment method of generating wrinkles, where a stiffer upper surface was created in the bulk material during treatment. Sharing another feature with the plasma treatment method, the generation of the wrinkles required the PDMS substrate to be pre-stretched before exposure to the strong acid. The acid oxidation was performed using a 1:3 mixture of nitric to sulphuric acid. Due to the strength of the reagents involved, the surface reaction occurred quickly, resulting in surface modification within a matter of seconds. Quenching with sodium hydroxide and water terminated the surface reaction immediately.

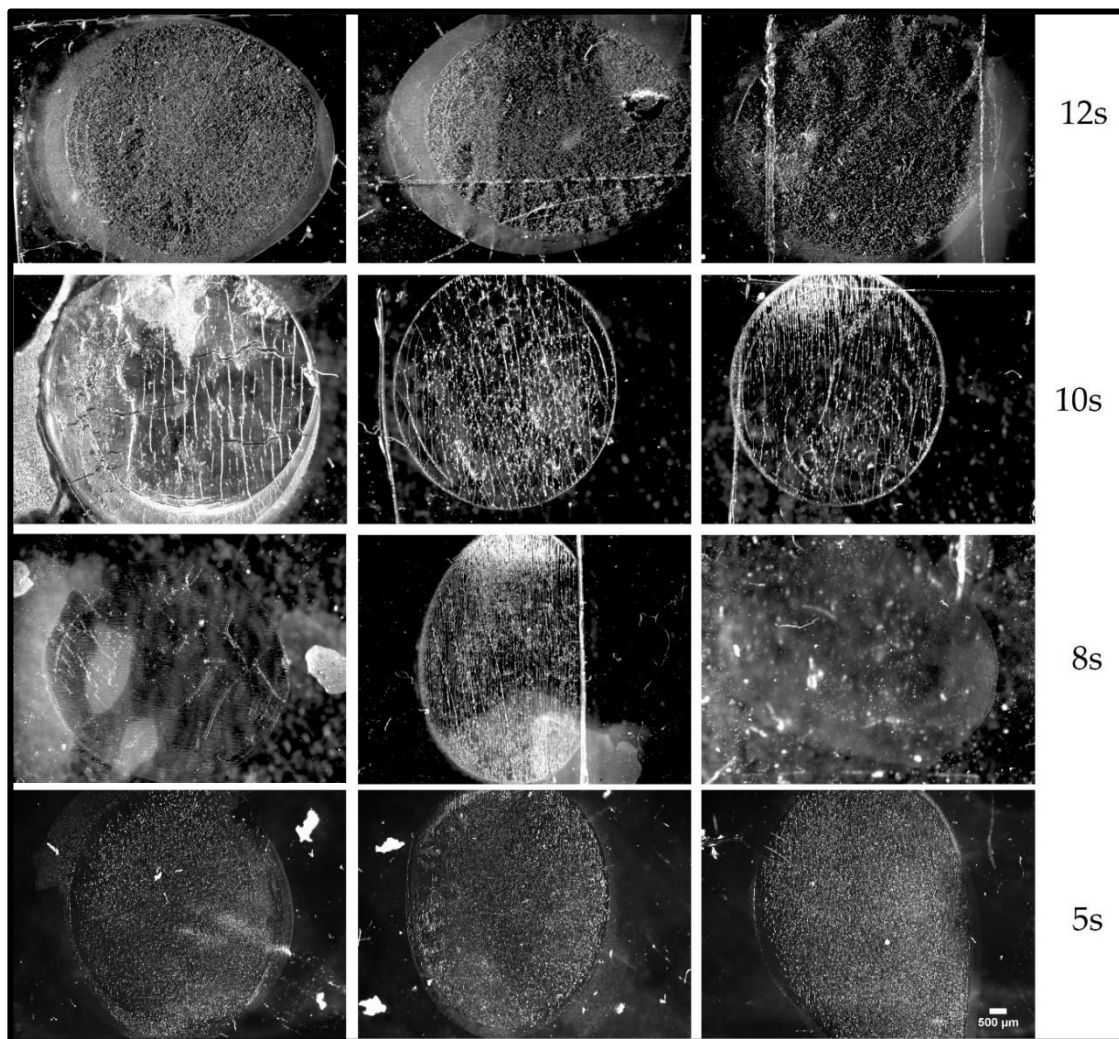


Figure 4.12: Bright-field micrographs of PDMS oxidized with sulfonic acid to produce topography. Substrates made with 3.33% curing agent were pre-strained to 5% and exposed to the acid for the specified amounts of time, ranging from 5 to 12 seconds. $N = 3$ for each time exposure and the scale bar in the lowest right-hand image is representative of all images in the panel and 500 μm in length.

Figure 4.12 shows the changeability in the produced topography through the variation in exposure time to 50 μl droplets of sulfonic acid. Due to the highly variable nature and definition of the produced features, quantification of the produced features in initial testing was not feasible. However, as a qualitative appreciation for the effect of acid exposure, 12 seconds did not produce any wrinkles, instead producing a textured and cracked surface. 10 second exposure produced an exfoliated and

cracked surface which showed evidence of some wider wrinkle generation in places. For 8 seconds, wrinkles were more defined and regular but interspersed with cracks and bifurcations. 5 seconds produced narrow features, with minimal surface cracking, but interspersed with regular intersecting features and bifurcations. However, this was the least damaged of the series.

After determining the ability to control surface feature generation using sulfonitric acid, it was ascertained that there was a requirement to increase the quality of wrinkle formation, moving towards limbal biomimicry. The priority was to increase the linearity of the wrinkles before alterations to wrinkle magnitude were affected. To this effect It was hypothesised that bending the substrates in a “U” shape, with the tails bent away from the upper surface would impart surface forces conducive to forming linear ordered wrinkling, propagating perpendicularly to the direction of bend release. To test this, 3 levels of bending were applied to the substrates; complete bending (total substrate folding), U-bending (bending around a glass rod to form a tight “U” shape) and slightly bent (utilizing a PTFE roller of diameter 45mm to apply a wide larger radius bend), the resultant wrinkling patterns are presented in Figure 4.13 Following the same form of interpretation as the time-dependent feature generation test, the interpretation of the bending tests is purely qualitative, due to the presented quality of the generated substrate features. From the levels of the bending test, it can be observed that the increase in bending (reducing bend radius) increased the ordering (and linearity) of the features formed.

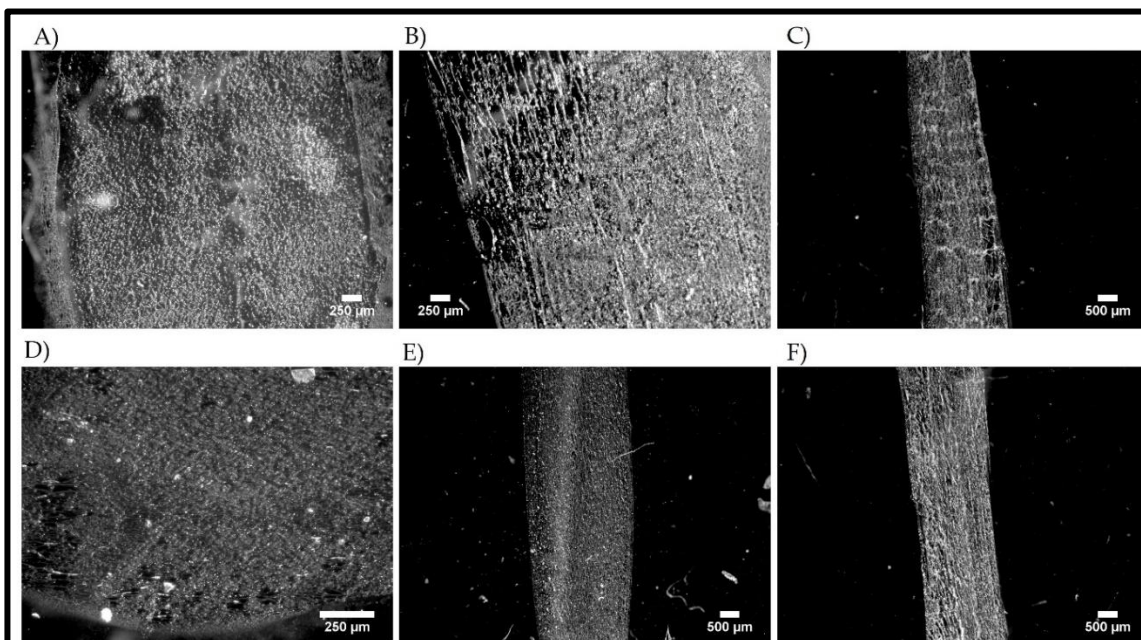


Figure 4.13: PDMS substrates which were bent to impose physical strain on the surface exposed to sulfonitric acid. A) Bent in a wide semicircle, B) Bent in a tight "U" shape and C) completely folded. D-F) are all completely folded, but with varying acid exposure times, D) instant exposure and quench, E) 5 seconds and F) 10 seconds exposure. All samples are representative of $n = 3$ replicate, scale bars are individually scaled in each image.

However, a side effect presented in the form of an increase in surface degradation in fracturing and exfoliation, with the greatest level of bending causing a near-total surface degradation. Conversely, the lower levels of bending resulted in a lesser level of ordering and presented far lesser surface features, but preserved surface integrity more.

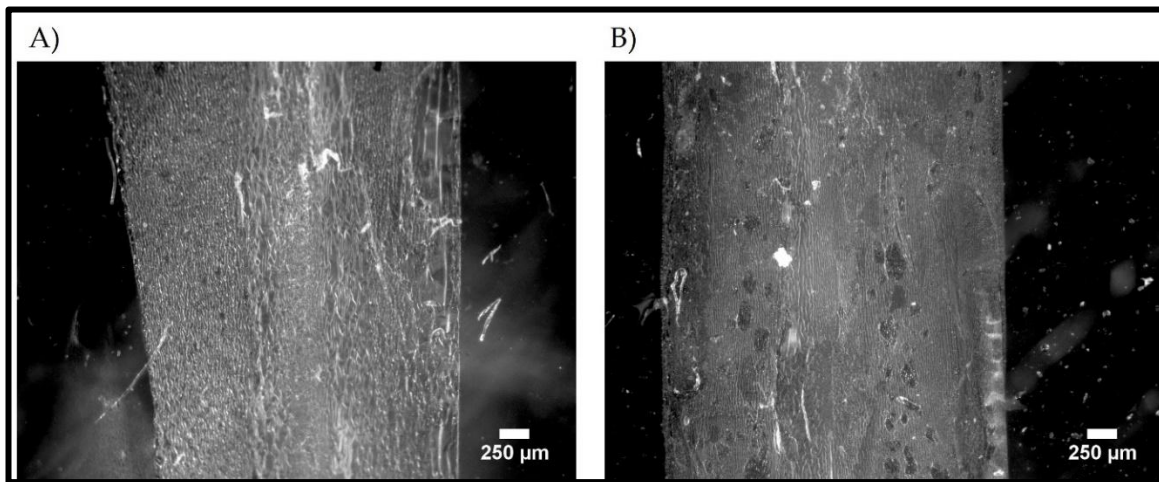


Figure 4.14: Variation of topography generation by PDMS stiffness. A) PDMS formulated with 5% curing agent and B) PDMS formulated with 10% PDMS. Both substrates were bent completely and exposed to the acid for 5 seconds, $n = 3$ and both scale bars are 250 μm in length.

Changing the stiffness of the PDMS demonstrated an ability to alter wrinkled feature presentation as demonstrated in Figure 4.14. However, in all surviving samples there is visual variation in the presentation of the generated topography, thus presenting a challenge for quantification. Bifurcations and lateral intersections of the wrinkles challenge the linearity of both groups, however, PDMS formulated with a 10% curing agent presented better linearity and wrinkle presentation. However, this was offset by surface exfoliation, cracking and pitting likely attributed to the increased stiffness and increasing stress on the surface upon the bend release. As an anecdotal reflection, substrates which were formulated with a 10% curing agent had a 25% failure rate during production due to snapping during acid exposure.

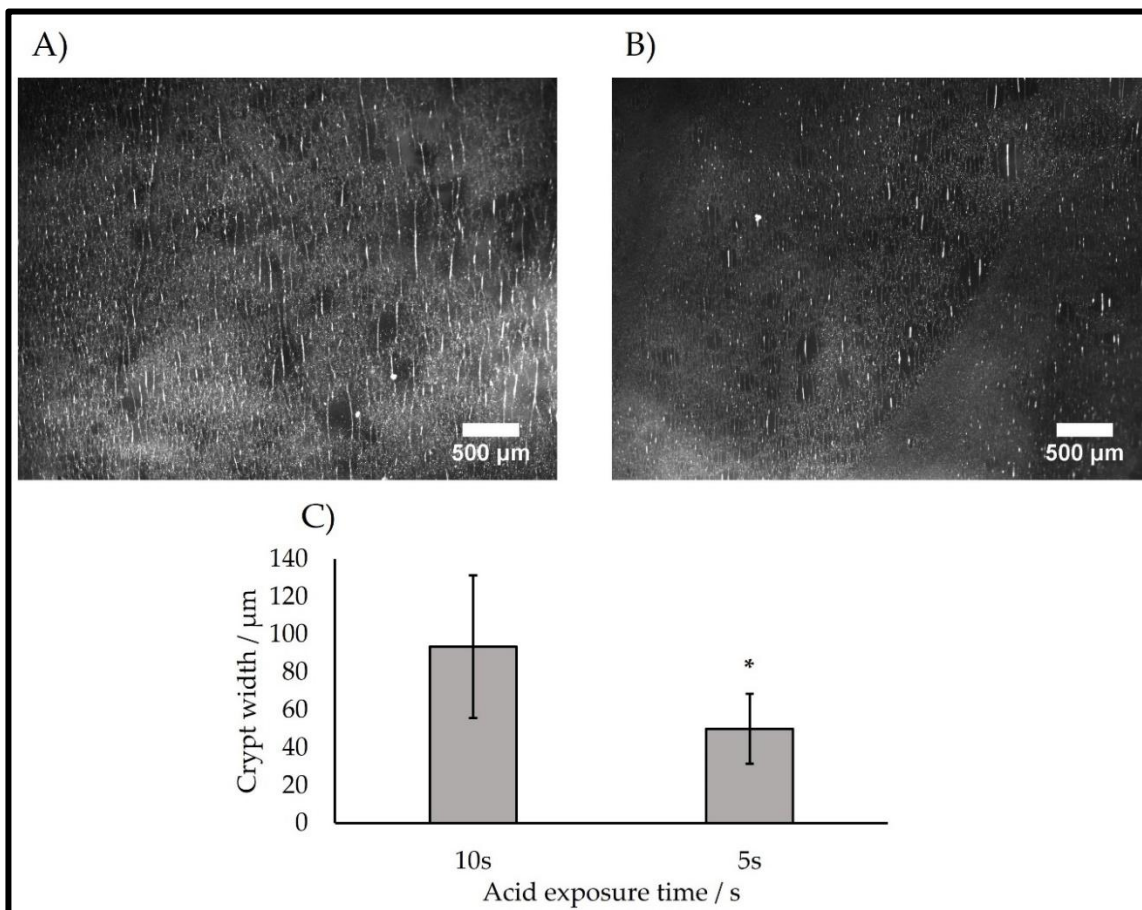


Figure 4.15: Immersed PDMS chips exposed to sulfonitric acid. A) exposure time of 5 seconds, B) exposure of 10 seconds. Images are representative of 3 samples each, and scale bars are individually scaled in each image. C) Bar chart describing peak-peak crypt widths acquired from the en-face images represented in A) and B). * Denotes statistical significance ascertained by Students T-Test where $P < 0.05$.

Peak-peak crypt width of the clearest aligned crypt features was measured for both acid exposure times, measurements from these images indicate a crypt width of $50.0 \pm 18.6 \mu\text{m}$ for 5s and $93.5 \pm 37.9 \mu\text{m}$ for 10s. These measurements were acquired as $N = 5$ from each image and a total sample number of $N = 3$ for each exposure. A Student' T-Test was performed between the two exposure times and determined that they were significantly different, with a P value of <0.001 , where $\alpha = 0.05$. This quantification is summarized in Figure 4.15.

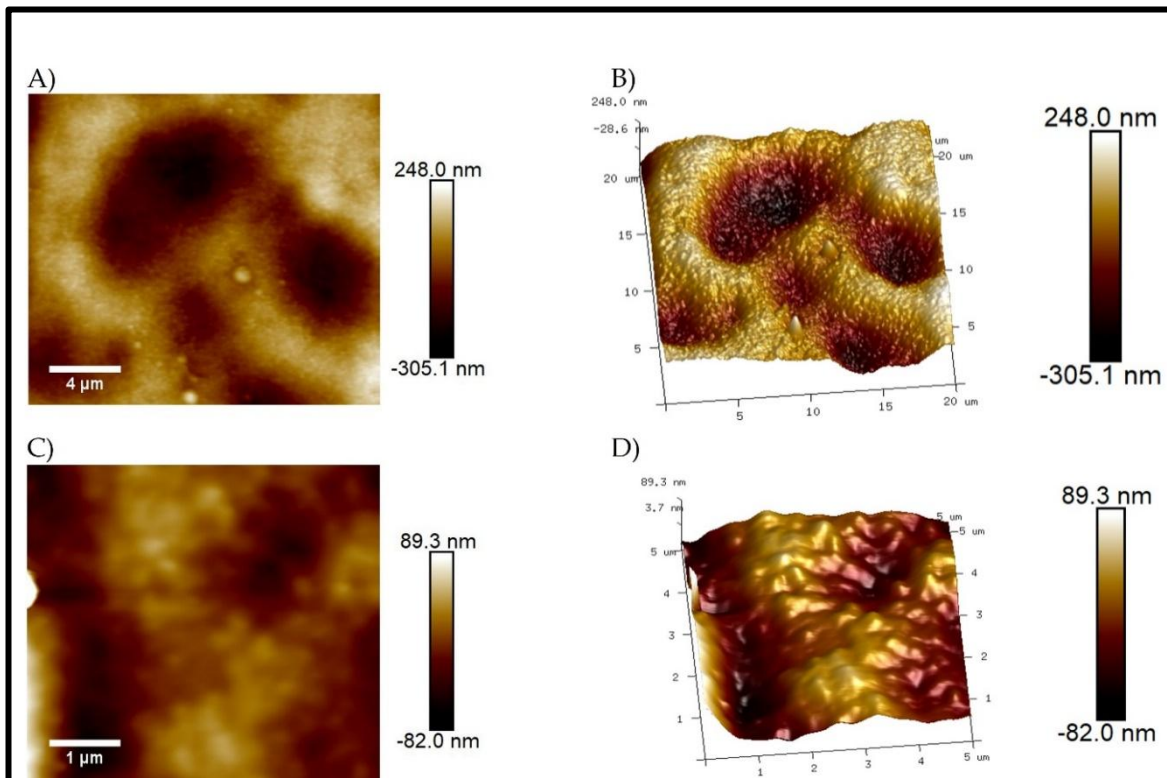


Figure 4.16: Atomic force microscopy imaging of acid-oxidized PDMS. A) en-face and 3D spatial rendering of AFM 20 μm x 20 μm window and B) en-face and 3D spatial rendering of AFM 5 μm x 5 μm window. The En-face image (left) is scaled to the nominated scale bar, whilst the 3D rendered image (right) is scaled to the associated XY grid.

Atomic force microscopy in Figure 4.16 revealed the acid-oxidized topography in most detail, showing both the random-oriented topography as observed in other modalities and also revealing nanoscale features attributed to the dual treatment method. In this method, the nanoscale features resemble a rough knobbled appearance, with an average roughness quotient of 24.9 nm taken from the 5 x 5 μm acquisition.

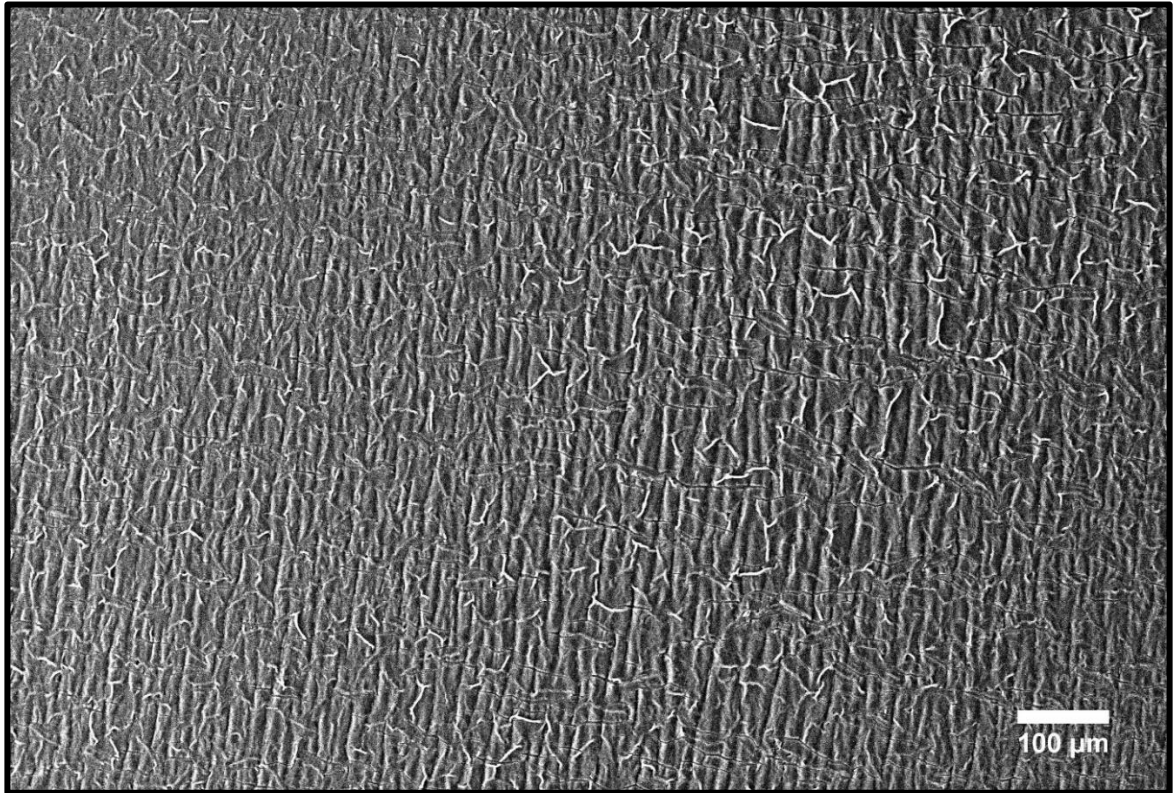


Figure 4.17: Scanning electron micrograph of wet chemical oxidized PDMS. The surface was exposed for 5 seconds using the immersion method on a stretching frame, representative of a sample set of $N = 3$ and the scale bar is 100 μm in length.

Despite the randomly ordered topography, in these 2-dimensional images, the peak-peak crypt width was able to be measured, however, measurements from these images indicate a crypt width of $22.9 \pm 10.4 \mu\text{m}$. These measurements were acquired as $N = 5$ from each SEM image as exemplified in Figure 4.17 and a total sample number of $N = 3$

4.3.7 Dual treatment

Dual treatment was the final advancement in the development of the bioreactor substrate. This method was a culmination of both acid oxidation and plasma treatment by combining these methods in a sequential surface treatment method. As per the specifications for the acid oxidation method, the same target dimension ranges (a crypt depth of up to 50 μm and a crypt width range of 15-150 μm) were employed. However, the native interpalisade crypt (ERP) width could be $\sim 30\mu\text{m}$, as found by OCT, therefore wrinkles of around this magnitude would be considered acceptable as the lowest boundary of acceptance. This method utilised a custom moulded chip which fitted into the 316L stainless steel stretching frame. These chips underwent stepwise treatments to stiffen the outer surface of the substrate. The first step is the wet chemical oxidation of the pre-stretched chips, followed by oxygen plasma treatment. The removal of the stretch imparted by the frames induced wrinkling over the upper surface of the dual-treated PDMS substrates. The decision to incorporate both wet chemical oxidation and plasma treatment together arose from anecdotal evidence of the improvement of the alignment of the resultant wrinkles. Additionally, the combination of the two methods (as outlined in Figure 4.18) facilitated the production of topographies with dimensions closer to the desired biomimicking widths when the PDMS was subjected to a dual treatment protocol.

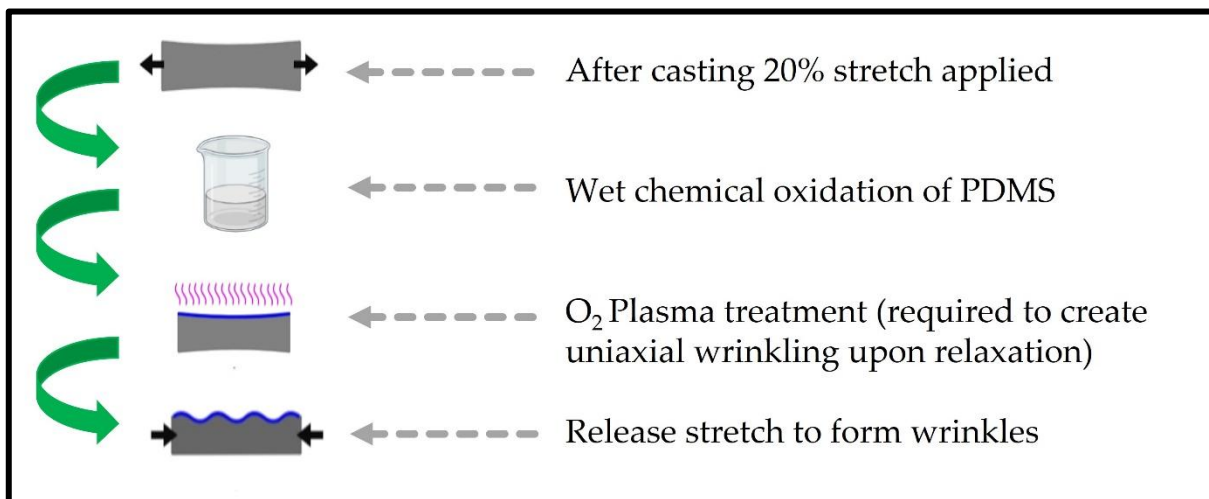


Figure 4.18: Schematic representation of the dual treatment protocol. The steps undertaken to achieve the dual-treated PDMS substrates are as outlined.

The OCT imaging in Figure 4.19 of the dual-treated PDMS chips revealed the ability of the dual treatment method to produce repeatable crypt topography with distinct undulations. Additionally, it is also demonstrated that the variation of the curing agent in the formulation of the PDMS substrate results in a change in crypt dimensions after the dual treatment process.

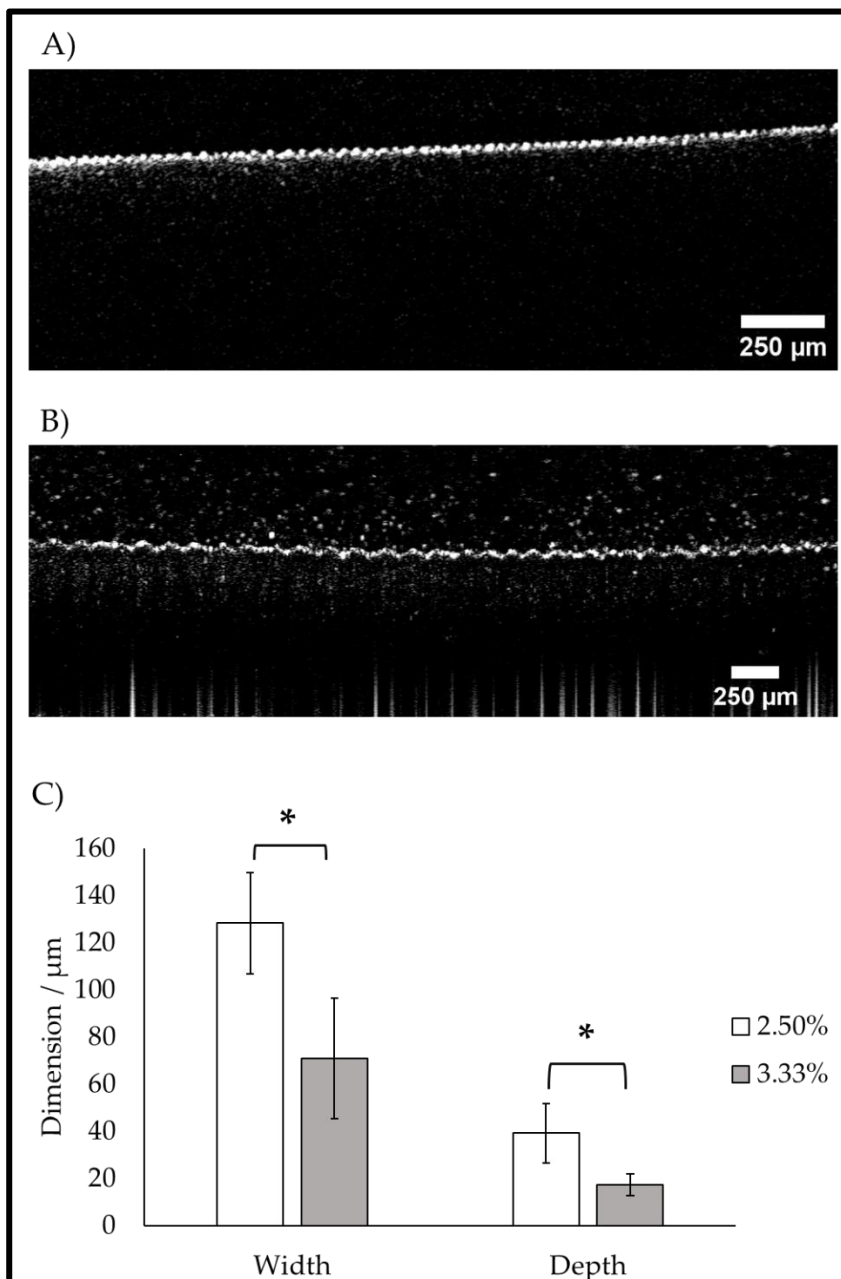


Figure 4.19: OCT analysis of dual-treated PDMS chips. A) Bright-field image of PDMS formulated with 3.33% curing agent, B) Bright-field image of PDMS formulated with 2.5% curing agent, scale bars are as represented in each image. Both images are representative of 3 replicate samples C) Bar chart describing crypt dimensions acquired from B-Scan OCT images. * Denotes statistical significance ascertained by students T-Test where $P < 0.05$, $n = 3$.

The OCT enabled the resolution of the crypt dimensions, in terms of peak-to-peak width and crypt depth, through depth-resolved imaging. It was found that the respective peak-to-peak widths of the 3.33% and 2.5% curing agent formulated chips were $70.9 \pm 25.39 \mu\text{m}$ and $128.2 \pm 17.7 \mu\text{m}$. The depths of the 3.33% and 2.5% curing

agent formulated chips were $17.1 \pm 4.64 \mu\text{m}$ and $39.1 \pm 10.3 \mu\text{m}$ respectively. Student's T-tests were employed to assess the statistical significance between the curing agent concentrations, scrutinising both dimensions. It was ascertained that in both dimensions the curing agent concentrations affected statistically significant different crypt dimensions, for peak-peak crypt width the P-value was 0.033 and for crypt depth, the P-value was 0.028, where $\alpha = 0.05$.

Figure 4.20 demonstrates the shape memory of the substrates, here the substrates were each subjected to the following scan procedure: first subjected to the dual treatment protocol > scan 1 (before relaxation) > +20% elongation stretch removed from each substrate > scan 2 (after relaxation) > +20% elongation stretch reapplied to each of the substrates > final scan (reapplication of original stretch). Whilst this does not cyclically load the substrates, it demonstrates the wrinkles topography to be near-completely reversible after formation. This is the point where it is not possible to accurately measure the re-stretched topographies by OCT image analysis.

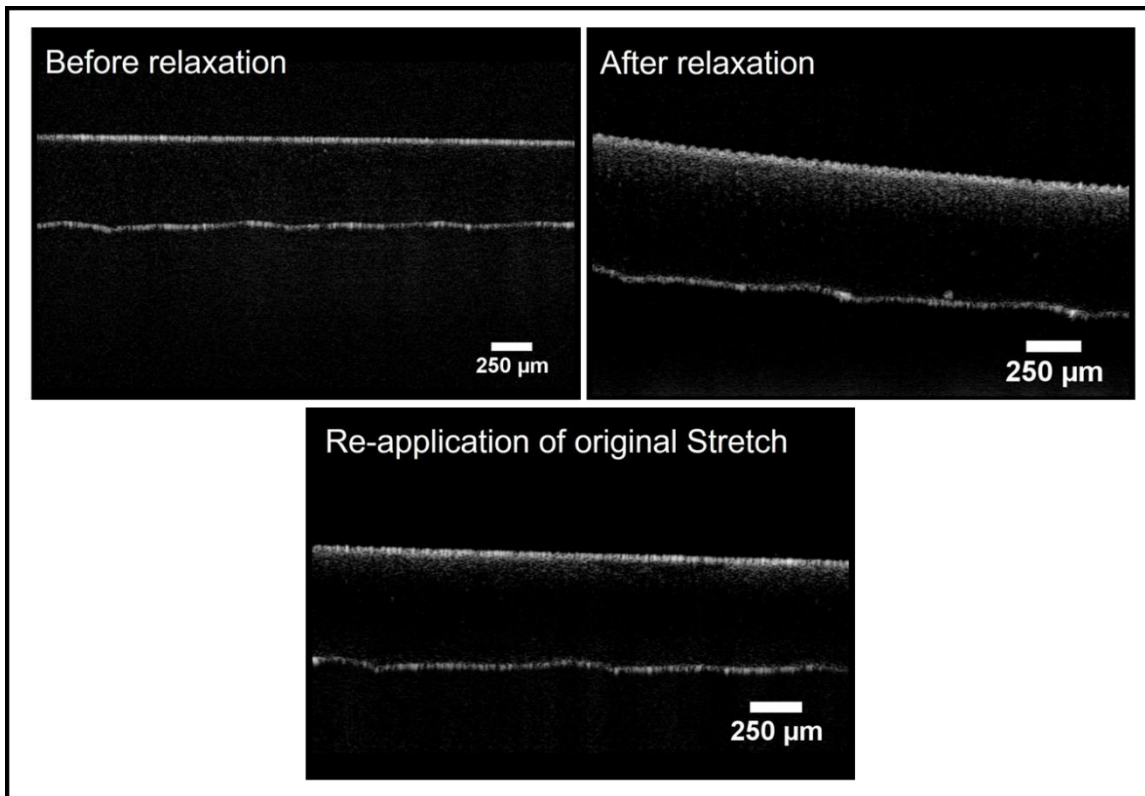


Figure 4.20: Optical Coherence Tomography Imaging of a dual-treated PDMS chip undergoing a cyclic load using the stretching frame. B-scan cross-sections demonstrate the returnable nature of the dual-treated topography ($N = 3$).

The scanning electron microscopy in Figure 4.21 revealed the surface in higher resolution of detail, similar to Figures 4.10 and 4.17 which depict acid-oxidation and plasma treatment. In visual observation, it is found there is a visually high density of perpendicular fault cracking across the surface of the material. However, in between these cracks, sinusoid-like undulations are observed to form, propagating from left to right as presented in Figure 21. In these 2 dimensional images, only peak-peak crypt width can be measured, with measurements from these images indicating a crypt width of $24.8 \pm 7.2 \mu\text{m}$. These measurements were acquired as $N = 5$ from each image and a total sample number of $N = 3$. These measurements were not found to agree with the measurements captured by OCT, with a P value of 0.004 being determined between the 3.33% dual-treated chips scanned by SEM and the OCT-scanned

samples of the same treatment and composition. Significance was tested using the Student's T-test where $\alpha = 0.05$. It is proposed the disparity in these recorded results may be explained by the harsh sample preparation for SEM (adhesion to sample mount and critical point drying) which may have damaged or shrunk the wrinkles formed on the 3.33% chips imaged.

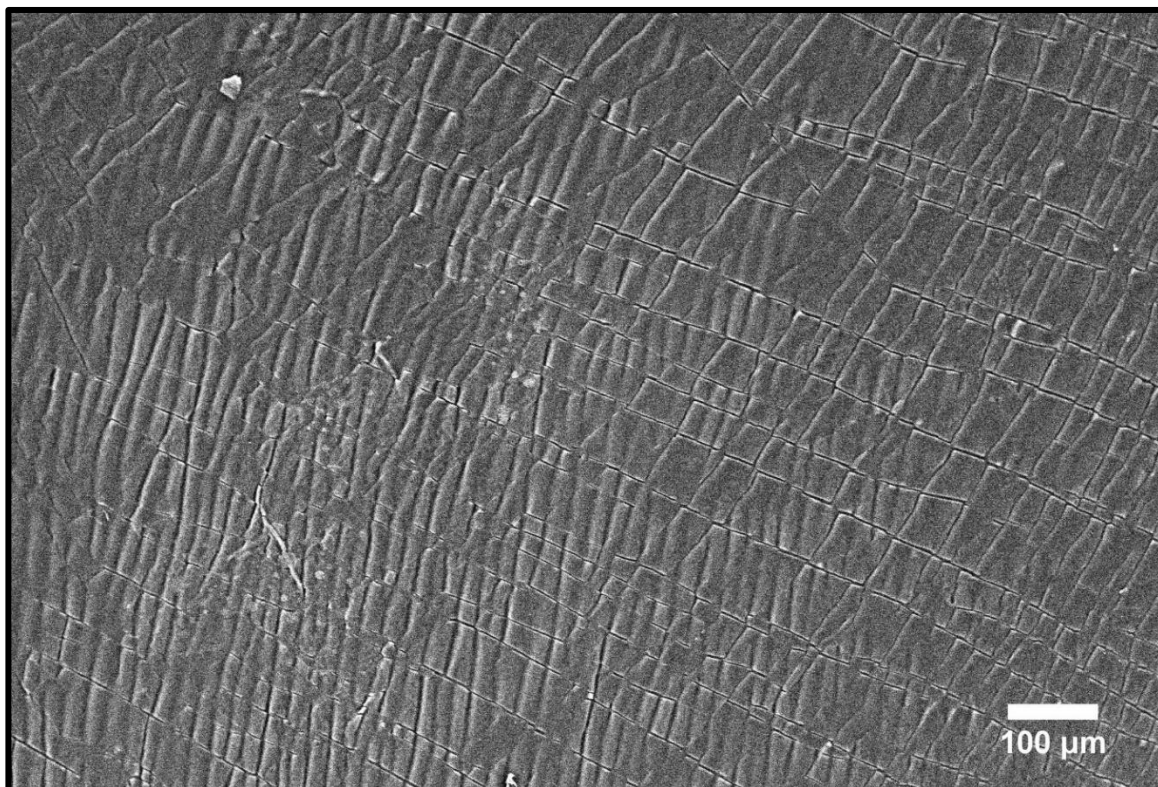


Figure 4.21: Scanning electron micrograph of a PDMS chip subjected to the dual treatment protocol. This image is representative of a sample set of $N = 3$ and the scale bar is 100 μm in length.

The atomic force microscopy in Figure 4.22 revealed the dual-treated topography in most detail, showing both the waveform/sinusoid topography as observed in other modalities and also revealing nanoscale features attributed to the wet chemical oxidation method. In the dual-treated substrates the nanoscale features resemble a fine gooseflesh appearance, having an average roughness quotient of 53.9 nm taken from the 5 x 5 μm acquisition.

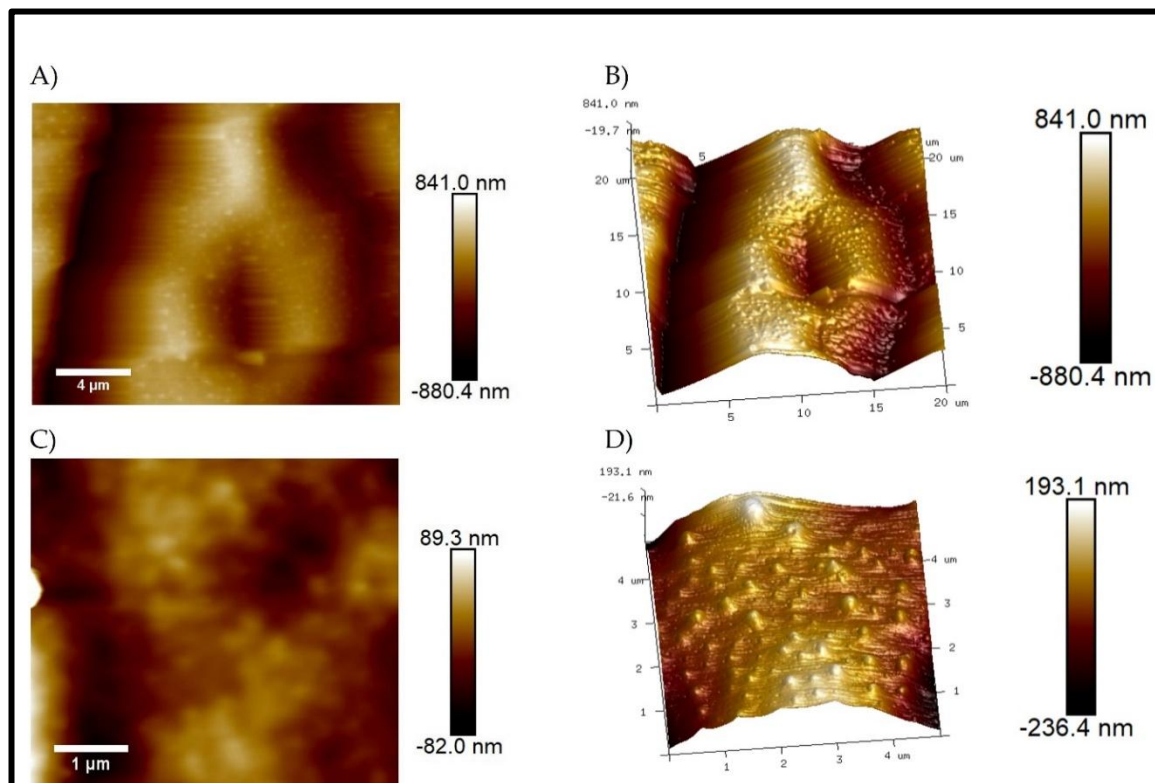


Figure 4.22: Atomic force microscopy imaging of dual-treated PDMS. A) en-face and 3D spatial rendering of AFM 20 μm x 20 μm window and B) en-face and 3D spatial rendering of AFM 20 μm x 20 μm window. The En-face image (left) is scaled to the nominated scale bar, whilst the 3D rendered image (right) is scaled to the associated XY grid.

4.3.8 Compositional Analysis of Materials Undergoing Treatments

Raman spectroscopy is typically used as a tool for chemical analysis; this tool uses the Raman scattering property to provide chemical bond compositional information about the substance being tested, e.g. biomaterial studies by (Soares et al., 2020, Kolodziej et al., 2021, Wang et al., 2023). As a spectroscopic technique, it provided a non-destructive analysis of the surfaces through all stages of the treatment process. The sampling protocol utilised in the analysis of the substrates was 5 acquisition points averaged for 3 samples per sample group. The changes detected by Raman spectroscopy are subtle but suitably aid in the characterisation of treatment-

induced changes to the substrates. It is observed that the sample group with the greatest overall Raman intensity was the dual-treated substrates. Significant peaks from the spectra in Figure 4.22 (which presented high intensity/cps) were observed in all groups at ~ 1400 , ~ 1250 , ~ 860 , ~ 780 , ~ 620 and $\sim 490\text{cm}^{-1}$ with double peaks at $\sim 2960\text{-}2910$, $\sim 150\text{-}200$ and $\sim 670\text{-}720\text{ cm}^{-1}$. These peaks correlate to PDMS identifying peaks at 2967 and 2906cm^{-1} (CH_3 stretching), 1413 and 1260 (CH_3 deformation) and 865 (CH_3 rocking), 492 cm^{-1} (Si-O-Si stretching) and 790cm^{-1} (C-Si-C stretching) (Vesna *et al.*, 2009). It is observed that the dual-treated substrates exhibited a greater average intensity across the entire profile compared to all other groups.

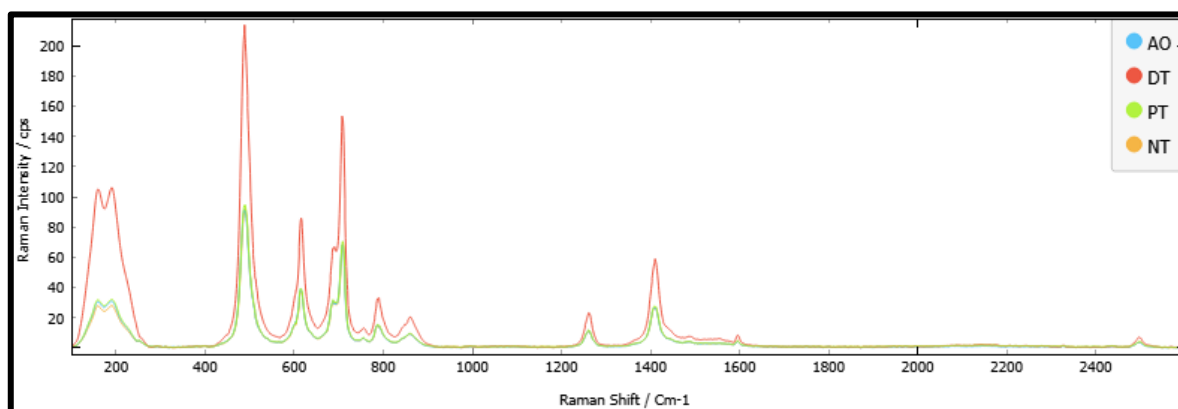


Figure 4.23: Raman spectra for PDMS treatment stages. The graph includes spectra from non-treated PDMS (NT), acid-oxidized PDMS (AO), plasma-treated PDMS (PT) and dual-treated PDMS (DT). Spectra are presented in terms of Raman intensity against wavenumber.

In conjunction with performing compositional analyses with spectroscopic techniques, the EdX technique was employed to analyse changes in surface elemental distribution between treatments. Principally EdX detects the scattering properties of electrons from a prepared sample's surface, which enabled the TM4000, whilst connected to the Oxford Instruments software, to determine the surface elemental composition of a sample. Table 4.2 summarises the output of the EdX analysis. It was found that surfaces exposed to sulfonitric acid exhibited a presence of elemental

sulphur in the detected compounds. However, due to the singular nature of the samples collected, this particular dataset should be appreciated as a more qualitative observation of the elements which were present between the samples.

	Elemental Presence / % Atomic						
	Oxygen	Silicon	Sulphur	Sodium	Calcium	Chlorine	Gold
Wet chemical	55.993	39.413	0.098	0.675	-	0.310	3.498
	<i>2.515</i>	<i>2.026</i>	<i>0.195</i>	<i>0.222</i>	-	<i>0.305</i>	<i>0.436</i>
Plasma treated	43.153	50.440	-	-	-	-	6.388
	<i>1.309</i>	<i>1.633</i>	-	-	-	-	<i>0.345</i>
Dual treated	46.695	51.705	1.515	-	0.043	-	-
	<i>4.641</i>	<i>4.764</i>	<i>0.206</i>	-	<i>0.085</i>	-	-
Non- treated	48.100	47.918	-	-	-	-	3.965
	<i>0.719</i>	<i>0.651</i>	-	-	-	-	<i>0.077</i>

Table 4.2: Average EdX values for the detected elements in each sample. Values expressed as percentage atomic presence with corresponding standard deviation noted in italics under each value.

The averages acquired in each sample were derived from n = 4 point acquisitions. Presented here are the elements detected by the system. The most notable detected elements are oxygen and silicon, present in all samples. Very minor signatures for other elements, including sulphur, sodium, calcium and chlorine were detected across the samples, however, signature presence was not homogenous, as outlined in Table 4.2. Gold was detected in 75% of the samples, however, the assumption is that the gold detected was a result of the coating sputtering of the samples before analysis.

To conclude the characterisation of the applied treatment methods to PDMS, 3.3% of PDMS chips were exposed to each of the treatment processes before tension testing. Customised tension testing adaptors were used to apply tension to the chips

as if they were in the bioreactor rigs. In (Figure 4.23) it is clear to see that acid oxidation and plasma treatment singularly increase the stiffness of the PDMS, however the dual treatment results in a definite decrease in stiffness compared to all other groups.

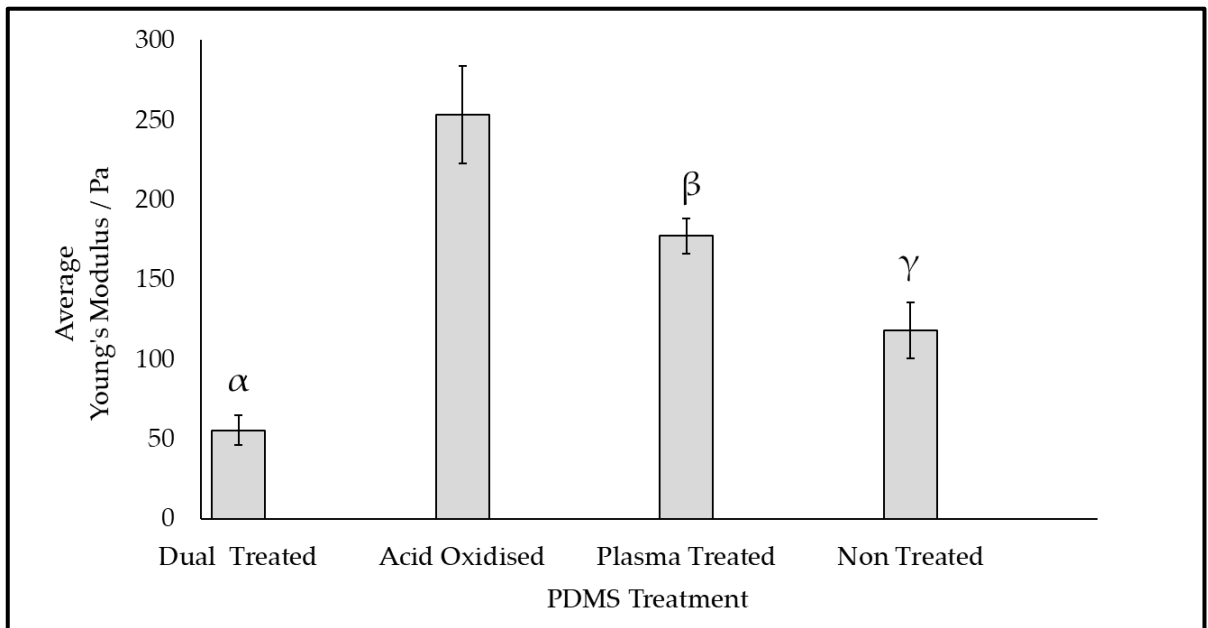


Figure 4.24: Tension testing of 3.3% PDMS chips which have been exposed to the different treatment methods. The annotations α, β, γ , denote groupings determined by one-way ANOVA where these sample groups were found to be statistically significantly different from each other and the un-noted (acid-oxidized) group. $N = 3$ for each group

The symbols denoted in Figure 4.24 represent groups which were statistically significant from un-like labelled groups, Non-treated (γ) was the control, whereas Acid-oxidized (unlabelled) had the greatest variability. Dual-treated (α) resided in the lowest percentile as analysed using one-way ANOVA. As determined, the dual treatment group was the physically weakest group subjected to testing, whilst the acid-oxidized group was the stiffest group tested.

4.3.9 Water Contact Angle Test to Predict Cytocompatibility

Water contact angle is commonly used as an assessment of hydrophobicity, (*Visalakshan et al., 2019, Pandey et al., 2019 and Leal et al., 2020*) are examples of a few studies where this tool has been used to assess hydrophobicity. Hydrophobicity is primarily used as an indicator for the wettability of a material, which itself lends to the material's utility as a biomaterial for the application of functional coatings and/or protein coatings. The hydrophobicity of the material directly controls what functional groups may interact with the surface. The study by (*Visalakshan et al.,*) into the application of various coatings to a substrate using plasma polymerisation exploits this effect to explore immunomodulatory effects by manipulating surface wettability and surface chemistry (*Visalakshan et al., 2019*). Figure 4.25 summarises the water contact angle results for the substrate surfaces to be employed in cell culture during this research. The two polymer membranes utilised in the laminated block method of wrinkling were included and were tested as single layer polymer membranes made after solvent casting. The four PDMS sample types were produced in the “chip” form and tested fully relaxed. The bilateral contact angle is an average of all frames taken within an acquisition step across both sides of the analysed water droplet. The angle detected is the enclosed angle of the water droplet, therefore the smaller the measured mean bilateral contact angle, the greater the hydrophilicity due to the greater spreading of the water droplet. Out of all material groups, PCL demonstrated the greatest hydrophilicity. Between the PDMS groups, interestingly the dual-treated substrate was deemed most hydrophobic by water contact angle, with acid oxidised PDMS having a similar result. Plasma treated PDMS had the lowest contact angle but retained the greatest variance.

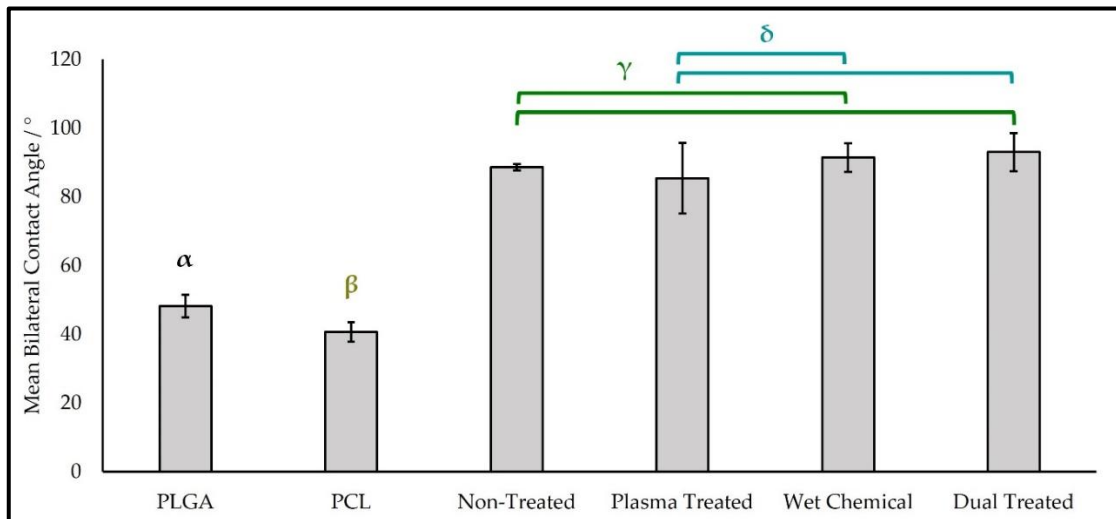


Figure 4.25: Bar chart depicting the water contact angles for the tested materials in this chapter. PLGA and PCL refer to polymer membrane samples relevant to the laminated blocks. Non-treated, plasma-treated, wet chemical and dual-treated refer to treatment protocols applied to PDMS 1mm thick substrates under pre-stretch conditions. $N = 3$ whilst α , β , γ and δ refer to groupings assigned by the Mann-Whitney U post hoc test of ANOVA, where $P > 0.05$.

4.3.10 Preliminary Assessment of Dual treatment Wrinkled Topography Using OCE

As part of the characterisation process for determining dual-treated substrate suitability for limbal biomimicry, the substrates were subjected to a series of preliminary optical coherence elastography (OCE) assessments utilizing the equipment setup as described in Chapter 3. At this stage, the characterisation process was split into two types of assessment, as presented in Figure 4.26. The first was the referenced assessment wherein the agar reference material was used to more accurately estimate the regional Young's modulus within the treated material, which averaged at 97.3 ± 47.5 KPa. The second variant relies on the lack of reference material, thus the material "self-references" enabling qualitative comparative resolution of the outer surface. However, this has the limitation of being inaccurate for the estimation of Young's modulus as these values would be based upon less sensitively acquired reference (the PDMS bulk

from compression testing). This preliminary assessment using OCE served to gain insight into the bulk and surface mechanical properties of the PDMS using the depth-resolved characterisation offered by OCE. In the agar referenced sample it is possible to resolve the bulk elasticity accurately (by having the reference) and see stress concentrations, the darkest red regions, within the material. It was observed that some of these concentrations coincided with the surface undulations and it is hypothesised that these stress concentrations may be a consequence of the wrinkling process. In the unreferenced samples the samples “self-referenced”, therefore the surface elasticity was more effectively revealed, albeit in a relative context. This means that, unlike the agar referenced elastogram, the PDMS only elastogram does not show the “true elasticity” but the comparative difference in elasticity in reference to the bulk of the PDMS chip.

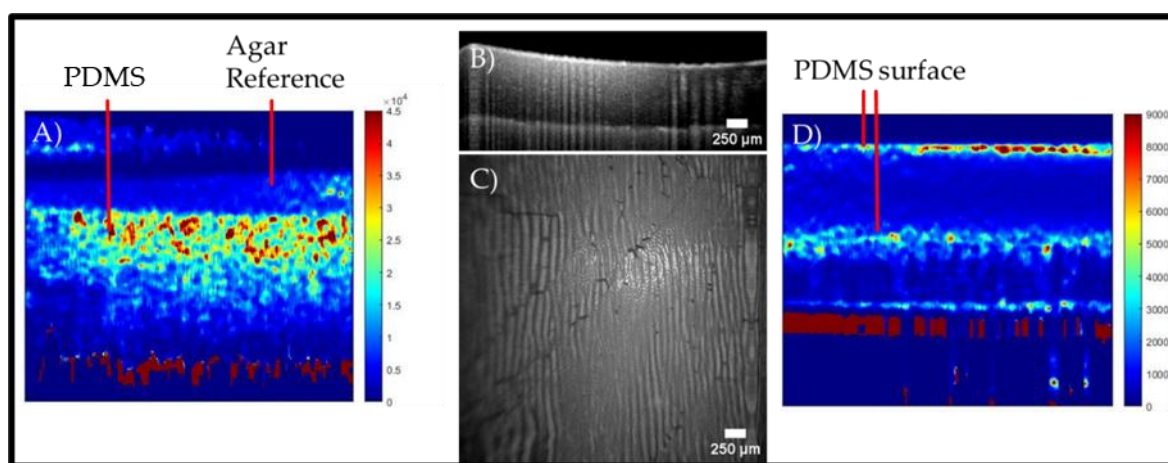


Figure 4.26: OCE of 3.33% dual-treated wrinkled PDMS. A) OCE elastogram of wrinkled PDMS where an agar reference was applied to the surface. B) Structural OCT cross-section of dual-treated PDMS C) en-face reconstruction of volumetric OCT scan of dual-treated wrinkled surface ($n = 4$). D) OCE elastogram of wrinkled PDMS without agar reference was applied to the surface, showing comparative surface stiffness resolution ($n = 2$ for both referenced and unreferenced). Scales on elastograms are relative to their respective images and represent $1/\text{strain}$. Scale bars in structural OCT images = $250\mu\text{m}$.

4.4 DISCUSSION

4.4.1 Bioreactor Design

In this chapter, the design and development of a compact bioreactor system has been explored. The development process featured multiple iterations to produce the 'final system'. The criteria for the ideal system were threefold: 1) sterility and practicality, 2) anatomical biomimicry and 3) surface biocompatibility.

In the context of bioreactor design, criteria 1) was the principle of concern. The foremost priority was to develop a material manipulation system for each substrate type which could fit into a conventional culturing vessel. Primarily the reason for this was to ensure the culturing environment was guaranteed sterile using conventional culture plasticware (Corning). Following the development of the acid-oxidized and dual-treated substrates, to replace the less effective laminated block method, a different mechanism for applying mechanical force was required. The main motivation for this development was the fact that the topography generation was dependent on the base substrate being stretched before surface treatment, and the subsequent formation of the topography upon relaxation of the substrate after treatment. This condition contrasts with the laminated blocks which form topography only upon compression, to then return to a flat surface upon relaxation. Another requirement of this particular frame design was that it had to be durable enough to withstand the rigours of acid oxidation and oxygen plasma treatment during the material modification stages of bioreactor preparation. With this considered, 316L stainless steel was opted for as the preferred material of choice as it displays anti-corrosion properties and is widely used in industrial applications but also features in biomedical applications due to this corrosion resistance (*Shih et al., 2004*). Coupled with this consideration, using

316l enhanced the capability of these frames by permitting the autoclaving of the treated substrates, whilst attached to the frames. Using one-step autoclaving not only shortened processing time but also conferred a greater degree of biological safety (when compared to the 3D printed frames) through more effective decontamination of both the substrates and bioreactor frames before culture.

In this transition of approach with the application of the bioreactor frames from compression to tension format, the approach used in the production of the material changed too. In the compression bioreactor approach, using the laminated blocks, two separate materials were produced: the polymer membranes and the PDMS bulk which were adhered together using adhesive. This approach did not yield a substrate fit for prolonged cell culture as visible delamination (membrane detachment from the block) and the compressed blocks were immersed in aqueous solutions. This delamination meant the compression bioreactor configuration could not maintain a wrinkled topography, therefore warranting the change in approach. The tension bioreactor configuration was subsequently developed, using the stainless steel frames and specially moulded PDMS chips. The PDMS chips were cast into moulds designed to fit the arms of the tension frames and 0.5mm thick by 20mm long by 10mm wide with a central working area of 10x10mm. These chips were used to develop the final dual treatment substrates through the evaluation and subsequent amalgamation of the oxygen plasma and acid oxidation PDMS treatment methods. Individually the plasma treatment and oxygen plasma treatment did not produce topography which was biologically representative of the LESC niche however, both methods of production were stable in terms of wrinkle retention and balanced by a middling substrate preservation during production. However, despite the observed failure of substrates during production (counted by producing excess substrates per run), these qualities

were considered especially advantageous when compared to the performance of the laminated blocks, which presented a near total substrate failure after submersion with compression and thus could not maintain a wrinkled topography, a feature the newer generations (plasma and oxygen plasma treatment) of substrate were able to maintain despite immersion and physical handling. The dual treatment substrates were trialled to amalgamate the best of the morphological features (improvement of wrinkle collimation, whilst maintaining biologically relevant dimensions) but preserve the manufacturing, handling and application perks that the chip-based approach presented in comparison to the compression-based method. In terms of manufacture all types of substrates, regardless of compression/tension approach, were produced by hand in small batches in numbers ranging from $n=3$ to $n=12$ maximum (mould, frame and membrane availability dependent). Whilst suitable for the nature of the preliminary nature of this project the small scale production of the substrates can be upscaled, however, this could not be achieved by the practical means described in this project. If the dual-treated chips were to be scaled up to an industrial/commercial scale of production then automation, involving mechanical elements to apply defined substrate tension, acid exposure and quenching steps with online monitoring of bath pH would be required to ensure precisely repeatable substrates could be produced. In hindsight, pH could have been tested regularly to ensure the treatment acid was consistently at the same pH and therefore imparting the same level of oxidation on the substrates. Additionally, measuring the pH after a treatment and monitoring the pH of the treatment acid (if there is a change) could be a preliminary indicator of effective treatment of the substrates, particularly as a quality control measure in the dual treatment process. Staged treatment processes should be kept in the same production room, ensuring contaminants are not introduced by transfer and reducing the risk of adverse incidents.

The system possessing the ability to fit into a 6-well plate was advantageous for experimental setup, due to the enabling of multi-condition and multi-replicate experimental arrangements over a minimal footprint (in comparison to larger footprint bioreactor setups which are commercially available). Examples of such commercially available systems include the systems offered by the CellScale mechanoculture series (CellScale, 2023). The 6 well-contained bioreactor frame setup developed in this research was comparable to the integrated flexible bottomed-plates of the Flexcell tension system (Flexcell, 2023), though it should be noted that the Flexcell systems (both tension and compression) when assembled have a larger footprint than an individual 6-well plate. Therefore the presented bioreactor frame setup is more advantageous due to increased incubator accessibility, increased device manoeuvrability and the setup possessing the ability to be viewed on a standard dissecting microscope to easily view the cells without needing device alterations. Additionally, the presented substrate system has a considerable advantage over systems such as the Flexcell, in which the culture substrate itself has the biomimicking topography which can be directly mechanically altered with a high degree of control. In contrast, the Flexcell, or similar vacuum-based deformation systems, can only impart mechanical deformation on a monolayer culture directly or indirectly onto material radially at best.

In tandem with the spatial footprint, the ability to sterilise/disinfect the bioreactor frames was paramount for their use in cell culture. Therefore the materials used had to (as a minimum) resist 70% industrial methylated spirit (IMS) for 40 minutes and then be cultured in a medium without obvious degradation or corrosion. The compression frames in the laminated block setup satisfied this requirement for disinfection before use, due to the use of 3D printed components which could not be autoclaved. When

the stretched chips were implemented, a full stainless-steel frame was designed and implemented. 361L stainless steel (and the alternate grade 304 for the bolts due to material availability) was considered the best compromise for workability and resistance to chemical corrosion, being utilised in the manufacture of medical implants (*Shih et al, 2004, Brooks et al, 2017*). The parts made completely from stainless steel were able to be autoclaved for a more assured degree of sterility compared to the state of disinfection realised using 70% IMS.

4.4.2 Material Production

In this chapter multiple substrate preparation methods were described. These ranged across vastly different methodologies, hence the differences between the laminated blocks and wrinkled PDMS chips, and the more subtle difference between the wrinkled chip methods. During the initial material optimisation stages, the selection of materials/material property analysis was performed to ensure the selected materials would perform as desired and satisfy the simple wrinkle model as discussed in Chapter 1. The compression testing of a gradient of PDMS which was formulated with different concentrations of curing agent, ranging from 2.5% to 10%. All of the tested fractions were able to satisfy the criteria of the simple wrinkling model, considering all formulations were maintained within the kilopascal range, which is concurrent to the lower range of measurements acquired for PDMS formulated with a lesser amount of curing agent (*Wang et al., 2014*).

It is appreciated that the results for mechanical testing of PDMS acquired in this chapter are at least an order of magnitude lower than results attained in the wider field (*Wang et al., 2014, Fitzgerald et al., 2019, Helgason et al., 2022*). Across these studies, the range in PDMS stiffness can vary from $\sim 0.1\text{MPa}$ to a maximum of 3.7MPa where

all observations across the variables within these studies fit within this narrow range. This deviation from the canonical results may be explained by the age/fatigue of the Bose Electroforce load cell used at the point of acquisition for this data set in Figure 4.4, which may explain the systematic error present in the data series acquired using this instrument. In reflection, if the opportunity to repeat the dataset on the Testometric machine was presented, then an inter-machine comparison could be drawn. However, despite the order of magnitude difference, the increase of stiffness from 0.239 ± 0.051 KPa (2.5% curing agent) through to 3.5 ± 0.6 KPa (10% curing agent) follows the expected trend. This trend is corroborated in studies that vary the curing agent concentration and determine the mechanical properties (*Wang et al., 2014, Yan et al., 2022*). However, the tension testing performed on PDMS chips subjected to the different treatment methods used the testometric system with the 3.33% PDMS formulation. The Young's moduli output for these tests was within the Kpa ranges for this formulation, concurrent with other research investigating the mechanical properties of PDMS (*Wang et al., 2014*) Tension testing of the fabricated membranes served two purposes, first and foremost was to assess whether they were mechanically suitable (by satisfying the requirements of the simple wrinkling model) to generate wrinkles when laminated to the PDMS blocks. Secondly, the elasticity of the membranes would serve as a subjective quality control for the membrane fabrication process. If the membranes were too brittle and could not stand up to a tension test, they may fracture on compression conversely if they were too elastic, they may not wrinkle correctly. Fortunately, both membrane types (PLGA and PCL) satisfied both of these criteria, exhibiting respective Young's moduli of 195 ± 52.4 KPa and 75.6 ± 40.0 KPa respectively, meaning that these films were stiffer than the PDMS bulks intended to be used for form wrinkled substrates in the laminated block method (maximum measured

3.5 ± 0.6 Kpa for 10%), therefore satisfying the conditions for the simple wrinkling model as outlined in section 1.6.5.

However, with consideration of Young's modulus found for PLGA film, another study which used the same solvent casting technique, measured the modulus of the membranes as 3.5 ± 0.2 GPa (*Shirazi et al., 2014*). The tension testing for the polymer films in this chapter should be appreciated as relative comparisons instead due to the consistently lower values attained as observed in the PDMS samples. In another study applying an alternate membrane production method, but a similar tension testing method, a lower value for Young's modulus was attained in a range of ~0.2--~0.8GPa (*Abbasnezhad et al., 2021*). Though this range of moduli is lower than the Shirazi et al. study this range highlights the disparity between the range of PLGA membrane stiffness in literature in comparison to the stiffness determined using the presented method. Although the PCL value attained in this study was found to be lower, it is within the same order of magnitude when compared to similar fabrication methods. For the solvent casting method, this study determined a modulus of 0.2623 GPa for PCL films (*Tiaw et al., 2007*). In comparison to PLGA, this stiffness is overall lower if all ranges are considered, this observation is consistent with the observed lower modulus of PCL attained in comparison to PLGA using the presented method. The cause for the observed discrepancies in this membrane dataset is considered idiopathic as the approach used followed a standard approach to tensile testing and current repeats were consistent. Importantly, specific tensile strength ranges were not targeted (or relevant) in this application. The significance was in determining the performance between the samples tested. Future investigation of these materials and their characterisation in this application may necessitate greater calibration in the materials testing.

The laminated block methodology should be appreciated as a good starting point in the development of a wrinkled substrate topographical model for generating a simple biomimetic limbal palisade of a Vogt-like structure. Multiple studies use imaging techniques including confocal microscopy to evaluate and resolve the shape structure of the limbal niche (*Grieve et al., 2015, Shanmuganathan et al., 2007, Patel et al., 2006*). They demonstrated the undulating structure, thus reinforcing the necessity for the undulating waveform produced by wrinkled surfaces (*Dimmock et al., 2022*). In terms of a reference value for the dimensions of crypt morphology, crypt width ranges from 35 μm to 120 μm have been measured in human tissue (*Grieve et al., 2015*). For a depth reference, another study which utilised optical coherence tomography to depth-resolve tissue found crypt amplitude to approximately ~ 50 μm in depth (*Bizheva et al., 2017*). From these reference values, it was possible to compare these references to the values output by the OCT imaging of the laminated block substrates. The laminated block average widths of 194.8 ± 43.4 μm and a height of 39.5 ± 5.1 μm for PLGA laminated blocks and a width of 72.4 ± 22.2 μm and a height of 14.2 ± 2.4 μm for PCL laminated blocks at 10% applied compression. These values fall slightly outside of the reference values covered in Chapter 3, with the lateral width being slightly too large for PLGA laminated blocks, however, the PCL laminated blocks do fall within the reference range for crypt width. In terms of depth, PLGA laminated blocks are closest to the desired reference value of 50 μm , while, PCL falls very short (*Grieve et al., 2015, Bizheva et al., 2017*).

Furthermore, the laminated blocks presented a useful trait where the amount of compression applied can change the morphology of the wrinkles. Uncompressed the substrates are flat, but under compression, the substrates begin to yield and wrinkle. As shown in Figure 4.7 the increase in compression, from 10% to 20% original

substrate width had changed the morphology of the wrinkles subtly, however, these changes were not statistically significant, as tested using ANOVA. Such compliant behaviour has important uses as a disease model and would have allowed the substrate to be employed in a dynamic scenario, with potential for inflammatory/LSCD modelling, improving upon current static limbal modelling such as the RAFT method (*Levis and Daniels, 2016*) and membrane methods (*Li et al., 2017, Deshpande et al., 2013 and Ma et al., 2010*). Where these methods presented good biomimicry of the limbal niche in the static form by forming well-defined crypts for LESC containment (*Levis and Daniels., 2016*) and the mimicry of the native matrix surface for limbal progenitor cultivation and expansion (*Deshpande et al., 2013, Li et al., 2017, Ma et al., 2010*).

However, despite the apparent benefits, including ease of material-to-compression rig assembly, obvious wrinkle generation and wrinkle tuneability, there were significant practical drawbacks encountered using this methodology. First and foremost of these drawbacks was the observed delamination of the adhered membranes from the bulk blocks which presented an insurmountable challenge. The reason this was such a challenge was the glue used must retain elastomeric flexibility similar to the bulk PDMS to facilitate wrinkling. Otherwise, the simple wrinkling model would be violated due to the interstitial interface of a stiffer medium in between the flexible bulk and the stiff membrane (*Li et al., 2012, Cerda and Mahadevan, 2003, Cai and Fu 2012*). Such changes in conditions would unpredictably change the wrinkling produced due to stress-shielding imparted by the glue (if wrinkling is possible). A comparison of such mechanical defects can be related to the effects of stress concentrations of modified material structures as simulated in silico by (*Murru and Rajagopal, 2021*) and visualised microscopically in metals with different grain defects

by (Robertson *et al.*, 1991). Identifying alternative glues to the tried-and-tested silicon adhesive proved a challenge as many commercially available glues are not compatible with plastics or adherent to silicone, this is in part due to solvent interaction degrading the membranes or the inability of the glue to form the necessary chemical bonding between the two structures to be bonded. Further compounding this point, glues which had a chance to adhere to PDMS such as cyanoacrylates (and similar compounds) and epoxies formed very stiff, (if not solid) glue layers, which completely inhibited wrinkle formation.

The second drawback to the initially designed system design was the question of sterility. Though the 3D printed parts were a benefit to the project in terms of being able to rapidly produce custom-formed parts which prevented block slip upon compression, there were incidences of contamination. Whilst 3D printed culture-ware features in other sections of this thesis and did not present contamination during culture, the compression arms (possibly due to their design) may have contributed to the increased risk due to assemble complexity and the inclusion of small semi-enclosed ridges increased the risk of contaminant inclusion in the material. The study by (Popescu *et al.*, 2021) highlights this well, showing decontaminant penetration in defect spaces, therefore the same risk of penetration can be assumed for biological contaminants before disinfection protocols. This issue was addressed in the design of the stretching rigs which were designed out of autoclavable stainless steel. Having considered these risks it was decided to switch to wrinkling the PDMS itself.

The adoption of the methodologies to wrinkle the PDMS itself took significant consideration and followed an iterative development pathway. It was already appreciated that the PDMS could be deformed and wrinkled to produce narrow wrinkles using oxygen plasma exposure (Glatz and Fery, 2018) and the use of oxygen

plasma-treated PDMS in direct cellular study (*Amerian et al., 2019*). However, the issue with this wrinkling method was the fact that the wrinkles were so small (up to a maximum of $5.68 \mu\text{m} \pm 3.07 \mu\text{m}$) that they would not be able to contain a single cell, though they may be able to facilitate cellular morphological or behavioural alterations. In this chapter and literature, the plasma-generated wrinkles fall very short of the desired crypt dimension range ($35 \mu\text{m}$ to $120 \mu\text{m}$ wide by $\sim 50 \mu\text{m}$ deep) as dictated by (*Grieve et al., 2015 and Bizheva et al., 2017*) and the measurements made of the human crypts in chapter 3.

Therefore, the other adopted methodology was considered, the wet chemical oxidation method. This method operated similarly in principle to the oxygen plasma method, using stretched substrates and exposing the PDMS substrate to the stiffening protocol. In this case, the sulphonic acid was doing the work. This produced wrinkle patterns which were more in line with the desired dimension. However, the wrinkling patterns were not stable. These findings were not consistent with the desired results as observed in the study by Watanabe and Mizukami *which* demonstrated an ability to produce intentionally well-ordered linearly aligned wrinkles (*Watanabe and Mizukami, 2012*). However, in practicality, the generated acid-oxidized (alone) topographies featured in this chapter, whilst exhibiting a degree of linearity, resemble the randomly ordered surface topography which appears to be more typically attributed to wet chemical methods (*Watanabe and Hashimoto, 2014 and Yin et al, 2014*).

The final optimised methodology settled upon, at the apex of the development process, was the dual treatment method. This method is an amalgamation of the previously discussed surface oxidation methods in sequential treatment steps. This method employed the stainless steel stretching arms in all phases of preparation; wrinkle formation, sterilisation and cell culture. The stainless steel arms which were

produced at this stage of development also facilitated further material characterisation. This is discussed in more detail subsequently. The topography generated by the dual treatment method was by far the most consistent generated so far in terms of feature shape and utility; provided the PDMS chips survive the protracted surface preparation process. The dimensions of which could reach the desired ranges in terms of both width (45.51 μm – 145.9 μm) and depth (12.46 μm – 49.4 μm) across the different curing agent concentrations (Grieve *et al.*, 2015 and Bizheva *et al.*, 2017). In the preparation of the substrates for any experiment/observation, an excess of substrates had to be prepared to account for the material failure by the chips snapping during treatment and sterilisation. However, it is important to note that after plasma treatment was completed, the likelihood of chips snapping was minimal and likely due to handling during (and after) sterilisation in the autoclave. It is also important to acknowledge that due to the superior ordering of the wrinkled features and handleability of surviving samples, the dual treatment wrinkled PDMS facilitated the dynamization of the substrate enabling *in situ* alteration of topographical features. This alteration of topographical features, namely the flattening of the features enables this substrate, in conjunction with the bioreactor frame to be used in LSCD modelling as the *in situ* “loss” of wrinkled features imparted by re-stretching matches niche anatomical degradation observed in LSCD.

4.4.3 Material Characterisation

This section considers the various methods of characterising the materials used, composition analysis and the subsequent generated wrinkled topographies are discussed. It is established that each of the different wrinkling methods produces different wrinkle characteristics. The smallest wrinkles by far were the plasma-treated

wrinkles whose widths were in the order of 10s of micrometres. This meant that whilst these surfaces may have cellular effects, including increased cell attachment and surface-guided cellular alignment, as ascribed to in other studies (*Mwale et al, 2006, Amerian et al., 2019 Gehlen et al., 2019*) they do not have the appropriate magnitude for sole use in limbal cell study. Though it can be said confidently, as established in atomic force microscopy and scanning electron microscopy, the features formed by plasma treatment were the most consistent and ordered, a trait not common to the other PDMS treatment methods.

Moving up to the next scale of magnitude, the dual treatment and the acid-oxidized surfaces were comparable, aside from the apparent differences in surface feature consistency and order. The wet chemical-treated surfaces were the most random ordered, complementary to the observations in other acid oxidation studies (*Watanabe and Hashimoto, 2014 Yin et al, 2014*). Due to the observable highly variable nature of the produced features by the wet chemical method, it was determined that further optimisation of the exposure method was required. This manifested in two major improvements to transition towards a more standardised process. The first was the development of a chip and mould regimen, PDMS substrates were cast in moulds as visualised in Figure 4.2 and pre-strained using the stretching frames as shown. The second optimisation was the manner of exposure, the chips were fully immersed in the sulfonitric acid (allowing full material surface coverage), followed by a neutralisation step (included for safety) then quenched in a large water bath. The outcome of these process optimisations was a distinct overall visual improvement in feature homogeneity. Whilst it can be confidently said that the homogeneity occurred, there was still a heavy presence of bifurcating wrinkles and there was directional randomness manifesting in lateral intersecting wrinkles. However, there is no

retrievable application or usage of a dual treatment using wet chemical and oxygen plasma treatment of PDMS in the literature.

Though the testing and analysis are in the preliminary stage for wrinkled PDMS material, the OCE revealed there was some detectable regional difference in stiffness between the surface and the bulk in non-referenced captures. This was not observed when the agar reference was applied to the surface, which yielded a more homogenous result for the distribution of stiffnesses but was able to yield an accurate average modulus for the tested material for this set: 97.3 ± 47.5 Kpa, which is close to the attained value for the testing of the untreated PDMS chips for the same PDMS composition, as determined in Figure 4.23 using the Testometric machine. Therefore there is promise in this technique for detailed structural and mechanical material analysis with future calibration/acquisition optimisation work.

As a pre-assessment of cytocompatibility, the water contact angle of the materials employed was tested. The hydrophilicity of a material is a general indication of how well cells may adhere to a particular surface, the greater the hydrophilicity, the lesser the repulsion of aqueous substances. In general terms, this effect may result in a greater adhesion of cells to the surface of interest (*Ferrari et al., 2019*). Both polymer membranes had a lesser water contact angle compared to all of the PDMS samples, meaning that both PLGA and PCL are more hydrophilic than the PDMS. PCL has the greatest affinity to water, which concurs with the current understanding of the hydrostatic properties of these materials (*Gümüşderelioğlu et al., 2011, Kaga et al., 2021, Feng et al., 2008*). The water contact angle test also confirms that oxidative reaction has taken place, as changes to the water contact angle are in positive correlation with observations in other studies (*Lawton et al., 2005, Kim et al., 2004*). Interestingly, among the PDMS treatment group, the plasma treatment affected the

greatest reduction in the water contact angle (with the greatest) variability whilst the acid oxidation and dual treatment effect had similar results. It is proposed that the larger topographies in the acid-oxidized and the dual-treated groups interfere with droplet spreading, truncating the water contact angle result.

To determine the composition of the surface of the materials tested, (particularly the treatments applied to PDMS), surface chemical analysis methods were employed to characterise the surface chemistry of each sample. The first objective of this approach was to observe chemical alterations between each treatment type. Subsequently, to infer whether these bond alterations (detectable by Raman spectroscopy) and elemental alterations detectable by SEM EdX (scanning electron microscopy -dispersive x-ray spectroscopy) could be attributed to the observed surface properties. For bond compositional change Raman spectroscopy was used, where significant peaks (which presented high intensity/cps) were observed in all groups at ~ 1400 , ~ 1250 , ~ 860 , ~ 780 , ~ 620 and $\sim 490\text{cm}^{-1}$ with double peaks at ~ 2960 - 2910 , ~ 150 - 200 and ~ 670 - 720 cm^{-1} . These spectra are comparable to existing profiles of untreated PDMS, the bonding profile shows predominantly $-\text{CH}_2/-\text{CH}_3$ with silicon bonding at ~ 1250 and ~ 1400 (Yadhuraj *et al.*, 2018, Bokobza *et al.*, 2015). It is observed that the dual-treated substrates exhibited a greater averaged intensity across the entire profile compared to all other groups, however no changes in bond composition were detected. It is proposed that the dual effects of acid oxidation and thin oxidized layer formation in oxygen plasma treatment confer a unique optical property which has resulted in a more intense overall Raman spectrum for the dual-treated group. In EdX analysis, the unit % elemental presence atomic is used (as defined in the Oxford Instruments software), this is a measure is the ratio of elemental atomic species detected within a spectral analysis point. It was found that there were

compositional changes detected across the PDMS chip treatments. In acid-oxidized and dual-treated PDMS, there was an increase in elemental sulphur found, with elemental atomic presences of 0.098% and 1.515% respectively. Whilst present in very low amounts, it could be inferred that there was a degree of immobilisation of sulphuric acidic species into the material surface. Interestingly the % elemental presence atomic for oxygen (the potential metric for degree of oxidation) (as defined in the Oxford Instruments software), measure is the ratio of elemental atomic species detected within a spectral analysis point varied between treatment processes. The greatest amount of oxidation was found in the wet chemical sample (55.993%) compared to the lowest which was the plasma-treated surface (43.153%). Dual treatment was determined to be in between these values (46.695%) but still lower than the control (untreated PDMS). These findings for the composition of the oxidised PDMS in comparison to untreated PDMS currently conflict with existing studies (*Sola et al., 2018, Adly et al., 2017*) but should be appreciated as preliminary findings and require further investigation. There was an expectation that the treatments singularly each should have increased oxygen presence. In line with this assumption, it was hypothesised that the dual treatment, being a dual treatment approach, should have increased the % elemental presence of atomic oxygen substantially. It should be noted that these EdX are averaged measurements taken from singular samples so future work could incorporate a greater range to assess whether oxidation of the PDMS surface is accurately quantifiable with available equipment.

4.5. CONCLUSION

In this chapter, the generation of multiple wrinkled surfaces using a variety of mechanisms has been explored. Following further investigation into the novel chip-based methods, it was validated that the wrinkling phenomenon was able to be

exploited to generate a topography which was relevant to limbal niche study. Here the material properties of the substrates have been scrutinized mechanically and chemically for their biological relevance in the biomimicry of the limbal epithelial stem cell niche. The characterisation of the PDMS showed that there were discernible changes to the surface of the PDMS imparted by the treatment methods. The water contact angle showed an increase in hydrophobicity, whilst tension testing showed changes to overall chip stiffness. Spectroscopic analysis using Raman and EdX yielded preliminary results that show, in particular, dual treatment was able to affect the surface composition of the PDMS with a largely increased peak around the $\sim 490\text{cm}^{-1}$ region (Si-O-Si stretch) indicating increased oxidation. EdX showed interestingly the presence of immobilised elemental sulphur in substrates wrinkled using acid (acid-oxidised and dual-treated). From these analyses, it can be determined that the “chip and stretching frame-based bioreactor system” coupled with PDMS undergoing the dual treatment protocol exhibited the most favourable properties for a limbal-biomimetic culturing system. This was determined through the dual treatment giving wrinkle width ranges of (45.51 μm – 145.9 μm) and depth ranges of (12.46 μm – 49.4 μm). These crypts were shown by OCT to have reversible qualities, demonstrating the capacity to be flattened and re-present wrinkles using the bioreactor system designed specifically for this application.

Chapter 5: Characterisation of the Cellular Response to Wrinkled Topography

Content from this chapter features in the publication: "Fabrication and Characterisation of Hydrogels with Reversible Wrinkled Surfaces for Limbal Study and Reconstruction" (Dimmock et al., 2023)

5.1. INTRODUCTION

The limbus is a unique anatomical structure located circumferentially around the central cornea. This feature is presented as a wide epithelial crypt that encircles the cornea. As described and structurally characterized in Chapter 3, this region comprises the structurally unique undulations known as the palisades of Vogt (POV). At the troughs of the POV reside the epithelial rete pegs (ERP) and at the crest, the palisade ridges (PR). This chapter focuses on determining the response of primary isolated limbal epithelial stem cells (LESCs), which are known to reside in the ERP (basal of the POV structure), with exposure to the wrinkled substrate system (*Schlötzer-Schrehardt and Kruse 2005, Vermunganti et al., 2009*). The LESC cells expand out of this niche to regenerate the cornea, first explained through the long-standing XYZ hypothesis (*Thoft and Friend., 1983*), then demonstrated practically using lineage tracking methods (*Meller et al., 2002; Song et al., 2005, Sartaj et al., 2017*).

LESC cell isolation and maintenance in culture face a set of specific challenges which is inherent to the cultivation of primary epithelial cells. First and foremost, these cell types require rigorous enzymatic extraction (*Gonzalez et al., 2013, Colanesi et al., 2015*). It is appreciated that a coupled enzyme digestion approach would be required to optimally break down the collagen-rich matrix and facilitate single-cell isolation, enabling monolayer expansion (*Polisetti et al., 2020*). Secondly, the cells demonstrate a tendency to lose their stemness in culture over time, despite the strategy employed to maintain the stem cell phenotype. Through assessment of markers such as the ATP-binding cassette transporter G2 (ABCG2) (a marker for LESC stemness) it was determined that even in optimised cell extraction, the extracted cells eventually committed into an epithelial phenotype (*Colanesi et al., 2015*). Other strategies include the optimisation of surface coatings, such as using amniotic membranes and amnion

preparations, where stemness was assessed by monitoring the positive stem cell markers p63 α and Δ Np63 (Karami et al., 2021, Bisevac et al., 2023)

5.2 MATERIALS AND METHODS

5.2.1 Limbal Cell Isolation, Expansion and Cell Culture

5.2.1.1 Limbal Cell Isolation

Before sterilisation, the tissue was dissected into quarters to isolate the limbal POV regions of interest for cellular isolation. In the human tissue, this was done by identifying the POV using polarised microscopy (ref. Chapter 3) and sectioning with a scalpel, in porcine tissue this was undertaken using the Thorlabs OCT equipment (ref. 2.2.1.3).

Porcine tissue was subjected to a triple stepwise antibiotic sanitization using 125 μ g/ml Amphotericin B (Gibco), 500 μ g/ml Gentamicin (Gibco) and 500 units/ml (5%) Penicillin Streptomycin (Lonza) for 1 min per wash, interspersed with PBS washes each in a clean well to remove the antibiotic. Human tissue did not require sterilisation as the tissue was subjected to serology testing at the tissue bank before delivery.

For porcine tissue, The eyes were obtained as whole globes from the abattoir (Staffordshire Meat Packers) within a maximum of 48 hours of slaughter. The eyes were transported in a high-antibiotic medium to pre-sanitise the eyes, (high glucose DMEM (Gibco)) containing 1000 units/ml penicillin/streptomycin (Lonza). The globes were transferred to a biological safety cabinet for dissection. All loose tissue was

initially removed, followed by the isolation of the corneoscleral button. The isolated button was debrided of the dark tissue and the lens was removed followed by thorough washing with sterile PBS. Subsequently, the buttons were transferred into the dedicated OCT vessel for LESC niche identification. Once the regions containing the limbal POV were identified the tissue was cut into quarters using a scalpel, and the pieces containing the LESC niches were retained to be sanitized with antibiotics.

Following quartering and sanitization (if necessary), the tissue was subjected to a 2-step enzyme-based cellular isolation process. The first step employed Dispase II (Sigma, UK) at 1.2 IU/ml, incubated at 37 °C for 2h, to loosen the limbal epithelial tissue to ease debridement. The debrided epithelium was then incubated in 1 mg/ml Collagenase A in a complete culture medium at 37 °C for 14-18h, with microscopic observation in the final 4h to ensure optimal cellular isolation. At this stage, the cellular/enzyme suspension was diluted 1:5 and centrifuged at 250 g for 5 min, and then the supernatant was completely removed to extract the enzyme. The cells were transferred to a 6-well plate for passage 0 outgrowth.

Once the cells were established to be growing by microscopy or using live cell imaging (sections 2.2.6.1 and 2.2.6.3) and nearing confluency the wells were trypsinized to passage 1 for routine sub-cultivation in 1X trypsin (Gibco) for 3 -6 min, at 37 °C with the application of a cell scraper used for colonies (typically for porcine isolates). Trypsinization was quenched using an equal volume culture medium. The passage 1 cells were centrifuged at 250 g for 5 min, the supernatant removed, resuspended in 1 ml, and then transferred into a T25 flask after counting. In single cell type culture, limbal cells were typically seeded at a density of 8K cells/cm² and passaged every 6-8 days. For immunophenotyping in well plates, cells were passaged

and seeded at 30 K cells/cm², with density adjusted for each well size, for both human and porcine cells.

For cell expansion, cells were cultured in DMEM/F12 (Gibco, UK) containing 10% foetal bovine serum (Corning, UK), 1 µl/ml of 100x insulin transferrin selenium solution (Gibco, UK), 100 U/ml penicillin/streptomycin (Lonza, UK), (2 mM L-glutamine (Gibco, UK), 2.43 µg/ml adenine (Sigma, UK), 0.4 µg/ml hydrocortisone (Sigma, UK) and isoproterenol 1 µg/ml (Sigma, UK). For the in-house *versus* commercial medium comparison, the extracted cells were cultivated in CNT-Prime Epithelial Proliferation Medium (CellnTec, Switzerland).

5.2.1.2 Co-Culture with 3T3-J2 Mouse Fibroblast

Extracted limbal cells were co-cultured with the 3T3-J2 mouse fibroblast cell line in the endeavour to preserve stemness and provide a native-like environment in vitro using 3T3-J2 acquired as a frozen cell line (AddexBio, USA). “Active 3T3” cultures were passaged by trypsinization with 0.5x trypsin for 3 minutes at 37 °C with 10x repeated rinsing of the flask culture surface to dislodge the cells. Full cellular dislodging was verified microscopically, quenched with equal volume culture medium and centrifuged at 1200 rpm. Cells were re-seeded at a ratio of 1:6 in the T75 flask for banking and preparation for inactivation. Once cells reached 70-90% confluency in selected flasks they were inactivated to prevent proliferation using mitomycin-C (Sigma, UK), in a working concentration of 10 µg/ml in a culture medium. 10ml of the inactivation medium was applied to each designated “inactivated” flask for 2 hours. After the inactivation period, the cells were washed 3 times with PBS and then trypsinized as per regular passage. Cells were counted and seeded in the destination vessel at 2x10⁴ 3T3 cells/cm². If not immediately used at the point of inactivation, cells

were cryopreserved in 10% DMSO/culture medium and placed into -80°C storage (before being transferred to liquid nitrogen for long-term storage). Inactivation of 3T3 cells was performed 24h before limbal cells were seeded, the inactivated 3T3 monolayer was visually inspected to ensure no further expansion of the 3T3 monolayer has been observed. Limbal cells were typically seeded onto the at 4×10^3 limbal cells/cm² in co-culture at a ratio of 2:1 limbal cells to feeder cells and passaged every 6-8 days. The 3T3-J2 cells were cultivated in high glucose DMEM (Gibco) containing 10% calf serum (ATCC, UK), 100 U/ml penicillin-streptomycin and 2mM L-glutamine.

5.2.1.3 Limbal Cell Culture with Wrinkled Substrates.

This chapter describes the two ways the dual treatment wrinkled substrates were used in culture, the static method and the dynamic method (see Figure 5.1). The static method was a pure contact-guidance method whereby the cells were seeded on a pre-wrinkled topography compared to the dynamic method where the cells were seeded on a flat surface (overnight for porcine droplet culture and 3 days for human immersion culture) and then the wrinkles were introduced. Subsequently, the wrinkles were altered *in situ* to be flattened. These changes in the topography state, while the cells were attached were a source of mechanical stimulus. Cells were seeded on the substrates at numbers between 20-60K cells/substrate, equivalent to 15-30 K cells/cm². When investigated, the acid-oxidized treatment followed the static method only due to the inability of the surface to facilitate a returnable surface.

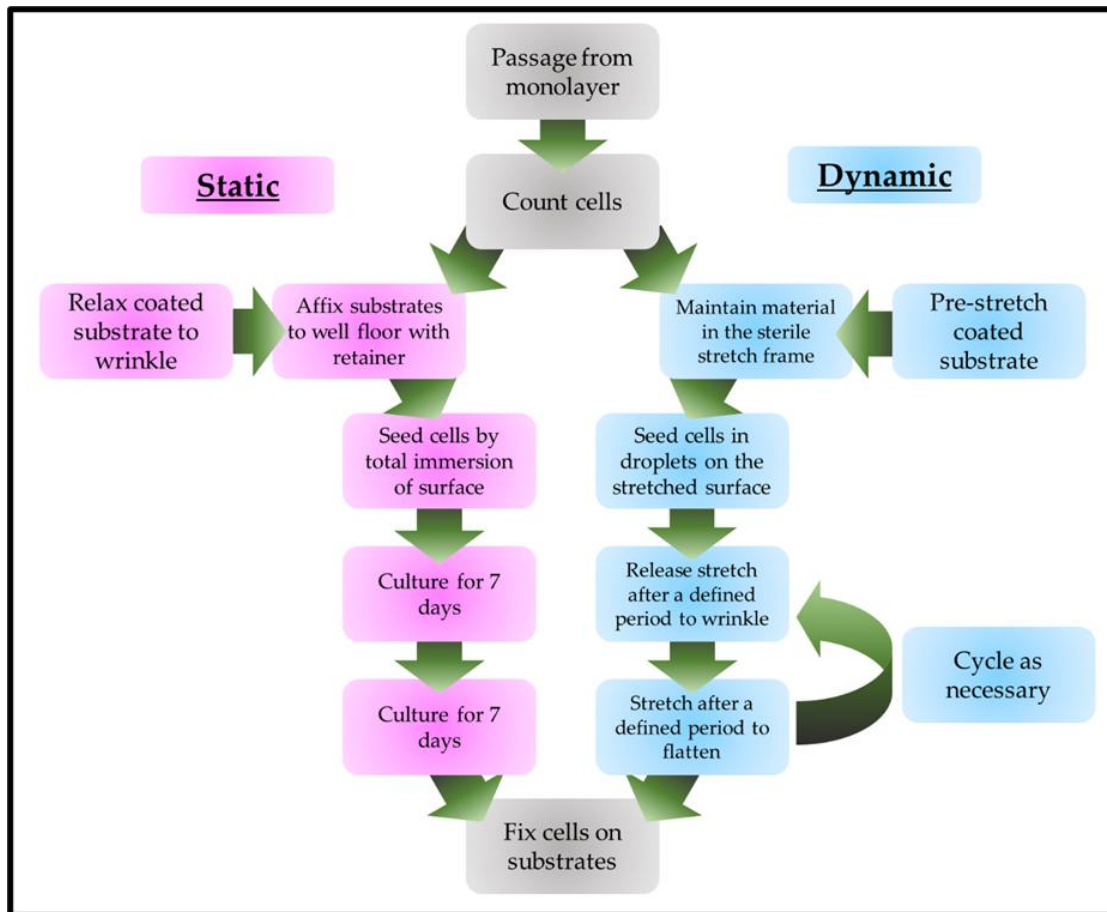


Figure 5.1: Schematic comparison of the static and dynamic wrinkled substrate culture processes. This diagram compares the culturing processes between static and dynamic wrinkled substrate cultures.

In all cultures, the PDMS was sterilized by autoclave, and dual treatment substrates at this stage were maintained on their stretching frames to facilitate coating before wrinkling/cell seeding. In static culture, cells were typically seeded at 30 K/cm². For dynamic culture, the droplets were seeded at 100 K/25 µl droplet for 1-5h

5.2.1.4 Culture of Rat Cardiomyoblasts

Rat cardiomyoblasts were kindly donated from the Dr George research group within the Guy Hilton Research Centre at Keele University. For expansion, the cells were primarily cultivated in uncoated T25 flasks. The basal medium used was DMEM

(Gibco, USA) supplemented with 10% foetal bovine serum (Corning, UK), 100 U/ml penicillin/streptomycin (Lonza, UK), 20 mM L-glutamine (Gibco, UK) and 2% B27 supplement (Thermofisher Scientific, UK). The cells were passaged at 60-90% confluence by trypsinization in 1% trypsin for 3 minutes at 37 °C with agitation of the flask after the incubation, the digest was quenched with an equal volume of FBS-supplemented medium before centrifugation at 1200 rpm for 3 minutes. The flasks were seeded at 250K cells/flask after passage. The cultures were passaged every 4-6 days. Rat cardiomyoblasts were typically seeded onto substrates at 20K cells/cm² and substrates were coated with vitronectin (Sigma) made up to 1:5000 dilution in PBS and incubated overnight before culture.

5.2.1.5 Cultivation of HEK-293 cells

Human embryonic kidney–293 (HEK-293) cells were kindly donated from the Dr George research group within the Guy Hilton Research Centre at Keele University. For expansion, the cells were cultivated in standard T25 and T75 flasks depending on the required cell number. The basal medium used was DMEM (Gibco, USA) containing: 10% foetal bovine serum (Corning, UK), 100 U/ml penicillin/streptomycin (Lonza, UK), 20mM L-glutamine (Gibco, UK) and 2% B27 supplement (Thermofisher Scientific, UK). The cells were passaged at 60-90% confluence by trypsinization in 1% trypsin for 3 minutes at 37 °C with agitation of the flask after the incubation, the digest was quenched with an equal volume medium before centrifugation at 1200 rpm for 3 minutes. The flasks were seeded at 250K cells/flask after passage.

5.2.2 Coatings for surface functionalisation

5.2.2.1 Collagen coating for cell expansion

Rat-tail collagen (low concentration-3-4 mg/ml (Corning, USA)) was diluted in PBS to a working concentration of 20 µg/ml. 5 ml of this solution was transferred to each T25 flask, resulting in a coating of 4 µg/cm² collagen coating. The flasks with the coating solution were incubated for 45 minutes at 37 °C before being used in culture on the same day. Alternatively, the flask caps were sealed with parafilm and they were incubated in the fridge at 4°C for a maximum of 48h before use in culture.

5.2.2.2 Polydopamine and Polydopamine + collagen coating

Tris-HCl buffer (acquired from in-house stocks) and polydopamine were dissolved into the buffer solution at a concentration of 0.05% w/v. The reaction began instantly, therefore after mixing the polydopamine Tris-HCl solution was immediately transferred to the wells containing the substrates, visible discolouration was visible as the reaction occurred. The well plate was transferred to an orbital shaker for incubation at room temperature with gentle agitation overnight. For additional coating of collagen, the same protocol was applied for same-day collagen application as prescribed in section 5.2.2.1.

5.2.2.3 Gelatin Methacrylate Production and Coating

Gelatin methacrylate was produced by the careful reaction of 250 bloom Gelatin dissolved in PBS with methacrylic anhydride in a fume hood whilst being stirred at 60°C with the pH being continuously checked (maintained at 8-8.5) to prevent methacrylate degradation. After all the reagents were added and mixed for 1h, the resultant mixture was allowed to cool to room temperature before being dialysed in distilled water for up

to 72h. After dialysis, the resultant product was freeze-dried into a solid, initially frozen at -80°C, then transferred to a freeze-dryer for up to 48h (Martin Christ, Germany). Solid GelMa was reconstituted in PBS at a concentration of 10% w/v and mixed with the photoinitiator Lithium phenyl-2,4,6-trimethylbenzoylphosphinate (LAP) at a concentration of 0.25% w/v. To coat, the master mix was syringe filtered into a sterile container followed with the appropriate amount of PBS to create a stock of the required coating solution of the correct coating percentage (typically 2ml total coating mixture at 15% GelMa concentration), this was vortex mixed to ensure an equal mixture. With autoclaved sterile substrates remaining on the stretching frame 25 µl was applied to each substrate and then evenly spread around the working surface area (the central 1 cm² square) using a cell scraper as a sterile spreader. The substrates were then exposed to 405 nm UV light in a shielded hood for 15 minutes before being used in culture.

5.2.3 Tissue Assessment using Optical Coherence Tomography (OCT)

Unlike the human tissue, the porcine tissue presented a unique challenge, the limbal POV structures were difficult to resolve using polarised light microscopy after dissection. A commercial spectral radar OCT machine (ThorLabs, UK) fitted with the LSM03 lens (ThorLabs), with a lateral resolution of 13 µm, an imaging window of 10x10 mm and a working substance penetration of ~1 mm was used to achieve the desired resolution. This device was employed to screen the tissue before the tissue was quartered for enzyme digestion. Cross-sectional B-scans were used to find the undulations of the POV, then the limbal niche regions were demarcated as stipulated in section 5.2.2.1.

5.2.4 Immunofluorescence and Fluorescent Imaging

Cellular features, such as phenotypic assessment of stemness/epithelial commitment or suspected epithelial-to-mesenchymal transition (EMT) were assessed using immunofluorescent and fluorescent imaging techniques. Included within these techniques are 2D and 3D modalities of fluorescent imaging.

5.2.3.1 Immunofluorescent staining (primary + secondary)

Before staining, cultures were fixed in 4% paraformaldehyde (Sigma, UK) in PBS at room temperature in a fume hood for 20 min for monolayer culture or 45 min for wrinkled substrate culture. All fixed cultures, substrates, and vessels were washed twice with PBS to remove traces of PFA after fixation. It should be noted that wash steps in staining differed between standard monolayer culture and substrate culture. In monolayer culture all PBS washes were performed once, however, in wrinkled substrate culture, a gentler single PBS soak was employed (to ensure a maximum of cells/clusters were preserved and retained). Cells were permeabilized in a solution of 0.3% Triton-X (Sigma, UK) with 5% bovine serum albumin (BSA) (Sigma, UK) or 5% human serum (Lonza, UK) for 10 min in monolayer or 15 min on wrinkled substrates. The permeabilisation solution was washed off with PBS. The primary antibody was mixed at a working concentration of 1:100 in 1% BSA/human serum PBS for mouse monoclonal anti-Cytokeratin 3, rabbit monoclonal anti-P63, rabbit monoclonal anti-ABCG2 and rabbit monoclonal Alexa Fluor 488 conjugated anti-K12 (Abcam, UK).

The rat monoclonal anti-vimentin primary antibody (R&D biosystems, UK) was mixed to a working concentration of 8 µg/ml in 1% BSA/human serum PBS. The primary antibodies were incubated at 4°C in the dark overnight and subsequently

washed off with PBS. The secondary antibodies were applied immediately after washing.

Donkey anti-mouse conjugated with NL493 and donkey anti-rabbit conjugated with NL637 antibodies were mixed in 1% BSA/human serum PBS to the same dilution ratio in correspondence to their related primary antibody. Secondary antibodies were incubated for 2 hours at room temperature in the dark before being washed in PBS. Cells were counterstained with the nuclear stain 4',6-diamidino-2-phenylindole (DAPI) (Thermofisher Scientific, UK) at the working concentration of 1 µg/ml in PBS and incubated in a monolayer in the dark at room temperature for 10 minutes or 15 for substrates. The DAPI dye is subsequently washed off with PBS. Stained monolayers/substrates were maintained in the dark in PBS after staining.

Phycoerythrin (PE) conjugated antibodies were also employed for immunophenotyping isolated limbal cells. These directly conjugated antibodies were employed in a single-step method. Mouse anti-hNestin, rat anti-hVimentin, and mouse anti-hABCG2 (R&D Biosystems, UK) were applied to monolayer cultures at the same concentration as the 2-step counterparts (1:100) and incubated at 4°C in the dark overnight. The PE-conjugated antibodies were washed off twice with PBS and the stained wells were maintained in the dark in PBS.

5.2.3.2 Cytoskeleton Staining

The cytoskeleton was stained using a phalloxin conjugated with Texas red; phalloidin Texas red (Thermofisher Scientific, UK). This dye permanently binds to the F-actin component of the cytoskeleton, thus is useful for cell morphological assessment. Due to incompatibility with methanol-containing fixatives, it was

preferable to fix the cells with a commercial fixative such as 10% formalin (Sigma, UK) which did not list methanol in the ingredients, following the same fixation procedure as outlined in 5.2.4.1. The cells were permeable as per the procedure outlined in 5.2.4.1. The Phalloidin powder was first solubilised in 300 µl DMSO to a stock concentration of 33 mM phalloidin in DMSO, this was aliquotted as 5 µl stock in 495 ml PBS resulting in a final working concentration of 0.55 mM. This working stain was applied on the permeabilised cells and incubated at room temperature, in the dark, for 45 minutes. After incubation, the cells were washed with PBS and counterstained with DAPI as stated in section 5.2.4.1. The stained cells/substrates were maintained in the dark in PBS.

5.2.5 Live Cell Imaging

5.2.5.1 Automated Live Cell Imaging Using the CellCyte

Automated live cell imaging was performed using the CellCyte live cell imaging system. There were two types of analyses performed on the imaging platform; basic confluence which used enhanced contrast (Bright-field only) and the counted analysis which required live fluorescent tracking.

For the enhanced contrast analyses, the cells were seeded as required, either as a monolayer in the well plate or on the substrates. The well plate was seated on the CellCyte machine and the acquisition parameters for the experimental duration were set up in the software. Each experimental acquisition exceeded no longer than the average time taken for cells to reach confluency (6-8 days). Enhanced contrast is an automatically adjusting feature within the software, thus adjustment was not

necessary, exposure frequency and images per well varied with well plate sizes, machine availability, and experimental constraints.

For the cell counting analysis, the cells were stained using a live cell tracking dye during the passage. After centrifugation and counting, the cells were resuspended in 1 ml medium with 2 μ l of CellTracker green CMFDA dye (Thermofisher Scientific, UK) and incubated at 37 °C for 30 min. After incubation the cells were centrifuged, the dye-laden supernatant removed and the cells resuspended in the requisite culture medium volume. After staining, the cells were seeded and the CellCyte was set up similarly to the enhanced contrast program, except for the selection and adjusting of the green channel.

5.2.5.2 Manual Live Cell Imaging

Cells were passaged from the monolayer following section 5.2.1.1, after centrifugation, whilst the cells were retained in the pellet, the pellet was resuspended in 1-2 ml of medium (dependent on cell number/dispersion requirements) containing 2-4 μ l of the CellTracker Green CMFDA (Thermofisher Scientific, UK). The suspension was incubated in the dark for 30 minutes before further centrifugation and suspension to the correct seeding volume. The substrates/wells were then seeded as required and tracked. Manual tracking was typically performed when wrinkled substrates were employed due to the difficulty of visualisation through the material, thus the fluorescent dissecting microscope (Leica MZ10F) was used to capture the green fluorescent images.

5.2.6 Image Analysis

5.2.6.1 Image-Based Counting and Morphology Analysis

ImageJ was used to count multi-channel fluorescent images and assess morphological changes imparted by condition changes. The first method of assessment relied on splitting the image into separate channels. The DAPI (nuclear) channel was thresholded and converted into a binary image. This binary image was subjected to a particle count within the area range of 100-1100 μm^2 , the number of particles constitutes a cell count for a given area. For morphology analysis, the channel which provides a morphology-conforming stain (eg. vimentin or ABCG2) was employed. This was smoothed to remove erroneous particles and gapped edges, providing a truer edge upon binary thresholding. These images were thresholded and converted into binary images. As per the cell count, these images were run through the particle count with the area parameters of 100-infinity μm^2 . The circularity metric was used as the output to determine morphological change/response to conditional change.

5.2.6.2 Assessment of Alignment

ImageJ was also employed to produce a graphical-format comparative assessment of alignment as a measure of contact guidance of cells on the wrinkled substrates. The cells were imaged using fluorescent modalities either as with live cell imaging or end-point staining. These images were then converted into greyscale images and the contrast was optimised for automated feature detection. These images were then manually stacked to facilitate the correct comparisons to be plotted on the

generated histograms. The directionality plugin for FIJI (ImageJ 2) was employed, using the Fourier components parameters.

5.2.7 3D Printing

5.2.7.1 CAD Design

Fusion 360 (Autodesk, USA) was used to design and export the 3D models for the cylindrical retainer rings (with a basal 0.5 mm x 11 mm cutout for chip seating) used in static culture. The retainer rings were vertically sized (22 mm) for 12 and 24 well plates. The substrates fit in a 12-well plate without the need for trimming and the dual treatment substrates fit into a 24-well plate when the 1cm² centre working portion is cut away from the rest of the chip.

5.2.7.2 3D Printing of cultureware

The STLs were sliced into the .x3g format for printing using the Flashforge FlashPrint 5 (Flashforge, China) printing using the fast settings. The print parameters were automatically set to as per table 2.2. The printing was performed using the Flashforge Creator Pro extrusion printer in polylactic acid (PLA). For culture, the retainer rings were sanitised in 70% ethanol or industrial methylated spirits for 40 minutes and dried in the biological safety cabinet immediately before use.

5.3 RESULTS

5.3.1 Isolation and Cultivation of Human Limbal Cells

5.3.1.1 Immunofluorescent Staining of Human Corneolimbal Tissue

To validate the presence of the markers, in both the limbus and the epithelium, the section of human tissue was dissected into stainable sections. A staining and imaging mount 3D printed for this special purpose, and the corneal section (sectioned tangentially), and the limbal POV region (also tangentially sectioned) were stained with the key markers referenced in this Chapter. Figure 5.2 shows the immunofluorescent stained tissue slices. Principally, the stem cell markers P93 and ABCG2, the epithelial markers K12 and CK3, the mesenchymal marker Vimentin, and the neuronal/ectodermal marker Nestin were used in this validation. Wet sectioning and staining without fixation and embedding were used to combat the structural degradation observed in Chapter 3 histology and provide a preliminary assessment of this technique of antigen-based assessment of fresh tissue however, due to the low yield of slices due to the thickness, secondary-only controls were sacrificed to enable all markers to be tested. Heavier P63 expression was observed in the limbal region compared to the corneal, with a wider dispersion, whilst ABCG2 maintains a higher spread between both regions, but shows a decrease in the cornea. Vimentin appears to demonstrate heavy localisation in the limbal region but is much scarcer in the cornea. Nestin is more ubiquitously found throughout the corneoscleral structure, with a higher concentration in the epithelial surface. The same is true of K12, but CK3 is more present in the limbal region but does not appear to show clear corneal epithelial commitment.

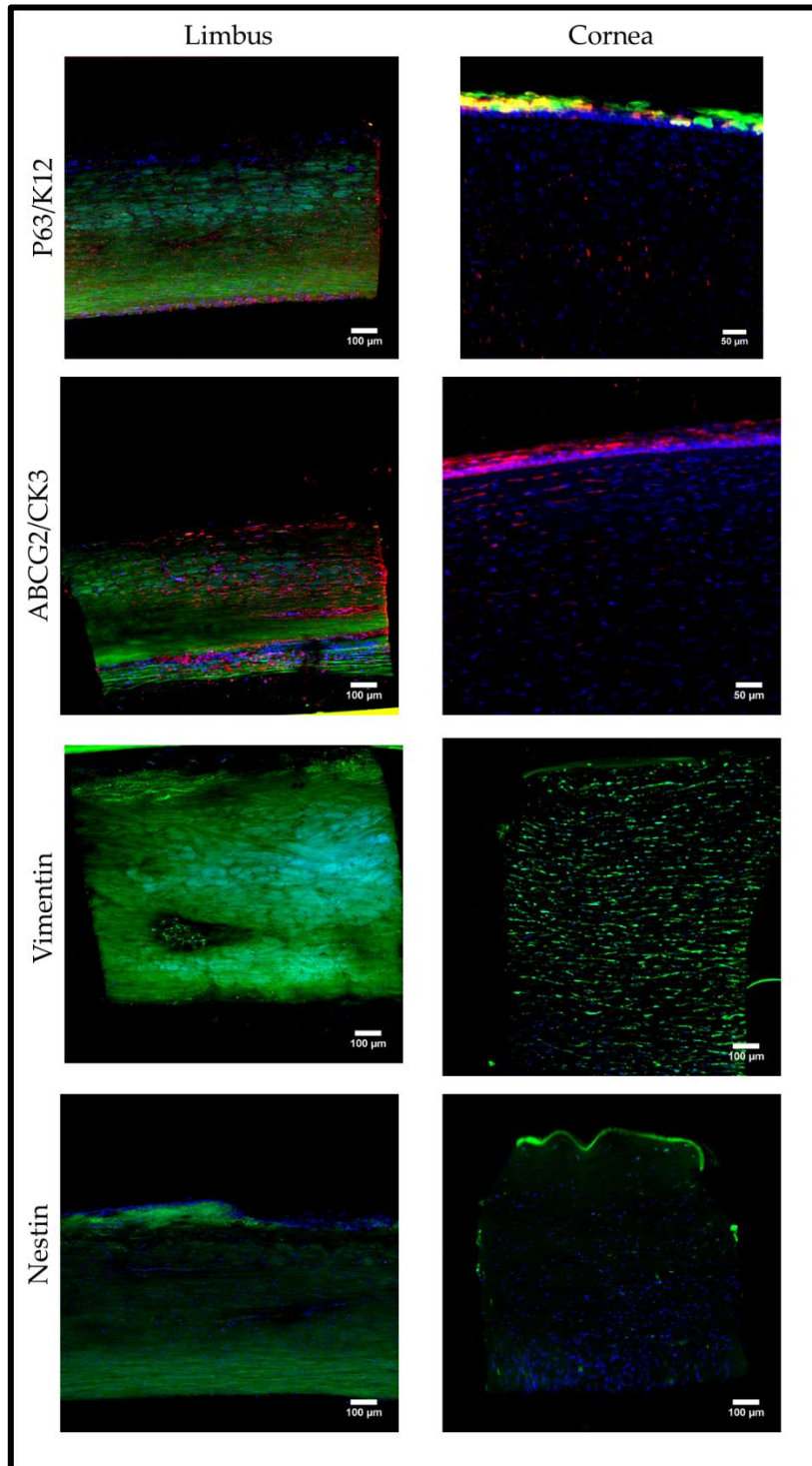


Figure 5.2: Immunofluorescent staining of corneolimbic tissue as marker validation. Tissue sections were cut and stained as wet sections, orientated with the outer epithelial surface always towards the top of each image, the left shows the staining of the indicated markers in the limbal section, right for the corneal section. K12, CK3, Vimentin and Nestin are represented as green fluorescence, whilst P63 and

ABCG2 are Red. In all images, nuclei are counterstained with DAPI (blue) and all scale bars represent 100µm, N=1 for each.

5.3.1.2 Isolation of Human Limbal Cells into Monolayer Culture

The marker validation revealed the presence of the key markers in the tissue, thus showing these tissues were relevant to performing cell extractions. Despite showing an (expected) decrease in stem cell presence in the limbal region by this observation, it was still worthwhile to retrieve and expand these cells using a selective isolation and expansion method. The principle method for performing selective isolation was using a 2 step enzymatic digestion. Dispase first loosened the epithelial layers from the rest of the tissue, ensuring isolation of the epithelial and the niche layers during final debridement, thus preventing deeper stromal cells from “contaminating” and overtaking the isolated cultures. Secondly, the collagenase digest broke down the remainder of the tissue matrix to isolate these debrided epithelial sheet fragments into cellular bundles and single cells which were able to finally expand into monolayers as demonstrated in Figure 5.3.

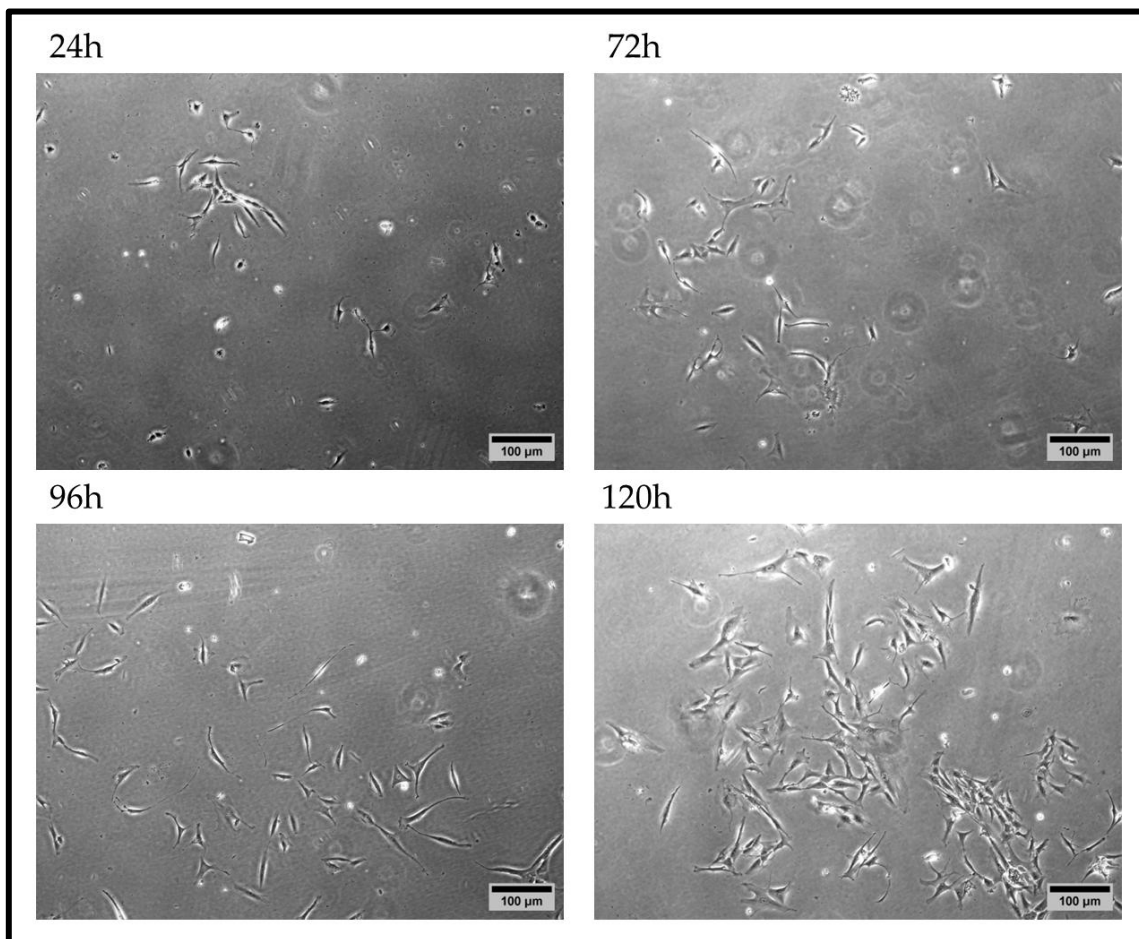


Figure 5.3: Bright-field micrographs showing the growth of human limbal cells post-isolation in a 6 well plate. The time points are as denoted, showing progression in monolayer expansion out of the second enzyme digest N=3 wells. Scale bars represent 100 µm.

5.3.1.3 Characterisation and Optimisation of Isolated Human Limbal Cell Culture

Following the successful isolation and expansion of human limbal cells in monolayer, it was determined that the ideal growth condition of the limbal cells needed to be established. There were three options for media in terms of optimizing the growth environment, they were as follows; the “simple” (DMEM F12 with 10% FBS, 1% Penicillin/Streptomycin and 20mM L-glutamine) which also performs as the control, the commercial option (and the most expensive) was the CNT-Prime an advertised

epithelial expansion medium with reported ocular applications. Finally, the Stem formulation, a composition formulated for this work based on literature is considered the “best of both worlds”. This formulation was; 100 U/ml penicillin/streptomycin (Lonza, UK), 20mM L-Glutamine (Gibco, UK), 0.1X insulin transferrin selenium (ITS) supplement (Gibco, UK), 1 µg/ml isoproterenol (Merck, UK), 0.4 µg/ml hydrocortisone (Merck, UK) and 2.43 µg/ml adenine (Merck, UK) in DMEM-F12 (Gibco, UK), supplemented with 10% foetal bovine serum (FBS).

This assessment was performed by immunostaining isolated cells, cultured in monolayer in each of these medium types, then assessing cell number at the point of fixation as a metric of rate of expansion in each medium. From the immunostaining, it can be seen the ABCG2 and P63 positivity is maintained across all medium types showing a preservation of stem cell phenotypes. CK3 had the lowest level expression of all the markers and was observed at this low level across all three media groups. K12 has low level expression in all media types indicating some low weak corneal epithelial phenotype presentation. The presentation of strong vimentin expression indicates a mesenchymal transition, it is proposed the length of time the tissue was in storage before the cells were isolated contributed to this transition and presentation of non-LESC phenotype. The circularity of the cells was also measured after creating binary images of the cytoskeletal marker images (Vimentin, CK3 and ABCG2 for each medium condition displayed), after binary image creation all markers filled the cell membrane boundary, thus could be used synergistically to determine circularity. The closer to 5 or 6 they were the better (indicative of a more rounded-like shape, with a morphology closer towards the canonical ideal LESK shape). Closer to 0.1 indicates a more fibroblastic/mesenchyme morphotype. An average near 1 would indicate near

total roundness, an indication of mass cell death/detachment in adherent cells. Viability curves performed using the cell counting kit-8 (CCK8) were used to validate the image-based counts performed in the medium compatibility assay. An increase in cell population increases the turnover of the CCK8 tetrazolium product (similarly to the MTT assay), thus producing a stronger colour change in the assay medium resulting in a stronger absorbance in spectrophotometry. These findings confirmed the same trend observed in micrographic nuclear cell counting as performed in the medium compatibility assay, wherein there was an observed greatest cell number and viability in the stem medium, a middling performance in the simple medium and the worst performance was accounted for by the CNT-Prime medium. The immunofluorescent characterisation and viability assessment are presented in Figure 5.4.

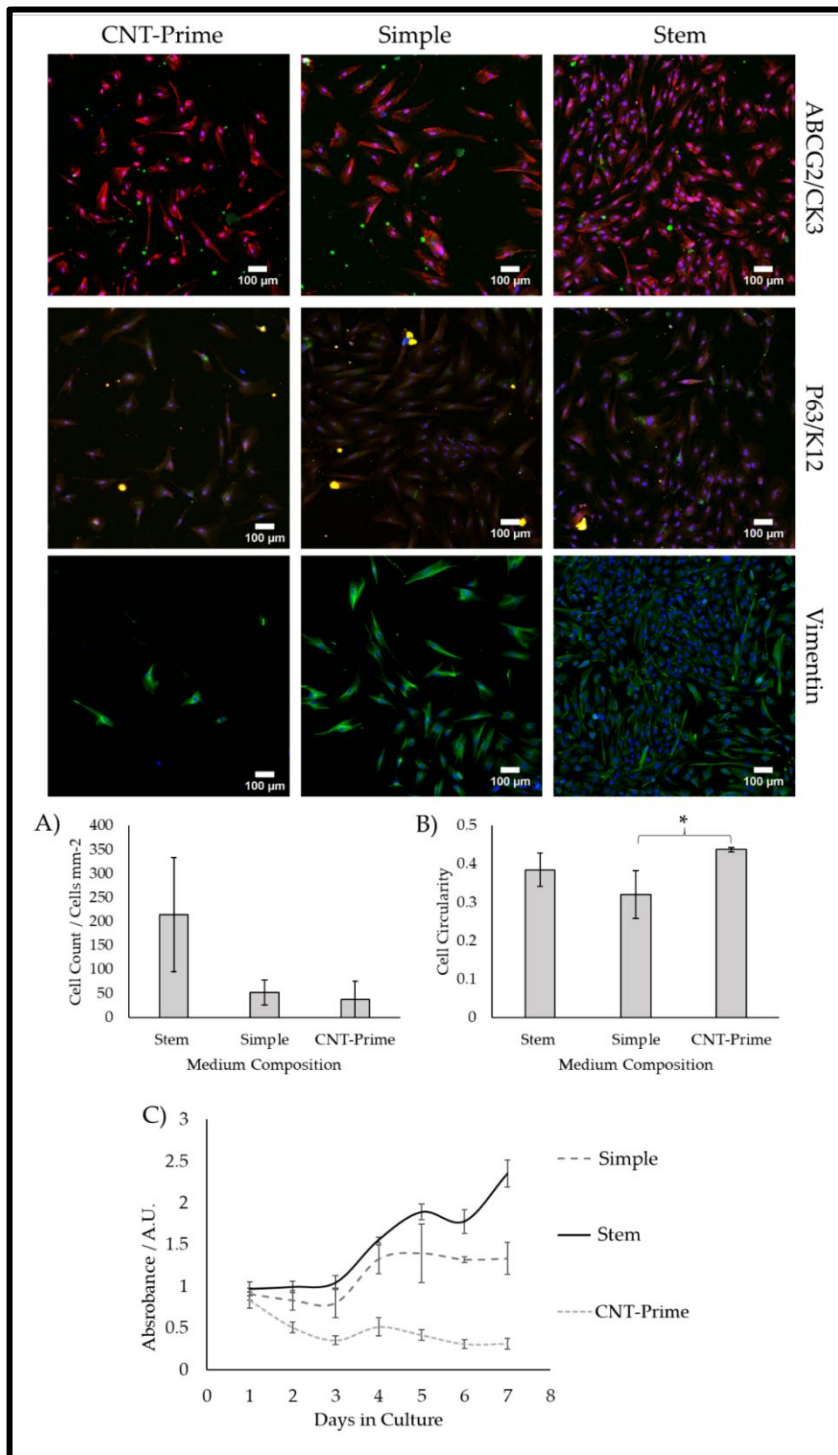


Figure 5.4: Assessment and quantification of cell quality and expansion in different media growth conditions. The top panel presents the immunofluorescent imaging of the different growth conditions as indicated. ABCG2 and P63 are presented as red fluorescence whilst K12, CK3 and vimentin are presented as green, demarcated in their rows as indicated. Cell nuclei are counterstained with DAPI as blue and all scale bars represent 100 μm. A) Presents a chart of cell counts from images using nuclei counting versus media composition and B) shows cell roundness as a function of cell morphology against media composition both charts are plotted from n = 3

replicates. C) Presents CCK8 viability curves for each medium type taken over 1 week, n = 4 for each.

5.3.2 Porcine Limbal Epithelial Cell Isolation

5.3.2.1 Pre-Dissection Tissue Screening and 3T3IN Co-Culture

At the initial porcine phase of the study, in the design and consideration stage, it was proposed that though the medium had been optimised and surface coatings had been explored further work was required. Therefore, an inactivated 3T3 layer was employed to assess whether a live biological support element was required to support limbal epithelial stem cell growth, population and stemness maintenance. To this effect, 3T3-J2 mouse embryonic fibroblasts were inactivated with mitomycin-c and then seeded as a feeder layer with a density of 2×10^4 cells/cm². To test the viability of the 3T3 cells in the limbal stem cell cultivation medium, the feeder cells were cultivated in the target medium and their viability was assessed using the cell counting kit 8 (CCK8) over 4 days. At day 0 it was observed the active cells registered a slightly higher viability than their inactivated counterparts. On day 1 both cultures exhibited an aberrantly distorted higher reading, which may be accounted for by operator error, however, the active cultures maintained a higher trend compared to the inactive culture. On day 4 the readings for CCK8 absorbance were more in line with expectations. The inactivated cells showed no significant increase in CCK8 turnover (and therefore no indication of proliferation), as determined by a T-test between days 0 and 4. In the active cell culture, there was a significant increase in CCK8 turnover between day 0 and 4 ($P = 0.003$), this shows that the cells were able to proliferate in the stem cell medium and therefore increase the rate of turnover of CCK8 compared to day 0. Overall this test indicated that 1. the inactivation by mitomycin-C is effective

and 2. the process is not cytotoxic when the feeder cells are transitioned into the stem cell medium and the cells can safely be cultivated in co-culture in the limbal stem cell medium.

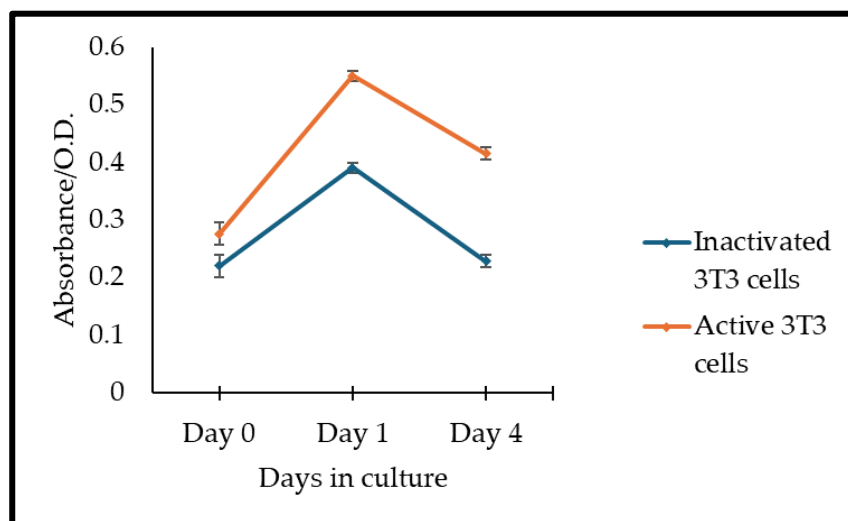


Figure 5.5: Assessment of 3T3 viability in limbal stem cell culture medium using the CCK8 kit. Inactivated cells were treated with mitomycin-c to inactivate the cells before the first viability measurement was taken on day 0, the active cells were not treated and allowed to proliferate. The error bars represent the standard error of the mean and each data point is plotted as an average of n=3 replicates.

In the first instance, the porcine tissue was processed in the same manner as the human tissue, however, due to differences in tissue optical properties, it could not be screened using polarised optical microscopy. Therefore, as demonstrated in Figure 5.5, OCT was employed to find the limbal niche (POV) regions in each of the tissues dissected for the cell extractions. These were readily identified by locating the undulating structures underneath the epithelial layer. Once this was located the sterile OCT vessel could be marked in the same manner as in which the limbal regions were demarcated in Chapter 3 for the OCT/OCE study.

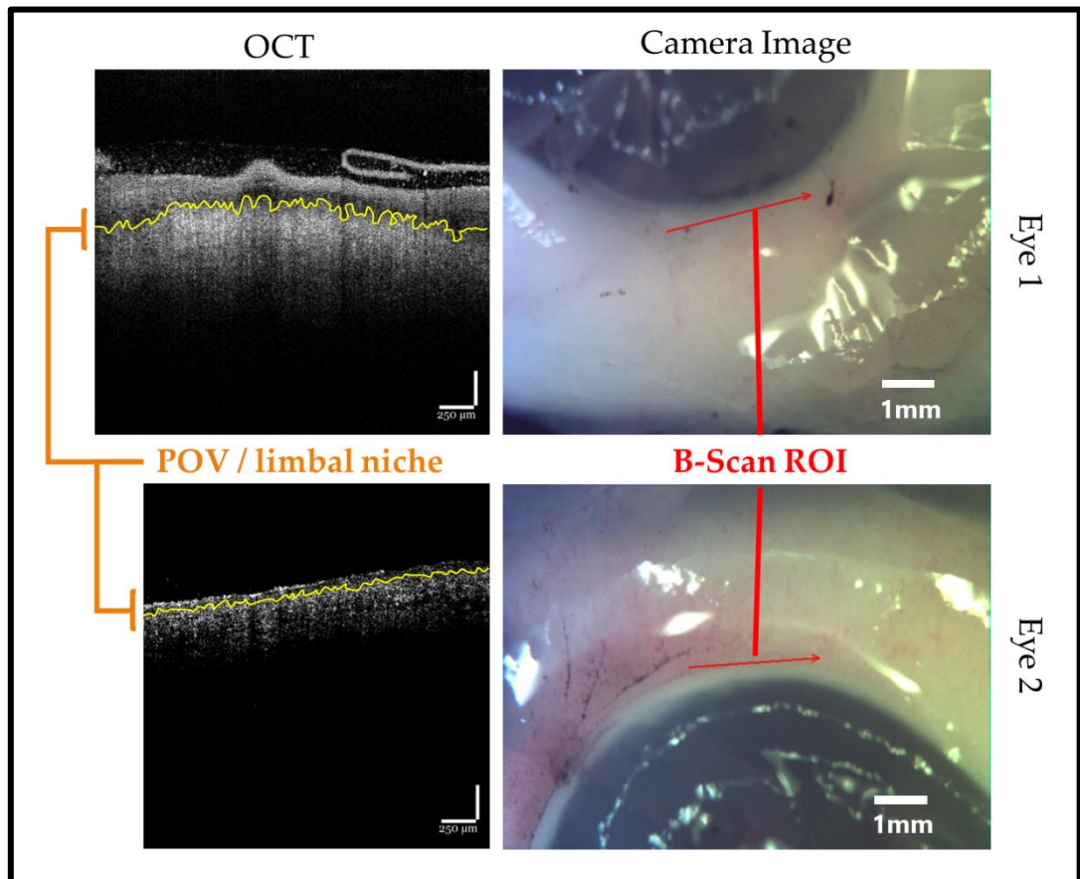


Figure 5.6: Porcine POV location using OCT to guide limbal dissection and LESC extraction. On the left-hand side are OCT B-Scan images of the limbal palisades of Vogt (POV), which contain the limbal epithelial stem cell niche. The yellow line follows the undulations of the niche as seen in the OCT imaging. The right-hand side images show the corresponding camera images for the OCT imaging and the red lines show both the ROI and the scan direction for the OCT acquisition. The scale bars on the OCT imaging represent 250 μm whilst the scale bars on the camera images represent 1mm. The figure presents a pair of eyes for extraction, representative of 4 extractions scanned.

After, the two-step enzymatic digestion method, the porcine limbal isolate was then seeded onto a pre-prepared inactivated 3T3 (3T3IN) layer for porcine limbal epithelial stem cell (PLESC) colonial expansion. The 3T3 cells were inactivated 24 hours before use and seeded into the isolation vessel (a 6 well plate) at 2×10^4 cells/cm² and the porcine limbal cell isolate was directly transferred into these wells (after removal of the enzymes by centrifugation) at a ratio of 1:3, using the entire isolate between 3 wells. The lower density of inactivated cells is intended to allow the isolated

porcine limbal cells to form colonies without inducing premature confluence within a short time. It was observed that after 96hrs of cultivation from passage 0 (isolation) colonies were beginning to form in small tight clusters with epithelial cobblestone morphology as highlighted in Figure 5.7, these were termed as pre-colonies due to this precursor structure. It was observed subsequently that after passaging (passage 1) these cells we then able to form large epithelial colonies, maintaining the epithelial cobblestone morphology.

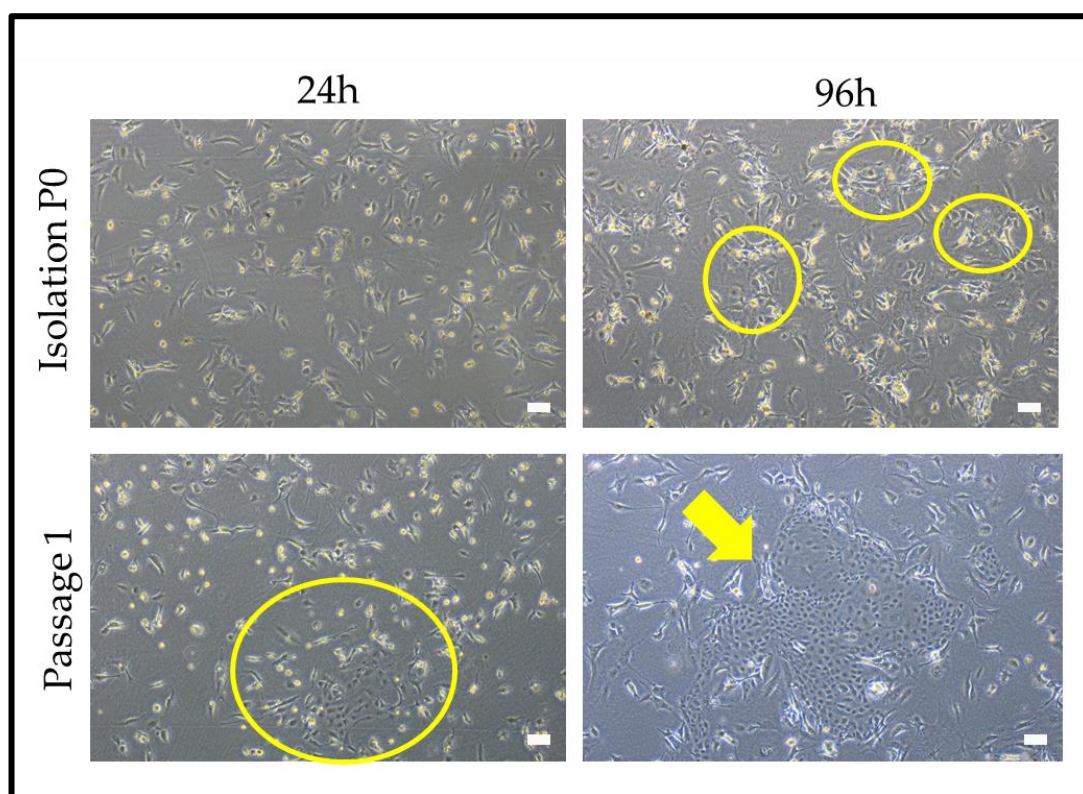


Figure 5.7: Bright-field microscopy of porcine limbal epithelial cells after isolation and the first passage. Cellular clusters encircled are examples of establishing and growing “pre-colonies” of isolated porcine limbal within a co-culture with an inactivated 3T3-J2 feeder layer which are the dispersed monolayer cells. The large arrow indicates a large epithelial colony that has established after 4 days after a single passage. All scale bars represent 100 μm . Images representative of $n=3$ extraction wells.

5.3.2.2 Porcine Limbal Cell Monolayer Characterisation

Once these cells were established as a viable culture, the cells were characterised to determine the phenotype of the cells isolated. The markers employed were P63 and ABCG2 to assess the stemness of the cells. CK3 was used to assess corneal epithelial commitment in the isolated cells, whilst K12 can be used to reinforce this, it has weak co-expression in the limbus. It was noted there was spectral overlapping with the green dyes (Alexafluor 588 and N493) and the blue DAPI, resulting in the cross-over of the detection and z-projection of these features, resulting in an over-intense final image. In monolayer assessment of the isolated porcine limbal cells and 3T3IN cells was performed with immunofluorescence using confocal microscopy. It was demonstrated that cells were positive for both stem cell markers (ABCG2 and P63) and weak to moderate positivity for CK3. Therefore, despite the DAPI aberration and the observed positivity with K12 and weak CK12, it can be surmised that these cells are PLESCs due to the positivity of the stem cell markers.

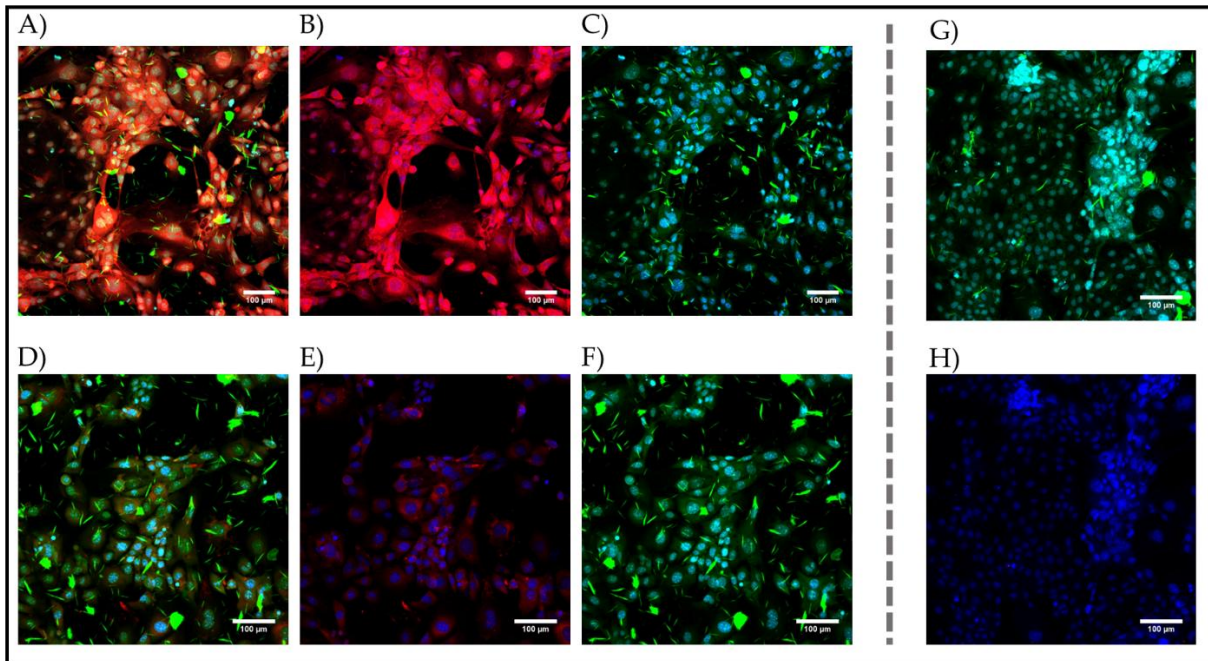


Figure 5.8: Immunostaining panel of isolated PLESCs. A) Merged fluorescent image of the stem cell marker ABCG2 (Red), the epithelial marker CK3 (Green) and the nuclear counterstain (DAPI-blue) B) ABCG2 and nuclear only, C) CK3 and nuclear only. D) Merged fluorescent image of the stem cell marker P63 (Red), the epithelial marker K12 (Green) and the nuclear counterstain (DAPI-blue). E) P63 and nuclear only. F) K12 and nuclear only. Images representative of n=3 replicates for sample images. G) Secondary only stain with Donkey anti-mouse conjugated with NL493 (green) counterstained with DAPI (Blue), H) Secondary only stain with Donkey anti-rabbit conjugated with NL637 (red) counterstained with DAPI (Blue). Secondary images show N = 1 for these controls.

5.3.2.3 Optimisation of PLESC Culture – Towards Monolayer Purity

Subsequently, it was decided that whilst the use of 3T3IN was suited for the preservation of stemness and morphological quality there was a question about the preservation of cell purity in phenotypical analysis. This would have been of particular concern in substrate studies where a live tracking dye or actin stain, phenotypically non-specific stains, could be employed. In the pursuit of cellular purity, using collagen-coated TCP, similar to the human cell culture was considered and tested. As shown in Figure 5.9 automated live cell imaging was used to capture the growth of PLESC and

the Cellcyte proliferation analysis system was used to evaluate cell outgrowth for both collagen-coated TCP culture and 3T3IN co-culture. Both groups were seeded from the same cell source and live-tracked simultaneously. The inactivated 3T3 layer was prepared before the PLESCs were seeded at the same density between groups (2×10^4 cells/cm² for 3T3 cells, 10×10^5 cells/well of PLESCs/well), due to having a co-culture of inactivated and target cells, the raw starting confluency is greater in the co-culture. Over a long culture period, the colonies formed by the seeded PLESCs were observed to grow very large, covering significant amounts of the imaging windows. A feature of this expansion (in the co-culture) was the physical dislocation of the more weakly attached inactivated feeder cells from the well surface by the more tightly compact and strongly bound PLESCs. This observation supports the necessity to use a cell scraper to detach the PLESC colonies and aid in trypsinisation, in comparison to the sole use of trypsin for the detachment of the 3T3 cells.

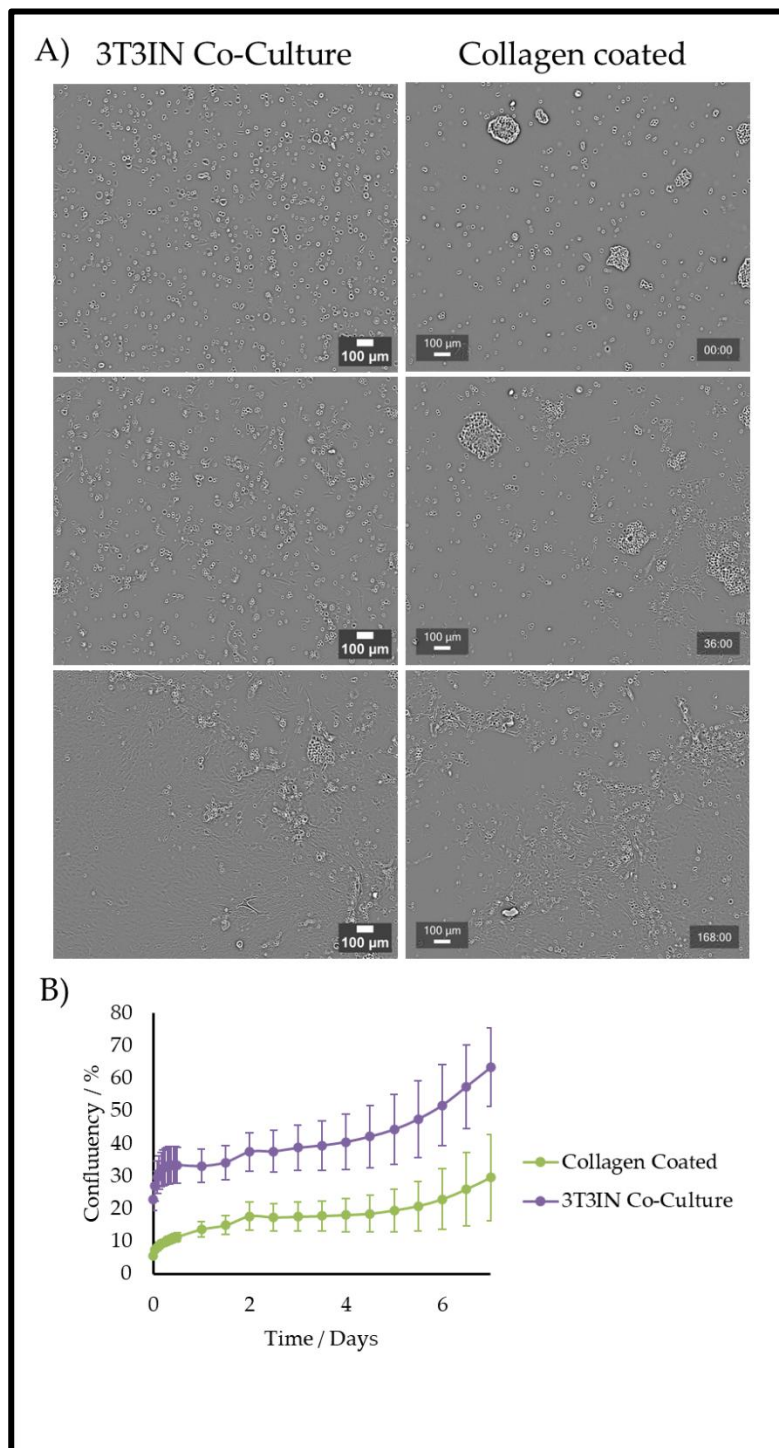


Figure 5.9: Comparison of 3T3IN co-culture and collagen-coated well culture. A) Is a panel showing the growth profile of each growth condition in time-series images, the time point for each row is annotated in the right-hand image. B) The growth profile represented in a graph of percentage confluency against the time in culture in days, as measured by the CellCyte automated live cell imaging system. Data points and images are taken from n=3 wells of a 6-well plate for each group.

After it was determined that the collagen-coated wells possessed both similar cell growth characteristics and colonial morphological maintenance properties to the 3T3IN co-culture, it was pertinent to assess whether this approach suitably maintained stemness in monolayer culture. As in the initial assessment, this was assayed using immunofluorescence. The most sensitive marker for stemness has been determined as P63, as this marker has previously displayed the greatest propensity to change apparent expression. However as demonstrated in Figure 5.10 the expression of P63 does not appear to be different, therefore it is proposed that there is no substantial change in stemness (by assessment using the P63 marker) between collagen-coated well culture and 3T3IN co-culture. The following assay was conducted in line with the experimental parameters of the assessment of the phenotype of the isolated PLESCs (Figure 5.8), the cultures were maintained for [n] days before fixation and staining and N=3 biological replicates were performed. However, the nuclear counterstain DAPI was omitted to prevent spectral overlap and a potential false positive of the CK3 marker.

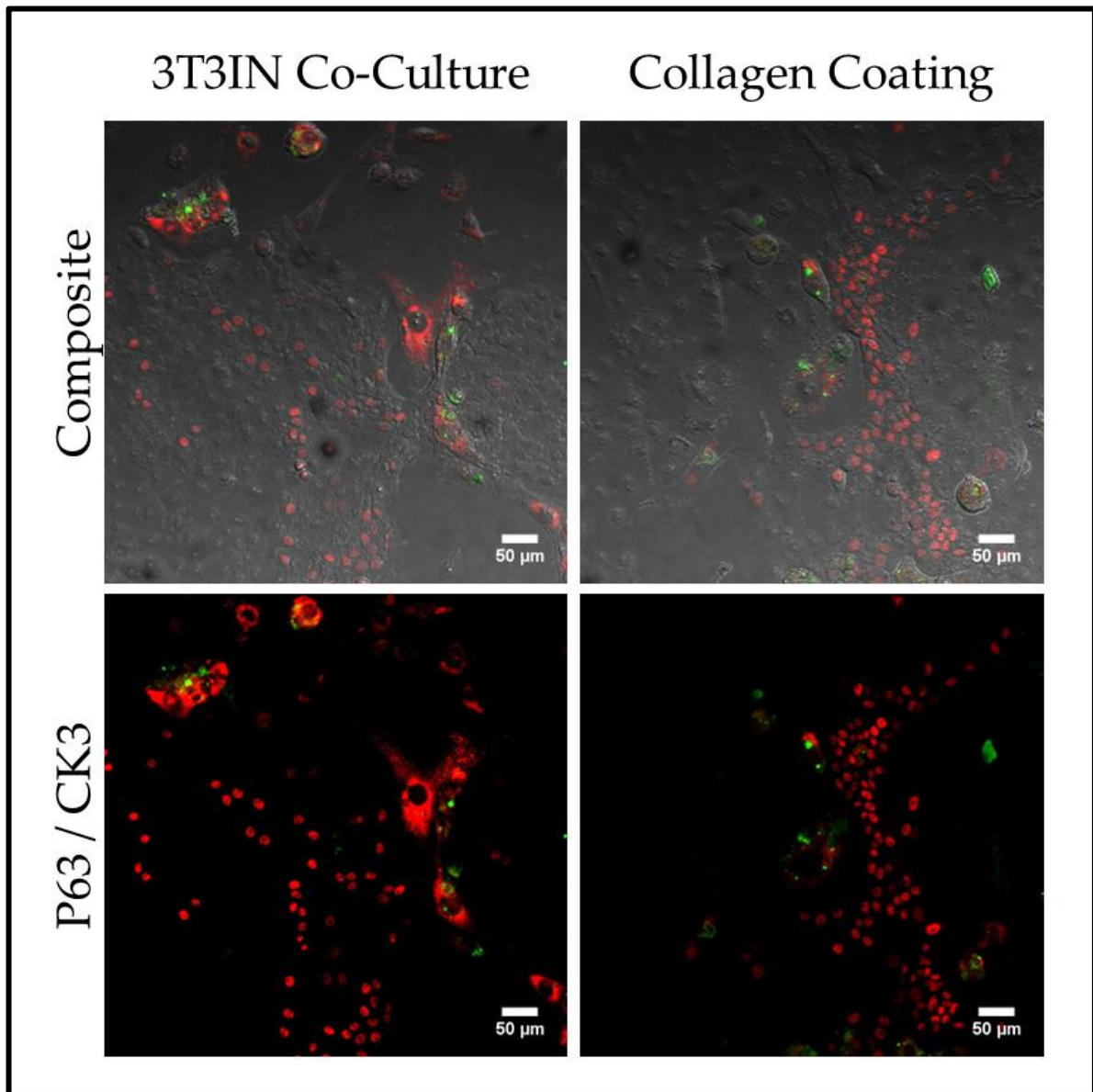


Figure 5.10: Immunofluorescent assessment of the collagen-coated well and 3T3IN co-culture methods of expanding PLESCs. The top row shows both Bright-field and fluorescent channels whilst the bottom row shows the fluorescence only for the respective representative images (n = 3). P63, the stem cell marker is shown as red fluorescence whilst the epithelial marker, CK3 is shown as green. All scale bars represent 50 μm .

5.3.3. Cultures Performed as Part of the Substrate Developmental Process

In subsequent work, the materials utilised as culturing substrates within the appropriate culturing and bioreactor setups employ the material production methods as described in Chapter 4. This section presents the initial trials in the development of the wrinkled substrates and their use in culture as bio-instructive surfaces. Additionally, these results clarify the reasons why the dual treatment substrates became the superior substrate option in the development of the bioreactor for LESC culture.

5.3.3.1 Laminated Block Wrinkled Substrate Cell Culture Trial

In the development of the optimum wrinkled substrate (the predominant technique discussed in this chapter), the dual treatment wrinkled PDMS, there were trials of the primordial substrate production protocols as outlined in Chapter 4.

During these trial stages, cell types originating from various species were employed, pending availability. For the pilot laminated block experiments, rat cardiomyoblasts were used as the available cell type to facilitate the refining/development of wrinkling methods by allowing preliminary assessment of surface biocompatibility. The laminated block was initially trialled as an alternate method, employing compression to induce wrinkling as opposed to relying on pre-applied tension to generate wrinkling. This system performed satisfactorily in “dry evaluation”, however in cell culture there were significant problems that could not be overcome. The first and foremost observation was of uncontrollable PLGA membrane delamination, this resulted in a less predictable cell culture surface (particularly when considering dynamization). Secondly, during imaging cell adhesion was variable and the application of coatings (past a simple vitronectin coating (a common

cardiomyocyte/cardiomyoblast coating)) to the membrane material was not considered a viable development process in this system set-up due to the instability of both the surface (by delamination) and bulk positional stability under compression. Finally, the amount of underlying bulk PDMS material required to accommodate for the compressive arms meant that staining, (even with hematoxylin and eosin) was not practical. Therefore the evaluation was performed using Bright-field microscopically as presented in Figure 5.11, with questionable degrees of specificity to the detection of cells on the surface. It is also observed that viability, as a function of observable qualitative cell attachment, appeared to decrease with time.

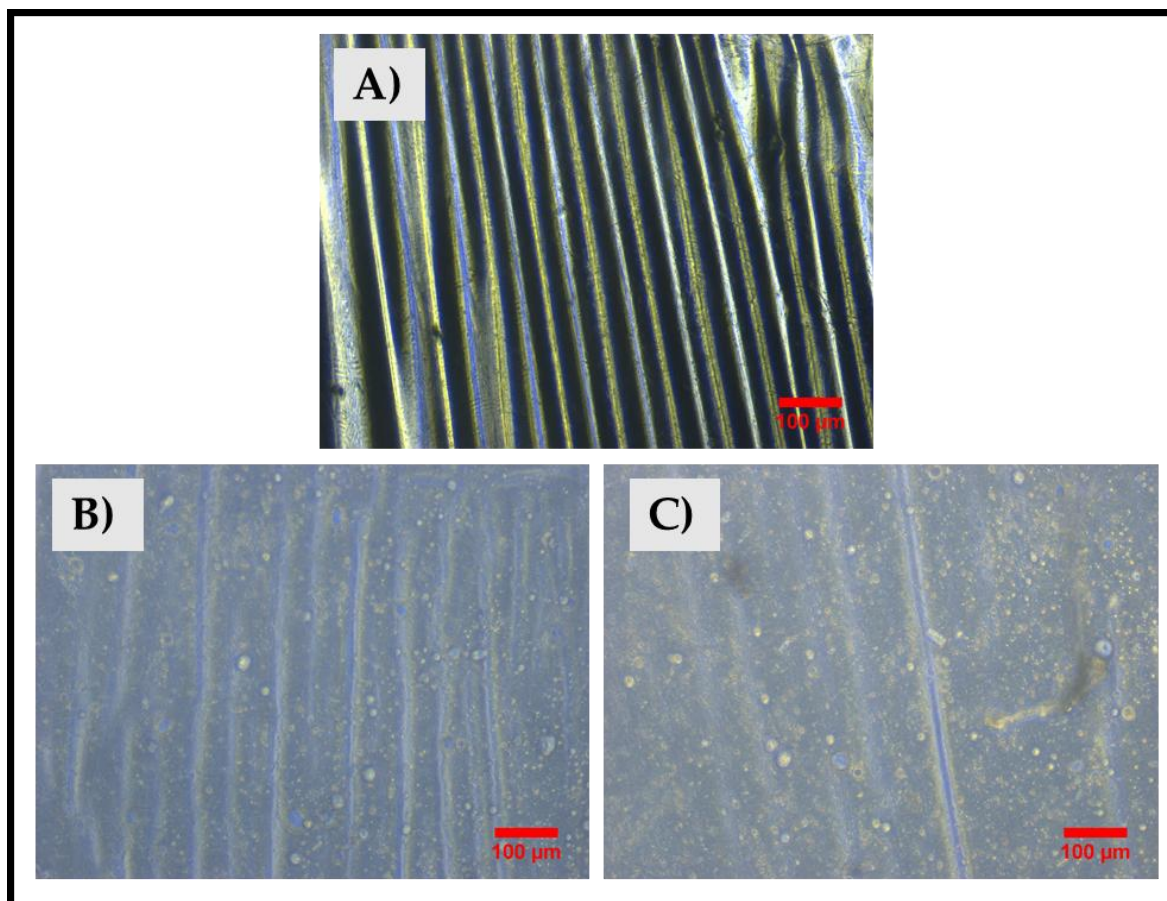


Figure 5.11: Generation of wrinkles on a PLGA laminated block, with a demonstration of wrinkle ‘decay’ in culture with rat cardiomyoblasts. A) Acellular PLGA laminated block, B) 24 hours in culture, and C) 48 hours in culture. Scale bars represent 100 µm, n = 3.

5.3.3.2 Plasma Oxidized PDMS Topography

As presented in Chapter 4, it is possible to create micron-scale ordered wrinkle topographical features using oxygen plasma treatment of pre-strained PDMS. In this trial, PDMS membranes formulated with 3.33% curing agent were cast and pre-stretched similarly to the dual treatment chip method. The resultant plasma topography, whilst practically invisible to the eye except for an iridescent optical glimmer had an apparent effect on the rat cardiomyoblasts cultured on this surface. A visible alignment of cells was demonstrated on this type of topography, the degree of alignment could be influenced by the amount of stretch imparted on the substrate during treatment, inferring that the cell alignment upon the surface visible in Figure 5.12 could be used as an approximative function of the degree of wrinkling produced underneath. The proposed assumption is that the greater the magnitude of wrinkles = the greater the contact guidance imparted upon the cardiomyoblasts.

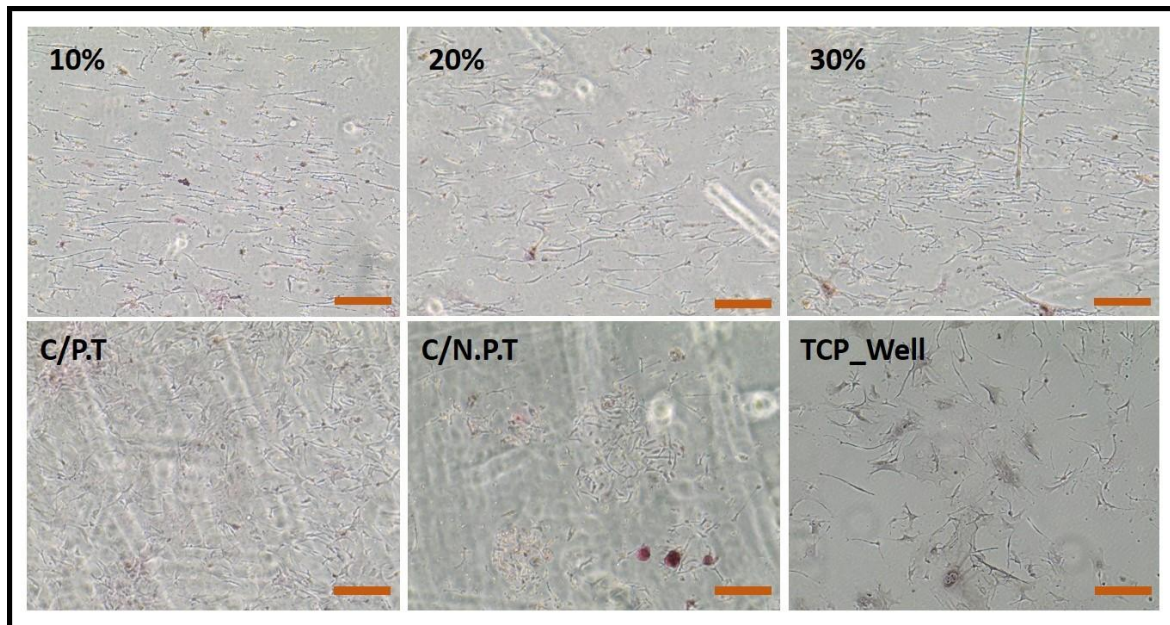


Figure 5.12: Haematoxylin and Eosin staining of Rat cardiomyoblasts seeded on Pre-stretched PDMS membrane which has been subjected to O₂ plasma treatment. The top 3 images are of substrates that have been pre-stretched to the annotated percentage strain before treatment. The bottom three images visualize the controls: C/P.T, the lower left image is the unstrained control with plasma treatment applied; C/N.P.T, the lower centre image is of the unstrained control without plasma treatment and TCP Well, the lower right image shows the tissue culture plastic of the well plate. The scale bars represent 100µm length. Images are representative of n=3 wells per annotated group.

5.3.3.3 Cultivation of Cells on Acid Oxidized Topography.

In isolation, acid oxidation can produce a wrinkled topography, as demonstrated and discussed in Chapter 4, it is also a key step in the production of the dual treatment topography.

It was pertinent to test the biocompatibility of acid oxidation alone as a culturing surface. This testing was performed using human embryonic kidney-293 (HEK293) cells, with actin staining (phalloidin Texas Red) being used to evaluate the cell morphological response to the topography. There were 3 key observations, exemplified in Figure 5.13, made in the prosecution of this evaluative phase. The first is that the reliability of cell adhesion was spurious at best. Being obvious at a qualitative

level of visual examination, thus not warranting image-based quantification. Secondly, the PDMS oxidation protocol (droplet acid-oxidized) was not effective in the collimation of wrinkles. Thirdly the visibly decreased cell population (in comparison to the control) observed on the acid-oxidized wrinkled topography did demonstrate a degree of contact guidance. In terms of the observed contact guidance, this was not presented as cellular morphological changes but as pseudocolonial clusters formed within the randomly ordered wrinkle troughs.

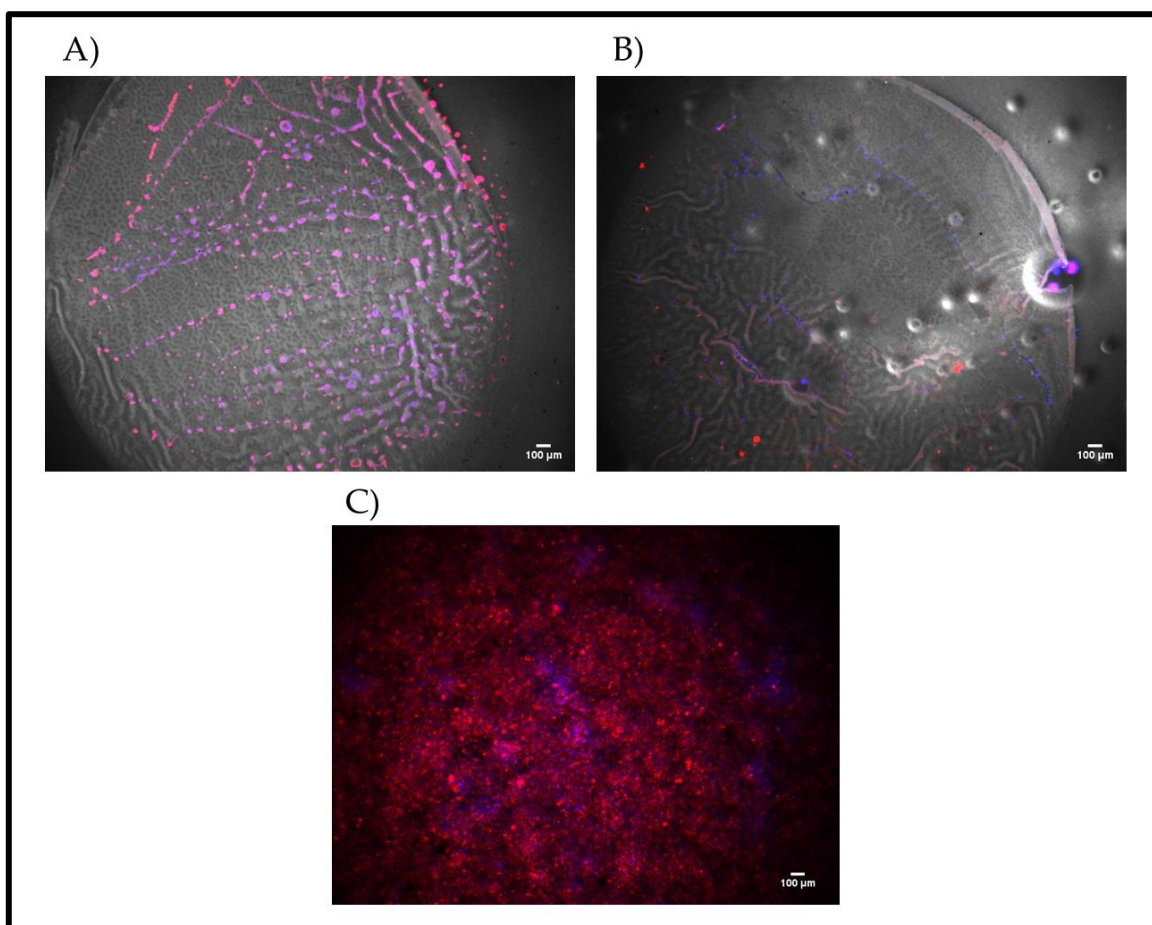


Figure 5.13: HEK293 cells cultivated on acid-oxidized PDMS formulated with 5% curing agent showing random ordered wrinkled surfaces. A) PDMS with an applied pre-strain of 20% before oxidation. B) PDMS with no pre-strain applied. C) Control culture of HEK-293 cells in a well, at the same seeding density (100K cells/24 well). Scale bars represent 100 µm. Material sample images are representative of n=3 seeded material surfaces whilst the control image is representative of n=2 control wells.

5.3.3.4 Cultivation of Human Limbal Cells a Matrix-Like Coating.

It is well appreciated in the field of epithelial cell/tissue culture, that the matrix conditions of the limbal niche are a requirement for the successful cultivation and maintenance of the limbal epithelial stem cell phenotype. Following this remit, the culturing conditions were further investigated through the alteration of a coating applied to the cells. In the first instance, this was trialled using a comparison of polydopamine coating against a polydopamine-collagen coating protocol. Figure 5.14 presents the bright field microscopy of these preliminary cultures. The cell morphology in these images, though less obvious due to the polydopamine fouling, can be seen to conform to the wrinkles surfaces in the acid-oxidised and dual-treated groups where wrinkle-based optical masking does not affect cellular visibility. In the flat controls (non-wrinkled plasma treated PDMS and no treatment) cells adopt a morphology similar to that observed in Figure 5.7.

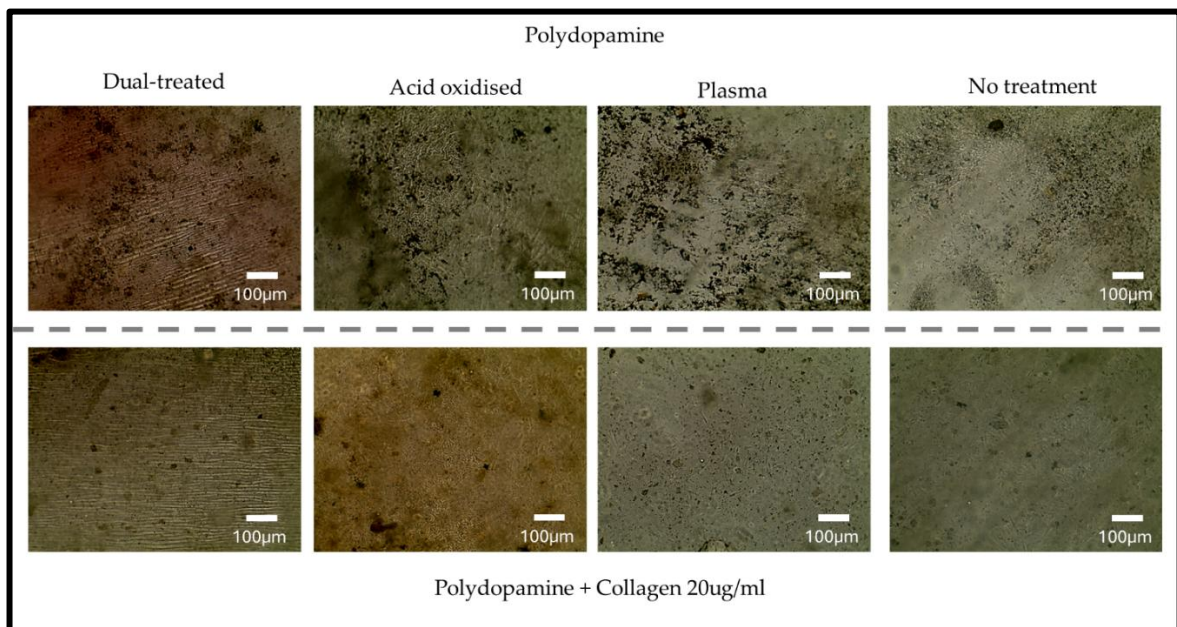


Figure 5.14: Bright-field imaging of human limbal cells cultivated in monolayer with Polydopamine or polydopamine-collagen coatings. N = 1 for each substrate type for each coating protocol, scale bars = 100µm.

Though both the polydopamine and polydopamine + collagen protocols visibly facilitated the adhesion of the limbal cells to the tested substrate (more so in comparison to the control) the visible black-particulate fouling by the polydopamine was a visible problem. To combat this visibility problem, it was proposed that a matrix alternative be utilised. This new coating needed to be strongly bound to the PDMS, resist the mechanical stresses of physical manipulation and be cytocompatible. GelMa was the ideal candidate in all of these respects due to its ability to be easily mixed with a photoinitiator and (as discovered) could be bound to the PDMS through this photocuring action. It was observed that after multiple washing of PDMS with (one side dip acid-oxidized for 5s and the opposing side masked to prevent oxidation) the photocured GelMa layer remained stuck fast to the oxidized region as demonstrated in Figure 5.15. In culture, the human cells grew well on this coating, demonstrating its biocompatibility.

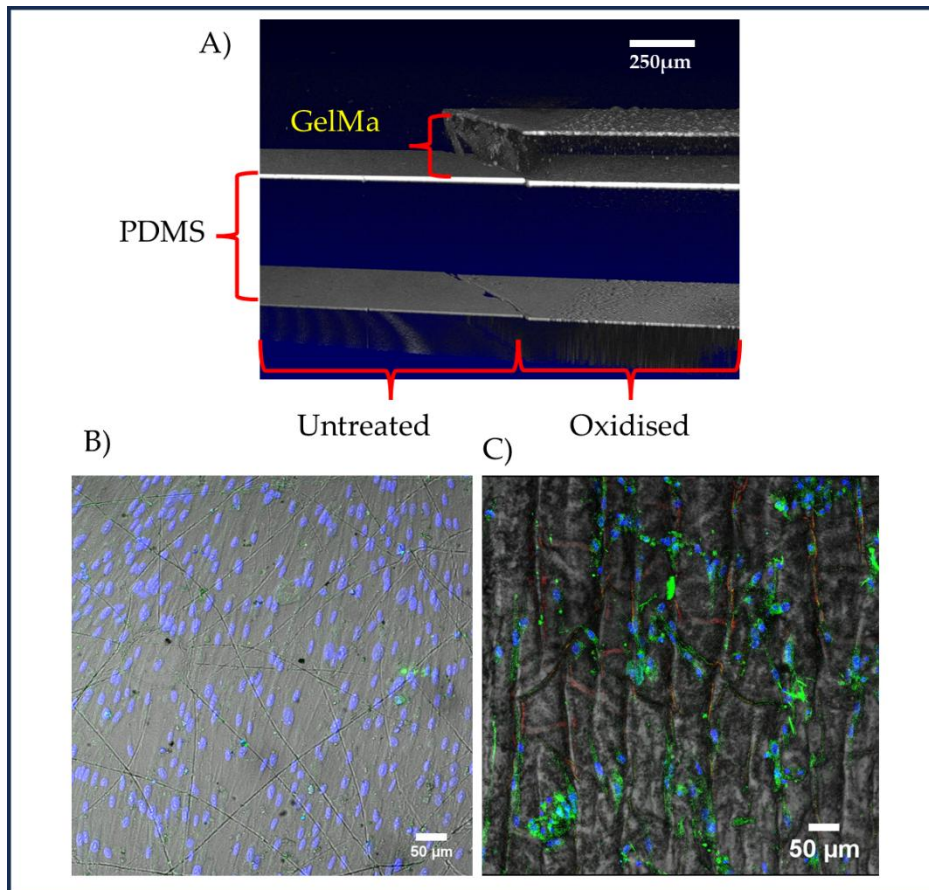


Figure 5.15: Trial of GelMa coated wrinkled PDMS for human limbal cell culture. A) An OCT image of the trial piece of PDMS which was dip acid-oxidized to assess the photocured binding of GelMa to the oxidized PDMS surface, n = 1. B) A flat plasma-treated control with a GelMa coating showing human limbal cells confluent on the surface, n = 1. C) Dual-treated wrinkled PDMS with a GelMa coating with human cells cultured on the surface in the static mode of culture, n = 3. For the immunofluorescent staining; Blue = DAPI (nucleus), Green = ABCG2 (stem cell marker) and Red = CK3 (Epithelial). Scale bars are as denoted.

5.3.3.5 Optimisation of GelMa Coating of Dual treatment Substrates for Cell Culture

From the variety of coating conditions tested, it was determined by visual assessment that GelMa (like in the human assays) was the most suitable coating for limbal stem cell cultivation on wrinkled substrates. Whilst this coating proved effective in the expansion of the human limbal cells and facilitated contact guidance in that cell type, in the porcine limbal epithelial stem cells the benefit of the GelMa coating extends

merely to the enhancement of cellular attachment. This is evident through the change in the number of cells detected on wrinkled substrates, where the percentage of GelMa was modified. It was also noted that increasing the concentration of GelMa had the potential to reduce the cellular sensitivity to the underlying topography, preventing the contact guidance or segregative effect of the wrinkles. Due to the high degree of variability observed in cellular distribution and image thresholding, quantification by particle count to assess distribution was considered inappropriate. However, the quality of the colonial morphology could be assessed even at low power, Figure 5.16 demonstrates this capacity to control cellular distribution by varying GelMa coating solution concentration. Thus preliminary assessment using the fluorescent dissecting microscope, using the actin stain, demonstrated that the 15% GelMa concentration facilitated the best balance between enhanced cellular attachment, colony formation capacity and cellular sensitivity to the underlying topography.

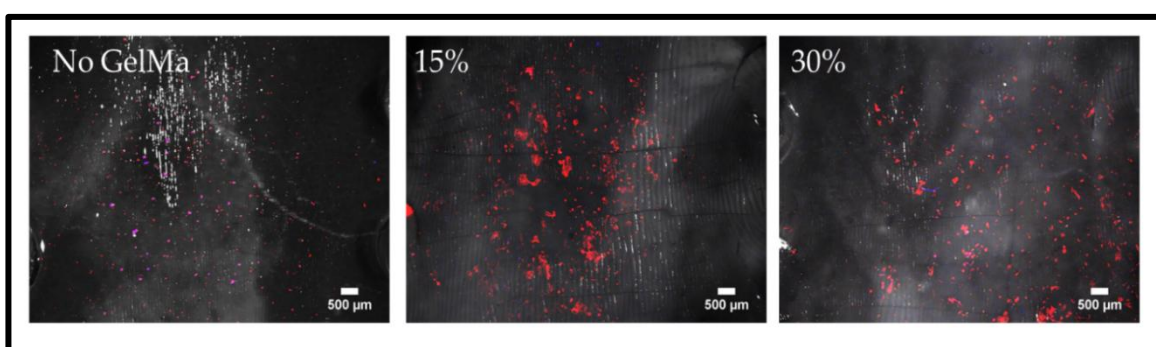


Figure 5.16: Variation in the concentration of GelMa in the coating process and the subsequent effect on cellular distribution. The leftmost image serves as a representation of the control substrates ($n = 4$), and the annotated images represent those substrates with the denoted GelMa concentration which survived through to cell culture ($n = 2$ each). DAPI (blue) was used to stain the nucleus, whilst Phalloidin (red) was employed to stain for actin. All scale bars represent 500 μm

5.3.4 Cultivation of Human Limbal Cells on Wrinkled Substrates

Following the assessment in monolayer, human limbal cells were seeded on wrinkled substrates and cultivated for 7 days. In the static mode of assessment, the substrates were autoclave sterilized and then allowed to wrinkle after being released from the stretching frame. Subsequently, they were affixed to the bottom of the wells using appropriately sized 3D-printed retaining rings. Retaining rings were used both in collagen/polydopamine and polydopamine coating stages in addition to the cultivation stages. The substrates were coated before wrinkling and then immersion seeded.

5.3.4.1 Immunophenotypic Assessment of Human Cells Grown on Static Wrinkled Substrates

After establishing the ability to cultivate the cells, followed by the optimization phase with media compatibility and surface interface coating, it was necessary to assess the effect of the wrinkled substrates on the human limbal cellular behaviour. The human limbal cells were first assessed for morphological and phenotypical changes using immunofluorescence after culture on static substrates for seven days as shown in Figure 5.17. The static topography elicited significant morphological changes and a strong contact guidance effect on the human limbal cells seeded upon the surface. The P63 expression appears to visually diminish but is weakly expressed. ABCG2 remains strong, whilst CK3 shows a visual increase in intensity. K12 demonstrates a patchy distribution, with non-specific binding to the GelMa layer. Vimentin retains a very bright, ubiquitous expression pattern. Nestin, also a corneal marker, presented with a patchy/weak expression. However it should be noted that in the static alignment experiment nestin presented strong expression, therefore whilst useful as a tracking marker in that experiment, its reliability as a marker is considered

tentative. In all examples shown, the cultivated cells align with the given topography, appearing to situate the cell body within the “crypt” of the wrinkles. Cellular elongation along the crypt, perpendicular to the direction of the direction of wrinkle propagation further indicated the cells were subject to contact guidance by the topography.

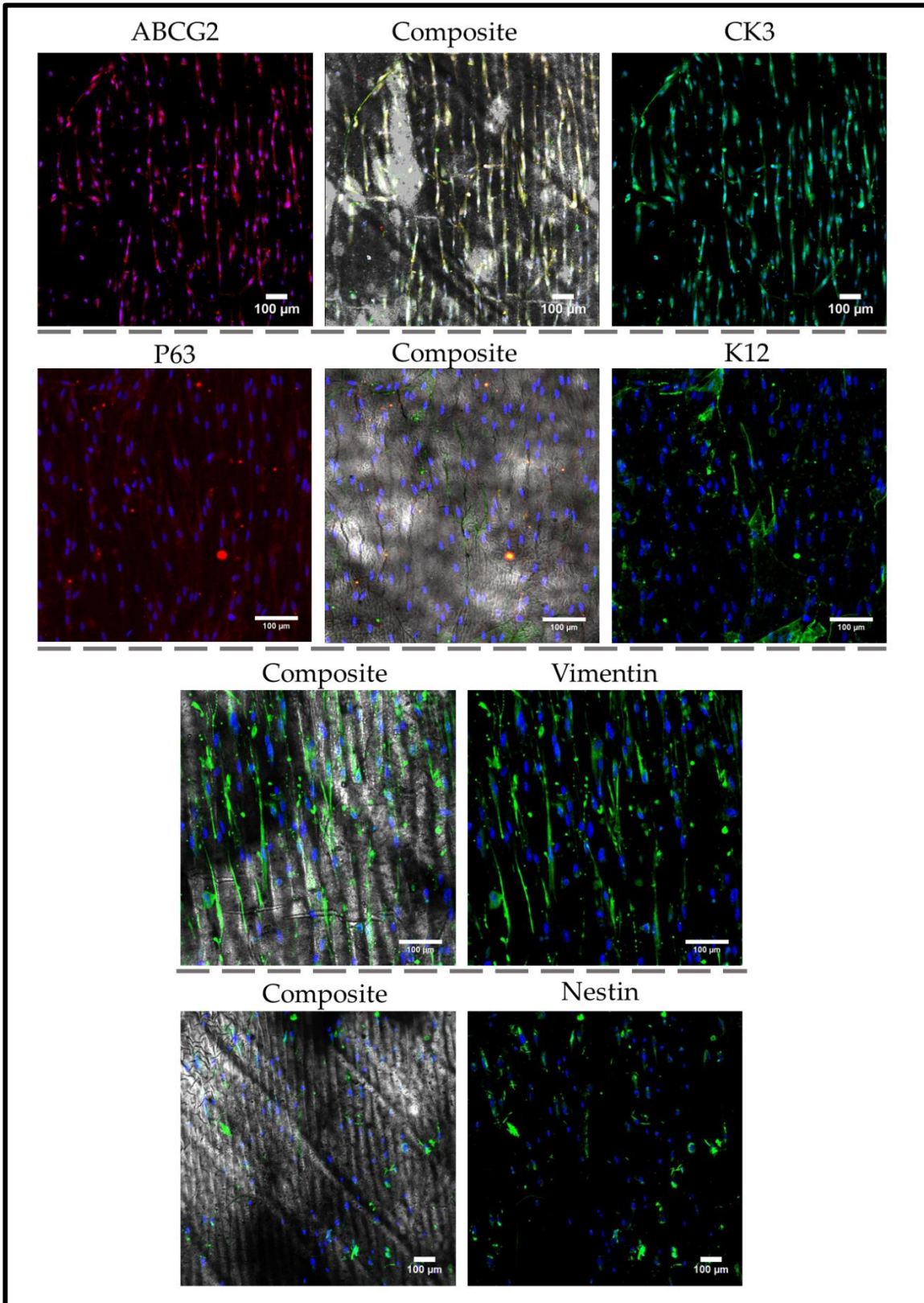


Figure 5.17: Immunofluorescent staining of human limbal cells seeded on static wrinkled topography. The markers are as denoted, all scale bars represent 100 μm. Images representative of n=3 samples.

5.3.4.2 *Wrinkled Surfaces as a Contact Guiding Bio-Instructive Surface*

To validate the visual observation of morphological change due to cellular alignment to the topography, the orientation of the cells was mapped as per the study carried out by *(Dimmock et al., 2023)*. The morphology and conformity to the topography of the cells were captured and analysed in ImageJ using OrientationJ as presented in Figure 5.18. The brightest markers were used for this image-based method, therefore images for CK3, vimentin and nestin staining were used for this analysis. This method demonstrated cell alignment could be graphically represented and compared using histogram plots of detected feature orientation in degrees against the count of detected features. Cells cultivated on wrinkled substrates showed a greater degree of order, resulting in a more defined bell curve on the histograms compared to the control images, which resulted in a more level distribution of orientations.

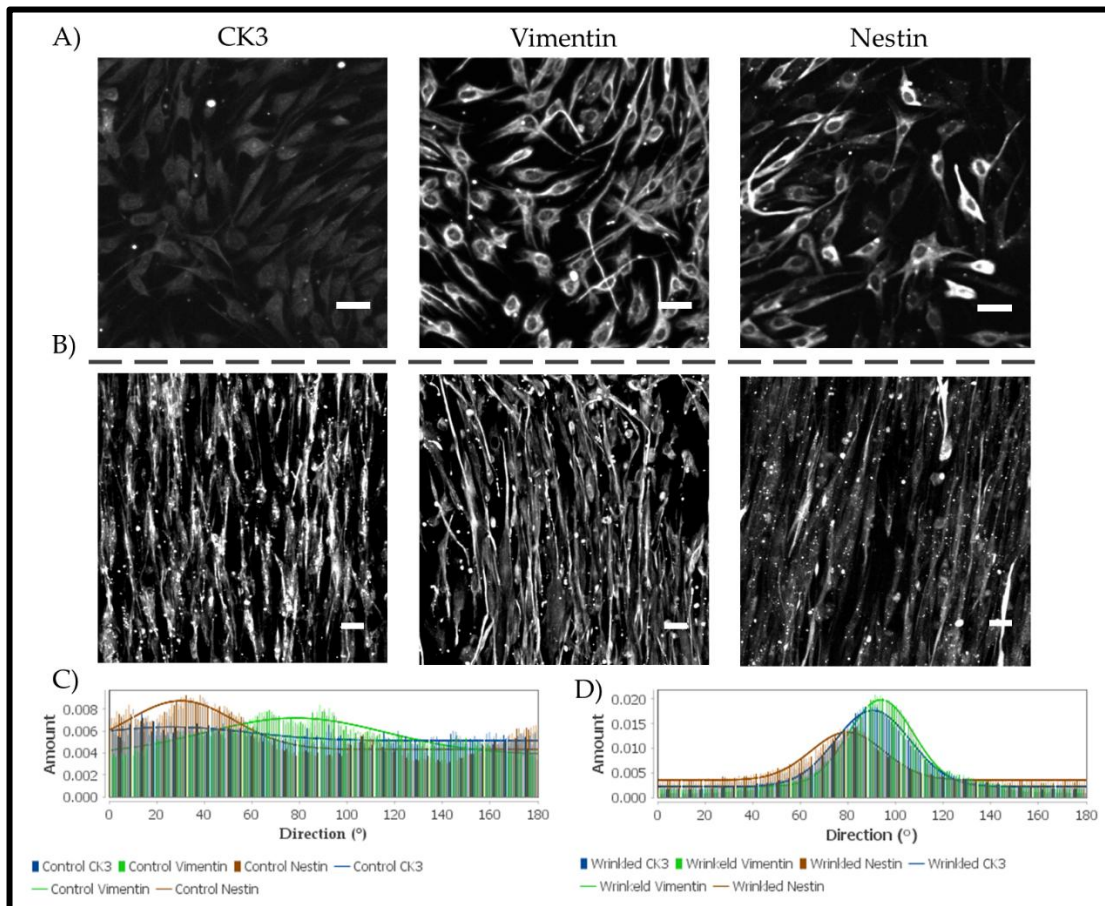


Figure 5.18: Analysis of alignment of human limbal cells on aligned substrates. Top panel: Single channel fluorescence images showing both morphology and alignment of cells. Row A) control cultures in monolayer and row B) shows the cells cultured on the substrates. Each set of images is representative of $n=3$. C) a Histogram of alignment of cell features (direction/o) against the count for control cultures and D) a histogram of direction/o against the count of cell features for the wrinkled substrate cultures. Each histogram line is plotted from a single image to form a representation of the whole dataset.

5.3.5 Cultivation of Porcine Limbal Epithelial Stem Cells on Wrinkled Substrates

5.3.5.1 Culture of Porcine Limbal Epithelial Stem Cells on Static Wrinkled Substrates

Once the isolation and expansion of the porcine limbal epithelial stem cells were established, this cell type was cultured on static wrinkled surfaces to assess the effect of the topography on the cell growth and distribution. As with the human cellular work, the assessment of the topographies' effect on the cells is preliminary. Initially, the porcine limbal epithelial stem cell attachment was unpredictable to the wrinkled substrates as demonstrated in Figure 5.19, with seemingly inconsistent instances of total seeding failure to both flattened and wrinkled substrates (using both droplet and immersion seeding methods). Therefore it was necessary to explore coating properties and culturing conditions to determine the most favourable for this cell type.

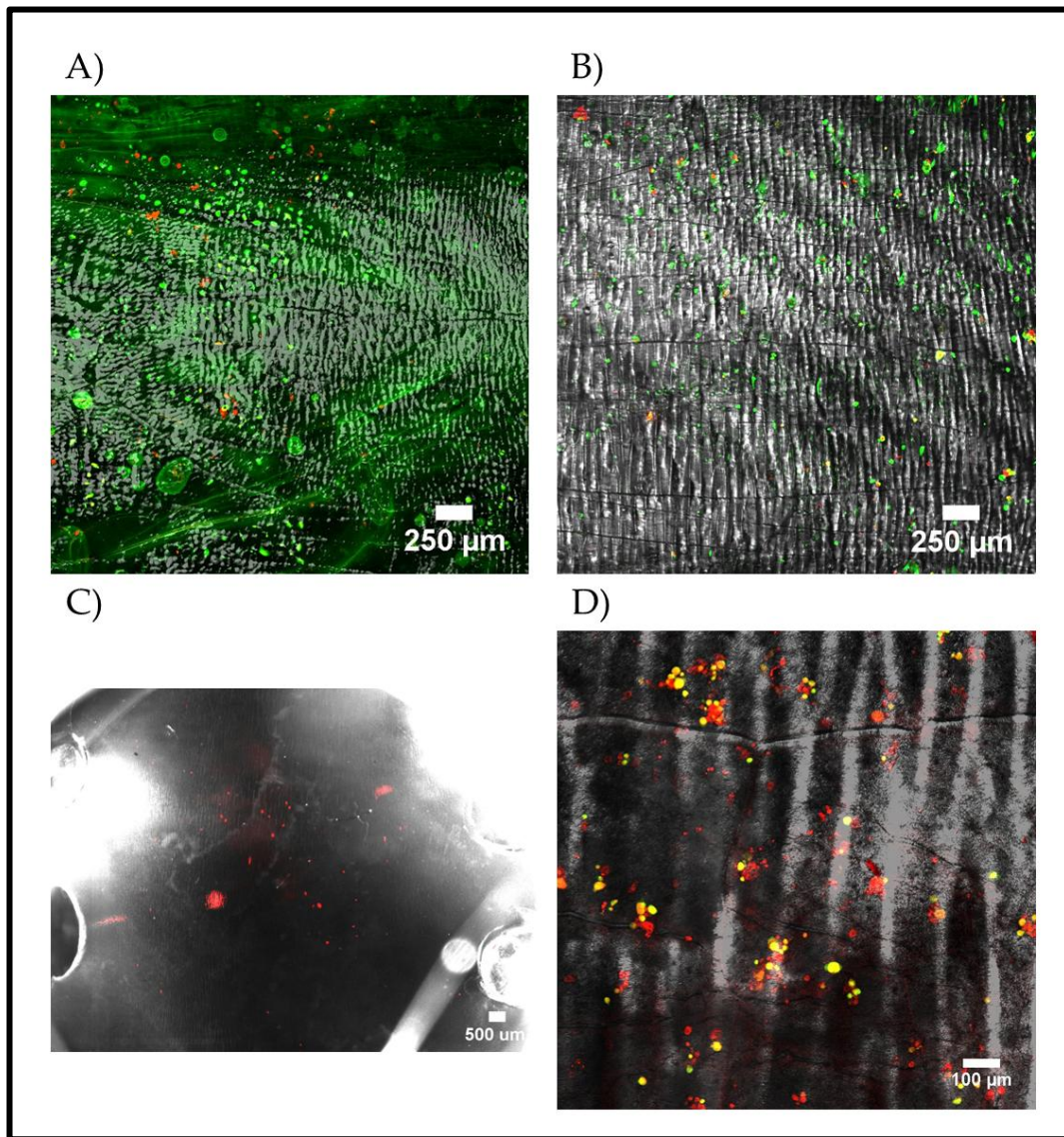


Figure 5.19: Porcine limbal epithelial cells cultivated on dual treatment wrinkled PDMS with various coatings. A) static co-culture with 3T3IN, stained with a Calcein (live/green) and propidium iodide (dead/red) stain. B) static control culture with no coating and no co-culture with the same live/dead stain as A) n=2 substrates each for A) and B). C) Collagen-coated dual treatment substrate, the cells were stained with an actin stain (Phalloidin Texas Red), n=3 substrates. D) Dual treatment PDMS with a photocured 15% GelMa coating, stained for the epithelial marker CK3 (green) and the stem cell marker P63 (red), n=3 substrates. The scale bars for each image are as denoted.

5.3.5.2 Wrinkle Morphology Variation in PLESC Culture

In addition to the coating and culturing conditions, the dimensions of the topography also played a role in the control of cellular behaviour, an effect observed in newly extracted PLESCs. It is proposed that maintaining an early passage number when performing such topographical studies is essential as these cell types are considered to retain their phenotypic and morphological plasticity at this point. Here, it is demonstrated that there is a difference between the 3.33% curing agent chips and the 2.5% curing agent chips. As ascribed before in Chapter 4, the lessening of the curing agent in the PDMS chip formulation results in a wider wrinkle crypt formation at the end of the dual treatment process. It was observed, and exemplified in Figure 5.20, that with greater crypt width there was lesser tight nucleation of cell clusters, with better distribution of cells within the crypts as observed through the wider dispersion of stained cells in the 2.5% chips compared to the 3.33% chips where the cells remain more tightly clustered. It is proposed that the wider crypt substrates enable truer sensing of the curvatures and truer biomimicry. It was observed in the cross-sectional views of the z-stacks that p63 was more basally expressed whereas CK3 appeared more apically expressed in cells on the 2.5% (wider and deeper crypt shape) chips. However, in the 3.33% substrates the expression manifested inversely, with CK3 appearing more basally and P63 more apically. These observations could be attributed to the formation of tight clusters of cells on the 3.33% substrates which may subsequently alter the spatial distribution of the markers in comparison to more topographically compliant 2.5% chip cultures.

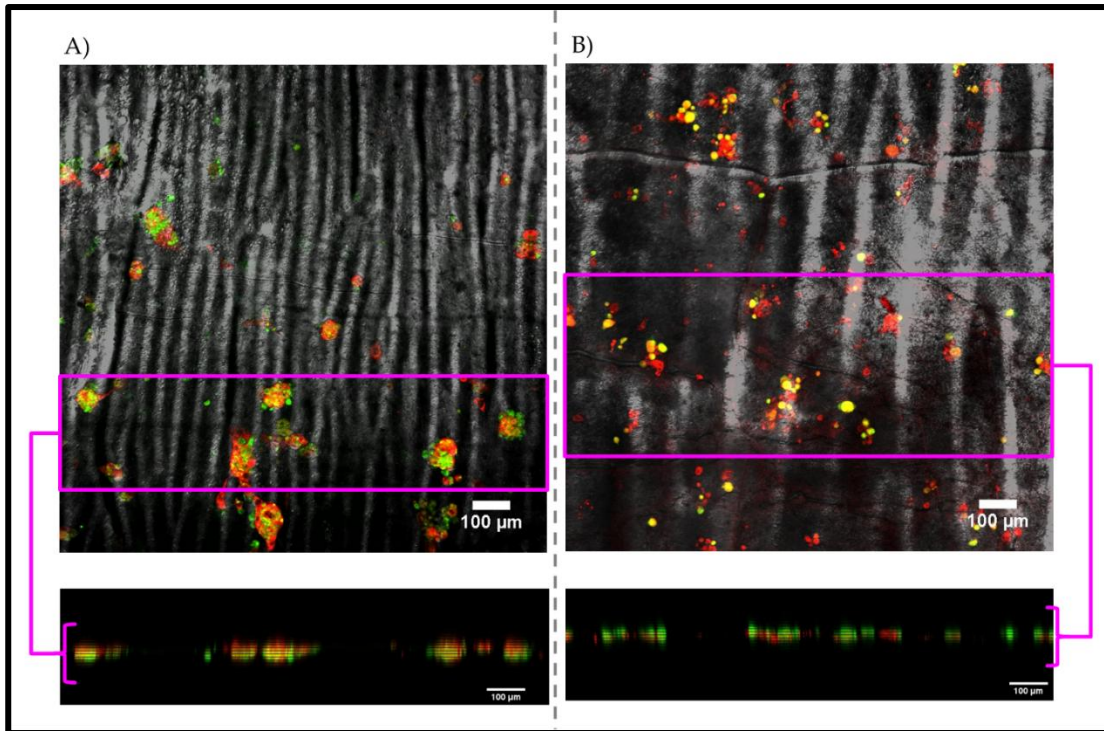


Figure 5.20: PLESCs cultivated on substrates of different crypt widths with immunofluorescent staining for the stem cell marker p63 (red) and the epithelial marker CK3 (green). A) PLESCs cultivated on PDMS wrinkled via the dual treatment method, formulated with a 3.33% curing agent with a 15% photocured GelMa coating. B) PLESCs cultivated on PDMS wrinkled via the dual treatment method, formulated with a 2.5% curing agent with a 15% photocured GelMa coating. All scale bars represent 100 μm . $N=3$ per substrate type.

5.3.5.3 Proliferation Profiling of the Growth of PLESCs on the Topographies

To validate the success of the cultivation of LESC on the substrates over time, the metabolic viability of the cells was assessed using the cell counting kit-8 (CCK8), the profiles of which are summarized in Figure 5.21. This kit, even without calibration curves (which were not produced due to insufficient cell and substrate numbers), can give a direct arbitrary comparison of cell proliferation over time between separate cultures of the same cells if seeding density is controlled and thus estimate the difference in population expansion profile between substrate types. In this assay, the porcine limbal epithelial stem cells (PLESCs) were cultivated over 15 days total, with assessment checkpoints wherein the amount of CCK8 reagent turnover was

measured. It was observed with interest that all groups present a descending serpentine trend, which contrasts against the control group of the LESC and 3T3IN co-culture, which had a positive proliferative trend. This means that the substrates throughout the whole culture period reduced the resultant number of viable cells available to turnover the CCK8 reagent into a readable product. Out of the substrate groups the PDMS formulated with a 3.33% curing agent presented a slightly higher overall viability compared to the 2.5% curing agent fractionated PDMS, Figure 5.21 shows these differences in trends.

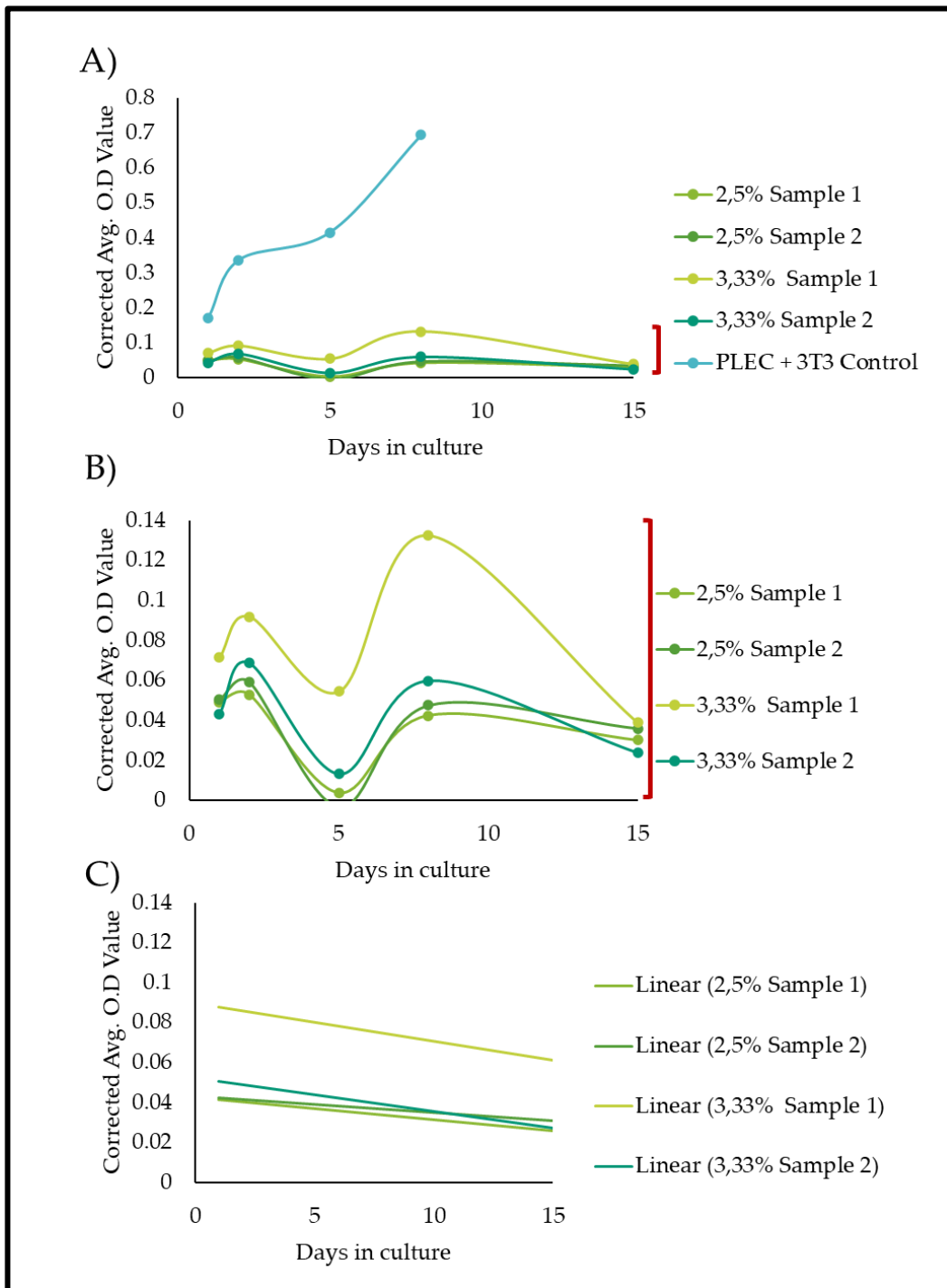


Figure 5.21: Graphs displaying the CCK8 proliferation profiles of the PLESC cells grown on the wrinkled surfaces. A) Presents the graphs of the time series as acquired for all cultures including the control (PLEC+3T3 control), B) shows the wrinkled-only culture and C) shows the linear trend extrapolated between the acquisition points between days 0 and 15. $N = 2$ for each wrinkled culture and 1 for the control culture.

5.3.6 Limbal Cell Cultivation on Dynamized Substrates

5.3.6.1 Cultivation of Human Limbal Cells on Dynamized Substrates

Once it was established that the human limbal cells were successfully grown on the static substrates and the contact guidance effect evaluated, the model progressed into the dynamic mode. In this mode, the cells were seeded on pre-stretched substrates and once the cells had attached, the substrates were relaxed in the bioreactor to enable wrinkles to form. Subsequently, the wrinkles were flattened by stretching to +20% material elongation and re-wrinkled to induce cell distributional changes between stages. Three-day intervals were used to ensure the cells had sufficient time to adjust to the modified topography. Figure 5.22 demonstrates a timeline, using fluorescent live-dyed cells and associated orientation analysis, to track the effects of wrinkled substrate dynamization. The associated histograms describe the alignment of the cells at each stage, as measured using the OrientationJ plugin on the images presented. Histograms with high and prominent central peaks indicate a large degree of alignment parallel to the vertical, and peaks to the far left and right indicate anti-parallel alignment. Histograms with less parallel peaks (or more even distributions) are considered to represent cell samples that are more randomly distributed.

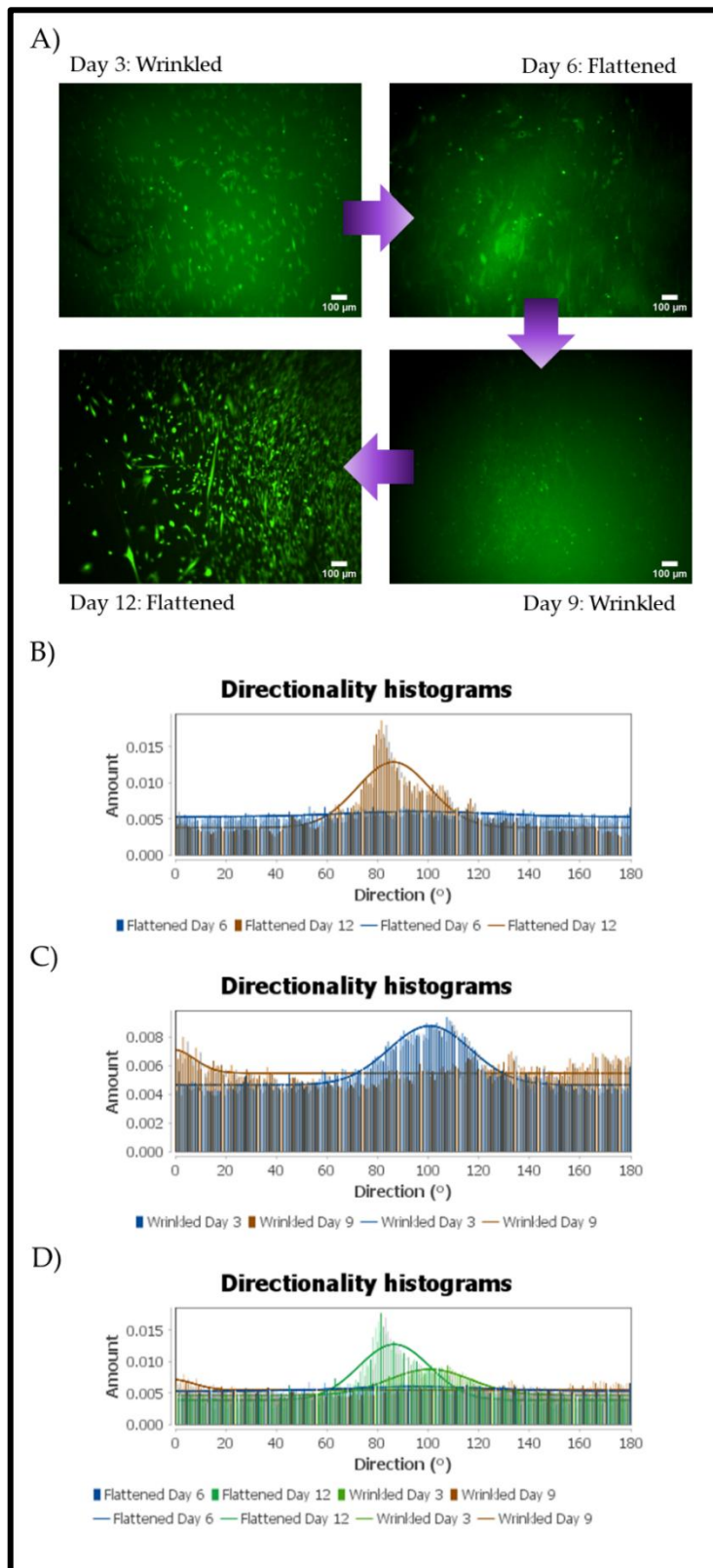


Figure 5.22: Human limbal cells cultivated on dynamized substrates with associated alignment analysis. A) Fluorescent tracked live imaging timeline of human limbal cells on wrinkled substrates, showing stages of wrinkled and flattened states with associated time points. B) Histogram of alignment for flattened time points. C) Histogram of alignment for wrinkled time points. D) Histogram of alignment for all time points. Each histogram line is plotted from a single image to be representative of the whole data set. The image panel is representative of $n=3$ bioreactor wells.

5.3.6.2 Preliminary Cultivation of PLESCs using a 3T3IN Feeder Layer

In preliminary model trials, dynamization was introduced to the cultivation of this isolated cell type. Firstly in these initial trials, the isolated cells were seeded upon the substrates with an accompanying 3T3IN feeder layer in co-culture (2×10^4 3T3IN cells/cm²) in a droplet on a flattened dual treatment wrinkled surface with a 30% GelMa coating surface. This culture was compared to a dynamized culture sans 3T3IN cells. Assessment of cellular retention after a single cycle was the only viable option in this assay due to widespread cell loss with examples of these surfaces presented in Figure 5.23 It was observed that between 3T3 and feeder-free cultures, there was very little difference cell death as determined by the calcein/propidium iodide assay, with only marginally more cell death in the 3T3 feeder cultures. This cell death can be attributed to the death of some of the inactivated 3T3 cells which are not present in the feeder free culture which may have been induced into cell death by the substrate dynamization.

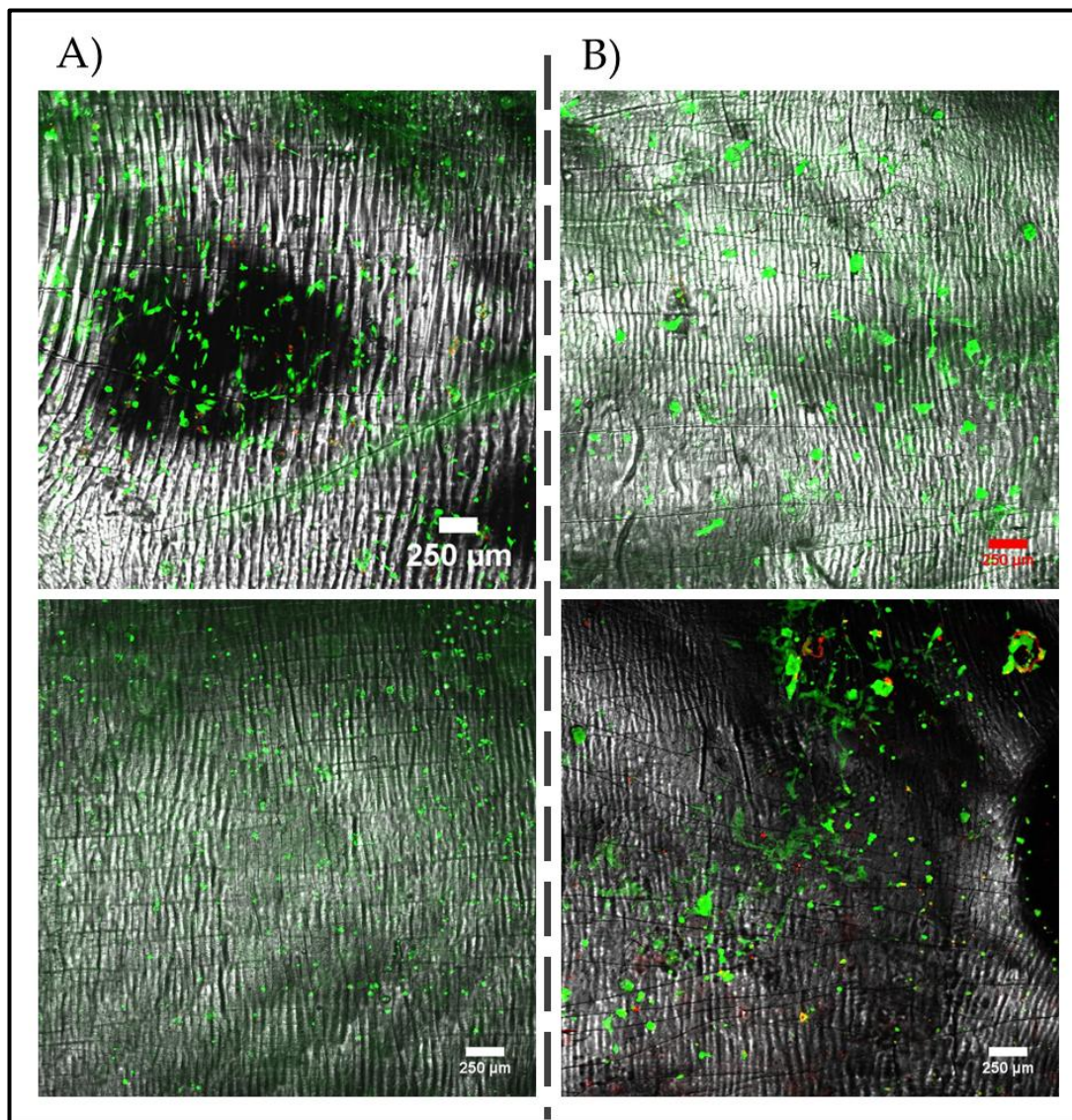


Figure 5.23: Live dead end-point of cultivation of isolated PLESCs on dynamized wrinkled substrates. A) shows substrates where the porcine cells were cultivated without a feeder layer whilst B) shows substrates with cells cultivated with a feeder layer. Live cells are stained with calcein (green), dead cells are stained with propidium iodide (red), and scale bars represent 250 μm ($n = 2$ for each).

Calcein (live) and propidium iodide (dead) facilitated the assessment of both cell attachment and the impact of cell viability imparted due to the dynamization of the substrates. Here it was demonstrated using a live-dead stain that dynamization of the substrates did not have a cytotoxic effect on attached cells but in this preliminary instance, it was not possible to ascertain levels of detachment as the before images were not able to be recorded due to an inability to facilitate fluorescent live-tracking at

that point. It was also observed that in the feeder negative substrates, the attached cells adopted more singular fibroblastic morphologies compared to the 3T3IN positive substrates wherein more of the attached PLESCs maintained small clustered morphologies after the induction of topography.

5.4 DISCUSSION

In biomedicine, there is a strong demand for novel approaches for both modelling capabilities and treatment modalities. Tissue-engineered constructs and cell-based therapies are beginning to fill this gap with tailored solutions where designed constructs facilitate powerful benchtop platforms. An example of static limbal culture is the Real Architecture For 3D Tissue (RAFT), a commercial-grade system that has been employed to cultivate and maintain 3D limbal stem cells (*Levis et al., 2013*). The raft system differs from the presented bioreactor system on two major principles; 1) the RAFT system morphology is static thus cannot be dynamically tuned during culture and 2) the topography in the RAFT system is made out of the matrix substance, whereas in the wrinkled substrate bioreactor, the topography is evolved on a supporting substrate which has the potential to be functionalised with different matrix or other functional molecules (a potential subject for future study). The advantage of the RAFT system over the wrinkled substrate bioreactor is that it is a commercial grade bioreactor, meaning the topography production (dimensionally and compositionally) fall within tightly bound parameters. These trait are not shared by the wrinkled bioreactor system where each wrinkled substrate (and gel coating) are handmade using a non-automated process resulting in a more variable topography/ substrate system being produced. Another example of ophthalmic tissue engineering is the utility of surface topography to create scaffold-free corneal lamellae, moving towards the ability to create layered corneal stromal structures (*Syed-Picard et al., 2016*). In vitro,

the modelling of optical structures drives drug development and the study of disease. The advantages of advancing away from reliance on in-patient and animal studies include improved validity and specificity of testing, improvement in accessibility and ease of performance. Additionally, the ethical concerns presented in using live animal/human subjects are averted (*Islam et al., 2019*). A prime example of such a model is the “mini-cornea”; an engineered cellular model developed for benchtop-based ocular irritation testing (*Kim et al., 2023*). In limbal niche modelling, work has mainly focused on replicating the matrix conditions, for example, the development of laminin-based culturing surfaces for limbal epithelial expansion (*Polisetti et al., 2017*) and analysis of modified collagen matrices in limbal cell stemness maintenance and epithelial differential potential (*Haagdorens et al., 2023*).

Presented in this chapter is the culmination of the preliminary assessment of the cellular responses of isolated primary limbal cells, from human and porcine sources to the wrinkled substrates. The development and optimisation of culture conditions utilizing the wrinkled substrates were driven towards supporting static and dynamized wrinkle surface culture. In terms of the applications of coatings, it was observed that the increase in concentration (the undiluted GelMa), though spread thin using a cell scraper whilst the substrate was still flat, still prevented the contact guidance of cells from topography. Polydopamine was utilised to aid in the application of collagen to the substrates and demonstrated the best contact guidance overall, however, the aggregation caused by the polydopamine (the black aggregates) reduced imaging quality and showed that the intermediate was not uniformly bonded to the surface during coating. Therefore there is a level of cellular control that can be determined by coating selection as it was demonstrated that there was a visual difference in the quality of contact guidance and cellular distribution between the variety of coating types

applied. Of the tried substrate coating methods trialled, GelMa proved both the most reliable to apply and demonstrated the ability to facilitate cell attachment and contact guidance.

This work provides the working stepping stone for the progression of a dynamic disease model, which with further characterisation, has the possibility of yielding important cellular response information to crypt conformational changes. This assessment of cellular response also validates the cytocompatibility of these surfaces and forms the latter stages of the developmental process for this multi-stage material fabrication and substrate treatment methodology. In parallel with this, the isolation and expansion of primary limbal cells from human tissue and primary limbal epithelial stem cells (LESC) from porcine tissue were validated *in vitro*. The decision to use porcine tissue as the alternative primary isolation source was related to its well-recognised similarity in anatomical structure (*Notara et al., 2011, Grieve et al., 2015*) and maintaining phenotypical consistency with human LESCs (*Notara et al., 2011*). The structural similarities are chiefly the mirroring and alike presentation of limbal niche microstructure, with the presence of the limbal palisades of Vogt, ERP and PR presenting in similar proportions, with minimal differences in dimensions. However, it was observed, particularly during dissection that the epithelial layers of the porcine tissue were thicker in comparison to the human donor corneas. This observation can be confirmed by comparing results obtained by studies measuring histological sections of porcine and OCT sections of human corneas. The porcine limbal epithelium was found to be $117 \pm 4.9 \mu\text{m}$ ($n=28$) (*Nautscher et al., 2015*) compared to human limbal epithelium which was found to be $84.3 \pm 10.1 \mu\text{m}$ ($n=10$) (*Francoz et al., 2011*). This difference in epithelial thickness may account for the increase in ease in the isolation of porcine LESCs in comparison to the isolation from human corneas. It is proposed

that having a thicker epithelium may present a greater depth of harvestable epithelium which can contain viable LESC which in turn will provide a greater yield of LESC from the digested tissue.

In the developmental testing, as presented in section 5.3.3, the preliminary assays explored the stages of wrinkling formation and their compatibility with cell culture. It is important to remember that due to the exploratory nature of these assays, non-limbal cell types were used due to immediate cell availability and the conservation of effort for optimised process development flow. However, Cell types such as the rat cardiomyocytes and HEK-293 types were considered suitable due to their adherent nature and apparent sensitivity to substrate surface topography. This effect is starkly demonstrated when both of these cell types were presented with fibrous topologies, forming elongated and fibre-conforming morphology compared to a flat surface (*Wychowaniec et al., 2020, Kobuszewska et al., 2021*). Additionally, it should also be noted that the cellular effects for these three surfaces are not extensively explored due to the sub-optimal nature of the substrate systems being employed.

Notably in 5.3.3.1, the laminated block topography, despite this method initially promising an interesting alternative method of wrinkling at a macro-scale proved to be disappointingly ineffectual in cell culture practice. First and foremost, as demonstrated in Figure 5.10 there is an obvious decay in wrinkle quality. Upon closer examination after fixation, it was observed the polymer membrane layer had delaminated from the PDMS bulk. Despite background trials of different glues including epoxy, as it currently stands the liquid silicon compound used as glue was the only adhesive safe for cell culture and facilitated wrinkling on compression without damaging the membrane. Although the sub-optimal cell adhesion observed could have feasibly been optimised

with collagen (similar to how PDMS can be coated (*Sharma et al., 2019*)) it was considered inefficient to attempt such optimisation with the laminated block method.

In the plasma treatment method, the rat cardiomyoblasts demonstrated both good adhesion and practicability in staining and proved the surfaces in all pre-stretched conditions could influence the cells through changes in alignment, proving there was a wrinkled surface present despite it visually indecipherable (*Glatz and Fery, 2018, Kobuszevska et al., 2021*). This proved to be a stark contrast in comparison to the laminated block topography, which showed no obvious cellular effect, could not be stained (even simply with haematoxylin and eosin) and was impractical for cell culture.

Despite these obvious significant advantages, however, there was one major downfall to this plasma treatment topography type, the size of the features generated. The crypts were only visible/measurable at the highest magnification in scanning electron microscopy. Therefore, even considering the visible effect upon the cardiomyoblast culture, it was determined an inappropriate substrate type due to not being biomimetic to the limbal crypt dimensions (which should be ideally approximately 50µm deep by approximately 35-120 µm (*Grieve et al., 2015, Bizheva et al 2017*)).

Finally, the acid oxidation step of the dual treatment method of wrinkle formation on PDMS was tested for basic cytocompatibility. HEK-293 cells were employed during this round of evaluation, due to ease of handling and reported use in a similar topographical study, this cell line was deemed appropriate for a basic cytocompatibility sensing model at this stage (*Wychowaniec et al., 2020*). This method of wrinkling produced typically randomly ordered wrinkles, even with the application of a pre-applied strain.

Consequently, the requirement for the dual treatment method, as discussed in Chapter 4, is the predominant method of wrinkled substrate employed throughout the later stages of the research. In terms of cytocompatibility, the acid oxidation testing highlighted a high degree of visually observed variability of retained cells. This is even after prolonged culture, demonstrating that this surface, even with collagen coating has sub-optimal cell attachment properties. To date there are no direct cell culture applications in literature attributable to this cell culture application, however, the work performed in the development of this wrinkling technique demonstrated a reduction in water contact angle (*Watanabe and Mizukami, 2012, Watanabe and Shinoda, 2014, Watanabe and Hashimoto 2015*). Reducing the water contact angle of a surface generally can relate to an increase in surface biocompatibility, or at least an increase in the prospect of cellular attachment (*Ferrari et al., 2019*). However, as observed in Figure 4.15, it is demonstrated by atomic force microscopy that the acid-oxidized surface has greater roughness, compared to both the dual treatment wrinkled surface and the plasma-treatment wrinkled surface. Thus it is proposed that an increase in nanoscale roughness may result in the inhibition of cellular attachment, similar in mechanism to the antibacterial antifouling surfaces which use surface roughness to prevent bacterial adhesion and biofilm formation (*Chien et al., 2020, Mu et al., 2023*).

In this chapter, it has been demonstrated that primary cells have been isolated from tissue from two primary sources. The first was human corneal buttons which were maintained in organ culture and received from an NHS tissue bank. The second source was freshly enucleated porcine eyeballs, typically extracted on the day of slaughter. Once the porcine eyes were dissected into corneal buttons the remaining and cell isolation methods were kept consistent with the human methods. Despite maintaining consistency between the methods, it was observed that from different tissue sources,

different cell types were isolated. The human tissue yielded cells which adopted a fibroblastic-like morphology, these cells were spindly and did not adopt the typical LESC morphology (*Polisetti et al., 2020*). However, they expressed the canonical limbal stem cell marker ATP-binding cassette binding protein G-2 ABCG2, the neural crest marker nestin and the limbal epithelial marker cytokeratin 3 (CK3). Additionally, these cells expressed the mesenchyme transitional marker vimentin, giving credence to the cells having a mesenchymal/fibroblastic lineage (*Schlötzer-Schrehart and Kruse, 2005*).

In contrast, the cells extracted from the porcine tissue adopted cobblestone-shaped morphology and formed large, discrete colonies. These morphological and expansion characteristics strongly indicate the isolation of limbal epithelial cells as these characteristics are concordant with numerous established methods which use isolation methods similar to the protocol used in this project (*Chen et al., 2011, Tovell et al., 2015, Kim et al., 2017, Polisetti et al., 2020*). These colony-forming cells, with both inactivated 3T3 cells and coated wells and substrates demonstrate the ability to maintain the stem cell marker p63 and a markedly limited expression of the epithelial marker cytokeratin 3. These observations together indicate strongly that the cells isolated from the porcine tissue were true of progenitor lineage and could be designated as limbal epithelial stem cells LESC (Schlötzer-Schrehart and Kruse, 2005). With consideration to the ability to extract true morphological and phenotypial LESC from porcine tissue, using the same dissection and digestion protocol, it was considered that the mesenchyme/fibroblastic type cells isolated from the human tissue arose from a pre-extraction condition.

The human corneal buttons were maintained in organ culture for up to 4 weeks before isolation, it is proposed that the time in organ culture without pro-stem cell

medium may have resulted in potentially one of two transformative pathways. The first, is the differentiation of the progenitor cells towards the epithelial phenotype following the XYZ/conventional growth and regenerative pattern, as described in Chapter 1 (*Thoft and Friend, 1983, Mort et al., 2009, Sartaj et al., 2017*). The second proposed pathway for cellular change during long-term organ culture storage is through the progenitor cells undergoing a cellular change akin to the epithelial-mesenchymal transition (EMT). This is a differential pathway associated with both cancer and epithelial cells dependent on the wnt-catenin pathway (*Kawakita et al., 2012, He and Jin 2017, Shibata et al., 2019*). There has been observation of fibrotic changes in the cornea with limbal invasion, indicating rudimentary regeneration, due to intervention by air exposure (*Kawakita et al., 2005*). In controlled in vitro studies such as growth factor controlled studies it is demonstrated that the modulation of Smad-7/notch pathways was facilitated through the alteration of TGF β 1 to manipulate EMT (*Kawakita et al., 2013, Tsai et al., 2014*). Therefore it is possible to suggest that cellular fibrotic changes might be mediated through the EMT, this is further reinforced by the strong experimentally ubiquitous presence of vimentin. This pervasive trend of vimentin expression was found by immunofluorescent staining at all stages: first in vivo in the staining of tissue sections (section 5.3.1.1), subsequently in monolayer post-isolation (section 5.3.2.3) and finally in wrinkled substrate culture (section 5.3.3.2). With both considerations in mind, it is possible to surmise that the cells isolated are, though limbal in origin, not LSCs and may have undergone a transition into another cell type. Whilst elevated CK3 indicated a potential epithelial commitment, elevated Vimentin indicated potential a mesenchymal transition (both by immunofluorescent observation). More future work is required to determine the precise cell type isolated. In this future work PCR should be used to validate both groups of markers including the corneal epithelial marker expression (CK3/K12) and the limbal stem cell marker expression

(P63/ABCG2). To more fully explore the involvement of the EMT pathway, vimentin should be validated by PCR but also additional mesenchymal markers should be explored both by immunofluorescence and PCR. N-cadherin and fibronectin are mesenchymal markers which are implicated in cells which undergo the EMT pathway (*Zeisberg and Nielson, 2009*). Future work could implement strategies for the mitigation of the apparent EMT to aid in the preservation of the LESC phenotype and morphology. Primarily, in this application EMT can be prevented by extracting the LESC from the corneal buttons within a small number of days after cornea donation. This time-dependent effect of preventing EMT/loss of LESC phenotype is observed in the cells isolated from the porcine tissue, from which cells were extracted at a maximum of 48h post-slaughter. To further investigate/manipulate the environmental conditions which may induce EMT, the use of a bioreactor, such as the twin-chambered perfusion system used for the long-term preservation of porcine corneas. This application used a chamber system to enable the separate perfusion of the anterior and exterior sides of a cornea, where the isolated corneoscleral button was used as a water-tight seal in between. Perfusion of two different medium compositions, suiting an endothelial surface on the anterior side and an epithelial composition on the exterior side resulted in better corneal viability and preservation of the basal LESC markers ABCG5 and K14 (*Guindolet et al., 2017*). The use of a perfusion bioreactor such as this may prevent EMT for the longer-term storage of human corneas, by replicating the more natural movement of fluid and enabling a constant refresh of the medium, preventing the accumulation of factors (such as TGF- β) in the medium which would encourage the propagation of the EMT (*Xu et al., 2009*).

It is considered that increasing the storage time of the porcine corneas in the same manner as the human corneas (storage in ocular medium in a sealed glass

bottle) would have a similar effect on time- dependent loss of harvestable LESC. Conversely in human tissue, extracting the LESC from donor patients within a short amount of time after donation would more likely retain a larger amount of viable LESC available to extract. However it has been found that corneas maintained in organ culture for up to 4 weeks were able to yield LESC presenting cobblestone morphology and positivity for the key marker P63 and negativity for cytokeratin 3 (Tovell *et al.*, 2015). These findings contradict the practical finding in this project, however, the inclusion of a feeder layer and use of stromal medium additives including dexamethasone, platelet-derived growth factor and L-ascorbic-2-phosphate, may account for these changes in observations.

In the porcine isolation and culture optimisation phase, the co-culture with inactivated 3T3 mouse fibroblasts versus collagen-coated wells was investigated. Using inactivated 3T3 cells is an established and recommended method for epithelial culture (Sharma *et al.*, 2011, Hynds *et al.*, 2018, Zekušić *et al.*, 2023). However, in an attempt to preserve cell purity, it was proposed that a matrix protein coating such as a simple collagen coating of the wells may suffice, in conjunction with the medium formulated for these isolated cell cultures. The confluency profile attained by automated live cell imaging coupled with the live Bright-field images of typical colony formation of cobble-stone cells indicated that this hypothesis held. This indicated that collagen-coated wells and plates are suitable, alongside the LESC medium formulation used in this study, for the cultivation and expansion of PLESCs.

In this preliminary work of testing the cellular response to the wrinkled substrates produced by the dual treatment method, human and porcine primary isolated cells were used, in both static and dynamised cultures. In both types of culture, there was an observed influence over the cells isolated in both species. These effects,

also are concordant with the initial observations found within the developmental cultures, whereby the surface topography was able to induce major contact guidance effects including alignment and cluster segregation. Incidentally, the type of contact guidance was considerably biased between either alignment or cluster segregation between the isolated cell types.

In the more fibroblast/mesenchymal type cells isolated from the human tissue, it was demonstrated that the cells were able to conform to the wrinkled topography, changing their morphology from a multi-directional spindled shape to a bi-directional shape. Furthermore, due to the change in morphology, the cells conformed to the topography, wherein the collimation of the cells ran parallel to the crests of the wrinkles containing the cells. This collimation was semi-quantified using image-processed analysis, where alignment was assessed as a function of orientation in degrees across fluorescent samples to produce histograms of orientation in degrees. Here it was found that there was a difference in histogram bias between wrinkled and monolayer cultures (Figure 5.17), wherein the monolayer cultures exhibited flatter histograms compared to the more traditionally normal-distributed and pronounced histograms of the orientation of the cells cultured on wrinkled substrate.

Due to the proposed type of the cells as determined by immunofluorescence (by the expression of vimentin) and the high degree of conformity of the cells, with the cells appear to neatly fit within the wrinkled topography, these more mesenchyme cells are considered to be more susceptible to the alignment type of contact guidance. This observation is supported by the highly motile nature of mesenchymal and fibroblastic cells, which has been well characterised by migration assays using both microfluidic and transwell methods (*Menon et al., 2015, Batarfi et al., 2023*). The porcine cells however elicited a different response to the surfaces, favouring the cell cluster

segregation form of contact guidance. This effect was most evident in the static culture. The PLESCs tended to form large and well-bordered colonies in standard monolayer culture with both coated vessel culture and 3T3 murine fibroblast co-culture, this behaviour being in agreement with wider LESC research (*Chen et al., 2011, Tovell et al., 2015*). However, in wrinkled substrate culture, it was observed that the cells only grew in clusters, which were segregated by the wrinkled surface features, the crests of the undulations appearing to serve as a physical barrier between these clusters. This behaviour of LESC is similarly seen in static systems that use channel-like topographies, the clustering behaviour observed in the RAFT system is more dispersed and adopts the appearance of more monolayer-like colonies (in diameter) with channel-depth distribution (*Levis and Daniels, 2016*). In the collagen matrix presented by Haagdoorens et al., the cells are much more tightly clustered before reaching confluency, whereby the cells occupy and conform to the entire channel profile (*Haagdoorens et al., 2019*). The determining factor in the clustering behaviours of the LESC between these studies was the channel width, a tighter channel width resulted in tighter clustering. This observation therefore provides a proposed explanation for the clustering behaviour seen in the PLESCs.

In cross-sectional rendering of confocal imaging of static wrinkled culture (Figure 5.19) it is possible to see these clusters conforming to the shape of the crypts, evident by the bowl-to-wave manifestation of the shape of the superposed fluorescent signals. This particular growth pattern was unique and warranted a proliferation profile (Figure 5.20) which showed over time there was a slight decrease in population, as determined arbitrarily by comparison to a non-wrinkled control culture. This accounted for the observed small cluster growth pattern observed by the PLESC which was ubiquitous to the work with dual treatment substrates. This consistency in growth

stagnation is curious however due to the observation of clear epithelial cell/LESC expansion in other static grooved constructs such as ridged collagen real architecture for 3D tissues (RAFT)(*Levis et al., 2013*) and grooved collagen-like peptide hydrogels (*Haagdorens et al., 2019*).

Despite the disparity between the cell behaviours between the isolated types from each species, there is a pervasive trend that the stem cell marker expression for each has been maintained. In the case of the human cells, the expression of the marker ABCG2 was maintained in static wrinkle culture in association with moderate p63 expression, both of which are appreciated LES C markers (*Schlötzer-Schrehardt and Kruze 2005, Kim et al., 2017*).

For the porcine cells, the p63 stem cell marker was also maintained between the control cultures and the static wrinkled culture, demonstrating the ability to preserve stemness despite the loss of viability. Through the use of the same antibodies in the assays between the species/isolated cell types, these observations run concurrently with the assertion that porcine tissue holds the same anatomical morphology and phenotypic qualities as humans, in particular, the presence of the same cellular markers such as p63 and integrin $\beta 1$ (*Notara et al., 2011*). In addition to the preservation of the stemness of the cells, in both types/species, there is a marked increase in apparent epithelization. This is asserted by the observation of the visually relative increase in expression of the epithelial marker CK3, which is attributable to the cornea (*Schlötzer-Schrehardt and Kruze, 2005*) across both human and porcine cells. In the human cells, K12 (cytokeratin 12) was also observed to be mildly increased relative to the control culture, increased expression of this marker indicates commitment towards the epithelial phenotype (*Chen et al., 2017*).

The success of the static wrinkled culture, particularly with the human cells, demonstrated that the dual treatment surfaces can serve as a bio-instructive surface through passive contact guidance (evident by the clear alignment) and are dimensionally biomimetic. Moving forward it was decided to further advance the model and introduce dynamic wrinkle topology as a novel way to simulate niche structural change. These dynamisations in both human and porcine cells involved the key transition from a flattened surface to a wrinkled surface with the cells attached. This particular topological transition was chosen due to the method involved in producing the dual-treated substrate, sterilisation, and application of coating. Maintaining the substrate on the stretching frame to keep a flattened surface with minimal intervention at this stage prevented substrate damage, ensuring the ability to effect further mechanical manipulations in the future.

In the cases of both cell types used, there was a notable fragility in the handling of the substrate chips for dynamic culture. However, the ease of access afforded by using a 6-well plate ensured sufficient access using sterile forceps to minimise substrate damage in basic manipulation in the relaxation transition from stretched flat to wrinkle formation *in situ* after cell seeding. In porcine cell culture, the use of a single dynamic transition demonstrated the ability to retain live cells without the induction of significant cell death as determined through the calcein CA/propidium iodide live/dead assay (Figure 5.22). This maintenance of viability was conserved regardless of co-culture with 3T3IN cells, however, it was observed that co-culture with the feeder cells ensured a more even distribution of cells without a “stressed” appearance of tight clusters of cells which manifested on substrates without the feeder layer. This effect implies that combined with single dynamization, the feeder does play a key role in maintaining cell proliferation quality. This conservation of cell population quality is

observed in other studies using epithelial cells and feeders, therefore the observations in dynamic culture are concurrent with existing approaches (*Sharma et al., 2012, Shen and Le, 2022*). However, it should be noted that both static culture and monolayer culture maintained better cell distribution in comparison to the dynamic cultures therefore as a point for future work cell retention during dynamization should be optimised.

In the porcine cyclic culture, it was shown that cell retention became progressively limited as more interventions were performed; with each topological deformation contributing to a loss of cells (Figure 5.23). This observation was witnessed, but to a much more limited degree, in the dynamized human cell culture. In dynamic human limbal cell culture, it was noted that there were some observable changes to contact guidance in association with the stages of stretch-to-flatten and relax-to-wrinkle in the cyclic periods of the culture. These changes were arbitrarily measured using image analysis of directionality, this analysis showed there was an increase in alignment of the cells as the culture progressed from day 3 through to 12 (Figure 5.21). However this method of analysis could not clearly define the orientation for day 9, therefore straightforward comparison using the histogram data alone is not feasible.

From the images however, it is possible to see the changes in cell morphology (cells are more elongated after wrinkled incubation periods). Also, it is possible to see visible changes in alignment (during wrinkled periods, cells tend to be more aligned with the vertical). The human cells were more responsive to the changes in topography due to their inferred mesenchyme/fibroblastic phenotype. The implied greater motility inherent in these types of cells means that they would show greater sensitivity to a cyclic protocol, to aid in the validation of the hypothesis that the cells themselves can

be dynamically influenced through the mechanical manipulation (removal and reinstatement) of the wrinkled topology (*Menon et al., 2015, Batarfi et al., 2023*).

Based on the preliminary nature of this work, it is possible to suggest that this bioreactor system has the potential to be used as a disease model for several diseases which include structural change over time. The structural changes would focus predominantly on cells contained within crypt structures such as the POV or wider limbal crypt as a whole, therefore only LSCs, early commitment corneal epithelial progenitors or committed corneal/limbal epithelial cells could conceivably be used in this model. The diseases that could be modeled can include those such as LSCD, which has had the loss of limbal stem cell containing features (the POV) correlated to patient clinically presenting with the disease (*Le et al., 2017*). In addition to LSCD other diseases with structural involvement such as injury-related conjunctivalisation, whereby the anatomy of the limbus has been physically or chemically disrupted which results in a breach of the cornea by the sclera with neovascularisation (*Lim et al., 2009, Jirvosa et al., 2011*). Modelling this pathology may require the addition of scleral cells however, the dynamic change in surface topography in addition to scleral co-culture could present further insight into how the limbal niche architecture helps resist conjunctivalisation.

5.5 CONCLUSION

Presented in this chapter is the preliminary characterisation of the limbal cell response across different cell types, (from different tissue sources) to wrinkled topography as a means to replicate the limbal epithelial stem cell niche. It was demonstrated that viable limbal cells, presenting the canonical limbal stem cell markers p63 and ABCG2, were able to be isolated from fresh tissue and subsequently manipulated by the wrinkled topographies in culture. However, further work is needed

to fully establish the purity of these isolated stem cell populations and refine the ability to isolate cells from the longer-term organ culture of human donor tissue. Such further work should include validating PCR to ensure marker expression is true and spans all marker groups; the LESC markers (P63/ABCG2), the corneal markers (CK3/K12) and include the mesenchymal markers such as vimentin, N-cadherin and fibronectin. These manipulations manifested predominantly in the observation of alignment in the human limbal cells and the forced clustering of the PLESCs. Additionally, it was also demonstrated that organ culture-stored tissue for long periods was able to still be able to produce viable and model-relevant motile cells, that were able to be visibly controlled by surface contact guidance. Whilst in the preliminary stage of assessment at the biological level, the assays presented demonstrated that the dual treatment wrinkled PDMS can influence and control limbal cell behaviour in both static and dynamic culture whilst maintaining stem cell phenotype, as ascertained by immunofluorescence in the static culture.

The implementation of collagen in monolayer culture (in well plates/flasks) was demonstrated to effectively facilitate LESC expansion whilst using photocured GelMa was a good immobilised gel coating, with the enhancement of limbal cell attachment, that was suitable for wrinkled PDMS applications.

There was also an obvious difference in growth patterns over time observed in the cells extracted from the different cell sources. The human limbal cells (with the more fibroblastic morphology) expanded to near-confluent coverage over the wrinkled substrates, whereas the LESC from the porcine eyes stagnated in proliferation. The human limbal cells that were cultured on the dynamized wrinkled substrates (as part of the stretching frame bioreactor) showed an alternating change in the LESC alignment. These observations indicate that wrinkled PDMS surfaces in the dynamic

bioreactor were able to dictate cell growth patterns. Due to the porcine LESC's tending to respond to the wrinkled substrates by clustering, it can be concluded that the alignment response was cell source dependent.

The major implications for this culturing system moving forward are, that there is a significant disease modelling capacity when other ocular disease variables are incorporated and the substrate presents an interesting tissue engineering foundation for ocular applications.

Chapter 6: Discussion and Overall Conclusion

6.1 SUMMATIVE DISCUSSION

With an ever-expanding and ageing population and the prevalence of blinding conditions such as limbal stem cell deficiency (LSCD) becoming more noticeable, there is a growing need for effective tissue-engineered models and treatments. Although LSCD is typically a disease induced through an injury such as a chemical burn, most often seen in middle-aged males (*Vazirani et al., 2018, Cartes et al., 2021*), contact lens wear, multiple ocular surgeries and ocular epithelial inflammation are attributed to the induction of LSCD (*Sejpal et al., 2013*). There is a significant quality of life and working economic motivations for developing long-term sight restorative corneal therapies, guided by proper tissue and disease modelling for the limbal niche and its associated pathologies (*Velthoven et al., 2023*). For example, the development of regenerative surgical techniques such as limbal stem cell transplant has demonstrated good outcomes after follow-up (average of 21 months) (*Le et al., 2020*) and long-term outcomes (up to 119 months) (*Miri et al., 2010*). Despite recent surgical enhancements, there is a prevailing national and worldwide shortage of donor corneal tissue, reducing the capacity to perform keratoplasties. Therefore tissue engineering has become an attractive approach, where the use of material scaffolds to facilitate the re-growth of donor tissue or donor cellular material in vitro is the end goal.

This research has sought to further this ambition by developing a smart material capable of firstly achieving biomimicry of the LESC niche in the static form and secondly facilitating the disease state simulation through topology dynamization. Polymeric wrinkling was utilised as the mechanism of choice, through the exploitation of mechanical phenomena typically associated with biological forms and material faults (*Zhao et al., 2020, Tian et al., 2020, Dimmock et al., 2020*). This mechanism of material deformation was exploited within a custom-designed bioreactor setup to simulate the limbal stem cell niche whilst facilitating cellular characterisation in vitro. Additionally, the bioreactor system developed in this project begins to explore the possibilities of recreating pathologically relevant structural conditions through the ability to dynamically alter the topography with minimal disturbance to the culture setup. The dynamization of the topography enables the investigation of conditions such as LSCD by allowing the removal of the crypt-like undulations during culture, thus being able to study the effect of anatomic feature loss on stem cell presence in vitro. Future work could focus on this aspect particularly considering conditions like LSCD have demonstrated a link between a loss of epithelial competency (measured by epithelial thickness by OCT) in patients with LSCD who present a lack of POV presence (*Le et al., 2016*). In this preliminary stage, however, short periods of dynamization were applied such as alternating cycling or single-period topographical alteration to assess the cells' tolerance to the induction of surface topographical change through the elastic material substrates.

Wrinkling was achieved using a novel method incorporating two separate wrinkling methods, amalgamated in such a way as to achieve a collimated wrinkled surface which possessed biologically relevant dimensions to the LESC niche. These material-to-LESC properties were validated against alternate methods in the wider

literature, in-depth tissue structural investigations using optical coherence tomography and mechanical characterisations by optical coherence elastography. As part of the anatomical investigation by non-destructive means, it was correlated that there was both structural and mechanical degradation in the tissue with advancing age (visible by both limbal/epithelial softening and loss of POV undulations). The dual treatment wrinkled substrates were finally validated for their cytocompatibility in primary limbal cell culture in the production of the culturing system for LESC expansion and model development. In the development of the ideal wrinkled substrate, different polymer wrinkling mechanisms, including the compression-based laminated block method were tested and excluded in favour of the superior dual treatment method of wrinkling PDMS chips.

6.1.1 Structural and Mechanical Characterisation of the LESC Niche

The limbal epithelial stem cell niche was structurally evaluated by using an in-house custom-built spectral domain optical coherence tomography, followed by mechanical characterisation by optical coherence tomography using the same equipment in a different configuration. This work was undertaken at and in collaboration with the University of Dundee. It was demonstrated that this system, in both the volumetric OCT and the OCE configurations together, effectively facilitated the virtual dissection of the LESC niche. These techniques followed a definable workflow wherein the structure and the mechanics of a particular region of interest within the human tissue samples were investigated, enabling a greater understanding of the microscale features of the POV. Using OCT and OCE presents multiple advantages over other modalities, in the first instance, OCT/OCE can produce higher resolution 3-dimensional imaging and elastographic information within the same

platform. Secondly, by using light incoherence-dependent image reconstruction, coupled with only needing to track particle oscillations over a small period, the agitations needed to perform elastography are minimal (Kennedy et al., 2014). Therefore OCE has the potential to resolve higher magnification images with less noise than acoustic methods (Gennison et al., 2013).

6.1.1.1 OCT for Tissue Structural Analysis

Using the OCT configuration the niche was quantified at the microscale level, the sample population was $n = 10$ total, segregated into two groups of $n = 5$ for those under 65 years old and $n = 5$ for those over 65 years old. This age was chosen as the most appropriate for segregation as it was the median age in the population. In each sample, the undulations of the palisades of Vogt (POV) and inclusive epithelial rete pegs (ERPs)/palisade ridges (PRs) were depth-resolved in the volumetric images, then intensity profiles were drawn from the en-face aspects of the volumetric cubes. From the intensity profiles the widths of the ERP and PR features were quantified using an image-processing method of extrapolating the profiles using primarily ImageJ to acquire the profile curves, then using simple 4-point moving averaging for smoothing. For the under 65-year-old group the ERP and PR widths were measured at $33.3 \pm 4.56 \mu\text{m}$ and $43.4 \pm 4.57 \mu\text{m}$ respectively whilst the ERP and PR widths for the over 65-year-old group were $42.8 \pm 7.8 \mu\text{m}$ and $29.9 \pm 3.22 \mu\text{m}$ respectively. These measurements were found to be concordant in magnitude with another study which used a similar method of limbal quantification by profiling the ERP and PR

(Haagdoorens et al., 2017). Additionally, these measurements are further reinforced by measurements made by other modalities including confocal microscopy (Grieve et al., 2015). Thus it can be confidently said that the processing of the output volumetric images, using ImageJ and extrapolating the profiles without using a coding package such as Matlab can give accurate and reliable quantification plots.

The average changes in the anatomy between age groups were challenging to apply in the analysis of the effect of ageing structurally using this modality. It was considered that the small population size of samples in each group may account for the population homogeneity. This effect and loss of testing power however could not be addressed due to tissue rarity. The average changes, as calculated show a 10.3% reduction in ERP and a 1.4% reduction in the PR widths from the over 65-year-old group and to the under 65-year-old group. These reductions in both dimensions translate into a reduction in total POV prominence, which is concordant to confocal, scanning electron microscopic and other OCT studies which have drawn similar conclusions of limbal niche structural degradation with age (Zheng and Xu, 2008, Notara et al., 2013, Haagdoorens et al., 2017).

6.1.1.2 Structure-Guided ROI Identification for OCE

Following the measurement of POV feature dimensions, Young's moduli of the epithelium and limbal niche layers were measured from the elastogram images, which were resolved from 2D vibrational OCE acquisitions of the images of the same region in OCT. In a method of prosecution similar to the intensity profiling of OCT, the analysis of the elastograms utilised a method reliant on an image analysis approach utilizing ImageJ to extract the arbitrary values of the stiffnesses for each anatomical region. Subsequently calculating the real values against the calibration values (the agar layer

of exact known stiffness: 14.6 ± 0.8 KPa). In all cases, the epithelium was measured using a linear ROI, as this layer did not present any anatomical undulations or distortions, therefore the population was measured and subdivided into the defined age groups. For the under 65-year-old group the epithelial modulus was measured at 41.1 ± 34.2 KPa and the over 65-year-old was measured at 31.5 ± 20.2 KPa the magnitude of which agrees with studies employing AFM to study corneal stiffness. In these studies, corneal modulus was measured to be 50 ± 17.8 kPa at the anterior basement membrane (*Last et al., 2009*) and 33.1 ± 6.1 kPa at the anterior stroma, (*Last et al., 2012*).

For the mechanical characterisation of the LESC niche, there was a comparison of two different ROI types. The linear ROI, which was considered the more objective (due to its uniformity in pixel coverage and being linear, aside from CSR14) and the undulating ROI, which was hand drawn to follow the undulations of the POV as seen in the accompanying structural images. The undulating ROI was considered a more subjective method due to the hand-drawn nature of this type of ROI. Although these ROIs were drawn following the structures, these can be interpreted differently between sample images and, therefore can introduce human error. Thus, it may be the difference in conceptual approaches of objectivity and subjectivity that has resulted in the overall difference in output moduli in the LESC niche regions between these methods. For the linear ROIs, across the entire ten sample population, the LESC niche modulus was found to be 42.9 ± 25.2 KPa and the drawn ROI was determined to be 32.9 ± 14.8 KPa. Though the difference was measurable, it was not a significant difference statistically due to the inherent variation.

6.1.1.3 Age-Related Changes in Stiffness

When separated into the age groups, for the linear method, the LESC elasticities were 51.8 ± 30.3 KPa and 31.8 ± 17.9 KPa for the under and over 65-year-old groups respectively. For the undulating method, the LESC elasticities were 34.7 ± 14.9 KPa and 27.2 ± 13.7 KPa for the under and over 65-year-old groups respectively. In both methods, there were discernable differences in average LESC niche modulus with age, with an average decrease in Young's modulus of 38.6% for the linear method and 25.3% for the drawn method whilst there was an average decrease in modulus of the epithelium using the drawn method of 24.3%. Despite none of the comparisons being found to be statistically significant due to the low test statistical power (due to subset size and variance), the average percentage differences are sizeable when appreciated on their own. Out of the two methods, the linear method shows the greatest difference in LESC niche modulus with age, and being linear to a specified pixel size is the most objective and, therefore more subjective to systematic error instead of human error or bias. The observed decrease of modulus with age also alludes to the idea that the LESC niche degrades with age, as corroborated by the various observations of limbal structural degradation with age (*Zheng and Xu, 2008, Notara et al., 2013, Haagdoorens et al., 2017*).

6.1.2 Production of wrinkled substrates for the replication of the LESC niche

The effective characterisation of the LESC niche aided in the primary validation of the fabrication of a wrinkled surface with a topography biomimetic to the limbal POV undulations. During the initial developmental stages of the project, multiple mechanisms of wrinkling were explored. Each method of generating wrinkles upon

PDMS has its benefits, ranging from simplicity of dynamic alteration (compression of the laminated blocks) to stability of wrinkle retention in culture (dual-treated substrate).

In conjunction with the development of the wrinkled substrates, the corresponding bioreactor frames which enabled both wrinkle formation and cell culture, were designed and produced. Once wrinkled materials were produced, the produced crypts were analysed for their shape and biomimetic quality. The dual-treated substrate also demonstrated the ability to undergo true dynamization (flat-wrinkle-flat) whilst maintaining substrate integrity, an improvement on the original laminated block. These developments were guided by material mechanical characterisation, allowing for careful material selection to satisfy the conditions for soft polymer wrinkling (*Cai and Fu 2019, Dimmock et al., 2020*).

6.1.2.1 Preliminary Development: the Evolution From Laminated PDMS Blocks to PDMS Surface Treatment to Form Wrinkles

In a preliminary evaluation, the compression of laminated blocks was abandoned as an effective mode of wrinkling due to the observation of delamination of the adhered membrane after compression underwater. The laminated blocks were initially promising due to their ability to easily produce visible wrinkles and afford visible reversible changes by changes in compression. However, even in the dry state after fabrication, full reversibility was not achieved – indicating a compromised layer. It was later revealed during incubation in an aqueous medium that the membranes had delaminated from the blocks, despite the use of silicone adhesive, after compression was applied. Other glue alternatives were considered, however, currently, there are none suitable for the research application. These considerations were threefold, the alternative adhesives either: (i) compromised wrinkling formation (by introduction of a

layer of vastly differing stiffness and compromising the conditions for wrinkling), (ii) contained incompatible solvents to either the PDMS (solvent swelling) or the polymer films (dissolution) and (iii) the others were simply considered to be potentially toxic for cell culture.

Thus it was decided to pursue more promising methods of wrinkling stretch-based methods. The most effective methods employed moving forward utilised the pre-stretching of thin PDMS membranes or specially moulded chips before surface stiffening treatments. Acid oxidation, plasma treatment and the combination of both into a novel protocol called “dual treatment” were subsequently exploited in the generation of biomimetic and stable wrinkled topography. These created substrates were characterised using imaging and physical techniques to assess both the physical and topographical features to formulate an appreciation of which surface would be the most biomimetic.

Overall, the pursuit of these types of substrates was predicted to be more biocompatible for cell culture when the three types of stretch-type wrinkled PDMS surfaces were compared against PCL and PLGA for their water contact angle. It was found from the water contact angle measurement that all treated PDMS groups were more hydrophilic compared to untreated PDMS and the PCL and PLGA membranes. The water contact angle is considered a good predictive measure of how well a surface may act as a cell-friendly culturing surface (provided it has non-toxic chemistry), based on the assumption that adherent cells prefer a hydrophilic surface (*Visalakshan et al., 2019*).

6.1.2.2 Characterisation of Wrinkled Substrates for Limbal Crypt Mimicry

The plasma treatment yielded the smallest width wrinkles ($4.12 \pm 1.1\mu\text{m}$) with dimensions so small that was impossible to measure the depth. Despite this minute depth, there is a known example of this type of substrate being used in contact guidance (*Amerian et al., 2019*). The largest wrinkles were measured in the dual-treated substrate formulated with 2.5% curing agent ($128.2 \pm 17.7 \mu\text{m}$ wide by $39.1 \pm 10.3 \mu\text{m}$ deep) with acid oxidation being intermediate-sized wrinkles. At this level, it was shown that it is possible to ordinally control the size of wrinkles used by selecting the method of wrinkling employed. However, this was able to be taken further as in compression testing it was validated that there was an increasing relationship between the increasing PDMS curing agent concentration and the Young's modulus of the PDMS bulk. Therefore following the simple wrinkle model, and indeed other more complex wrinkling models, (*Allen, 1969, Cai and Fu 2019, Dimmock et al., 2020*) changing the bulk modulus followed by the stiffening by the treatments allowed for a secondary level of point-of-fabrication control of wrinkle dimensions.

Out of the three stretch-based approaches trialled, only one satisfied all of the desired properties for use in culture; reversibility of topography, biologically relevant crypt width and depth and appropriate continuity of wrinkles. The dual treatment evolved wrinkles satisfied all of these criteria shortly followed up by the plasma treatment evolved topography, which exhibited the best linearity out of all of the methods (as determined by scanning electron microscopy and atomic force microscopy) which was concordant with other examples of this technique (*Glatz and Fery, 2018*).

Acid oxidation of PDMS was an efficient way of producing wrinkles, being the fastest way to produce wrinkles on PDMS substrates, however, it was the most unpredictable, riddled with bifurcations, pits cracks and non-collimated features. It is noted that acid-oxidising PDMS readily produced wrinkled features (when measurable) of widths ranging from a minimum of 31.4 μm to a maximum of 131.4 μm which fall comfortably around biomimetic ranges for limbal replication (*Grieve et al., Bsheva et al., 2017, Haagdoorens et al., 2017*). Generally, this method produced random order wrinkles despite the application of pre-stretching either by the bending of blocks to stretch a single exposure surface or the application of bilateral stretch to PDMS chips which were fully immersed. Practical uses of acid oxidation to create wrinkled polymeric surfaces are on a micro-scale to create wrinkled beads, which do not require an ordered surface applicable to cell culture for limbal recreation (*Zheng et al., 2018, Xu et al., 2020*).

6.1.2.3 Dual treatment of PDMS as an Ideal Substrate Production Method

However, despite acid oxidation not being directly relevant as a method for generating wrinkles biomimetic to the LESC niche in this case, it was vital in the development of the dual treatment method. The decision to develop the dual treatment method came from the realisation that both plasma treatment and acid oxidation on their own have opposing pros and cons to each other. Thus it was surmised that the combination of both of these methods would produce an ideal substrate. It is proposed that the dual treatment achieved the satisfaction of desirable traits by its stepwise nature of modifying PDMS to produce a gradient of increasing stiffness from the centre outwards. The centre is considered to remain unmodified proceeding through to a moderately stiffened microscale outward layer, created by acid oxidation, to a finally

silicate-like nano-scale very stiff upper-most shell. This proposal requires further material testing and high-fidelity mechanical characterisation with other techniques to validate. However, as explored in Chapter 4, the preliminary OCE demonstrated some detectable regional differences in stiffness between the surface and the bulk in the non-referenced acquisitions. This observation was countered by the more homogenous result observed for the distribution of stiffnesses when the agar reference was applied to the surface.

An advantage to using the reference material however was the ability to an accurate average modulus for the tested material for tested dual-treated samples (97.3 ± 47.5 KPa) which is close to the attained value for the tension testing of the untreated PDMS chips of the same PDMS composition. Thus with future work with this modality (with further calibration and optimisation), these findings can be unified to give a more clearly defined correlation of structure and mechanical properties for the material similar in manner to the tissue in Chapter 3. However, tension testing of the entire chips post-treatment revealed that each of the treatments was able to change the mechanical properties of the PDMS by altering the elasticity of the entire substrate compared to the untreated controls, with all of the treatments except dual treatment (which requires further validation) stiffening the PDMS chips. The evolution of the wrinkles was visually apparent, both by eye and microscopically.

The wrinkles were quantified using various imaging techniques including SEM and OCT, analysis of the compositional changes imparted by treatment methods to the PDMS proved challenging to resolve at high fidelity. Raman spectroscopy was used due to its ability to detect the PDMS as a non-control transparent substrate on that piece of equipment. Despite this advantage, the spectra acquired indicated that only dual treatment had a significant effect on the resultant output. An increase in the

Raman intensity of the overall spectrum was the only difference, showing only that the optical properties have changed; an observation that could be made by eye through the combined increase in substrate opacity and iridescence.

Additionally, EdX was performed on the sampled at the time of SEM analysis, this only showed rudimental changes in elemental composition, with few significant changes, most notable being the detection of sulphur in samples exposed to sulphonitric acid (acid oxidation). In terms of both elemental analysis and spectroscopy, these are challenging areas requiring future deeper investigation with these treated PDMS substrates.

A future focus on the material production aspect of this project would be the refinement of the production of the dual treatment surfaces. Whilst the dual treatment surfaces possess many advantages over the different substrate types e.g. maintenance of better feature linearity, reversibility and feature stability in culture, there are still some issues to address. These issues include the reduction of the wrinkle dimension variation, improving linearity and preventing substrate failure during production. As these substrates are produced by hand, the introduction of automation would facilitate the standardisation of wrinkle production. Automation would be required to control and performance of the immersion and the removal of the substrates from the acid, followed by the enaction of the quenching steps, whilst precisely controlling the timing of each of these steps to maintain standardisation. In addition to the automation of the steps, further engineering of the frames may be required to enhance the application of tension and most specifically enable easy relaxation of the substrates at the required steps in the production of the substrates. Finally, monitoring of the storage of the thermally denatured solution may be required to ensure the sulphonitric acid does not degrade over time in storage, despite being stored in the

dark, in a sealed Nalgene container. In retrospect, monitoring of treatment acid may have provided a preliminary elucidation to the variation observed in the production of both the acid oxidised and dual-treated substrates. pH measurements at regular intervals of the acid mixture could be an appropriate measure of treatment solution quality, with comparison being drawn between the solution immediately after inactivation (when acid reaches room temperature) and after each treatment. A change in acid pH immediately after treatment could also be used as a preliminary measure of successful acid oxidation of the PDMS in the wet phase of the dual treatment process.

6.1.2.4 Reversibility of Wrinkled Substrates for Dynamic Limbal Simulation in a Novel Bioreactor Setup

The material surface and the ability to generate a reversible topography are the critical aspects of the novel device that was developed. To facilitate the reversibility of the substrate a stretching frame was designed and assembled using materials which were resistant to repeated use for frames' dual purpose. The frames proved successful as both a tool for facilitating the creation of the wrinkled surface and also importantly as a sterilisable cell culture device, forming a micro-scale bioreactor system. The scope of bioreactor systems for mechanical stimulation has generally included bulky systems that impart large stimuli in expansive culture, examples being the flexcell pneumatic flexible plate system (*Flexcell, USA*) or (to measure parameters on a small scale) such as the TC-3F bioreactor (*Don Whitley scientific, UK*). However, in the context of the limbal niche, more subtle mechanical manipulations were required, since typically the LESC niche changes observed occur at the microscale (*Zheng and Xu, 2008, Grieve et al., 2015*). It was deemed inappropriate to use a commercial bioreactor as these mechanical manipulations would have been too vast for limbal applications.

Therefore a small-scale device was required. A minimalist approach to the design of the system was undertaken with the core criteria of ease (i) of manipulation, (ii) ability to apply variable stretch, (iii) facilitate replicates and (iv) having material durability sufficient to withstand corrosion, sterilisation and handling. The bioreactor developed comprised of the wrinkled substrate suspended between the pins of the 316L stainless steel stretching frame, within a 6-well plate (which could accommodate up to six of these setups within a small footprint) immersed in culture medium. Relaxation of the substrates from stretched flat to wrinkled could be performed by either adjusting the inside nuts with forceps *in situ* or by carefully lifting the PDMS chip away from the frame. The frame with the attached wrinkled PDMS was autoclaved before culture. This was one of the steps crucial to maintaining “sterile” conditions, preventing bacterial/fungal infection of the cultures using the steel frame system. In addition to the combined autoclaving (and thermal inactivation) of the substrate and frame together, the GelMa was sterile filtered after reconstitution in PBS and kept in a sterile container at -20°C in the liquid uncured state, shielded from the light, between uses. Finally, the porcine cells were isolated using a combination of penicillin, streptomycin, gentamycin and amphotericin (refer to section 2.2.9.1) and then maintained in a culture medium containing penicillin and streptomycin. In the isolation and use of human cells, antibiotic treatment at isolation was not necessary as the donated corneas were serologically tested for infections at the tissue bank. However, the isolated human cells were maintained in penicillin and streptomycin containing medium, the same as the porcine cells, to reduce the risk of infection post isolation. Throughout this research, there have been no observed fungal or bacterial infections as a result of material and bioreactor preparation using wrinkled PDMS chips prepared using the stretching frame for cell culture. This highlights the advantages of using simpler, small-scale devices to impart the desired mechanical signals to the cells via the suspended substrates.

Although this design currently lacks the online monitoring or automation that commercial systems have, this proof of concept forms a very solid foundation for adding such layers of sophistication in future work. In dynamic cell culture, the use of the live-tracking stain enabled the visualisation of the cells on the substrates whilst they were on the frames utilizing the Leica MZ10F fluorescent dissecting microscope (*Leica, Germany*), demonstrating how this simple bioreactor setup has the potential to facilitate on-line imaging.

6.1.3 Preliminary Limbal Niche Model Investigation Using Primary Cells

The developed wrinkled substrates and specially designed bioreactor frames were tested for both optimisation purposes and the preliminary characterization of primary limbal cell responses to the wrinkled surfaces. To this effect, both static and dynamic simulations of the limbal niche have been explored to assess stem cell marker maintenance, cellular retention on the material surface and cellular viability. Together this presented an overall justification that the bioreactor system, with the wrinkled surfaces inside, was able to influence primary limbal cell behaviour from both species.

6.1.3.1 Isolation of Primary Limbal Epithelial Cells from Human and Porcine Sources

The isolation of primary cells utilised a two-stage enzymatic digestion protocol, which was applied to both species' tissues. Despite consistency in the use of isolation method, and the use of screening imaging (polarised light microscopy and OCT) to identify, and demarcate the limbal POV, there was a difference in the cell types isolated.

The human tissue yielded cells with a distinctly mesenchymal-like morphology and presented the mesenchymal/transitional marker vimentin, alongside the canonical limbal epithelial stem cell markers ABCG2 and P63 (*Schlötzer-Shrehardt and Kruse, 2005*). Additionally, there was K12 positivity and a weak presentation of CK3. In the porcine tissue, the cells yielded from the extraction procedure presented the expected epithelial cobblestone cell morphology alongside the typical LESC stem cell markers (P63, ABCG2) and weak presentation of the epithelial marker CK3 with nearly no clear presentation of K12 (*Schlötzer-Shrehardt and Kruse, 2005*).

It is proposed that storage time in enclosed organ culture may have been primarily responsible for the loss of LESC retrievable from the human tissue, whereas the cells were isolated from the porcine tissues within 48 hours of slaughter, the eyes were not maintained in organ culture, therefore, were fresh and as close to “in life” as possible. Although it is reported that it is possible to obtain LESC from long-term organ-cultured human corneas (*Tovell et al., 2015*), throughout this project it has not been possible to extract ABCG2+/P63+ cells with cobblestone morphology from human corneas procured from the tissue bank. The hypothesised mechanism is that prolonged and undisturbed organ culture, whilst may keep the tissues viable, may have promoted the LESC to undergo the epithelial-mesenchymal transition (*Kawakita et al., 2005*). This effect may have been induced through the removal of pro-limbal stimuli (such as modulating shear forces) (*Kang et al., 2014*) or through the removal of pro-epithelial signals such as the air surface interface (*Tang et al., 2023*) by culturing the tissue in undisturbed suspension.

6.1.3.2 Initial Cellular Testing and Optimisation of the Wrinkled Substrates for Use Within the Bioreactor System

During the substrate developmental process, cellular test assays were performed to assess the practical viability and surface compatibility of the trial substrates being developed. At this stage non-limbal cells were available and in terms of practicality, it was considered that for such an unknown and at times unstable system (in particular the laminated block substrates) performing limbal cell isolations at this stage would have been premature. Therefore, the acquisition of cells from group stocks which possessed suitable sensitivity to microenvironmental alterations (therefore were adequate sensors of surface/conditional biocompatibility) was deemed appropriate. To this end, rat cardiomyoblasts and human embryonic kidney-293 (HEK-293) cell lines were employed, when they were available to test the substrates during this developmental trial process.

First, the laminated blocks were tested using the rat cardiomyoblasts, in this first instance it was proven that during the culture period, the membranes delaminated, as evident through the visible loss of wrinkle prominence over time. Additionally, there was an apparent loss of cells over time, however, it was conjectured whether this was due to the mechanical deformation, as in later assays intentional mechanical manipulation of dual treatment topographies also led to cellular loss, or there is a surface-dependent mechanism. However, observations that discredit surface-based cytotoxicity were the witnessing of viable cells growing on PLGA surfaces in other studies. Examples of this include the contact-guided controlled growth of hBMCs, neuronal cells and myoblasts on micropatterned PLGA membrane (*Piscioneri et al., 2023*) and the use of PLGA to create membrane-based multilayer liver models which were viable at nearly two weeks in culture (*De Maria et al., 2020*). However, ultimately

the delamination was the critical fail condition for this substrate type for both wrinkle maintenance and as a culturing system.

Following this discovery, the stretch-based methods for the formation of wrinkling were tested for their cytocompatibility and their utility as limbal replication models. Firstly the plasma-treated substrates were explored. Oxygen plasma-treated PDMS has already been used as a cell culture substrate and also demonstrated the ability to modulate cytocompatibility through length of plasma exposure (*Amerian et al., 2019*). With the application of pre-stretch before plasma treatment, it was demonstrated that a microscale topography of the smallest order was able to be generated, as shown in Chapter 4. Despite these wrinkles not being deep enough to be biomimetic of the limbal POV, it was demonstrated in rat cardiomyoblast culture that plasma-treated PDMS was able to instigate contact guidance alignment of these cells.

This alignment was visible through the observable difference between control and wrinkled culture cellular morphologies, the wrinkled topography culture morphologies were elongated and collimated in the same direction whereas the control cellular morphology was more spread out and multidirectional. However, due to the crypt size limitation plasma treatment as a sole wrinkling method was considered a sub-optimal substrate for anatomical replication. Subsequently, the acid oxidation protocol for generating wrinkled PDMS was tested for its suitability in the generation of the model. For this validation, HEK-293 cells were employed, at this stage they were employed based on cell availability in group stocks but also were deemed a suitable adherent cell line for validating topographical models. This assumption was based on recorded applications of HEK-293 in the analysis of the effect of topology on cell behaviour (*Wychowaniec et al., 2020*).

Though the easiest substrate type to manufacture overall, the acid oxidation alone was by far the least consistent. The topography was prone to pits, bifurcations and surface aberrations, this led to very random topographies, even with the application of stretching before acid application. It was observed during cell culture with the HEK-293 cells that cell distribution at the endpoint of static culture with substrate type indicated highly variable surface compatibility with the cultured cells. It is also worthy of note that the randomly ordered wrinkling type, although showing some capacity for cellular retention, did not exhibit either a 2.5D or a topological 3D cell model properties in terms of cellular density, proliferation into/around features or non-adverse cellular morphological response to the surface. Such responses are typical to tissue engineering applications and have been investigated in static surface models such as the RAFT model (*Levis et al., 2013*) and the study into limbal matrix replication through topographical and mechanical mimicry with PDMS and polyacrylamide gels (*Kauppila et al., 2023*).

The current apex of wrinkled substrate development was the dual treatment wrinkled PDMS substrates which overall provided the best balance in wrinkling dimensions and stability. The superiority of the dual treatment method was also the case when the bioreactor setup was used in limbal simulatory experiments due to the reversibility of the substrates and their durability on the frames. Therefore after the successful isolation of both human and porcine limbal cells, it was the dual-treated wrinkled PDMS which was favoured for investigation using primary limbal cells.

6.1.3.3 Coating Selection for an Optimised Wrinkled Surface for Limbal Simulation

Successful isolation of primary cells and selection of the most appropriate substrate for the bioreactor setup facilitated the testing of the LESC niche simulation

model. This work encompassed both human and porcine cells, owing to the similarity in the porcine limbus structurally and phenotypically (*Notara et al., 2011, Grieve et al., 2015*) and the utility of having different primary limbal cell sub-types available. The primary human cells were used to optimise the coating strategy, which was deemed a vital strategy due to the primary cells not adhering well to non-coated substrates.

The use of coatings, in association with the enhancement of attachment and cell compatibility (as was their primary function in this project), can serve other cellular interactive and instructive functions. For example, the use and incorporation of matrix proteins such as hyaluronic acid can serve a pro-proliferative component in a coating gel or 3D matrix. Sodium Hyaluronate biopolymer, a form of hyaluronic acid, has been tested for application in corneal wound regeneration. It was found that the incorporation of Hyaluronate in culture increases human corneal epithelial cell rate of proliferation substantially in comparison to the control culture and in the wound healing assay. In histological staining of rabbit corneas which were treated with hyaluronate, there was a maintained positivity in the basal limbal stem cell population after wound simulation and healing, visualised by a presence of CK15 expression (*Suárez-Barrío et al., 2019*). A second key example, which used another matrix component was the exploration of laminin isoforms as coatings for the expansion of limbal progenitor cells. From this study laminins-511 and -521 reported a marked increase in rate of proliferation using the BrdU tracking assay. In addition, incorporation of laminin-511 maintained the expression of the key limbal progenitor markers Ck15 and P63, an important characteristic demonstrating that using a pro-proliferative coating can maintain stemness characteristics (*Polisetti et al., 2017*). Use of a pro-proliferative coating in monolayer can also have a secondary utility in the immortalisation of the isolated cells. Immortalisation is defined by the achievement of a pseudo-senecent state by the by

the of the loss of function of the p53, pRb and p16 cell-cycle checkpoint pathways whilst maintaining a proliferative capacity. These characteristics are pro-tumorigenic characteristics, but prevent cell death. Alternatively this state can be induced by the introduction and expression of telomerase, either by viral transfection of the active gene (*Maqsood et al., 2013*). The longer cells are maintained through increased passage numbers the greater the chance the cells acquiring pro-tumorigenic characteristics which are required to become immortalised by natural chance, rather than requiring chemical or viral-mediated transformation. A prime example of this is the establishment of multiple murine embryonic fibroblast lines after primary isolation by maintaining them until high passage numbers (*Camarasa et al., 2009*). Although there has been no specific current studies found in the immortalisation of LESC using coating-based protocols, the maintenance of primary isolated cells, with a coating designed to promote cell attachment (such as collagen and GelMa as explored in this project) conjoined with a pro-proliferative component such as laminin could potentially be used to immortalise the LESC type. This could be a focus for future work in the refinement of isolating LESC and achieving immortalisation, whilst preserving native stem cell characteristics, for use in research and potential medical applications.

The first coating trial was polydopamine and polydopamine collagen, as they are reasonably inexpensive and give a very visible process in the modification of PDMS for matrix protein immobilisation and have had recorded uses in the culture of cells in PDMS microfluidic devices and biocompatibility testing (*Dabaghi et al., 2021, Yang et al., 2022, Li et al., 2023*). However, due to the presence of black deposits interfering with imaging, polydopamine-incorporated coatings were abandoned.

A photocured gelatin methacrylate (GelMa) coating was instead developed, wherein a photocuring agent incorporated in the gel mixture, enabled the GelMa to

bind to the surface of treated PDMS (and resist washing) after photocuring with 405nm UV light. Both human and porcine cells seeded on this coating demonstrated good outcomes and sensitivity to the underlying wrinkled topography.

6.1.3.4 Cellular Response to the Static and Dynamic Wrinkled Topography

In static wrinkled culture, the human cells displayed cellular morphological adaptations which were arbitrarily measurable through orientation analysis of the fluorescent images. This analysis showed that the wrinkled surfaces induced cellular alignment which conformed to the topography. However, phenotypic expression was not significantly altered, demonstrating that the wrinkled surfaces were able to preserve the stem cell phenotype by preserving the ABCG2+ and P63+ expression in these cells. Additionally, when cultured on wrinkled surfaces, there was a noticeable increase in the expression of CK3, indicating a potential commitment towards a more epithelial phenotype.

In human dynamic culture, the results were more difficult to define, though it is safe to conclude that mechanical intervention significantly reduces cellular retention on wrinkled surfaces. However, throughout the application of tension to the substrates to remove the wrinkles and tension removal to (re)produce the wrinkles there were some visible changes to cell distribution and morphology. During the formation of wrinkles, the cells appeared to adopt a bipolar-spindled morphology and be more aligned compared to the relatively random orientation of the cells when the substrates were flattened. These observations are supported by the notion that these human cells are mesenchymal-like and, therefore have an increased motility and inclination to change their morphology to conform to a given surface topography, as a contact guidance mechanism (*Menon et al., 2015 Hileuskaya et al., 2023*).

The isolated porcine cells maintained their cobblestone morphology through passages and showed good proliferative capacity through the effective implementation of collagen-coated flasks/wells. However, when transferred into the wrinkled culture the cells adopted a clustered morphology and a truncated proliferation profile, displaying a declining trend with time as determined using the CCK8 metabolic viability assay. This pattern indicates that such a configuration of topography and the GelMa layer may not be entirely adequate for the cultivation of a purer population of LESC.

In such a complex model it is difficult to accurately pinpoint with a definitive hypothesis the cause of the truncated growth pattern. Altering the Gelma composition to affect surface stiffness properties in the gel layer (in concordance with the underpinning theory behind compressed collagen studies where the stiffness of matrices was studied on limbal cell growth (*Jones et al., 2012*)) may be a viable approach. Alternatively, the topography itself may be the issue where the more mesenchymal-like cells of the human isolate cells were more readily plastic in terms of topological conformity and proliferated to near confluence in static wrinkled culture.

The porcine cells' preference to form colonies may have spatially impeded cell proliferation after attachment. It is considered this may be due to the presence of relatively stiff topological formations causing physical barriers, resulting in the clustering effect. There are no findings or characterisations for this observed phenomenal cellular mechanism in wider literature or works, within limbal cells or epithelial cells as a wider field to make a comparison. Considering the cells were still alive in culture (albeit at a slow decline with time), this phenomenon would suggest that the induction of clustering would have gradually induced an anti-proliferative pathway (but not to such an extent to be detectable with live/dead staining). Somewhat similar (at a couple of orders of magnitude larger) to the nanostructures used to inhibit breast

cancer cell proliferation (*Tavangar et al., 2016*). However, considering the atypical growth pattern, the porcine cell maintained their P63+ stem cell positivity but also expressed CK3, the epithelial marker. This indicates there was a potential differential transitional effect towards corneal epithelium (*Schlötzer-Schrehardt and Kruse, 2005, Gouveia et al., 2019*), even in the cells' proliferative decline.

6.3 CONCLUSION

6.3.2 Research Conclusion

The research which is the subject of this thesis sought to establish answers to several questions concerning the simulation and characterization of the corneal limbal epithelial stem cell niche. This thesis describes how the work undertaken satisfies these research questions (as outlined in Chapter 1, section 1.7) and the further objectives and aims of the research.

This research aimed to (i) characterize the LESC Niche using the non-destructive modalities; (ii) validate the concept of engineered, tunable wrinkled polymer topographies which effectively replicate the limbus; and (iii) produce a dependable bioreactor with the capacity for biomimicry of the LESC Niche.

In terms of whether a biomaterial system has been designed as validated against in-depth characterization of human tissue, it can be said that this has been achieved. Through an intensive investigation using OCT and OCE, the human LESC niche was characterized structurally and mechanically, with age-dependent effects

observed in the tissue. This characterization has served as a suitable reference for the bioreactor/material development.

When considering whether wrinkled polymer substrates can be consistently produced to a standard which simulates the LESC niche for practical application the findings are that the stretch-based methods each have their merits. Each of the explored methods has its separate applications for the generation of wrinkled topographies of different morphologies at different scales and utility, with the dual-treated substrates being the most favourable.

In assessing the extent to which the surface engineering process configured wrinkled topographies that replicate the LESC niche and enable limbal stem cell growth with fate control. It was determined that after coating optimization alongside the use of dual-treated substrates (which were deemed to be the optimum surface) both limbal cell growth and fate control could be enabled with these surfaces. These effects were observed to the extent of being able to visually influence CK3 expression (the epithelial marker) and mechanically influence cell growth patterns by contact guidance/inhibition on the surface of the wrinkled substrates in both species.

The research determined that the ability to modify the generated wrinkles enables the mimicking of either the ageing process or a diseased state through the use of returnable biomimetic wrinkled substrate surfaces. Out of all methods tested (including the laminated blocks), it was the dual treatment method which tolerated low-repeat cyclic dynamization, with minimal material failure, fitting with the requirements of a cell-safe and functioning dynamic bioreactor system.

In determining the benefits of the dynamic model compared to the static model, the conclusion is that dynamization induced cell loss during topographical transitions.

However, the remaining cells were shown to be susceptible to morphological changes imparted by the changes in topography. Concerning developing practical applications for the dynamic model, it is the opinion of the author that future improvements to cellular retention and exploration in higher cell density (towards tissue density) studies would hold value in the limbal epithelial disease model. In particular, this value could be extended further by incorporating OCE with the dynamic model.

Overall this work has set out to achieve three major objectives. Firstly to further the characterisation of the limbal epithelial stem cell niche using non-destructive modalities. In concert with this characterisation, a substrate-centric bioreactor system was designed and developed to replicate and investigate the limbal anatomy in an in vitro setting. Finally, the last objective was to begin to test the bioreactor model through the preliminary analysis of the cellular response to the topographies.

The utilisation of non-destructive imaging techniques has brought deeper insight into the microstructure of the LESC niche, using high-resolution volumetric OCT it was possible to “virtually” dissect the samples. From these virtual dissections, it was possible to obtain limbal anatomic dimensions using basic image processing techniques which rival using more complex programs to achieve similar results. In addition to using simplified methods, these also revealed that even in a small sample size of low statistical power (ultimately leading to limiting the statistical significance). There was a reduction in crypt prominence with advancing age as evidenced by reductions in both PR and ERP width in the older age groups .

In OCE, a similar image analysis approach was used to analyse the tangential cross-sectional elastograms acquired from the limbus. Using this method of analysis

the pervasive limitation in statistical power remained, however with advancing age there was a decrease in Young's modulus of the LESC niche region, no matter how it was defined using ROI selection. The limbal niche stiffness, as found by the drawn method was shown to decrease from 38.7 ± 14.9 Kpa in the under 65-year-old group to 27.2 ± 13.8 KPa in the over 65-year-old group (29.8% decrease). However, it was determined that there was a large disparity in the percentage difference between a straight ROI through the LESC niche layer and an undulating ROI which followed the undulations of the POV as drawn following the structural images. It was calculated that the drawn method yielded results which were 23.3% softer, leading to the assumption that linear ROI's incorporate more stress concentrations which are avoided by structure-guided undulating ROI's. Together these characterisations of LESC niche dimensions and mechanical properties give a correlated perspective of LESC niche microstructure niche and microscale elastic properties and demonstrate there were resolvable changes with age, even in a small and varied population.

The design and development of a novel bioreactor took a dual pathway, first, the design of a frame suitable for small-scale culture facilitated ease of access, and manipulation of materials and were able to be sterilised suitably. Ultimately these criteria were satisfied with a frame designed to fit within commercially available cultureware and designed specifically for substrate chips produced for use in this frame for static and dynamic culture. Through the choice of highly robust materials in the frame design, coupled with the all-round simple functional design of both material substrate chip mould shape and frame arm shape, the frames were not only useful as the actuator of the bioreactor but also as the primary mechanism for producing wrinkles. In conjunction with the bioreactor development, wrinkled material substrates to fit within the bioreactor frame were also developed. Initial trials revealed that a

tension-based system was considered the most useful system, with wrinkle retention and substrate integrity being the foremost concerns with previously discarded methods. Within the tension-based methods of producing wrinkle substrates, there are three different principle methods, (i) plasma treatment, (ii) acid oxidation and (iii) dual treatment methods.

Out of these three methods, the dual treatment proved to create the most stable wrinkles which possessed dimensions closest to the undulations of the POV within the LESC niche. These dimensions were the peak-to-peak width ranges of (45.51 μm – 145.9 μm) and depth ranges of (12.46 μm – 49.4 μm), values which can be correlated to observations of the limbal architecture made during the exploration of the LESC niche using OCT. The dual-treated wrinkled PDMS was the only stretch-based group to be able to undergo the flat-wrinkle-flat transition, thus allowing crypt morphological changes at the micro-anatomical level *in situ* during culture in a highly accessible platform.

In the pursuit of the final aim wherein the effect imparted upon the cells was explored in this preliminary study. Firstly the cells were isolated from two different primary sources, human corneoscleral buttons acquired from an NHS tissue bank and porcine eyeballs acquired from an abattoir. Between the two sources, it was observed that the two different tissue sources seemed to produce slightly different cell types, despite being isolated from the same anatomical region, using the same method and pre-screening steps to verify POV presence before cell isolation. However, both of these cell types presented the stem cell phenotype associated with LESC and weak presentation of the epithelial phenotypes in both cells. The substrate culture appeared to strengthen the expression of the epithelial phenotype by increasing the visible expression of CK3 in both species but maintained the expression of the limbal stem

cell markers as seen by the maintenance of ABCG2 positivity in the human cells and P63 positivity in both species. Culturing the limbal cells from both sources on static wrinkled substrates revealed differing effects unique to each tissue source. The more mesenchymal-like human cells demonstrated more exaggerated and elongation alignment (when cultured on the substrate-bioreactor system) in comparison to the PLESCs which tended to form tighter clusters rather than the expanded colonies observed in monolayer. The dynamic culture was established in both species wherein changes in cellular retention were observed during transitions of state between the stretch and relaxation of the substrates. However, particularly in the human limbal cells, changes to the alignment and the morphology of the cells between transitions were noticeable. Due to the porcine LESC's tending to respond to the wrinkled substrates by clustering, it can be concluded that the alignment response was cell source dependent. The species-specific response to the wrinkled substrates could be an avenue of potential optimisations to be considered in future work.

This thesis presents the case that the practical method for in vitro LESC growth demonstrates an original contribution to knowledge, through the design and validation of a novel bioreactor and surface wrinkling technique with dynamic modification capabilities. The author concludes that the research aims and objectives, defined in section 1.7, have been satisfied through the application of appropriate research and development activities and the subsequent analysis described in this thesis.

6.3.2 Future Work

The overall objectives of the project have been achieved but there is an exciting wealth of future work which could be taken forward with this system to further characterise the effect of the wrinkling process on the materials and the effect of the

wrinkles surface topography on the cell biology. In turn, this will provide key insight into the propagation of degenerative disease after the observed loss of anatomy in diseases such as LSCD, fibrosis from injury and ageing, therefore have potential application as a clinical modelling tool for limbal epithelial disease.

The virtual exploration of the limbal epithelial stem cell niche revealed that both the structural and mechanical properties of this sensitive and architecturally sophisticated tissue could be resolved and correlated together at the microscale. However, the potential variance between the operator and the method of analysis was witnessed. In this research, ImageJ was primarily used as the method of extrapolating OCE data, this was due to MATLAB software accessibility and machine capability. As a limitation however, ImageJ compressed the elastogram data, which may have been a source of variation. In future work, with access to MATLAB, further processing refinements can be made to increase the accuracy of the final results (by analysing the raw uncompressed elastography data) and reduce variation within the analysed datasets. Additionally, expansion of the overall dataset number would increase the statistical power of the dataset by reducing the overall variation, facilitating better grouping of the data which would subsequently reduce the range within the groups. There is a need for further work in the standardisation of the analysis of both OCT and OCE data so that the analysis of datasets can be more unified and in agreement. Once standardised the OCE technology has a potential application to be used in corneal defect screening and analysing the limbus as a predictive effector for these defects by detecting stiffening of the limbus and a loss of limbal niche micro-architecture. Coupling the mechanical measurement with the structural imaging is a much more powerful tool for diagnosis than OCT (visual structural analysis only) alone. With future work, mechanical and structural profiles for different disease states including pterygium,

LSCD and natural aging could be built up to aid in more efficient diagnosis. To facilitate this, cadaveric corneas containing these defects would need to be acquired to test the current system. Following this subsequent test the OCE configuration would need to be altered and tested to optimise the application of the vibrational shaker to the face and determine the optimal placement for the transmission of the vibrations through to the ocular surface to acquire accurate elastograms. An additional advantage of this future would be the more precise monitoring of applied treatments. With frequent monitoring, post operative fibrotic changes or graft rejection may be detected sooner by surface mechanical measurements, before more obvious visual changes (detected by eye or OCT) are seen or subtle changes in sensation (which may be masked by pain medication) are detected, enabling sooner and more effective ameliorative interventions.

This research aimed to broadly design, develop and use a novel biotechnological application to investigate the limbal epithelial stem cell niche. This thesis describes the working small-scale bioreactor designed for multi-replicate testing using *in situ* modifiable biomaterial constructs during culture. There is still a huge scope for further work. For example, on the material front, there is a requirement to further characterise the surface chemistry modification of the PDMS through the dual treatment process, using either high fidelity spectroscopic techniques, for example, liquid nitrogen cooled Fourier Transform Infrared Spectrometry would potentially give a higher resolution of surface bonding compositional analysis (*Finton et al., 2022*) or dedicating resources to refining the collection and analysis of Energy Dispersive X-Ray data (EDX) using scanning electron microscopy. Additionally, there is some room for further exploration in the mechanical testing of material, firstly refining the optical coherence elastography of the materials. Secondly, micro-scale resolution techniques

such as nanoindentation have already been used in testing silver fiber-embedded PDMS for electronic applications (*Maithani et al., 2021*).

Out of all tested substrates only the dual-treated came out as the most biologically relevant. In terms of generating a tuneable wrinkled surface, further exploration is required for either the refinement of the current dual—treatment wrinkling technique or an overhaul to improve the depth dimension evolved from the substrate. Whilst the lateral width (peak to peak) of the wrinkles was the most promising, particularly using the softer formulations of PDMS, to create dimensionally biomimetic structures to replicate the POV horizontally (*Grieve et al., 2015*), they have yet to fully achieve this vertically to achieve the biomimetic crypt depth (*Dua et al., 2005, Haagdoorens et al., 2017*).

The most expansive and exciting prospect for future endeavours lies in the characterisation of the cellular response to the topography. Presented here are the preliminary findings of the cellular responses, which have provided some valuable insight into how the limbal cells behave in this model environment. However, where this model currently falls short is in the in-depth molecular analysis of how the cells respond, currently, flow cytometric and PCR analysis has proven to be outside of the current capacity with these cells. That said, with further investment into outsourced technologies and custom applications, there is significant potential to elucidate precise mechanisms at the molecular level involved in anatomy-dependent stem cell maintenance. Particularly of interest would be the investigation of the wnt-catenin pathways and the YAP-TAZ pathways, the former being a known limbal stem cell maintenance pathway (*González et al., 2019*) Whilst the latter is defined as a mechanobiological pathway associated with corneal epithelial stem cell control (*Gouveia et al., 2019*). This study could take the form of the comparison of the

expression of key pathway components, for example analysing the expression of β -catenin accumulation (and correspondence to LESC phenotypical marker preservation) in both monolayer and static wrinkled culture or conversely the expression of SMADs (and their correspondence to corneal phenotypical marker expression) to monitor and assess corneal differentiation . To assess the involvement of the YAP-TAZ mechanobiological pathway, assessment of the effect of dynamization of the substrate topography during culture and the effect on the pathway components expression would elucidate the involvement of a mechanobiological “switch” in response to a dynamic niche. The involvement of the YAP-TAZ pathway could be checked by comparing the expression of YAP during static culture, wrinkled culture and finally at various timepoints during dynamic culture.

This material substrate-bioreactor system has great potential in the biomimicry of the LESC niche. As already established there is a capacity for substrate dynamization *in situ* in culture to enable fine control of the artificial niche dynamics. Where further optimisation is required is in the improvement of cellular adhesion during transition phases, whether this is in the utility of a more gradiented approach to substrate stretch and relaxation, modification of seeding density at the start or the modification of artificial matrix coating used in substrate design. When these optimisations are complete, this system could be a very powerful tool as a surface-based mechanobiological bioreactor system for micro-scale anatomical disease modelling, in particular LSCD and other corneolimbic conditions. On the basis of this disease modelling, the bioreactor system using primary isolated LSCs could be used as an *in vitro* testing platform for limbal remedial approaches and optimisation of treatments applied to the limbal region. This could provide pre-clinical testing information in a treatment development process in a way that circumvents the technical

and ethical issues which arise from relying on animal models. Additionally, if cell coverage and distribution could be further optimised in LESC culture, the static substrate culture could be used as a way of maintaining isolated stem cells for transplant for potentially longer periods of time *ex vivo*. It is hypothesised that both matrix and anatomical biomimicry could enable the isolated cells to maintain their stemness for longer and improve transplant efficiency after a longer period of storage, enabling an “intermediate length of time” option for the maintenance of donor transplant cells before the procedure. This could remove the complication of precise and short time constraints on donation to transplant procedure scheduling and allow further expansion of cells for transplant if donation numbers are small.

References

Abaci, Hasan Erbil, Coffman, Abigail, Doucet, Yanne, Chen, James, Jacków, Joanna, Wang, Etienne, Guo, Zongyou, Shin, Jung U., Jahoda, Colin A. and Christiano, Angela M. (2018). Tissue engineering of human hair follicles using a biomimetic developmental approach. *Nature Communications*, 9(1), p. 5301, doi:10.1038/s41467-018-07579-y.

Abbas, Adel T., Anwar, Saqib, Abdelnasser, Elshaimaa, Luqman, Monis, Qudeiri, Jaber E. Abu and Elkaseer, Ahmed (2021). Effect of Different Cooling Strategies on Surface Quality and Power Consumption in Finishing End Milling of Stainless Steel 316. *Materials (Basel, Switzerland)*, 14(4), p. 903, doi:10.3390/ma14040903.

Abbasnezhad, N., Zirak, N., Shirinbayan, M., Tcharkhtchi, A. and Bakir, F. (2021). On the importance of physical and mechanical properties of PLGA films during drug release. *Journal of Drug Delivery Science and Technology*, 63, p. 102446, doi:10.1016/j.jddst.2021.102446.

Ahmadiankia, Naghmeh, Ebrahimi, Marzieh, Hosseini, Ahmad and Baharvand, Hossein (2009). Effects of different extracellular matrices and co-cultures on human limbal stem cell expansion in vitro. *Cell Biology International*, 33(9), p. 978–987, doi:10.1016/j.cellbi.2009.06.019.

Ajalloueiian, Fatemeh, Nikogeorgos, Nikolaos, Ajalloueiian, Ali, Fossum, Magdalena, Lee, Seunghwan and Chronakis, Ioannis S. (2018). Compressed collagen constructs with optimized mechanical properties and cell interactions for tissue engineering applications. *International Journal of Biological Macromolecules*, 108, p. 158–166, doi:10.1016/j.ijbiomac.2017.11.117.

Aghayan, Hamid Reza, Hosseini, Motahareh Sheikh, Gholami, Mahdi, Mohamadi-jahani, Fereshteh, Tayanloo-Beik, Akram, Alavi-Moghadam, Sepideh, Payab, Moloud, Goodarzi, Parisa, Abdollahi, Mohammad, Larijani, Bagher and Arjmand, Babak (2022). Mesenchymal stem cells' seeded amniotic membrane as a tissue-engineered dressing for wound healing. *Drug Delivery and Translational Research*, 12(3), p. 538–549, doi:10.1007/s13346-021-00952-3.

Akther, Fahima, Yakob, Shazwani Binte, Nguyen, Nam-Trung and Ta, Hang T. (2020). Surface Modification Techniques for Endothelial Cell Seeding in PDMS Microfluidic Devices. *Biosensors*, 10(11), p. 182, doi:10.3390/bios10110182.

Allen, H. G. (Howard Godfrey) (1969). *Analysis and design of structural sandwich panels*. Pergamon Press.

Almenario, Fatima M., Asi, Ranelle JI, Jacinto, Sonia D. and Mazahery, Ahmad Rf (2020). Reducing mitomycin-C-induced ROS levels in mouse feeder cells improves induced pluripotent stem cell colony growth. *BioTechniques*, 68(5), p. 270–274, doi:10.2144/btn-2019-0118.

Amadeo, Francesco, Boschetti, Federica, Polvani, Gianluca, Banfi, Cristina, Pesce, Maurizio and Santoro, Rosaria (2018). Aortic valve cell seeding into decellularized animal pericardium by perfusion-assisted bioreactor. *Journal of Tissue Engineering and Regenerative Medicine*, 12(6), p. 1481–1493, doi:10.1002/term.2680.

Amerian, Mehrnaz, Amerian, Mahshid, Sameti, Mahyar and Seyedjafari, Ehsan (2019). Improvement of PDMS surface biocompatibility is limited by the duration of oxygen plasma treatment. *Journal of Biomedical Materials Research Part A*, 107(12), p. 2806–2813, doi:10.1002/jbm.a.36783.

Aptel, Michel, Claudon, Laurent and Marsot, Jacques (2002). Integration of Ergonomics Into Hand Tool Design: Principle and Presentation of an Example. *International Journal of Occupational Safety and Ergonomics*, 8(1), p. 107–115, doi:10.1080/10803548.2002.11076518.

Asejczyk-Widlicka, M., Śródka, D. W., Kasprzak, H. and Pierscionek, B. K. (2007). Modelling the elastic properties of the anterior eye and their contribution to maintenance of image quality: the role of the limbus. *Eye*, 21(8), p. 1087–1094, doi:10.1038/sj.eye.6702464.

Aumann, Silke, Donner, Sabine, Fischer, Jörg and Müller, Frank (2019). Optical Coherence Tomography (OCT): Principle and Technical Realization. In: Bille, Josef F. (ed.) *High Resolution Imaging in Microscopy and Ophthalmology: New Frontiers in Biomedical Optics*. Cham: Springer International Publishing, p. 59–85.

Bai, Haiqing, Teng, Yufei, Wong, Lee, Jhanji, Vishal, Pang, Chi-Pui and Yam, Gary Hin-Fai (2010). Proliferative and migratory aptitude in pterygium. *Histochemistry and Cell Biology*, 134(5), p. 527–535, doi:10.1007/s00418-010-0751-5.

Bakunts, Karina, Gillum, Nikki, Karabekian, Zaruhi and Sarvazyan, Narine (2008). Formation of cardiac fibers in Matrigel matrix. *BioTechniques*, 44(3), p. 341–348, doi:10.2144/000112682.

Barbetta, Andrea and Costantini, Marco (2017). Gas foaming technologies for 3D scaffold engineering. In: *Functional 3D Tissue Engineering Scaffolds: Materials, Technologies, and Applications*.

Bashir, Hasan, Seykora, John T. and Lee, Vivian (2017). Invisible Shield: Review of the Corneal Epithelium as a Barrier to UV Radiation, Pathogens, and Other Environmental Stimuli. *Journal of Ophthalmic & Vision Research*, 12(3), p. 305–311, doi:10.4103/jovr.jovr_114_17.

- Batarfi, Wafa Ali, Mohd Yunus, Mohd Heikal and Hamid, Adila A. (2023). The Effect of Hydroxytyrosol in Type II Epithelial-Mesenchymal Transition in Human Skin Wound Healing. *Molecules*, 28(6), p. 2652, doi:10.3390/molecules28062652.
- Baudouin, C., Bourcier, T., Brignole, F., Bertel, F., Moldovan, M., Goldschild, M. and Goguel, A. (2000). Correlation between tear IgE levels and HLA-DR expression by conjunctival cells in allergic and nonallergic chronic conjunctivitis. *Graefe's Archive for Clinical and Experimental Ophthalmology = Albrecht Von Graefes Archiv Fur Klinische Und Experimentelle Ophthalmologie*, 238(11), p. 900–904, doi:10.1007/s004170000179.
- Behaegel, Joséphine, Zakaria, Nadia, Tassignon, Marie-José, Leysen, Inge, Bock, Felix, Koppen, Carina and Ní Dhubhghaill, Sorcha (2019). Short- and Long-Term Results of Xenogeneic-Free Cultivated Autologous and Allogeneic Limbal Epithelial Stem Cell Transplantations. *Cornea*, 38(12), p. 1543–1549, doi:10.1097/ICO.0000000000002153.
- Benhabiles, Hana, Jia, Jieshuang and Lejeune, Fabrice (2016). Pathologies Susceptible to be Targeted for Nonsense Mutation Therapies. p. 77–105.
- Biswal, Trinath, BadJena, Sushant Kumar and Pradhan, Debabrata (2020). Sustainable biomaterials and their applications: A short review. *Materials Today: Proceedings*, 30, p. 274–282, doi:10.1016/j.matpr.2020.01.437.
- Bizheva, Kostadinka, Tan, Bingyao, MacLellan, Benjamin, Hosseinaee, Zohreh, Mason, Erik, Hileeto, Denise and Sorbara, Luigina (2017). In-vivo imaging of the palisades of Vogt and the limbal crypts with sub-micrometer axial resolution optical coherence tomography. *Biomedical Optics Express*, 8(9), p. 4141–4151, doi:10.1364/BOE.8.004141.
- Bisevac, Jovana, Moe, Morten Carstens, Drolsum, Liv, Kristianslund, Olav, Petrovski, Goran and Noer, Agate (2023). A Novel Technique of Amniotic Membrane Preparation Mimicking Limbal Epithelial Crypts Enhances the Number of Progenitor Cells upon Expansion. *Cells*, 12(5), p. 738, doi:10.3390/cells12050738.
- Blanpain, Cédric, Horsley, Valerie and Fuchs, Elaine (2007). Epithelial stem cells: turning over new leaves. *Cell*, 128(3), p. 445–58, doi:10.1016/j.cell.2007.01.014.
- Blazejewska, Ewa Anna, Schlötzer-Schrehardt, Ursula, Zenkel, Matthias, Bachmann, Björn, Chankiewicz, Erik, Jacobi, Christina and Kruse, Friedrich E. (2009). Corneal Limbal Microenvironment Can Induce Transdifferentiation of Hair Follicle Stem Cells into Corneal Epithelial-like Cells. *Stem Cells*, 27(3), p. 642–652, doi:10.1634/stemcells.2008-0721.
- Bradley, J. C., Yang, W., Bradley, R. H., Reid, T. W. and Schwab, I. R. (2010). The science of pterygia. *The British Journal of Ophthalmology*, 94(7), p. 815–820, doi:10.1136/bjo.2008.151852.
- Bokobza, Liliane, Bruneel, Jean-Luc and Couzi, Michel (2015). Raman Spectra of Carbon-Based Materials (from Graphite to Carbon Black) and of Some Silicone Composites. *C*, 1(1), p. 77–94, doi:10.3390/c1010077.
- Borderie, Vincent M., Ghoubay, Djida, Georgeon, Cristina, Borderie, Marie, Sousa, Céline, Legendre, Anne and Rouard, Hélène (2019). Long-Term Results of Cultured

- Limbal Stem Cell Versus Limbal Tissue Transplantation in Stage III Limbal Deficiency. *Stem Cells Translational Medicine*, 8(12), p. 1230–1241, doi:10.1002/sctm.19-0021.
- Borjanovic, Vesna, Bistričić, Lahorija, Vlasov, I., Furić, Krešimir, Zamboni, Ivana, Jaksic, Milko and Shenderova, O. (2009). Influence of proton irradiation on the structure and stability of poly(dimethylsiloxane) and poly(dimethylsiloxane)-nanodiamond composite. *Journal of Vacuum Science & Technology B: Microelectronics and Nanometer Structures*, 27, p. 2396–2403, doi:10.1116/1.3258156.
- Boutin, P., Christel, P., Dorlot, J. M., Meunier, A., de Roquancourt, A., Blanquaert, D., Herman, S., Sedel, L. and Witvoet, J. (1988). The use of dense alumina-alumina ceramic combination in total hip replacement. *Journal of Biomedical Materials Research*, 22(12), p. 1203–1232, doi:10.1002/jbm.820221210.
- Bowden, N., Brittain, S., Evans, A. G., Hutchinson, J. W. and Whitesides, G. M. (1998). Spontaneous formation of ordered structures in thin films of metals supported on an elastomeric polymer. *Nature*, 393(6681), p. 146–149, doi:10.1038/30193.
- Bowden, Ned, Huck, Wilhelm T. S., Paul, Kateri E. and Whitesides, George M. (1999). The controlled formation of ordered, sinusoidal structures by plasma oxidation of an elastomeric polymer. *Applied Physics Letters*, 75(17), p. 2557–2559, doi:10.1063/1.125076.
- Brandao, Livia M., Ledolter, Anna A., Schötzau, Andreas and Palmowski-Wolfe, Anja M. (2016). Comparison of Two Different OCT Systems: Retina Layer Segmentation and Impact on Structure-Function Analysis in Glaucoma. *Journal of Ophthalmology*, 2016, p. e8307639, doi:10.1155/2016/8307639.
- Bray, Laura J., George, Karina A., Suzuki, Shuko, Chirila, Traian V. and Harkin, Damien G. (2013). Fabrication of a corneal-limbal tissue substitute using silk fibroin. *Methods in Molecular Biology (Clifton, N.J.)*, 1014, p. 165–178, doi:10.1007/978-1-62703-432-6_11.
- Brooks, Emily K., Brooks, Richard P. and Ehrensberger, Mark T. (2017). Effects of simulated inflammation on the corrosion of 316L stainless steel. *Materials Science and Engineering: C*, 71, p. 200–205, doi:10.1016/j.msec.2016.10.012.
- Bueno, Ericka M., Saeidi, Nima, Melotti, Suzanna and Ruberti, Jeffrey W. (2009). Effect of Serum and Insulin Modulation on the Organization and Morphology of Matrix Synthesized by Bovine Corneal Stromal Cells. *Tissue Engineering Part A*, 15(11), p. 3559–3573, doi:10.1089/ten.tea.2008.0404.
- Burdick, Jason A. and Vunjak-Novakovic, Gordana (2009). Engineered Microenvironments for Controlled Stem Cell Differentiation. *Tissue Engineering Part A*, 15(2), p. 205–219, doi:10.1089/ten.tea.2008.0131.
- Cai, Z. X. and Fu, Y. B. (2019). Effects of pre-stretch, compressibility and material constitution on the period-doubling secondary bifurcation of a film/substrate bilayer. *International Journal of Non-Linear Mechanics*, 115, p. 11–19, doi:10.1016/j.ijnonlinmec.2019.05.001.
- Cai, Zongxi and Fu, Yibin (1999a). On the imperfection sensitivity of a coated elastic half-space. *Proceedings of the Royal Society of London. Series A: Mathematical*,

Physical and Engineering Sciences, 455(1989), p. 3285–3309, doi:10.1098/rspa.1999.0451.

Cai, Zongxi and Fu, Yibin (1999b). On the imperfection sensitivity of a coated elastic half-space. *Proceedings of the Royal Society A: Mathematical, Physical and Engineering Sciences*, 455(1989), p. 3285–3309, doi:10.1098/rspa.1999.0451.

Camarasa, Mavi, Brison, Daniel, Kimber, Susan J. and Handyside, Alan H. (2009). *Naturally Immortalised Mouse Embryonic Fibroblast Lines Support Human Embryonic Stem Cell Growth*. <https://home.liebertpub.com/clo>. <https://www.liebertpub.com/doi/10.1089/clo.2008.0082>

Cartes, Cristian, Lako, Majlinda and Figueiredo, Francisco C. (2021). Referral Patterns of Patients with Limbal Stem Cell Deficiency to a Specialized Tertiary Center in the United Kingdom. *Ophthalmology and Therapy*, 10(3), p. 535–545, doi:10.1007/s40123-021-00349-y.

Cellscale. (2023). *Products* | *CellScale*. https://www.cellscale.com/products/?_vsrefdom=adwords&gclid=CjwKCAjw6vviBhB_EiwAQJRopnN0CTzUDnNhi0OvI7X-JwxxJXiKm7qxE58VWMRrkG4Pxad6N6T0ARoCdI4QAvD_BwE

Cerda, E. and Mahadevan, L. (2003a). Geometry and Physics of Wrinkling. *Physical Review Letters*, 90(7), p. 074302, doi:10.1103/PhysRevLett.90.074302.

Cerda, E. and Mahadevan, L. (2003b). Geometry and Physics of Wrinkling. *Physical Review Letters*, 90(7), p. 4, doi:10.1103/PhysRevLett.90.074302.

Ceylan, Seda, Dimmock, Ryan and Yang, Ying (2023). Development of Boron-Containing PVA-Based Cryogels with Controllable Boron Releasing Rate and Altered Influence on Osteoblasts. *Polymers*, 15(7), p. 1653, doi:10.3390/polym15071653.

Chang, Chiung-Ying, Pasolli, H. Amalia, Giannopoulou, Eugenia G., Guasch, Géraldine, Gronostajski, Richard M., Elemento, Olivier and Fuchs, Elaine (2013). NFIB is a governor of epithelial-melanocyte stem cell behaviour in a shared niche. *Nature*, 495(7439), p. 98–102, doi:10.1038/nature11847.

Chavoshnejad, Poorya, Foroughi, Ali H., Dhandapani, Niranjana, German, Guy K. and Razavi, Mir Jalil (2021). Effect of collagen degradation on the mechanical behavior and wrinkling of skin. *Physical Review E*, 104(3), p. 034406, doi:10.1103/PhysRevE.104.034406.

Chen, D., Qu, Y., Hua, X., Zhang, L., Liu, Z., Pflugfelder, S. C. and Li, D. Q. (2017). A hyaluronan hydrogel scaffold-based xeno-free culture system for ex vivo expansion of human corneal epithelial stem cells. *Eye (London, England)*, 31(6), p. 962–971, doi:10.1038/eye.2017.8.

Chen, Jialin, Zhang, Wei, Kelk, Peyman, Backman, Ludvig J. and Danielson, Patrik (2017). Substance P and patterned silk biomaterial stimulate periodontal ligament stem cells to form corneal stroma in a bioengineered three-dimensional model. *Stem Cell Research and Therapy*, 8(1), p. 260, doi:10.1186/s13287-017-0715-y.

Chen, Szu-Yu, Hayashida, Yasutaka, Chen, Mei-Yun, Xie, Hua Tao and Tseng, Scheffer C. G. (2011). A New Isolation Method of Human Limbal Progenitor Cells by Maintaining Close Association with Their Niche Cells. *Tissue Engineering Part C: Methods*, 17(5), p. 537–548, doi:10.1089/ten.tec.2010.0609.

Chen, Zhuo, Paiva, Cintia S. de, Luo, Lihui, Kretzer, Francis L., Pflugfelder, Stephen C. and Li, De-Quan (2004). Characterization of Putative Stem Cell Phenotype in Human Limbal Epithelia. *STEM CELLS*, 22(3), p. 355–366, doi:10.1634/stemcells.22-3-355.

Chien, Hsiu-Wen, Chen, Xiang-Yu, Tsai, Wen-Pei and Lee, Mengshan (2020). Inhibition of biofilm formation by rough shark skin-patterned surfaces. *Colloids and Surfaces B: Biointerfaces*, 186, p. 110738, doi:10.1016/j.colsurfb.2019.110738.

Cohrs, Nicholas H., Schulz-Schönhagen, Konstantin, Mohn, Dirk, Wolint, Petra, Meier Bürgisser, Gabriella, Stark, Wendelin J. and Buschmann, Johanna (2019). Modification of silicone elastomers with Bioglass 45S5® increases in ovo tissue biointegration. *Journal of Biomedical Materials Research. Part B, Applied Biomaterials*, 107(4), p. 1180–1188, doi:10.1002/jbm.b.34211.

Colanesi, Sarah, Käsmann-Kellner, Barbara, Stachon, Tanja, Szentmáry, Nóra and Seitz, Berthold (2015). Efficacy of different protocols for ex vivo expansion of limbal epithelial stem cell. *Investigative Ophthalmology & Visual Science*, 56(7), p. 3473.

Costello, Cait M., Phillipsen, Mikkel B., Hartmanis, Leonard M., Kwasnica, Marek A., Chen, Victor, Hackam, David, Chang, Matthew W., Bentley, William E. and March, John C. (2017). Microscale Bioreactors for *in situ* characterization of GI epithelial cell physiology. *Scientific Reports*, 7(1), p. 12515, doi:10.1038/s41598-017-12984-2.

Dabaghi, Mohammadhossein, Shahriari, Shadi, Saraei, Neda, Da, Kevin, Chandiramohan, Abiram, Selvaganapathy, Ponnambalam Ravi and Hirota, Jeremy A. (2021). Surface Modification of PDMS-Based Microfluidic Devices with Collagen Using Polydopamine as a Spacer to Enhance Primary Human Bronchial Epithelial Cell Adhesion. *Micromachines*, 12(2), p. 132, doi:10.3390/mi12020132.

Damala, Mukesh, Sahoo, Abhishek, Pakalapati, Naveen, Singh, Vivek and Basu, Sayan (2023). Pre-Clinical Evaluation of Efficacy and Safety of Human Limbus-Derived Stromal/Mesenchymal Stem Cells with and without Alginate Encapsulation for Future Clinical Applications. *Cells*, 12(6), p. 876, doi:10.3390/cells12060876.

De Maria, Carmelo, Fortunato, Gabriele Maria, Chiesa, Irene and Vozzi, Giovanni (2020). Microfabricated and multilayered PLGA structure for the development of co-cultured in vitro liver models. *Bioprinting*, 18, p. e00084, doi:10.1016/j.bprint.2020.e00084.

Delaine-Smith, R. M., Burney, S., Balkwill, F. R. and Knight, M. M. (2016). Experimental validation of a flat punch indentation methodology calibrated against unconfined compression tests for determination of soft tissue biomechanics. *Journal of the Mechanical Behavior of Biomedical Materials*, 60, p. 401–415, doi:10.1016/j.jmbbm.2016.02.019.

DelMonte, Derek W. and Kim, Terry (2011). Anatomy and physiology of the cornea. *Journal of Cataract and Refractive Surgery*, 37(3), p. 588–598, doi:10.1016/j.jcrs.2010.12.037.

de la Mata, Ana, Nieto-Miguel, Teresa, López-Paniagua, Marina, Galindo, Sara, Aguilar, María Rosa, García-Fernández, Luis, Gonzalo, Sandra, Vázquez, Blanca, Román, Julio San, Corrales, Rosa María and Calonge, Margarita (2013). Chitosan-gelatin biopolymers as carrier substrata for limbal epithelial stem cells. *Journal of*

Materials Science. Materials in Medicine, 24(12), p. 2819–2829, doi:10.1007/s10856-013-5013-3.

Deshpande, Pallavi, Ramachandran, Charanya, Sefat, Farshid, Mariappan, Indumathi, Johnson, Claire, McKean, Robert, Hannah, Melanie, Sangwan, Virender S., Claeysens, Frederik, Ryan, Anthony J. and MacNeil, Sheila (2013). Simplifying corneal surface regeneration using a biodegradable synthetic membrane and limbal tissue explants. *Biomaterials*, 34(21), p. 5088–5106, doi:10.1016/j.biomaterials.2013.03.064.

Dhamodaran, Kamesh, Subramani, Murali, Matalia, Himanshu, Jayadev, Chaitra, Shetty, Rohit and Das, Debashish (2016). One for all: A standardized protocol for ex vivo culture of limbal, conjunctival and oral mucosal epithelial cells into corneal lineage. *Cytotherapy*, 18(4), p. 546–561, doi:10.1016/j.jcyt.2016.01.003.

Dhar, Sarit, Chrisman, Timothy and Simman, Richard (2023). Clinical Indications of Cultured Epithelial Autografts. *Annals of Plastic Surgery*, 91(4), p. 433–440, doi:10.1097/SAP.0000000000003558.

Dimmock, Ryan L., Wang, Xuyiling, Fu, Yibin, Haj, Alicia J. El and Yang, Ying (2020). Biomedical Applications of Wrinkling Polymers. *Recent Progress in Materials 2020, Vol. 2, Page 1, 2(1)*, p. 1–1, doi:10.21926/RPM.2001005.

Dimmock, Ryan, Zhang, Yilong, Butt, Gibran F., Rauz, Saaeha, Huang, Zhihong and Yang, Ying (2024). Characterizing Biomechanics of Limbal Niche Using Vibrational Optical Coherence Elastography. *Journal of Biophotonics*, n/a(n/a), p. e202400172, doi:10.1002/jbio.202400172.

Dimmock, Ryan, Zhang, Yilong, Butt, Gibran, Huang, Zhihong, Rauz, Saaeha and Yang, Ying (2023). Characterisation and quantification of the limbal architecture and biomechanical properties using optical coherence tomography or elastography (Conference Presentation). In: *Biomedical Applications of Light Scattering XIII*. Presented at the Biomedical Applications of Light Scattering XIII, p. PC1239304.

Dimmock, Ryan L., Rotherham, Michael, El Haj, Alicia J. and Yang, Ying (2023). Fabrication and Characterisation of Hydrogels with Reversible Wrinkled Surfaces for Limbal Study and Reconstruction. *Gels*, 9(11), p. 915, doi:10.3390/gels9110915.

Dobrowolski, Dariusz, Orzechowska-Wylegala, Boguslawa, Wowra, Bogumil, Wróblewska-Czajka, Ewa, Grolik, Maria and Wylegala, Edward (2021). An Analysis of the Progression of Conjunctivalisation after Transplantation of Cultivated Corneal Epithelium. *Journal of Ophthalmology*, 2021(1), p. 8499640, doi:10.1155/2021/8499640.

Doğan, Emine, Çakır, Burçin, Aksoy, Nilgün, Köse, Elif and Alagöz, Gürsoy (2021). Does pterygium morphology affect corneal astigmatism? *Therapeutic Advances in Ophthalmology*, 13, p. 25158414211030423, doi:10.1177/25158414211030423.

Drexler, Wolfgang (2004). Ultrahigh-resolution optical coherence tomography. *Journal of Biomedical Optics*, 9(1), p. 47–74, doi:10.1117/1.1629679.

Drexler, Wolfgang, Liu, Mengyang, Kumar, Abhishek, Kamali, Tschackad, Unterhuber, Angelika and Leitgeb, Rainer A. (2014). Optical coherence tomography today: speed, contrast, and multimodality. *Journal of Biomedical Optics*, 19(7), p. 071412, doi:10.1117/1.JBO.19.7.071412.

- Dua, H. and Azuara-Blanco, A. (1999). Allo-limbal transplantation in patients with limbal stem cell deficiency. *The British Journal of Ophthalmology*, 83(4), p. 414–419.
- Dua, H. S., Shanmuganathan, V. A., Powell-Richards, A. O., Tighe, P. J. and Joseph, A. (2005). Limbal epithelial crypts: a novel anatomical structure and a putative limbal stem cell niche. *British Journal of Ophthalmology*, 89(5), p. 529–532, doi:10.1136/bjo.2004.049742.
- Duan, Chao-Ye, Xie, Hua-Tao, Zhao, Xin-Yue, Xu, Wen-Han and Zhang, Ming-Chang (2019). Limbal niche cells can reduce the angiogenic potential of cultivated oral mucosal epithelial cells. *Cellular & Molecular Biology Letters*, 24(1), p. 3, doi:10.1186/s11658-018-0133-x.
- Durdáková, Tereza-Markéta, Hrdlička, Zdeněk, Dendisová, Marcela, Švecová, Marie and Vopička, Ondřej (2020). Swelling and plasticization of PDMS and PTMSP in methanol and dimethyl carbonate vapors and liquids: Volume, mechanical properties, Raman spectra. *Polymer*, 188, p. 122140, doi:10.1016/j.polymer.2019.122140.
- Eberwein, Philipp, Nohava, Jiri, Schlunck, Günther and Swain, Michael (2014a). Nanoindentation Derived Mechanical Properties of the Corneoscleral Rim of the Human Eye. *Key Engineering Materials*, 606, p. 117–120, doi:10.4028/www.scientific.net/KEM.606.117.
- Eberwein, Philipp, Nohava, Jiri, Schlunck, Günther and Swain, Michael (2014b). Nanoindentation Derived Mechanical Properties of the Corneoscleral Rim of the Human Eye. *Key Engineering Materials*, 606, p. 117–120, doi:10.4028/www.scientific.net/KEM.606.117.
- Elhousseiny, Abdelrahman M., Soleimani, Mohammad, Eleiwa, Taher K., ElSheikh, Reem H., Frank, Charles R., Naderan, Morteza, Yazdanpanah, Ghasem, Rosenblatt, Mark I. and Djalilian, Ali R. (2022). Current and Emerging Therapies for Limbal Stem Cell Deficiency. *Stem Cells Translational Medicine*, 11(3), p. 259–268, doi:10.1093/stcltm/szab028.
- Elsheikh, Ahmed, Geraghty, Brendan, Rama, Paolo, Campanelli, Marino and Meek, Keith M. (2010). Characterization of age-related variation in corneal biomechanical properties. *Journal of The Royal Society Interface*, 7(51), p. 1475–1485, doi:10.1098/rsif.2010.0108.
- EMA. (2024). *Xenogeneic cell-based medicinal products -Scientific guideline | European Medicines Agency*. <https://www.ema.europa.eu/en/xenogeneic-cell-based-medicinal-products-scientific-guideline>
- Eslani, Medi, Cheung, Albert Y., Kurji, Khaliq, Pierson, Kasey, Sarnicola, Enrica and Holland, Edward J. (2019). Long-term outcomes of conjunctival limbal autograft in patients with unilateral total limbal stem cell deficiency. *The Ocular Surface*, 17(4), p. 670–674, doi:10.1016/j.jtos.2019.09.003.
- Fagan, Shawn, Hassan, Zaheed, Homsombath, Bounthavy, Sood, Rajiv, Hardy, Kade, Craft-Coffman, Beretta, Hartman, Brett C., Cramer, Caryn and Griswold, John (2024). Report of outcomes in burn patients enrolled in the Cultured epidermal autograft prospective Registry. *Burns Open*, 8(1), p. 29–34, doi:10.1016/j.burnso.2023.12.001.
- Fan, Nai-Wen, Ho, Tsung-Chuan, Wu, Cheng-Wen and Tsao, Yeou-Ping (2019). Pigment epithelium-derived factor peptide promotes limbal stem cell proliferation

- through hedgehog pathway. *Journal of Cellular and Molecular Medicine*, 23(7), p. 4759–4769, doi:10.1111/jcmm.14364.
- Fang, Haiqin, Zhi, Yuan, Yu, Zhou, Lynch, Robert A. and Jia, Xudong (2018). The embryonic toxicity evaluation of deoxynivalenol (DON) by murine embryonic stem cell test and human embryonic stem cell test models. *Food Control*, 86, p. 234–240, doi:10.1016/j.foodcont.2017.10.018.
- Feng, Jiang-Tao and Zhao, Ya-Pu (2008). Influence of different amount of Au on the wetting behavior of PDMS membrane. *Biomedical Microdevices*, 10(1), p. 65–72, doi:10.1007/s10544-007-9110-2.
- Fernández-Pérez, Julia, Binner, Marcus, Werner, Carsten and Bray, Laura J. (2017). Limbal stromal cells derived from porcine tissue demonstrate mesenchymal characteristics in vitro. *Scientific Reports*, 7(1), p. 1–13, doi:10.1038/s41598-017-06898-2.
- Ferrari, Michele, Cirisano, Francesca and Morán, M. Carmen (2019). Mammalian Cell Behavior on Hydrophobic Substrates: Influence of Surface Properties. *Colloids and Interfaces*, 3(2), p. 48, doi:10.3390/colloids3020048.
- Finkbeiner, Stacy R., Freeman, Jennifer J., Wieck, Minna M., El-Nachef, Wael, Altheim, Christopher H., Tsai, Yu-Hwai, Huang, Sha, Dyal, Rachel, White, Eric S., Grikscheit, Tracy C., Teitelbaum, Daniel H. and Spence, Jason R. (2015). Generation of tissue-engineered small intestine using embryonic stem cell-derived human intestinal organoids. *Biology Open*, 4(11), p. 1462–1472, doi:10.1242/bio.013235.
- Finton, Drew M., Breshike, Christopher J., Kendziora, Christopher A., Furstenberg, Robert and McGill, R. Andrew (2022). Infrared backscatter imaging spectroscopy for standoff detection of hazardous materials. In: *Chemical, Biological, Radiological, Nuclear, and Explosives (CBRNE) Sensing XXIII*. Presented at the Chemical, Biological, Radiological, Nuclear, and Explosives (CBRNE) Sensing XXIII, SPIE, p. 202–207.
- Fisher, Matthew L., Balinth, Seamus and Mills, Alea A. (2020). p63-related signalling at a glance. *Journal of Cell Science*, 133(17), p. jcs228015, doi:10.1242/jcs.228015.
- Fitzgerald, Matthew L., Tsai, Sara, Bellan, Leon M., Sappington, Rebecca, Xu, Yaqiong and Li, Deyu (2019). The relationship between the Young's modulus and dry etching rate of polydimethylsiloxane (PDMS). *Biomedical Microdevices*, 21(1), p. 26, doi:10.1007/s10544-019-0379-8.
- Flexcell (2023). *Cell Stretching Bioreactors | Flexcell International*. <https://flexcellint.com>.
- Francoz, Marlène, Karamoko, Issouf, Baudouin, Christophe and Labbé, Antoine (2011). Ocular Surface Epithelial Thickness Evaluation with Spectral-Domain Optical Coherence Tomography. *Investigative Ophthalmology & Visual Science*, 52(12), p. 9116–9123, doi:10.1167/iovs.11-7988.
- Gehlen, David B., De Lencastre Novaes, Leticia C., Long, Wei, Ruff, Anna Joelle, Jakob, Felix, Haraszti, Tamás, Chandorkar, Yashoda, Yang, Liangliang, van Rijn, Patrick, Schwaneberg, Ulrich and De Laporte, Laura (2019). Rapid and Robust Coating Method to Render Polydimethylsiloxane Surfaces Cell-Adhesive. *ACS Applied Materials & Interfaces*, 11(44), p. 41091–41099, doi:10.1021/acsami.9b16025.

Gennisson, J. L., Deffieux, T., Fink, M. and Tanter, M. (2013). Ultrasound elastography: Principles and techniques. *Diagnostic and Interventional Imaging*, 94(5), p. 487–495, doi:10.1016/j.diii.2013.01.022.

Genzer, Jan and Groenewold, Jan (2006). *Soft matter with hard skin: From skin wrinkles to templating and material characterization*.

Geraghty, Brendan, Whitford, Charles, Boote, Craig, Akhtar, Riaz and Elsheikh, Ahmed (2015). Age-Related Variation in the Biomechanical and Structural Properties of the Corneo-Scleral Tunic. In: Derby, Brian and Akhtar, Riaz (eds.) *Mechanical Properties of Aging Soft Tissues*. Cham: Springer International Publishing, p. 207–235. https://doi.org/10.1007/978-3-319-03970-1_9.

Ghoubay-Benallaoua, Djida, Sousa, Céline De, Martos, Raphaël, Latour, Gaël, Schanne-Klein, Marie Claire, Dupin, Elisabeth and Borderie, Vincent (2017). Easy xeno-free and feeder-free method for isolating and growing limbal stromal and epithelial stem cells of the human cornea. *PLoS ONE*, 12(11), doi:10.1371/journal.pone.0188398.

Glatz, Bernhard Alexander and Fery, Andreas (2018). The influence of plasma treatment on the elasticity of the *in situ* oxidized gradient layer in PDMS: towards crack-free wrinkling. *Soft Matter*, 15(1), p. 65–72, doi:10.1039/C8SM01910J.

Góes, Rejane Maira, Barbosa, Flávia Leão, De Faria-e-sousa, Sidney Júlio and Haddad, Antonio (2008). Morphological and Autoradiographic Studies on the Corneal and Limbal Epithelium of Rabbits. *The Anatomical Record*, 291(2), p. 191–203, doi:10.1002/ar.20635.

Gómez-Varela, Ana Isabel, Carnero, Bastián, Álvarez, Ezequiel, Flores-Arias, María Teresa and Bao-Varela, Carmen (2021). Biocompatibility analysis of thermal and UV-curable polydimethylsiloxane for semi blood vessel-like model fabrication. In: *2021 Conference on Lasers and Electro-Optics Europe & European Quantum Electronics Conference (CLEO/Europe-EQEC)*. Presented at the 2021 Conference on Lasers and Electro-Optics Europe & European Quantum Electronics Conference (CLEO/Europe-EQEC), p. 1–1.

Gonzales, Kevin Andrew Uy and Fuchs, Elaine (2017). Skin and Its Regenerative Powers: An Alliance between Stem Cells and Their Niche. *Developmental Cell*, 43(4), p. 387–401, doi:10.1016/J.DEVCEL.2017.10.001.

González, Sheyla, Mei, Hua, Nakatsu, Martin N., Baclagon, Elfren R. and Deng, Sophie X. (2016). A 3D culture system enhances the ability of human bone marrow stromal cells to support the growth of limbal stem/progenitor cells. *Stem Cell Research*, 16(2), p. 358–364, doi:10.1016/j.scr.2016.02.018.

GONZALEZ, SHEYLA, Nakatsu, Martin, Mei, Hua and Deng, Sophie (2013). Comparison of Different Limbal Epithelial Stem Cell Isolation Methods to Improve the Epithelial Sheet Quality for Transplantation. *Investigative Ophthalmology & Visual Science*, 54(15), p. 989.

González, Sheyla, Oh, Denise, Baclagon, Elfren R., Zheng, Jie J. and Deng, Sophie X. (2019). Wnt Signalling Is Required for the Maintenance of Human Limbal Stem/Progenitor Cells In vitro. *Investigative Ophthalmology & Visual Science*, 60(1), p. 107–112, doi:10.1167/iovs.18-25740.

- González, Sheyla, Uhm, Heui and Deng, Sophie X. (2019). Notch Inhibition Prevents Differentiation of Human Limbal Stem/Progenitor Cells in vitro. *Scientific Reports*, 9(1), p. 1–11, doi:10.1038/s41598-019-46793-6.
- Gouveia, Ricardo M., Vajda, Flora, Wibowo, Jason A., Figueiredo, Francisco, Connon, Che J., Gouveia, Ricardo M., Vajda, Flora, Wibowo, Jason A., Figueiredo, Francisco and Connon, Che J. (2019). YAP, Δ Np63, and β -Catenin Signalling Pathways Are Involved in the Modulation of Corneal Epithelial Stem Cell Phenotype Induced by Substrate Stiffness. *Cells*, 8(4), p. 347, doi:10.3390/cells8040347.
- Grieve, K., Ghoubay, D., Georgeon, C., Thouvenin, O., Bouheraoua, N., Paques, M. and Borderie, V. M. (2015a). Three-dimensional structure of the mammalian limbal stem cell niche. *Experimental Eye Research*, 140, p. 75–84, doi:10.1016/j.exer.2015.08.003.
- Guillemette, Maxime D., Cui, Bo, Roy, Emmanuel, Gauvin, Robert, Giasson, Claude J., Esch, Mandy B., Carrier, Patrick, Deschambeault, Alexandre, Dumoulin, Michel, Toner, Mehmet, Germain, Lucie, Veres, Teodor and Auger, Francois A. (2009). Surface topography induces 3D self-orientation of cells and extracellular matrix resulting in improved tissue function. *Integrative Biology: Quantitative Biosciences from Nano to Macro*, 1(2), p. 196–204, doi:10.1039/b820208g.
- Guindolet, Damien, Crouzet, Emmanuel, He, Zhiguo, Herbepin, Pascal, Jumelle, Clotilde, Perrache, Chantal, Dumollard, Jean Marc, Forest, Fabien, Peoc'h, Michel, Gain, Philippe, Gabison, Eric and Thuret, Gilles (2017). Storage of Porcine Cornea in an Innovative Bioreactor. *Investigative Ophthalmology & Visual Science*, 58(13), p. 5907–5917, doi:10.1167/iovs.17-22218.
- Gümüşderelioğlu, Menemşe, Betül Kaya, F. and Beşkardeş, Işıl Gerçek (2011). Comparison of epithelial and fibroblastic cell behavior on nano/micro-topographic PCL membranes produced by crystallinity control. *Journal of Colloid and Interface Science*, 358(2), p. 444–453, doi:10.1016/j.jcis.2011.03.026.
- Haagdorens, M., Cèpla, V., Melsbach, E., Koivusalo, L., Skottman, H., Griffith, M., Valiokas, R., Zakaria, N., Pintelon, I. and Tassignon, M. J. (2019). In vitro Cultivation of Limbal Epithelial Stem Cells on Surface-Modified Crosslinked Collagen Scaffolds. *Stem Cells International*, Special Issue(Engineering Cell Systems), doi:10.1155/2019/7867613.
- Haagdorens, Michel, Behaegel, Joséphine, Rozema, Jos, Gerwen, Veerle Van, Michiels, Sofie, Dhuhghaill, Sorcha Ní, Tassignon, Marie-José and Zakaria, Nadia (2017). A method for quantifying limbal stem cell niches using OCT imaging. *The British journal of ophthalmology*, 101(9), p. 1250–1255, doi:10.1136/bjophthalmol-2016-309549.
- Håskjold, E., Bjerknes, R. and Bjerknes, E. (1989). Migration of cells in the rat corneal epithelium. *Acta Ophthalmologica*, 67(1), p. 91–96, doi:10.1111/j.1755-3768.1989.tb00730.x.
- He, Ping and Jin, Xiaojie (2018). SOX10 induces epithelial–mesenchymal transition and contributes to nasopharyngeal carcinoma progression. *Biochemistry and Cell Biology*, 96(3), p. 326–331, doi:10.1139/bcb-2017-0160.

Heide, David, Verbraeken, B., Hoogenboom, R., Dargaville, Tim R. and Hickey, D. (2017). Porous poly (2-oxazoline) scaffolds for developing 3D primary human tissue culture.

Helgason, Rick, Fathy, Jino and Lai, Yongjun (2023). The effect of laser cutting on the Young's modulus of Polydimethylsiloxane. *Journal of Micromanufacturing*, 6(1), p. 60–65, doi:10.1177/25165984221131400.

Helling, Ayelen L., Viswanathan, Priyalakshmi, Cheliotis, Katerina S., Mobasseri, Seyedeh Atefeh, Yang, Ying, Haj, Alicia J. El and Watt, Fiona M. (2019). Dynamic Culture Substrates That Mimic the Topography of the Epidermal-Dermal Junction. *Tissue Engineering -Part A*, 25(3–4), p. 214–223, doi:10.1089/ten.tea.2018.0125.

Hileuskaya, Kseniya, Kakasi, Balazs, Kulikouskaya, Viktoryia, Vonderviszt, Ferenc, Nikalaichuk, Viktoryia, Dubatouka, Katsiaryna, Chyshankou, Ihnat, Kraskouski, Aliaksandr, Muravsky, Alexander, Murauski, Anatoli, Pinchuk, Sergei, Vasilevich, Irina, Volotovskii, Igor and Agabekov, Vladimir (2023). Contact guidance of mesenchymal stem cells by flagellin-modified substrates: Aspects of cell-surface interaction from the point of view of liquid crystal theory. *Colloids and Surfaces A: Physicochemical and Engineering Aspects*, 663, p. 131113, doi:10.1016/j.colsurfa.2023.131113.

Hjørtdal, J. O. (1996). Regional elastic performance of the human cornea. *Journal of Biomechanics*, 29(7), p. 931–942, doi:10.1016/0021-9290(95)00152-2.

Horwitz, Vered, Dachir, Shlomit, Cohen, Maayan, Gutman, Hila, Cohen, Liat, Gez, Rellie, Buch, Hillel, Kadar, Tamar and Gore, Ariel (2018). Differential expression of corneal and limbal cytokines and chemokines throughout the clinical course of sulfur mustard induced ocular injury in the rabbit model. *Experimental Eye Research*, 177, p. 145–152, doi:10.1016/j.exer.2018.08.008.

Hourd, Paul, Chandra, Amit, Medcalf, Nick and Williams, David J. (2008). Regulatory challenges for the manufacture and scale-out of autologous cell therapies. In: *StemBook*. Cambridge (MA): Harvard Stem Cell Institute. <http://www.ncbi.nlm.nih.gov/books/NBK201975/>.

Hsueh, Yi-Jen, Ma, David Hui-Kang, Ma, Kathleen Sheng-Chuan, Wang, Tze-Kai, Chou, Cheng-Hung, Lin, Chien-Cheng, Huang, Min-Chang, Luo, Li-Jyuan, Lai, Jui-Yang and Chen, Hung-Chi (2019). Extracellular Matrix Protein Coating of Processed Fish Scales Improves Human Corneal Endothelial Cell Adhesion and Proliferation. *Translational Vision Science & Technology*, 8(3), p. 27, doi:10.1167/tvst.8.3.27.

Hsu, Ting-Wei, Lu, Yu-Jen, Lin, Yu-Jie, Huang, Yu-Ting, Hsieh, Li-Hung, Wu, Bing-Huan, Lin, Yu-Chun, Chen, Li-Chi, Wang, Hsin-Wen, Chuang, Jui-Che, Fang, Yi-Qiao and Huang, Chieh-Cheng (2021). Transplantation of 3D MSC/HUVEC spheroids with neuroprotective and proangiogenic potentials ameliorates ischemic stroke brain injury. *Biomaterials*, 272, p. 120765, doi:10.1016/j.biomaterials.2021.120765.

Hu, Minyi, Tian, Guowei, Gibbons, Daniel E., Jiao, Jian and Qin, Yi-Xian (2015). Dynamic Fluid Flow Induced Mechanobiological Modulation of *In situ* Osteocytic Calcium Oscillations. *Archives of biochemistry and biophysics*, 579, p. 55–61, doi:10.1016/j.abb.2015.05.012.

Hynds, Robert E., Gowers, Kate H. C., Nigro, Ersilia, Butler, Colin R., Bonfanti, Paola, Giangreco, Adam, Prêle, Cecilia M. and Janes, Sam M. (2018). Cross-talk between human airway epithelial cells and 3T3-J2 feeder cells involves partial activation of

human MET by murine HGF. *PLOS ONE*, 13(5), p. e0197129, doi:10.1371/journal.pone.0197129.

Ionescu, Ana Maria, Chato-Astrain, Jesus, Pérez, Juan de la Cruz Cardona, Campos, Fernando, Gómez, Maria M. Pérez, Alaminos, Miguel and Bello, Ingrid Garzón (2020). Evaluation of the optical and biomechanical properties of bioengineered human skin generated with fibrin-agarose biomaterials. *Journal of Biomedical Optics*, 25(5), p. 055002, doi:10.1117/1.JBO.25.5.055002.

Irfan Maqsood, Muhammad, Matin, Maryam M., Bahrami, Ahmad Reza and Ghasroldasht, Mohammad M. (2013). Immortality of cell lines: challenges and advantages of establishment. *Cell Biology International*, 37(10), p. 1038–1045, doi:10.1002/cbin.10137.

Ishida, Shutaro and Nishizawa, Norihiko (2012). Quantitative comparison of contrast and imaging depth of ultrahigh-resolution optical coherence tomography images in 800–1700 nm wavelength region. *Biomedical Optics Express*, 3(2), p. 282–294, doi:10.1364/BOE.3.000282.

Islam, Mohammad Mirazul, Sharifi, Roholah and Gonzalez-Andrades, Miguel (2019). Corneal Tissue Engineering. In: Alió, Jorge L., Alió del Barrio, Jorge L., and Arnalich-Montiel, Francisco (eds.) *Corneal Regeneration: Therapy and Surgery*. Cham: Springer International Publishing, p. 23–37.

Ismail, Edhuan, Lazim, Nurul Hakimah, Nakata, Ayako, Iwasawa, Ayumi, Yamanaka, Risako and Ichinose, Izumi (2020). Plasma-induced Interfacial Crosslinking of Liquid Polydimethylsiloxane Films and Their Organic Solvent Permeation Performance. *Chemistry Letters*, doi:10.1246/cl.200504.

jamovi - open statistical software for the desktop and cloud. <https://www.jamovi.org/>

Jang, Jinah, Park, Hun-Jun, Kim, Seok-Won, Kim, Heejin, Park, Ju Young, Na, Soo Jin, Kim, Hyeon Ji, Park, Moon Nyeo, Choi, Seung Hyun, Park, Sun Hwa, Kim, Sung Won, Kwon, Sang-Mo, Kim, Pum-Joon and Cho, Dong-Woo (2017). 3D printed complex tissue construct using stem cell-laden decellularized extracellular matrix bioinks for cardiac repair. *Biomaterials*, 112, p. 264–274, doi:10.1016/j.biomaterials.2016.10.026.

Jirsova, Katerina, Dudakova, Lubica, Kalasova, Sarka, Vesela, Viera and Merjava, Stanislava (2011). The OV-TL 12/30 Clone of Anti-cytokeratin 7 Antibody as a New Marker of Corneal Conjunctivalization in Patients with Limbal Stem Cell Deficiency. *Investigative Ophthalmology & Visual Science*, 52(8), p. 5892–5898, doi:10.1167/iovs.10-6748.

Jones, Roanne R., Hamley, Ian W. and Connon, Che J. (2012). Ex vivo expansion of limbal stem cells is affected by substrate properties. *Stem Cell Research*, 8(3), p. 403–409, doi:10.1016/j.scr.2012.01.001.

Joussen, Antonia M., Poulaki, Vassiliki, Mitsiades, Nicholas, Stechschulte, Stephen U., Kirchhof, Bernd, Dartt, Darlene A., Fong, Guo-Hua, Rudge, John, Wiegand, Stanley J., Yancopoulos, George D. and Adamis, Anthony P. (2003). VEGF-Dependent Conjunctivalization of the Corneal Surface. *Investigative Ophthalmology & Visual Science*, 44(1), p. 117–123, doi:10.1167/iovs.01-1277.

Kaga, Naoyuki, Fujimoto, Hiroki, Morita, Sho, Yamaguchi, Yuichiro and Matsuura, Takashi (2021). Contact Angle and Cell Adhesion of Micro/Nano-Structured Poly(lactic-co-glycolic acid) Membranes for Dental Regenerative Therapy. *Dentistry Journal*, 9(11), p. 124, doi:10.3390/dj9110124.

Kang, Yun Gyeong, Shin, Ji Won, Park, So Hee, Oh, Min Jae, Park, Hyo Soon, Shin, Jung Woog and Kim, Su Hyang (2014). Effects of flow-induced shear stress on limbal epithelial stem cell growth and enrichment. *PLoS ONE*, 9(3), doi:10.1371/journal.pone.0093023.

Karami, Samira, Balaghali, Sahar, Kanavi, Mozghan Rezaei, Alizadeh, Shaban, Dabbaghi, Rasul and Sayadi, Mahtab (2021). Promoting limbal stem cells proliferation and maintenance using post-thaw human amniotic membranes fortified by platelet lysate. *Gene Reports*, 23, p. 101084, doi:10.1016/j.genrep.2021.101084.

Karamichos, Dimitrios, Funderburgh, Martha L., Hutcheon, Audrey E. K., Zieske, James D., Du, Yiqin, Wu, Jian and Funderburgh, James L. (2014). A Role for Topographic Cues in the Organization of Collagenous Matrix by Corneal Fibroblasts and Stem Cells. *PLOS ONE*, 9(1), p. e86260, doi:10.1371/journal.pone.0086260.

Kasetti, Ramesh Babu, Gaddipati, Subhash, Tian, Shifu, Xue, Lei, Kao, Winston W. Y., Lu, Qingxian and Li, Qiutang (2016). Study of corneal epithelial progenitor origin and the Yap1 requirement using keratin 12 lineage tracing transgenic mice. *Scientific Reports*, 6(1), p. 35202, doi:10.1038/srep35202.

Katikireddy, Kishore Reddy, Dana, Reza and Jurkunas, Ula V. (2014). Differentiation potential of limbal fibroblasts and bone marrow mesenchymal stem cells to corneal epithelial cells. *Stem Cells (Dayton, Ohio)*, 32(3), p. 717–729, doi:10.1002/stem.1541.

Katikireddy, Kishore Reddy, Schmedt, Thore, Price, Marianne O., Price, Francis W. and Jurkunas, Ula V. (2016). Existence of Neural Crest–Derived Progenitor Cells in Normal and Fuchs Endothelial Dystrophy Corneal Endothelium. *The American Journal of Pathology*, 186(10), p. 2736–2750, doi:10.1016/j.ajpath.2016.06.011.

Kaupilla, Maija, Mörö, Anni, Valle-Delgado, Juan José, Ihalainen, Teemu, Sukki, Lassi, Puistola, Paula, Kallio, Pasi, Ilmarinen, Tanja, Österberg, Monika and Skottman, Heli (2023). Toward Corneal Limbus In vitro Model: Regulation of hPSC-LSC Phenotype by Matrix Stiffness and Topography During Cell Differentiation Process. *Advanced Healthcare Materials*, 12(29), p. 2301396, doi:10.1002/adhm.202301396.

Kawakita, Tetsuya, Espana, Edgar M., He, Hua, Li, Wei, Liu, Chia-Yiang and Tseng, Scheffer C. G. (2005). Intrastromal Invasion by Limbal Epithelial Cells Is Mediated by Epithelial-Mesenchymal Transition Activated by Air Exposure. *The American Journal of Pathology*, 167(2), p. 381–393, doi:10.1016/S0002-9440(10)62983-5.

Kawakita, Tetsuya, Espana, Edgar M., Higa, Kazunari, Kato, Naoko, Li, Wei and Tseng, Scheffer C. G. (2013). Activation of Smad-mediated TGF- β signalling triggers epithelial–mesenchymal transitions in murine cloned corneal progenitor cells. *Journal of Cellular Physiology*, 228(1), p. 225–234, doi:10.1002/jcp.24126.

Kawashima, Motoko, Kawakita, Tetsuya, Higa, Kazunari, Satake, Yoshiyuki, Omoto, Masahiro, Tsubota, Kazuo, Shimmura, Shigeto and Shimazaki, Jun (2010). Subepithelial corneal fibrosis partially due to epithelial-mesenchymal transition of ocular surface epithelium. *Molecular Vision*, 16, p. 2727–2732.

- Kennedy, Brendan F., Kennedy, Kelsey M. and Sampson, David D. (2014). A Review of Optical Coherence Elastography: Fundamentals, Techniques and Prospects. *IEEE Journal of Selected Topics in Quantum Electronics*, 20(2), p. 272–288, doi:10.1109/JSTQE.2013.2291445.
- Khoo, Lin Wei, Attzs, Michelle, Srinivasan, Sathish and Roberts, Fiona (2018). Limbal Stem Cell Deficiency Secondary to Diffuse Non-necrotizing Anterior Scleritis: A Clinicopathological Report. *Cornea*, 37(9), p. 1175–1177, doi:10.1097/ICO.0000000000001615.
- Kim, B., Peterson, E. T. K. and Papautsky, I. (2004). Long-term stability of plasma oxidized PDMS surfaces. In: *The 26th Annual International Conference of the IEEE Engineering in Medicine and Biology Society*. Presented at the The 26th Annual International Conference of the IEEE Engineering in Medicine and Biology Society, p. 5013–5016.
- Kim, Eung Kweon, Lee, Ga-Hyun, Lee, Boram and Maeng, Yong-Sun (2017). Establishment of Novel Limbus-Derived, Highly Proliferative ABCG2⁺/ABCB5⁺ Limbal Epithelial Stem Cell Cultures. *Stem Cells International*, 2017, p. e7678637, doi:10.1155/2017/7678637.
- Kim, Joong Hyun, Park, HyeungWoo and Seo, Soo Won (2017). *In situ* synthesis of silver nanoparticles on the surface of PDMS with high antibacterial activity and biosafety toward an implantable medical device. *Nano Convergence*, 4(1), p. 33, doi:10.1186/s40580-017-0126-x.
- Kim, Seon-Hwa, Jo, Sung-Han, Kim, Byeong Kook and Park, Sang-Hyug (2023). Tissue Engineered Mini-Cornea Model for Eye Irritation Test. *Tissue Engineering and Regenerative Medicine*, 20(2), p. 213–223, doi:10.1007/s13770-022-00504-x.
- Kobuszevska, Anna, Kolodziejek, Dominik, Wojasinski, Michal, Jastrzebska, Elzbieta, Ciach, Tomasz and Brzozka, Zbigniew (2021). Lab-on-a-chip system integrated with nanofiber mats used as a potential tool to study cardiovascular diseases (CVDs). *Sensors and Actuators B: Chemical*, 330, p. 129291, doi:10.1016/j.snb.2020.129291.
- Kolli, Sai, Ahmad, Sajjad, Lako, Majlinda and Figueiredo, Francisco (2010). Successful clinical implementation of corneal epithelial stem cell therapy for treatment of unilateral limbal stem cell deficiency. *Stem Cells (Dayton, Ohio)*, 28(3), p. 597–610, doi:10.1002/stem.276.
- Kołodziej, Anna, Długoń, Elżbieta, Świątek, Małgorzata, Ziabka, Magdalena, Dawiec, Emilia, Gubernat, Maciej, Michalec, Marek and Weselucha-Birczyńska, Aleksandra (2021). A Raman Spectroscopic Analysis of Polymer Membranes with Graphene Oxide and Reduced Graphene Oxide. *Journal of Composites Science*, 5(1), p. 20, doi:10.3390/jcs5010020.
- Kosta, Tomislav, Krawietz, Thomas R. and Mares, Jesus O. (2020). Sylgard 184 mixture and natural aging study via quasi-static compressive modulus. *AIP Conference Proceedings*, 2272(1), p. 040007, doi:10.1063/12.0001037.
- Kumar, Ajay, Yun, Hongmin, Funderburgh, Martha L. and Du, Yiqin (2022). Regenerative therapy for the Cornea. *Progress in Retinal and Eye Research*, 87, p. 101011, doi:10.1016/j.preteyeres.2021.101011.

Lagali, Neil, Edén, Ulla, Utheim, Tor Paaske, Chen, Xiangjun, Riise, Ruth, Dellby, Anette and Fagerholm, Per (2013). In vivo morphology of the limbal palisades of Vogt correlates with progressive stem cell deficiency in aniridia-related keratopathy. *Investigative Ophthalmology and Visual Science*, 54(8), p. 5333–5342, doi:10.1167/iovs.13-11780.

Lahoti, Sejal, Weiss, Menachem, Johnson, Daniel A. and Kheirkhah, Ahmad (2022). Superior limbic keratoconjunctivitis: a comprehensive review. *Survey of Ophthalmology*, 67(2), p. 331–341, doi:10.1016/j.survophthal.2021.05.009.

Lam, Ngoc Thien, Lam, Hanh, Sturdivant, Nasya M. and Balachandran, Kartik (2017). Fabrication of a matrigel-collagen semi-interpenetrating scaffold for use in dynamic valve interstitial cell culture. *Biomedical Materials (Bristol, England)*, 12(4), p. 045013, doi:10.1088/1748-605X/aa71be.

Lan, Gongpu, Aglyamov, Salavat, Larin, Kirill V. and Twa, Michael D. (2021). In vivo human corneal natural frequency quantification using dynamic optical coherence elastography: Repeatability and reproducibility. *Journal of Biomechanics*, 121, p. 110427, doi:10.1016/j.jbiomech.2021.110427.

Lanir, Yoram (2017). Multi-scale Structural Modeling of Soft Tissues Mechanics and Mechanobiology. *Journal of Elasticity*, 129(1–2), p. 7–48, doi:10.1007/s10659-016-9607-0.

Lathrop, Kira L., Gupta, Divya, Kagemann, Larry, Schuman, Joel S. and Sundarraj, Nirmala (2012). Optical coherence tomography as a Rapid, Accurate, noncontact method of visualizing the palisades of Vogt. *Investigative Ophthalmology and Visual Science*, 53(3), p. 1381–1387, doi:10.1167/iovs.11-8524.

Lawton, Renée A., Price, Colin R., Runge, Anne F., Doherty, Walter J. and Saavedra, S. Scott (2005). Air plasma treatment of submicron thick PDMS polymer films: effect of oxidation time and storage conditions. *Colloids and Surfaces A: Physicochemical and Engineering Aspects*, 253(1), p. 213–215, doi:10.1016/j.colsurfa.2004.11.010.

Last, Julie A., Liliensiek, Sara J., Nealey, Paul F. and Murphy, Christopher J. (2009). Determining the mechanical properties of human corneal basement membranes with atomic force microscopy. *Journal of Structural Biology*, 167(1), p. 19–24, doi:10.1016/j.jsb.2009.03.012.

Last, Julie A., Thomasy, Sara M., Croasdale, Christopher R., Russell, Paul and Murphy, Christopher J. (2012). Compliance profile of the human cornea as measured by atomic force microscopy. *Micron (Oxford, England: 1993)*, 43(12), p. 1293–1298, doi:10.1016/j.micron.2012.02.014.

Le, Qihua, Chauhan, Tulika, Yung, Madeline, Tseng, Chi-Hong and Deng, Sophie X. (2020a). Outcomes of Limbal Stem Cell Transplant: A Meta-analysis. *JAMA Ophthalmology*, 138(6), p. 660–670, doi:10.1001/jamaophthalmol.2020.1120.

Le, Qihua, Chauhan, Tulika, Yung, Madeline, Tseng, Chi-Hong and Deng, Sophie X. (2020b). Outcomes of Limbal Stem Cell Transplant: A Meta-analysis. *JAMA Ophthalmology*, 138(6), p. 660–670, doi:10.1001/jamaophthalmol.2020.1120.

Le, Qihua, Yang, Yujing, Deng, Sophie X. and Xu, Jianjiang (2017). Correlation between the existence of the palisades of Vogt and limbal epithelial thickness in limbal

- stem cell deficiency. *Clinical & Experimental Ophthalmology*, 45(3), p. 224–231, doi:10.1111/ceo.12832.
- Leal, Salomé, Cristelo, Cecília, Silvestre, Sara, Fortunato, Elvira, Sousa, Aureliana, Alves, Anabela, Correia, D. M., Lanceros-Mendez, S. and Gama, Miguel (2020). Hydrophobic modification of bacterial cellulose using oxygen plasma treatment and chemical vapor deposition. *Cellulose*, 27(18), p. 10733–10746, doi:10.1007/s10570-020-03005-z.
- Lee, Eun Jung, Seo, Chan Eol and Lee, Myung Chul (2023). Extended Suprabrow Lift with Relief of Glabellar Wrinkles. *Aesthetic Plastic Surgery*, 47(1), p. 156–165, doi:10.1007/s00266-022-03007-1.
- Lee, Seung Tae, Gong, Seung Pyo, Yum, Kyung Eun, Lee, Eun Ju, Lee, Chae Hyun, Choi, Jun Hee, Kim, Dae Yong, Han, Hojae, Kim, Kye-Seong, Hysolli, Eriona, Ahn, Ji Yeon, Park, In-Hyun, Han, Jae Yong, Jeong, Jae-Wook and Lim, Jeong Mook (2013). Transformation of somatic cells into stem cell-like cells under a stromal niche. *The FASEB Journal*, 27(7), p. 2644–2656, doi:10.1096/fj.12-223065.
- Lekhanont, Kaevalin, Choubtum, Lulin, Chuck, Roy S., Sa-ngiampornpanit, Tarinee, Chuc KPaiwong, Varintorn and Vongthongsri, Anun (2009). A serum-and feeder-free technique of culturing human corneal epithelial stem cells on amniotic membrane. *Molecular Vision*, 15, p. 1294–1302.
- Levis, Hannah J. and Daniels, Julie T. (2016). Recreating the Human Limbal Epithelial Stem Cell Niche with Bioengineered Limbal Crypts. *Current Eye Research*, 41(9), p. 1153–1160, doi:10.3109/02713683.2015.1095932.
- Levis, Hannah J., Kureshi, Alvena K., Massie, Isobel, Morgan, Louise, Vernon, Amanda J. and Daniels, Julie T. (2015). Tissue Engineering the Cornea: The Evolution of RAFT. *Journal of Functional Biomaterials*, 6(1), p. 50–65, doi:10.3390/jfb6010050.
- Levis, Hannah J., Massie, Isobel, Dziasko, Marc A., Kaasi, Andreas and Daniels, Julie T. (2013). Rapid tissue engineering of biomimetic human corneal limbal crypts with 3D niche architecture. *Biomaterials*, 34(35), p. 8860–8868, doi:10.1016/j.biomaterials.2013.08.002.
- Li, Bo, Cao, Yan-Ping, Feng, Xi-Qiao and Gao, Huajian (2012). Mechanics of morphological instabilities and surface wrinkling in soft materials: a review. *Soft Matter*, 8(21), p. 5728–5745, doi:10.1039/C2SM00011C.
- Li, C., Li, S., Wei, C., Wang, R. K. and Huang, Z. (2015). Depth Evaluation of Soft Tissue Mimicking Phantoms Using Surface Acoustic Waves. *Physics Procedia*, 63, p. 177–181, doi:10.1016/j.phpro.2015.03.029.
- Li, Jie, Barlow, Leah N. and Sask, Kyla N. (2023). Enhancement of protein immobilization on polydimethylsiloxane using a synergistic combination of polydopamine and micropattern surface modification. *Journal of Biomaterials Science, Polymer Edition*, 34(17), p. 2376–2399, doi:10.1080/09205063.2023.2248799.
- Li, Peng, An, Lin, Reif, Roberto, Shen, Tueng T., Johnstone, Murray and Wang, Ruikang K. (2011). In vivo microstructural and microvascular imaging of the human corneo-scleral limbus using optical coherence tomography. *Biomedical Optics Express*, 2(11), p. 3109, doi:10.1364/boe.2.003109.

- Li, Chunhui, Guan, Guangying, Reif, Roberto, Huang, Zhihong and Wang, Ruikang K. (2012). Determining elastic properties of skin by measuring surface waves from an impulse mechanical stimulus using phase-sensitive optical coherence tomography. *Journal of the Royal Society Interface*, 9(70), p. 831–841, doi:10.1098/rsif.2011.0583.
- Li, Mingsen, Huang, Huaxing, Wang, Bofeng, Jiang, Shaoshuai, Guo, Huizhen, Zhu, Liqiong, Wu, Siqi, Liu, Jiafeng, Wang, Li, Lan, Xihong, Zhang, Wang, Zhu, Jin, Li, Fuxi, Tan, Jieying, Mao, Zhen, Liu, Chunqiao, Ji, Jianping, Ding, Junjun, Zhang, Kang, Yuan, Jin, Liu, Yizhi and Ouyang, Hong (2022). Comprehensive 3D epigenomic maps define limbal stem/progenitor cell function and identity. *Nature Communications*, 13(1), p. 1293, doi:10.1038/s41467-022-28966-6.
- Li, Shengwei, Yu, Haozhe, Wang, Pu and Feng, Yun (2022). Evaluation of the Effects of Pterygium and Aging on Limbal Structure Using Optical Coherence Tomography. *Journal of Clinical Medicine*, 11(19), p. 5879, doi:10.3390/jcm11195879.
- Li, Xia, Dai, Yiqin, Xu, Weiwei and Xu, Jianjiang (2018). Essential role of ultraviolet radiation in the decrease of corneal endothelial cell density caused by pterygium. *Eye*, 32(12), p. 1886–1892, doi:10.1038/s41433-018-0188-y.
- Liu, Ting, Wang, Yao, Duan, Hao-Yun, Qu, Ming-Li, Yang, Ling-Ling, Xu, Yuan-Yuan, Zang, Xin-Jie and Zhou, Qing-Jun (2012). Effects of preservation time on proliferative potential of human limbal stem/progenitor cells. *International Journal of Ophthalmology*, 5(5), p. 549, doi:10.3980/j.issn.2222-3959.2012.05.02.
- Li, Yijian, Yang, Yuli, Yang, Lei, Zeng, Yuxiao, Gao, Xiaowei and Xu, Haiwei (2017). Poly(ethylene glycol)-modified silk fibroin membrane as a carrier for limbal epithelial stem cell transplantation in a rabbit LSCD model. *Stem Cell Research & Therapy*, 8(1), p. 256, doi:10.1186/s13287-017-0707-y.
- Lim, Pauline, Fuchsluger, Thomas A. and Jurkunas, Ula V. (2009). Limbal Stem Cell Deficiency and Corneal Neovascularization. *Seminars in Ophthalmology*, 24(3), p. 139–148, doi:10.1080/08820530902801478.
- Liskova, Petra, Dudakova, Lubica, Evans, Cerys J., Rojas Lopez, Karla E., Pontikos, Nikolas, Athanasiou, Dimitra, Jama, Hodan, Sach, Josef, Skalicka, Pavlina, Stranecky, Viktor, Kmoch, Stanislav, Thaug, Caroline, Filipec, Martin, Cheetham, Michael E., Davidson, Alice E., Tuft, Stephen J. and Hardcastle, Alison J. (2018). Ectopic GRHL2 Expression Due to Non-coding Mutations Promotes Cell State Transition and Causes Posterior Polymorphous Corneal Dystrophy 4. *American Journal of Human Genetics*, 102(3), p. 447–459, doi:10.1016/j.ajhg.2018.02.002.
- Lo, Bernard and Parham, Lindsay (2009). Ethical issues in stem cell research. *Endocrine Reviews*, 30(3), p. 204–213, doi:10.1210/er.2008-0031.
- Longobardo, Luca, Mattesini, Alessio, Valente, Serafina and Di Mario, Carlo (2019). OCT-guided Percutaneous Coronary Intervention in Bifurcation Lesions. *Interventional Cardiology Review*, 14(1), p. 5–9, doi:10.15420/icr.2018.17.2.
- Lu, Jiajun, Sheng, Minjie, Yao, Panpan, Ran, Chaochao, Liu, Hao, Chen, Li, Liu, Rui and Li, Bing (2018). High Concentration of Glucose Increases Reactive Oxygen Species Generation and Apoptosis Induced by Endoplasmic Reticulum Stress Pathway in Rabbit Corneal Epithelial Cells. *Journal of Ophthalmology*, 2018, p. 8234906, doi:10.1155/2018/8234906.

Luk, Jing Zhong, Cooper-White, Justin, Rintoul, Llew, Taran, Elena and Grøndahl, Lisbeth (2013). Functionalised polycaprolactone films and 3D scaffolds via gamma irradiation-induced grafting. *Journal of Materials Chemistry B*, 1(33), p. 4171–4181, doi:10.1039/C3TB20267D.

Ma, David Hui-Kang, Lai, Jui-Yang, Cheng, Hsiao-Yun, Tsai, Chen-Chi and Yeh, Lung-Kun (2010). Carbodiimide cross-linked amniotic membranes for cultivation of limbal epithelial cells. *Biomaterials*, 31(25), p. 6647–6658, doi:10.1016/j.biomaterials.2010.05.034.

Ma, Guoqin, Cai, Jing, Zhong, Rijian, He, Weichao, Ye, Haoxi, Duvvuri, Chaitanya, Song, Chengjin, Feng, Jinping, An, Lin, Qin, Jia, Huang, Yanping, Xu, Jingjiang, Twa, Michael D. and Lan, Gongpu (2023). Corneal Surface Wave Propagation Associated with Intraocular Pressures: OCT Elastography Assessment in a Simplified Eye Model. *Bioengineering*, 10(7), p. 754, doi:10.3390/bioengineering10070754.

Mahadik, Bhushan P., Pedron Haba, Sara, Skertich, Luke J. and Harley, Brendan A. C. (2015). The use of covalently immobilized stem cell factor to selectively affect hematopoietic stem cell activity within a gelatin hydrogel. *Biomaterials*, 67, p. 297–307, doi:10.1016/j.biomaterials.2015.07.042.

Mahoney, John E., Mori, Munemasa, Szymaniak, Aleksander D., Varelas, Xaralabos and Cardoso, Wellington V. (2014). The Hippo Pathway Effector Yap Controls Patterning and Differentiation of Airway Epithelial Progenitors. *Developmental Cell*, 30(2), p. 137–150, doi:10.1016/j.devcel.2014.06.003.

Maithani, Yogita, Mehta, Bodh Raj and Singh, Jitendra Pratap (2021). Investigating the effect of silver nanorods embedded in polydimethylsiloxane matrix using nanoindentation and its use for flexible electronics. *Journal of Applied Polymer Science*, 138(14), p. 50141, doi:10.1002/app.50141.

Mariappan, Yogesh K., Rossman, Phillip J., Glaser, Kevin J., Manduca, Armando and Ehman, Richard L. (2009). Magnetic resonance elastography with a phased-array acoustic driver system. *Magnetic Resonance in Medicine*, 61(3), p. 678–685, doi:10.1002/mrm.21885.

Massie, Isobel, Dziasko, Marc, Kureshi, Alvena, Levis, Hannah J., Morgan, Louise, Neale, Michael, Sheth, Radhika, Tovell, Victoria E., Vernon, Amanda J., Funderburgh, James L. and Daniels, Julie T. (2015). Advanced Imaging and Tissue Engineering of the Human Limbal Epithelial Stem Cell Niche. In: Rich, Ivan N. (ed.) *Stem Cell Protocols*. New York, NY: Springer, p. 179–202.

Mastropasqua, Rodolfo, Agnifili, Luca, Fasanella, Vincenzo, Curcio, Claudia, Brescia, Lorenza, Lanzini, Manuela, Fresina, Michela, Mastropasqua, Leonardo and Marchini, Giorgio (2015). Corneoscleral Limbus in Glaucoma Patients: In vivo Confocal Microscopy and Immunocytological Study. *Investigative Ophthalmology & Visual Science*, 56(3), p. 2050–2058, doi:10.1167/iovs.14-15890.

Mazhari, Ramesh and Hare, Joshua M. (2007). Mechanisms of action of mesenchymal stem cells in cardiac repair: potential influences on the cardiac stem cell niche. *Nature Clinical Practice. Cardiovascular Medicine*, 4 Suppl 1, p. S21-26, doi:10.1038/ncpcardio0770.

Mazza, Giuseppe, Rombouts, Krista, Rennie Hall, Andrew, Urbani, Luca, Vinh Luong, Tu, Al-Akkad, Walid, Longato, Lisa, Brown, David, Maghsoudlou, Panagiotis, Dhillon, Amar P., Fuller, Barry, Davidson, Brian, Moore, Kevin, Dhar, Dipok, De Coppi, Paolo, Malago, Massimo and Pinzani, Massimo (2015). Decellularized human liver as a natural 3D-scaffold for liver bioengineering and transplantation. *Scientific Reports*, 5, p. 13079, doi:10.1038/srep13079.

McLaren, A. (2001). Ethical and social considerations of stem cell research. *Nature*, 414(6859), p. 129–131, doi:10.1038/35102194.

Mehtani, Amit, Agarwal, Mahesh Chandra, Sharma, Sushant and Chaudhary, Santosh (2017). Diagnosis of limbal stem cell deficiency based on corneal epithelial thickness measured on anterior segment optical coherence tomography. *Indian Journal of Ophthalmology*, 65(11), p. 1120–1126, doi:10.4103/ijo.IJO_218_17.

Meller, D., Pires, R. T. F. and Tseng, S. C. G. (2002). Ex vivo preservation and expansion of human limbal epithelial stem cells on amniotic membrane cultures. *The British Journal of Ophthalmology*, 86(4), p. 463–471, doi:10.1136/bjo.86.4.463.

Menon, Nishanth V., Chuah, Yon Jin, Phey, Samantha, Zhang, Ying, Wu, Yingnan, Chan, Vincent and Kang, Yuejun (2015). Microfluidic Assay To Study the Combinatorial Impact of Substrate Properties on Mesenchymal Stem Cell Migration. *ACS Applied Materials & Interfaces*, 7(31), p. 17095–17103, doi:10.1021/acsami.5b03753.

Mi, Shengli, Chen, Bo, Wright, Bernice and Connon, Che J. (2010). Ex vivo Construction of an Artificial Ocular Surface by Combination of Corneal Limbal Epithelial Cells and a Compressed Collagen Scaffold Containing Keratocytes. *Tissue Engineering Part A*, 16(6), p. 2091–2100, doi:10.1089/ten.tea.2009.0748.

Miri, Ammar, Al-Aqaba, Muhamed, Otri, Ahmad Muneer, Fares, Usama, Said, Dalia G., Faraj, Lana Akram and Dua, Harminder S. (2012). In vivo confocal microscopic features of normal limbus. *British Journal of Ophthalmology*, 96(4), p. 530–536, doi:10.1136/bjophthalmol-2011-300550.

Miri, Ammar, Al-Deiri, Bushra and Dua, Harminder S. (2010). Long-term Outcomes of Autolimbic and Allolimbic Transplants. *Ophthalmology*, 117(6), p. 1207–1213, doi:10.1016/j.ophtha.2009.10.028.

Morrison, Sean J. and Spradling, Allan C. (2008). Stem cells and niches: mechanisms that promote stem cell maintenance throughout life. *Cell*, 132(4), p. 598–611, doi:10.1016/j.cell.2008.01.038.

Mort, Richard L., Ramaesh, Thaya, Kleinjan, Dirk A., Morley, Steven D. and West, John D. (2009). Mosaic analysis of stem cell function and wound healing in the mouse corneal epithelium. *BMC Developmental Biology*, 9(1), p. 4, doi:10.1186/1471-213X-9-4.

Moshirfar, Majid, Masud, Maliha, Harvey, Devon Hori, Payne, Carter, Bruce, Elayna, Ronquillo, Yasmyne C. and Hoopes, Philip C. (2023). The Multifold Etiologies of Limbal Stem Cell Deficiency: A Comprehensive Review on the Etiologies and Additional Treatment Options for Limbal Stem Cell Deficiency. *Journal of Clinical Medicine*, 12(13), p. 4418, doi:10.3390/jcm12134418.

- Moshirfar, Majid, Thomson, Andrew C. and Ronquillo, Yasmyne (2024). Limbal Epithelial Transplant. In: *StatPearls*. Treasure Island (FL): StatPearls Publishing.
- Mu, Minchen, Liu, Shuhao, DeFlorio, William, Hao, Li, Wang, Xunhao, Salazar, Karla Solis, Taylor, Matthew, Castillo, Alejandro, Cisneros-Zevallos, Luis, Oh, Jun Kyun, Min, Younjin and Akbulut, Mustafa (2023). Influence of Surface Roughness, Nanostructure, and Wetting on Bacterial Adhesion. *Langmuir*, 39(15), p. 5426–5439, doi:10.1021/acs.langmuir.3c00091.
- Murru, Pavitra and Rajagopal, K. r. (2021). Stress concentration due to the bi-axial deformation of a plate of a porous elastic body with a hole. *ZAMM - Journal of Applied Mathematics and Mechanics / Zeitschrift für Angewandte Mathematik und Mechanik*, 101(11), p. e202100103, doi:10.1002/zamm.202100103.
- Mwale, Fackson, Wang, Hong Tian, Nelea, Valentin, Luo, Li, Antoniou, John and Wertheimer, Michael R. (2006). The effect of glow discharge plasma surface modification of polymers on the osteogenic differentiation of committed human mesenchymal stem cells. *Biomaterials*, 27(10), p. 2258–2264, doi:10.1016/j.biomaterials.2005.11.006.
- Nair, Achuth, Singh, Manmohan, Aglyamov, Salavat R. and Larin, Kirill V. (2020). Heartbeat OCE: corneal biomechanical response to simulated heartbeat pulsation measured by optical coherence elastography. *Journal of Biomedical Optics*, 25(5), p. 055001, doi:10.1117/1.JBO.25.5.055001.
- Nautscher, Nadine, Bauer, Achim, Steffl, Martin and Amselgruber, Werner M. (2016). Comparative morphological evaluation of domestic animal cornea. *Veterinary Ophthalmology*, 19(4), p. 297–304, doi:10.1111/vop.12298.
- NHS. (2020). *Eye cancer*. nhs.uk. <https://www.nhs.uk/conditions/eye-cancer/>
- NHS. (2020). *Cornea transplant*. nhs.uk. <https://www.nhs.uk/conditions/cornea-transplant/>
- NICE. (2023). *Glaucoma: diagnosis and management*. NICE. <https://www.nice.org.uk/researchrecommendation/optical-coherence-tomography-for-glaucoma-what-is-the-effectiveness-and-cost-effectiveness-of-optical-coherence-tomography-oct-for-diagnosing-and-monitoring-glaucoma> [Accessed: 2023w-10-25].
- NICE. (2020). *Overview | Insertion of hydrogel keratoprosthesis | Guidance | NICE*. <https://www.nice.org.uk/guidance/ipg69>
- NICE. (2020). *Overview | Tissue-cultured limbal stem cell allograft transplantation for regrowth of corneal epithelium | Guidance | NICE*. <https://www.nice.org.uk/guidance/ipg216>
- NICE. (2020). *Overview | Corneal endothelial transplantation | Guidance | NICE*. <https://www.nice.org.uk/guidance/ipg304>
- NICE. (2020). *Overview | Photochemical corneal collagen cross-linkage using riboflavin and ultraviolet A for keratoconus and keratectasia | Guidance | NICE*. <https://www.nice.org.uk/guidance/ipg466>
- NICE. (2023). *Overview | Optical coherence tomography to guide percutaneous coronary intervention | Guidance | NICE*. <https://www.nice.org.uk/guidance/ipg481>

NICE. (2020). *Overview | Autologous chondrocyte implantation for treating symptomatic articular cartilage defects of the knee | Guidance | NICE*. <https://www.nice.org.uk/guidance/ta477>

Notara, M., Behboudifard, S., Kluth, M. A., Maßlo, C., Ganss, C., Frank, M. H., Schumacher, B. and Cursiefen, C. (2018). UV light-blocking contact lenses protect against short-term UVB-induced limbal stem cell niche damage and inflammation. *Scientific Reports*, 8(1), p. 12564, doi:10.1038/s41598-018-30021-8.

Notara, M., Shortt, A. J., O'Callaghan, A. R. and Daniels, J. T. (2013a). The impact of age on the physical and cellular properties of the human limbal stem cell niche. *AGE*, 35(2), p. 289–300, doi:10.1007/s11357-011-9359-5.

Notara, M., Shortt, A. J., O'Callaghan, A. R. and Daniels, J. T. (2013b). The impact of age on the physical and cellular properties of the human limbal stem cell niche. *AGE*, 35(2), p. 289–300, doi:10.1007/s11357-011-9359-5.

Notara, Maria, Lentzsch, Anna, Clahsen, Thomas, Behboudifard, Sara, Braun, Gabriele and Cursiefen, Claus (2019). Bevacizumab Induces Upregulation of Keratin 3 and VEGFA in Human Limbal Epithelial Cells in vitro. *Journal of Clinical Medicine*, 8(11), p. 1925, doi:10.3390/jcm8111925.

Notara, Maria, Schrader, Stefan and Daniels, Julie T. (2011). The Porcine Limbal Epithelial Stem Cell Niche as a New Model for the Study of Transplanted Tissue-Engineered Human Limbal Epithelial Cells. *Tissue Engineering Part A*, 17(5–6), p. 741–750, doi:10.1089/ten.tea.2010.0343.

Oladapo, Bankole I., Zahedi, S. Abolfazl, Ismail, Sikiru O., Omigbodun, Francis T., Bowoto, Oluwole K., Olawumi, Matthew A. and Muhammad, Musa A. (2021). 3D printing of PEEK–cHAp scaffold for medical bone implant. *Bio-Design and Manufacturing*, 4(1), p. 44–59, doi:10.1007/s42242-020-00098-0.

Orellana Barrasa, Jaime, Ferrández-Montero, Ana, Ferrari, Begoña and Pastor, José Ygnacio (2021). Characterisation and Modelling of PLA Filaments and Evolution with Time. *Polymers*, 13(17), p. 2899, doi:10.3390/polym13172899.

Ortega, Ilida, McKean, Robert, J. Ryan, Anthony, MacNeil, Sheila and Claeysens, Frederik (2014). Characterisation and evaluation of the impact of microfabricated pockets on the performance of limbal epithelial stem cells in biodegradable PLGA membranes for corneal regeneration. *Biomaterials Science*, 2(5), p. 723–734, doi:10.1039/C3BM60268K.

Ostrem, Bridget E. L., Lui, Jan H., Gertz, Caitlyn C. and Kriegstein, Arnold R. (2014). Control of outer radial glial stem cell mitosis in the human brain. *Cell Reports*, 8(3), p. 656–664, doi:10.1016/j.celrep.2014.06.058.

de Paiva, Cintia S., Chen, Zhuo, Corrales, Rosa M., Pflugfelder, Stephen C. and Li, De-Quan (2005). ABCG2 Transporter Identifies a Population of Clonogenic Human Limbal Epithelial Cells. *Stem Cells*, 23(1), p. 63–73, doi:10.1634/stemcells.2004-0093.

Pandey, Vivek Kumar, Srivastava, Kumar Rohit, Ajmal, Gufran, Thakur, Vijay Kumar, Gupta, Vijai Kumar, Upadhyay, Siddh Nath and Mishra, Pradeep Kumar (2019). Differential Susceptibility of Catheter Biomaterials to Biofilm-Associated Infections and Their Remedy by Drug-Encapsulated Eudragit RL100 Nanoparticles. *International Journal of Molecular Sciences*, 20(20), p. 5110, doi:10.3390/ijms20205110.

Park, Jong Woo, Ko, Jung Hwa, Kim, Bo Hee, Ryu, Jin Suk, Kim, Hyun Ji, Kim, Mee Kum and Oh, Joo Youn (2019). Inhibition of mTOR by Rapamycin Aggravates Corneal Epithelial Stem Cell Deficiency by Upregulating Inflammatory Response. *Stem Cells (Dayton, Ohio)*, 37(9), p. 1212–1222, doi:10.1002/stem.3036.

Park, Ki-Sook, Lim, Chae Ho, Min, Byung-Moo, Lee, Jae Lim, Chung, Hee-Yong, Joo, Choun-Ki, Park, Chan-Woong and Son, Youngsook (2006). The Side Population Cells in the Rabbit Limbus Sensitively Increased in Response to the Central Cornea Wounding. *Investigative Ophthalmology & Visual Science*, 47(3), p. 892–900, doi:10.1167/iovs.05-1006.

Park, Mijeong, Richardson, Alex, Delic, Naomi, Nguyen, Kim, Biazik, Joanna, Zhang, Richard, Sprogyte, Lina, Nureen, Lamia, Lees, Justin, Fajardo, Angelica, Kunicki, Ursula, Watson, Stephanie L., Males, John and Girolamo, Nick Di (2023). A Bioengineering-Regenerative Medicine Approach for Ocular Surface Reconstruction Using a Functionalized Native Cornea-Derived Bio-Scaffold. *Advanced Functional Materials*, 33(46), p. 2304856, doi:10.1002/adfm.202304856.

Patel, Dipika V., Sherwin, Trevor and McGhee, Charles N. J. (2006). Laser Scanning In vivo Confocal Microscopy of the Normal Human Corneoscleral Limbus. *Investigative Ophthalmology & Visual Science*, 47(7), p. 2823–2827, doi:10.1167/iovs.05-1492.

Pathak, Meeta, Olstad, O. K., Drolsum, Liv, Moe, Morten C., Smorodinova, Natalia, Kalasova, Sarka, Jirsova, Katerina, Nicolaissen, Bjørn and Noer, Agate (2016a). The effect of culture medium and carrier on explant culture of human limbal epithelium: A comparison of ultrastructure, keratin profile and gene expression. *Experimental Eye Research*, 153, p. 122–132, doi:10.1016/j.exer.2016.09.012.

Pathak, Meeta, Olstad, O. K., Drolsum, Liv, Moe, Morten C., Smorodinova, Natalia, Kalasova, Sarka, Jirsova, Katerina, Nicolaissen, Bjørn and Noer, Agate (2016b). The effect of culture medium and carrier on explant culture of human limbal epithelium: A comparison of ultrastructure, keratin profile and gene expression. *Experimental Eye Research*, 153, p. 122–132, doi:10.1016/j.exer.2016.09.012.

Pauklin, Mikk, Fuchsluger, Thomas A., Westekemper, Henrike, Steuhl, Klaus-P. and Meller, Daniel (2010). Midterm Results of Cultivated Autologous and Allogeneic Limbal Epithelial Transplantation in Limbal Stem Cell Deficiency, doi:10.1159/000315020.

Phillips, Estelle (1992). The PhD: assessing quality at different stages of its development. In: Zuber-Skerritt, Ortrun (ed.) *Starting Research*. Brisbane, Queensland: Tertiary Education Institute, University of Queensland, p. 132–151.

Pires, Filipa, Ferreira, Quirina, Rodrigues, Carlos A. V., Morgado, Jorge and Ferreira, Frederico Castelo (2015). Neural stem cell differentiation by electrical stimulation using a cross-linked PEDOT substrate: Expanding the use of biocompatible conjugated conductive polymers for neural tissue engineering. *Biochimica et Biophysica Acta (BBA) -General Subjects*, 1850(6), p. 1158–1168, doi:10.1016/j.bbagen.2015.01.020.

Piscioneri, Antonella, Ahmed, Haysam Mohamed Magdy, Morelli, Sabrina, Khakpour, Shervin, Giorno, Lidetta, Drioli, Enrico and De Bartolo, Loredana (2018). Membrane bioreactor to guide hepatic differentiation of human mesenchymal stem cells. *Journal of Membrane Science*, 564, p. 832–841, doi:10.1016/j.memsci.2018.07.083.

Piscioneri, Antonella, Morelli, Sabrina, Ritacco, Tiziana, Giocondo, Michele, Peñaloza, Rafael, Drioli, Enrico and De Bartolo, Loredana (2023). Topographical cues of PLGA

- membranes modulate the behavior of hMSCs, myoblasts and neuronal cells. *Colloids and Surfaces B: Biointerfaces*, 222, p. 113070, doi:10.1016/j.colsurfb.2022.113070.
- Polisetti, Naresh, Schlunck, Günther, Reinhard, Thomas, Kruse, Friedrich and Schlötzer-Schrehardt, Ursula (2020). Isolation and ex vivo Expansion of Human Limbal Epithelial Progenitor Cells. *BIO-PROTOCOL*, 10(18), doi:10.21769/BioProtoc.3754.
- Polisetti, Naresh, Sorokin, Lydia, Okumura, Naoki, Koizumi, Noriko, Kinoshita, Shigeru, Kruse, Friedrich E. and Schlötzer-Schrehardt, Ursula (2017). Laminin-511 and -521-based matrices for efficient ex vivo-expansion of human limbal epithelial progenitor cells. *Scientific Reports*, 7(1), p. 1–15, doi:10.1038/s41598-017-04916-x.
- Polisetti, Naresh, Zenkel, Matthias, Menzel-Severing, Johannes, Kruse, Friedrich E. and Schlötzer-Schrehardt, Ursula (2016). Cell Adhesion Molecules and Stem Cell-Niche-Interactions in the Limbal Stem Cell Niche. *STEM CELLS*, 34(1), p. 203–219, doi:10.1002/stem.2191.
- Popescu, Diana, Baciu, Florin, Amza, Catalin Gheorghe, Cotrut, Cosmin Mihai and Marinescu, Rodica (2021). The Effect of Disinfectants Absorption and Medical Decontamination on the Mechanical Performance of 3D-Printed ABS Parts. *Polymers*, 13(23), p. 4249, doi:10.3390/polym13234249.
- Prabowo, Firdaus, Wing-Keung, Adrian Law and Shen, Hayley H. (2015). Effect of Curing Temperature and Cross-Linker to Pre-Polymer Ratio on the Viscoelastic Properties of a PDMS Elastomer. *Advanced Materials Research*, 1112, p. 410–413, doi:10.4028/www.scientific.net/AMR.1112.410.
- Qiao, Yunsheng, Tan, Chen, Zhang, Min, Sun, Xinghuai and Chen, Junyi (2019). Comparison of spectral domain and swept source optical coherence tomography for angle assessment of Chinese elderly subjects. *BMC Ophthalmology*, 19(1), p. 142, doi:10.1186/s12886-019-1145-7.
- Rahmany, Maria B. and Van Dyke, Mark (2013). Biomimetic approaches to modulate cellular adhesion in biomaterials: A review. *Acta Biomaterialia*, 9(3), p. 5431–5437, doi:10.1016/j.actbio.2012.11.019.
- Rama, Paolo, Matuska, Stanislav, Paganoni, Giorgio, Spinelli, Alessandra, Luca, Michele De and Pellegrini, Graziella (2010). Limbal Stem-Cell Therapy and Long-Term Corneal Regeneration. *New England Journal of Medicine*, 363(2), p. 147–155, doi:10.1056/NEJMoa0905955.
- Ramier, Antoine, Eltony, Amira M., Chen, YiTong, Clouser, Fatima, Birkenfeld, Judith S., Watts, Amy and Yun, Seok-Hyun (2020). In vivo measurement of shear modulus of the human cornea using optical coherence elastography. *Scientific Reports*, 10(1), p. 17366, doi:10.1038/s41598-020-74383-4.
- Rana, Deepti, Ramasamy, Keerthana, Leena, Maria, Pasricha, Renu, Manivasagam, Geetha and Ramalingam, Murugan (2017). Surface Functionalization of Biomaterials. In: *Biology and Engineering of Stem Cell Niches*. Elsevier Inc., p. 331–343.
- Reda, Ahmed Mohamed, Shaaban, Yasmine Maher Mohamed and Saad El-Din, Somaia Ahmad (2018). Histopathological Parameters in Pterygia and Significant Clinical Correlations. *Journal of Ophthalmic & Vision Research*, 13(2), p. 110–118, doi:10.4103/jovr.jovr_31_17.

- Reya, Tannishtha and Clevers, Hans (2005). Wnt signalling in stem cells and cancer. *Nature*, 434(7035), p. 843–850, doi:10.1038/nature03319.
- Riccio, Rachel E., Park, Seo J., Longnecker, Richard and Kopp, Sarah J. (2019). Characterization of Sex Differences in Ocular Herpes Simplex Virus 1 Infection and Herpes Stromal Keratitis Pathogenesis of Wild-Type and Herpesvirus Entry Mediator Knockout Mice. *mSphere*, 4(2), p. e00073-19, doi:10.1128/mSphere.00073-19.
- Riestra, A. C., Vazquez, N., Chacon, M., Berisa, S., Sanchez-Avila, R. M., Orive, G., Anitua, E., Meana, A. and Merayo-Lloves, J. (2017). Autologous method for ex vivo expansion of human limbal epithelial progenitor cells based on plasma rich in growth factors technology. *The Ocular Surface*, 15(2), p. 248–256, doi:10.1016/j.jtos.2017.01.003.
- Rizvi, Adnan Z. and Wong, Melissa H. (2005). Epithelial stem cells and their niche: there's no place like home. *Stem Cells (Dayton, Ohio)*, 23(2), p. 150–165, doi:10.1634/stemcells.2004-0096.
- Rocha, Karolinne Maia, Perez, -Straziota E., Stulting, R. Doyle and Randleman, J. Bradley (2013). SD-OCT Analysis of Regional Epithelial Thickness Profiles in Keratoconus, Postoperative Corneal Ectasia, and Normal Eyes. *Journal of Refractive Surgery*, 29(3), p. 173–179, doi:10.3928/1081597X-20130129-08.
- Robertson, Sarah Y. T., Roberts, JoAnn S. and Deng, Sophie X. (2021). Regulation of Limbal Epithelial Stem Cells: Importance of the Niche. *International Journal of Molecular Sciences*, 22(21), p. 11975, doi:10.3390/ijms222111975.
- Rödling, Lisa, Schwedhelm, Ivo, Kraus, Saskia, Bieback, Karen, Hansmann, Jan and Lee-Thedieck, Cornelia (2017). 3D models of the hematopoietic stem cell niche under steady-state and active conditions. *Scientific Reports*, 7(1), p. 4625, doi:10.1038/s41598-017-04808-0.
- Rosli, Amirah Azwani, Shuib, Raa Khimi, Ishak, Ku Marsilla Ku, Hamid, Zuratul Ain Abdul, Abdullah, Muhammad Khalil and Rusli, Arjulizan (2020). Influence of bed temperature on warpage, shrinkage and density of various acrylonitrile butadiene styrene (ABS) parts from fused deposition modelling (FDM). *AIP Conference Proceedings*, 2267(1), p. 020072, doi:10.1063/5.0015799.
- Rossant, Janet and Tam, Patrick P. L. (2017). New Insights into Early Human Development: Lessons for Stem Cell Derivation and Differentiation. *Cell Stem Cell*, 20(1), p. 18–28, doi:10.1016/j.stem.2016.12.004.
- Rui, Domingues, Silvia, Chiera, Pavel, Gershovich, Antonella, Motta, Rui, Reis and Manuela, Gomes (2016). Fabrication of anisotropically aligned nanofibrous scaffolds based on natural/synthetic polymer blends reinforced with cellulose nanocrystals for tendon tissue engineering. *Frontiers in Bioengineering and Biotechnology*, 4, doi:10.3389/conf.FBIOE.2016.01.01963.
- Sagga, Nada, Kuffová, Lucia, Vargesson, Neil, Erskine, Lynda and Collinson, J. Martin (2018). Limbal epithelial stem cell activity and corneal epithelial cell cycle parameters in adult and aging mice. *Stem Cell Research*, 33, p. 185–198, doi:10.1016/j.scr.2018.11.001.
- Saika, Shizuya, Muragaki, Yasuteru, Okada, Yuka, Miyamoto, Takeshi, Ohnishi, Yoshitaka, Ooshima, Akira and Kao, Winston W. Y. (2004). Sonic Hedgehog

- Expression and Role in Healing Corneal Epithelium. *Investigative Ophthalmology & Visual Science*, 45(8), p. 2577–2585, doi:10.1167/iov.04-0001.
- Sales, Flaminio C. P., Ariati, Ronaldo M., Noronha, Verônica T. and Ribeiro, João E. (2022). Mechanical Characterization of PDMS with Different Mixing Ratios. *Procedia Structural Integrity*, 37, p. 383–388, doi:10.1016/j.prostr.2022.01.099.
- Sánchez-Avila, Ronald M., Merayo-Llodes, Jesus, Fernández, Maria Laura, Rodríguez-Gutiérrez, Luis Alberto, Rodríguez-Calvo, Pedro Pablo, Fernández-Vega Cueto, Andres, Muruzabal, Francisco, Orive, Gorka and Anitua, Eduardo (2018). Plasma rich in growth factors eye drops to treat secondary ocular surface disorders in patients with glaucoma. *International Medical Case Reports Journal*, 11, p. 97–103, doi:10.2147/IMCRJ.S153918.
- Sangwan, Virender S., Basu, Sayan, MacNeil, Sheila and Balasubramanian, Dorairajan (2012). Simple limbal epithelial transplantation (SLET): a novel surgical technique for the treatment of unilateral limbal stem cell deficiency. *The British Journal of Ophthalmology*, 96(7), p. 931–934, doi:10.1136/bjophthalmol-2011-301164.
- Sanie-Jahromi, Fatemeh, Eghtedari, Masoomah, Mirzaei, Esmaeil, Jalalpour, Mohammad Hassan, Asvar, Zahra, Nejabat, Mahmood and Javidi-Azad, Fahimeh (2020). Propagation of limbal stem cells on polycaprolactone and polycaprolactone/gelatin fibrous scaffolds and transplantation in animal model. *BiolImpacts*, 10(1), p. 44–54, doi:10.15171/bi.2020.06.
- Sareen, Dhruv, Saghizadeh, Mehrnoosh, Ornelas, Loren, Winkler, Michael A., Narwani, Kavita, Sahabian, Anais, Funari, Vincent A., Tang, Jie, Spurka, Lindsay, Punj, Vasu, Maguen, Ezra, Rabinowitz, Yaron S., Svendsen, Clive N. and Ljubimov, Alexander V. (2014). Differentiation of Human Limbal-Derived Induced Pluripotent Stem Cells Into Limbal-Like Epithelium. *STEM CELLS Translational Medicine*, 3(9), p. 1002–1012, doi:10.5966/sctm.2014-0076.
- Sartaj, R., Zhang, C., Wan, P., Pasha, Z., Guaiquil, V., Liu, A., Liu, J., Luo, Y., Fuchs, E. and Rosenblatt, M. I. (2017). Characterization of slow cycling corneal limbal epithelial cells identifies putative stem cell markers. *Scientific Reports*, 7(1), p. 3793, doi:10.1038/s41598-017-04006-y.
- Sayed-Ahmed, Ibrahim O., Palioura, Sotiria, Galor, Anat and Karp, Carol L. (2017). Diagnosis and Medical Management of Ocular Surface Squamous Neoplasia. *Expert Review of Ophthalmology*, 12(1), p. 11–19, doi:10.1080/17469899.2017.1263567.
- Schlötzer-Schrehardt, U., Dietrich, T., Saito, K., Sorokin, L., Sasaki, T., Paulsson, M. and Kruse, F. E. (2007). Characterization of extracellular matrix components in the limbal epithelial stem cell compartment. *Experimental Eye Research*, 85(6), p. 845–860, doi:10.1016/j.exer.2007.08.020.
- Schlötzer-Schrehardt, Ursula and Kruse, Friedrich E. (2005). Identification and characterization of limbal stem cells. *Experimental Eye Research*.
- Sei, Yoshitatsu, Feng, Jianying, Chow, Carson C. and Wank, Stephen A. (2019). Asymmetric cell division-dominant neutral drift model for normal intestinal stem cell homeostasis. *American Journal of Physiology. Gastrointestinal and Liver Physiology*, 316(1), p. G64–G74, doi:10.1152/ajpgi.00242.2018.

- Sejpal, Kunjal, Bakhtiari, Pejman and Deng, Sophie X. (2013). Presentation, Diagnosis and Management of Limbal Stem Cell Deficiency. *Middle East African Journal of Ophthalmology*, 20(1), p. 5–10, doi:10.4103/0974-9233.106381.
- Selbach, J. Michael, Posielek, Kathrin, Steuhl, Klaus-Peter and Kremmer, Stephan (2005). Episcleral venous pressure in untreated primary open-angle and normal-tension glaucoma. *Ophthalmologica. Journal International D'ophtalmologie. International Journal of Ophthalmology. Zeitschrift Fur Augenheilkunde*, 219(6), p. 357–361, doi:10.1159/000088378.
- Seo, Jungmok, Shin, Jung-Youn, Leijten, Jeroen, Jeon, Oju, Bal Öztürk, Ayça, Rouwkema, Jeroen, Li, Yuancheng, Shin, Su Ryon, Hajjali, Hadi, Alsberg, Eben and Khademhosseini, Ali (2018). Interconnectable Dynamic Compression Bioreactors for Combinatorial Screening of Cell Mechanobiology in Three Dimensions. *ACS Applied Materials & Interfaces*, 10(16), p. 13293–13303, doi:10.1021/acsami.7b17991.
- Seonwoo, Hoon, Bae, Won-Gyu, Park, Sunho, Kim, Hong-Nam, Choi, Kyoung Soon, Lim, Ki Taek, Hyun, Hoon, Kim, Jin-Woo, Kim, Jangho and Chung, Jong Hoon (2016). Hierarchically Micro-and Nanopatterned Topographical Cues for Modulation of Cellular Structure and Function. *IEEE Transactions on NanoBioscience*, 15(8), p. 835–842, doi:10.1109/TNB.2016.2631641.
- Shahraki, Toktam, Arabi, Amir and Feizi, Sepehr (2021). Pterygium: an update on pathophysiology, clinical features, and management. *Therapeutic Advances in Ophthalmology*, 13, p. 25158414211020152, doi:10.1177/25158414211020152.
- Shanmuganathan, Vijay A., Foster, Toshana, Kulkarni, Bina B., Hopkinson, Andrew, Gray, Trevor, Powe, Des G., Lowe, James and Dua, Harminder S. (2007). Morphological characteristics of the limbal epithelial crypt. *British Journal of Ophthalmology*, 91(4), p. 514–519, doi:10.1136/bjo.2006.102640.
- Sharma, Dhavan, Jia, Wenkai, Long, Fei, Pati, Shweta, Chen, Qinghui, Qyang, Yibing, Lee, Bruce, Choi, Chang Kyong and Zhao, Feng (2019). Polydopamine and collagen coated micro-grated polydimethylsiloxane for human mesenchymal stem cell culture. *Bioactive Materials*, 4, p. 142–150, doi:10.1016/j.bioactmat.2019.02.002.
- Sharma, Sandhya M., Fuchsluger, Thomas, Ahmad, Sajjad, Katikireddy, Kishore R., Armant, Myriam, Dana, Reza and Jurkunas, Ula V. (2012a). Comparative Analysis of Human-Derived Feeder Layers with 3T3 Fibroblasts for the Ex vivo Expansion of Human Limbal and Oral Epithelium. *Stem Cell Reviews and Reports*, 8(3), p. 696–705, doi:10.1007/s12015-011-9319-6.
- Sharma, Sandhya M., Fuchsluger, Thomas, Ahmad, Sajjad, Katikireddy, Kishore R., Armant, Myriam, Dana, Reza and Jurkunas, Ula V. (2012b). Comparative Analysis of Human-Derived Feeder Layers with 3T3 Fibroblasts for the Ex vivo Expansion of Human Limbal and Oral Epithelium. *Stem Cell Reviews and Reports*, 8(3), p. 696–705, doi:10.1007/s12015-011-9319-6.
- Sheehy, Guillaume, Picot, Fabien, Dallaire, Frédérick, Ember, Katherine J., Nguyen, Tien, Petrecca, Kevin, Trudel, Dominique and Leblond, Frédéric (2023). Open-sourced Raman spectroscopy data processing package implementing a baseline removal algorithm validated from multiple datasets acquired in human tissue and biofluids. *Journal of Biomedical Optics*, 28(2), p. 025002, doi:10.1117/1.JBO.28.2.025002.

Shen, Carl, Chan, Clara C. and Holland, Edward J. (2015). Limbal Stem Cell Transplantation for Soft Contact Lens Wear–Related Limbal Stem Cell Deficiency. *American Journal of Ophthalmology*, 160(6), p. 1142–1149.e1, doi:10.1016/j.ajo.2015.07.038.

Shen, Yan and Le, Qihua (2023). The progress in techniques for culturing human limbal epithelial stem cells. *Human Cell*, 36(1), p. 1–14, doi:10.1007/s13577-022-00794-2.

Shi, Lei, Stachon, Tanja, Käsmann-Kellner, Barbara, Seitz, Berthold, Szentmáry, Nóra and Latta, Lorenz (2020). Keratin 12 mRNA expression could serve as an early corneal marker for limbal explant cultures. *Cytotechnology*, 72(2), p. 239–245, doi:10.1007/s10616-020-00373-z.

Shibata, Shun, Hayashi, Ryuhei, Okubo, Toru, Kudo, Yuji, Baba, Koichi, Honma, Yoichi and Nishida, Kohji (2019). The secretome of adipose-derived mesenchymal stem cells attenuates epithelial–mesenchymal transition in human corneal epithelium. *Regenerative Therapy*, 11, p. 114–122, doi:10.1016/j.reth.2019.06.005.

Shih, Chun-Che, Shih, Chun-Ming, Su, Yea-Yang, Su, Lin Hui Julie, Chang, Mau-Song and Lin, Shing-Jong (2004). Effect of surface oxide properties on corrosion resistance of 316L stainless steel for biomedical applications. *Corrosion Science*, 46(2), p. 427–441, doi:10.1016/S0010-938X(03)00148-3.

Shirazi, Reyhaneh Neghabat, Aldabbagh, Fawaz, Erxleben, Andrea, Rochev, Yury and McHugh, Peter (2014). Nanomechanical properties of poly(lactic-co-glycolic) acid film during degradation. *Acta Biomaterialia*, 10(11), p. 4695–4703, doi:10.1016/j.actbio.2014.08.004.

Shirzadeh, Ebrahim, Keshel, Saeed Heidari, Ezzatizadeh, Vahid, Jabbehdari, Sayena and Baradaran-Rafii, Alireza (2018). Unrestricted somatic stem cells, as a novel feeder layer: Ex vivo culture of human limbal stem cells. *Journal of Cellular Biochemistry*, 119(3), p. 2666–2678, doi:10.1002/jcb.26434.

Shortt, Alex J., Secker, Genevieve A., Munro, Peter M., Khaw, Peng T., Tuft, Stephen J. and Daniels, Julie T. (2007). Characterization of the Limbal Epithelial Stem Cell Niche: Novel Imaging Techniques Permit In vivo Observation and Targeted Biopsy of Limbal Epithelial Stem Cells. *Stem Cells*, 25(6), p. 1402–1409, doi:10.1634/stemcells.2006-0580.

Sola, D., Lavieja, C., Orera, A. and Clemente, M. J. (2018). Direct laser interference patterning of ophthalmic polydimethylsiloxane (PDMS) polymers. *Optics and Lasers in Engineering*, 106, p. 139–146, doi:10.1016/j.optlaseng.2018.03.007.

Soliman, Wael and Mohamed, Tarek A. (2012). Spectral domain anterior segment optical coherence tomography assessment of pterygium and pinguecula. *Acta Ophthalmologica*, 90(5), p. 461–465, doi:10.1111/j.1755-3768.2010.01994.x.

Song, E., Yang, Wei, Cui, Zhi-hua, Dong, Yu, Sui, Dong-ming, Guan, Xiao-kang and Ma, Yan-ling (2005). Transplantation of human limbal cells cultivated on amniotic membrane for reconstruction of rat corneal epithelium after alkaline burn. *Chinese Medical Journal*, 118(11), p. 927–935.

Song, Shaozhen, Huang, Zhihong, Nguyen, Thu-Mai, Wong, Emily Y., Arnal, Bastien, O'Donnell, Matthew and Wang, Ruikang K. (2013). Shear modulus imaging by direct

visualization of propagating shear waves with phase-sensitive optical coherence tomography. *Journal of Biomedical Optics*, 18(12), p. 121509, doi:10.1117/1.JBO.18.12.121509.

Sporea, I., Sirli, R. L., Deleanu, A., Popescu, A., Focsa, M., Danila, M. and Tudora, A. (2011). Acoustic Radiation Force Impulse Elastography as Compared to Transient Elastography and Liver Biopsy in Patients with Chronic Hepatopathies. *Ultraschall in der Medizin -European Journal of Ultrasound*, 32(S 1), p. 46–52, doi:10.1055/s-0029-1245360.

Sridhar, Mittanamalli S. (2018). Anatomy of cornea and ocular surface. *Indian Journal of Ophthalmology*, 66(2), p. 190–194, doi:10.4103/ijo.IJO_646_17.

Stefano, Vinícius Silbiger De and William J. Dupps, Jr (2017). BIOMECHANICAL DIAGNOSTICS OF THE CORNEA. *International ophthalmology clinics*, 57(3), p. 75, doi:10.1097/IIO.000000000000172.

Stone, Robert and McCloy, Rory (2004). Ergonomics in medicine and surgery. *BMJ*, 328(7448), p. 1115–1118, doi:10.1136/bmj.328.7448.1115.

Suárez-Barrio, Carlota, Etxebarria, Jaime, Hernández-Moya, Raquel, del Val-Alonso, Marina, Rodríguez-Astigarraga, Maddalen, Urkaregi, Arantza, Freire, Vanesa, Morales, María-Celia, Durán, Juan Antonio, Vicario, Marta, Molina, Irene, Herrero-Vanrell, Rocío and Andollo, Noelia (2019). Hyaluronic Acid Combined with Serum Rich in Growth Factors in Corneal Epithelial Defects. *International Journal of Molecular Sciences*, 20(7), p. 1655, doi:10.3390/ijms20071655.

Syed-Picard, Fatima N., Du, Yiqin, Hertszenberg, Andrew J., Palchesko, Rachelle, Funderburgh, Martha L., Feinberg, Adam W. and Funderburgh, James L. (2018). Scaffold-free tissue engineering of functional corneal stromal tissue. *Journal of Tissue Engineering and Regenerative Medicine*, 12(1), p. 59–69, doi:10.1002/term.2363.

Szabó, Dóra Júlia, Noer, Agate, Nagymihály, Richárd, Josifovska, Natasha, Andjelic, Sofija, Veréb, Zoltán, Facskó, Andrea, Moe, Morten C. and Petrovski, Goran (2015). Long-Term Cultures of Human Cornea Limbal Explants Form 3D Structures Ex vivo – Implications for Tissue Engineering and Clinical Applications. *PLoS ONE*, 10(11), p. e0143053, doi:10.1371/journal.pone.0143053.

Talbot, Mariève, Carrier, Patrick, Giasson, Claude J., Deschambeault, Alexandre, Guérin, Sylvain L., Auger, Francois A., Bazin, Richard and Germain, Lucie (2006). Autologous transplantation of rabbit limbal epithelia cultured on fibrin gels for ocular surface reconstruction. *Molecular Vision*, 12, p. 65–75.

Tan, Yongyao, Chen, Dan, Wang, Yunming, Wang, Wei, Xu, Lingjuan, Liu, Rong, You, Chunxiu, Li, Guigang, Zhou, Huamin and Li, Dequn (2022). Limbal Bio-Engineered Tissue Employing 3D Nanofiber-Aerogel Scaffold to Facilitate LSCs Growth and Migration. *Macromolecular Bioscience*, p. 2100441, doi:10.1002/MABI.202100441.

Tang, Huilin, Bi, Fei, Chen, Guoqing, Zhang, Shuning, Huang, Yibing, Chen, Jiahao, Xie, Li, Qiao, Xiangchen and Guo, Weihua (2022). 3D-bioprinted Recombination Structure of Hertwig's Epithelial Root Sheath Cells and Dental Papilla Cells for Alveolar Bone Regeneration. *International Journal of Bioprinting*, 8(3), p. 512, doi:10.18063/ijb.v8i3.512.

Tang, Qiangqiang, Li, Xiaoyu, Lai, Chen, Li, Lei, Wu, Hongkai, Wang, Yingjun and Shi, Xuetao (2021). Fabrication of a hydroxyapatite-PDMS microfluidic chip for bone-related cell culture and drug screening. *Bioactive Materials*, 6(1), p. 169–178, doi:10.1016/j.bioactmat.2020.07.016.

Tavangar, Amirhossein, Premnath, Priyatha, Tan, Bo and Venkatakrishnan, Krishnan (2016). Noble Hybrid Nanostructures as Efficient Anti-Proliferative Platforms for Human Breast Cancer Cell. *ACS Applied Materials & Interfaces*, 8(16), p. 10253–10265, doi:10.1021/acsami.6b02720.

Theerakittayakorn, Kasem, Thi Nguyen, Hong, Musika, Jidapa, Kunkanjanawan, Hataiwan, Imsoonthornruksa, Sumeth, Somredngan, Sirilak, Ketudat-Cairns, Mariena and Parnpai, Rangsun (2020). Differentiation Induction of Human Stem Cells for Corneal Epithelial Regeneration. *International Journal of Molecular Sciences*, 21(21), p. 7834, doi:10.3390/ijms21217834.

Thoft, R. A. and Friend, J. (1983). The X, Y, Z hypothesis of corneal epithelial maintenance. *Investigative Ophthalmology & Visual Science*, 24(10), p. 1442–1443.

Thomas, Padmaja B., Liu, Yi Hsin, Zhuang, Feng Feng, Selvam, Shivaram, Song, Sang W., Smith, Ronald E., Trousdale, Melvin D. and Yiu, Samuel C. (2007). Identification of Notch-1 expression in the limbal basal epithelium. *Molecular Vision*, 13, p. 337–344.

Tian, Yan, Li, Guang-Yue, Zhang, Hang, Wang, Jie-Ping, Ding, Zi-Zhao, Guo, Rui, Cheng, Huan and Liang, Ying-Hua (2020). Molecular basis for coke strength: Stacking-fault structure of wrinkled carbon layers. *Carbon*, 162, p. 56–65, doi:10.1016/j.carbon.2020.02.026.

Tiaw, Kay Siang, Teoh, Swee Hin, Chen, Ran and Hong, Ming Hui (2007). Processing Methods of Ultrathin Poly(ϵ -caprolactone) Films for Tissue Engineering Applications. *Biomacromolecules*, 8(3), p. 807–816, doi:10.1021/bm060832a.

Tong, Liping, Zhou, Wenhua, Zhao, Yuetao, Yu, Xuefeng, Wang, Huaiyu and Chu, Paul K. (2016). Enhanced cytocompatibility and reduced genotoxicity of polydimethylsiloxane modified by plasma immersion ion implantation. *Colloids and Surfaces B: Biointerfaces*, 148, p. 139–146, doi:10.1016/j.colsurfb.2016.08.057.

Totaro, Antonio, Castellan, Martina, Battilana, Giusy, Zanconato, Francesca, Azzolin, Luca, Giulitti, Stefano, Cordenonsi, Michelangelo and Piccolo, Stefano (2017). YAP/TAZ link cell mechanics to Notch signalling to control epidermal stem cell fate. *Nature Communications*, 8, p. 15206, doi:10.1038/ncomms15206.

Tóth, Enikő, Beyer, Dániel, Zsebik, Barbara, Vereb, György and Takács, Lili (2017). Limbal and Conjunctival Epithelial Cell Cultivation on Contact Lenses-Different Affixing Techniques and the Effect of Feeder Cells. *Eye & Contact Lens*, 43(3), p. 162–167, doi:10.1097/ICL.0000000000000259.

Tovell, Victoria E., Massie, Isobel, Kureshi, Alvena K. and Daniels, Julie T. (2015). Functional Limbal Epithelial Cells Can Be Successfully Isolated From Organ Culture Rims Following Long-Term Storage. *Investigative Ophthalmology & Visual Science*, 56(6), p. 3531–3540, doi:10.1167/iovs.14-15429.

Townsend, W. M. (1991). The limbal palisades of Vogt. *Transactions of the American Ophthalmological Society*, 89, p. 721–756.

Tsai, Tung-Han, Sun, Ming-Hui, Ho, Tsung-Chuan, Ma, Hsin-I., Liu, Ming-Ying and Tsao, Yeou-Ping (2014). Notch prevents transforming growth factor-beta-assisted epithelial–mesenchymal transition in cultured limbal progenitor cells through the induction of Smad7. *Molecular Vision*, 20, p. 522–534.

Tseng, S. C., Prabhasawat, P., Barton, K., Gray, T. and Meller, D. (1998). Amniotic membrane transplantation with or without limbal allografts for corneal surface reconstruction in patients with limbal stem cell deficiency. *Archives of Ophthalmology (Chicago, Ill.: 1960)*, 116(4), p. 431–441, doi:10.1001/archoph.116.4.431.

Tumbar, Tudorita, Guasch, Geraldine, Greco, Valentina, Blanpain, Cedric, Lowry, William E., Rendl, Michael and Fuchs, Elaine (2004). Defining the epithelial stem cell niche in skin. *Science (New York, N.Y.)*, 303(5656), p. 359–363, doi:10.1126/science.1092436.

Varma, Shobhit, Shanbhag, Swapna S., Donthineni, Pragnya Rao, Mishra, Dilip Kumar, Singh, Vivek and Basu, Sayan (2021). High-Resolution Optical Coherence Tomography Angiography Characteristics of Limbal Stem Cell Deficiency. *Diagnostics*, 11(6), p. 1130, doi:10.3390/diagnostics11061130.

Vazirani, Jayesh, Ali, Mohammed Hasnat, Sharma, Namrata, Gupta, Nidhi, Mittal, Vikas, Atallah, Marwan, Amescua, Guillermo, Chowdhury, Tuhin, Abdala-Figuerola, Alexandra, Ramirez-Miranda, Arturo, Navas, Alejandro, Graue-Hernández, Enrique O. and Chodosh, James (2016). Autologous simple limbal epithelial transplantation for unilateral limbal stem cell deficiency: multicentre results. *The British Journal of Ophthalmology*, 100(10), p. 1416–1420, doi:10.1136/bjophthalmol-2015-307348.

Vazirani, Jayesh, Nair, Dhanyasree, Shanbhag, Swapna, Wurity, Siva, Ranjan, Abhishek and Sangwan, Virender (2018). Limbal Stem Cell Deficiency—Demography and Underlying Causes. *American Journal of Ophthalmology*, 188, p. 99–103, doi:10.1016/j.ajo.2018.01.020.

van Velthoven, Arianne J. H., Utheim, Tor P., Notara, Maria, Bremond-Gignac, Dominique, Figueiredo, Francisco C., Skottman, Heli, Aberdam, Daniel, Daniels, Julie T., Ferrari, Giulio, Grupcheva, Christina, Koppen, Carina, Parekh, Mohit, Ritter, Thomas, Romano, Vito, Ferrari, Stefano, Cursiefen, Claus, Lagali, Neil, LaPointe, Vanessa L. S. and Dickman, Mor M. (2023). Future directions in managing aniridia-associated keratopathy. *Survey of Ophthalmology*, 68(5), p. 940–956, doi:10.1016/j.survophthal.2023.04.003.

Vemuganti, Geeta K., Fatima, Anees, Madhira, Soundarya Lakshmi, Basti, Surendra and Sangwan, Virender S. (2009). Limbal stem cells: application in ocular biomedicine. *International Review of Cell and Molecular Biology*, 275, p. 133–181, doi:10.1016/S1937-6448(09)75005-1.

Versura, Piera, Giannaccare, Giuseppe, Vukatana, Gentiana, Mulè, Rita, Malavolta, Nazzarena and Campos, Emilio C. (2018). Predictive role of tear protein expression in the early diagnosis of Sjögren's syndrome. *Annals of Clinical Biochemistry*, 55(5), p. 561–570, doi:10.1177/0004563217750679.

Visalakshan, Rahul M., MacGregor, Melanie N., Sasidharan, Salini, Ghazaryan, Artur, Mierczynska-Vasilev, Agnieszka M., Morsbach, Svenja, Mailänder, Volker, Landfester, Katharina, Hayball, John D. and Vasilev, Krasimir (2019a). Biomaterial Surface

- Hydrophobicity-Mediated Serum Protein Adsorption and Immune Responses. *ACS Applied Materials & Interfaces*, 11(31), p. 27615–27623, doi:10.1021/acsami.9b09900.
- Visalakshan, Rahul M., MacGregor, Melanie N., Sasidharan, Salini, Ghazaryan, Artur, Mierczynska-Vasilev, Agnieszka M., Morsbach, Svenja, Mailänder, Volker, Landfester, Katharina, Hayball, John D. and Vasilev, Krasimir (2019b). Biomaterial Surface Hydrophobicity-Mediated Serum Protein Adsorption and Immune Responses. *ACS Applied Materials & Interfaces*, 11(31), p. 27615–27623, doi:10.1021/acsami.9b09900.
- Volckaert, Thomas, Yuan, Tingting, Yuan, Jie, Boateng, Eistine, Hopkins, Seantel, Zhang, Jin-San, Thannickal, Victor J., Fässler, Reinhard and De Langhe, Stijn P. (2019). Hippo signalling promotes lung epithelial lineage commitment by curbing Fgf10 and β -catenin signalling. *Development*, 146(2), p. dev166454, doi:10.1242/dev.166454.
- Wan, Yuqing, Qu, Xue, Lu, Jun, Zhu, Chuanfeng, Wan, Lijun, Yang, Junlin, Bei, Jianzhong and Wang, Shenguo (2004). Characterization of surface property of poly(lactide-co-glycolide) after oxygen plasma treatment. *Biomaterials*, 25(19), p. 4777–4783, doi:10.1016/j.biomaterials.2003.11.051.
- Wang, Zhongying, Tonderys, Daniel, Leggett, Susan E., Williams, Evelyn Kendall, Kiani, Mehrdad T., Spitz Steinberg, Ruben, Qiu, Yang, Wong, Ian Y. and Hurt, Robert H. (2016). Wrinkled, wavelength-tunable graphene-based surface topographies for directing cell alignment and morphology. *Carbon*, 97, p. 14–24, doi:10.1016/j.carbon.2015.03.040.
- Wang, Hui-Xian, Gao, Xiao-Wei, Ren, Bing, Cai, Yan, Li, Wen-Jing, Yang, Yu-Li and Li, Yi-Jian (2017). Comparative analysis of different feeder layers with 3T3 fibroblasts for culturing rabbits limbal stem cells. *International Journal of Ophthalmology*, 10(7), p. 1021–1027, doi:10.18240/ijo.2017.07.01.
- Wang, Liqiang, Ma, Ruijue, Du, Gaiping, Guo, Huiling and Huang, Yifei (2015). Biocompatibility of helicoidal multilamellar arginine-glycine-aspartic acid-functionalized silk biomaterials in a rabbit corneal model. *Journal of Biomedical Materials Research. Part B, Applied Biomaterials*, 103(1), p. 204–211, doi:10.1002/jbm.b.33192.
- Wang, Wei, Li, Shen, Xu, Lingjuan, Jiang, Menglin, Li, Xinyu, Zhang, Yuan, Tighe, Sean, Zhu, Yingting and Li, Guigang (2020). Differential Gene Expression between Limbal Niche Progenitors and Bone Marrow Derived Mesenchymal Stem Cells. *International Journal of Medical Sciences*, 17(4), p. 549–557, doi:10.7150/ijms.40881.
- Wang, Ximo, Chen, Chen, Wang, Ruiqiang, Qiao, Xuguang, Waterhouse, Geoffrey I. N. and Xu, Zhixiang (2023). Performance evaluation of novel Ag@GO-biomaterial SERS substrates for the ultrasensitive detection of neomycin in foods. *Sensors and Actuators B: Chemical*, 380, p. 133250, doi:10.1016/j.snb.2022.133250.
- Wang, Zhixin, Volinsky, Alex A. and Gallant, Nathan D. (2014). Crosslinking effect on polydimethylsiloxane elastic modulus measured by custom-built compression instrument. *Journal of Applied Polymer Science*, 131(22), doi:10.1002/app.41050.
- Watanabe, Masashi and Hashimoto, Ryoma (2015). Area-selective microwrinkle formation on poly(dimethylsiloxane) by treatment with strong acid. *Journal of Polymer Science Part B: Polymer Physics*, 53(3), p. 167–174, doi:10.1002/polb.23599.

- Watanabe, Masashi and Mizukami, Koujiro (2012). *Well-Ordered Wrinkling Patterns on Chemically Oxidized Poly(dimethylsiloxane) Surfaces*. ACS Publications. <https://pubs.acs.org/doi/pdf/10.1021/ma301143m> [Accessed: 2023-05-27].
- Watanabe, Masashi and Shinoda, Kensuke (2014). Self-structured serrated edges of chemically oxidized poly(dimethylsiloxane) disks. *Journal of Applied Polymer Science*, 131(18), doi:10.1002/app.40767.
- Werkmeister, René M., Sapeta, Sabina, Schmidl, Doreen, Garhöfer, Gerhard, Schmidinger, Gerald, Santos, Valentin Aranha dos, Aschinger, Gerold C., Baumgartner, Isabella, Pircher, Niklas, Schwarzhans, Florian, Pantalon, Anca, Dua, Harminder and Schmetterer, Leopold (2017). Ultrahigh-resolution OCT imaging of the human cornea. *Biomedical Optics Express*, 8(2), p. 1221–1239, doi:10.1364/BOE.8.001221.
- Wicklow, Eryn, Blij, Stephanie, Frum, Tristan, Hirate, Yoshikazu, Lang, Richard A., Sasaki, Hiroshi and Ralston, Amy (2014). HIPPO Pathway Members Restrict SOX2 to the Inner Cell Mass Where It Promotes ICM Fates in the Mouse Blastocyst. *PLOS Genetics*, 10(10), p. e1004618, doi:10.1371/journal.pgen.1004618.
- Worp, H. Bart van der, Howells, David W., Sena, Emily S., Porritt, Michelle J., Rewell, Sarah, O'Collins, Victoria and Macleod, Malcolm R. (2010). Can Animal Models of Disease Reliably Inform Human Studies? *PLOS Medicine*, 7(3), p. e1000245, doi:10.1371/journal.pmed.1000245.
- Wright, Bernice, Mi, Shengli and Connon, Che J. (2013). Towards the use of hydrogels in the treatment of limbal stem cell deficiency. *Drug Discovery Today*, 18(1–2), p. 79–86, doi:10.1016/j.drudis.2012.07.012.
- Wychowanec, Jacek K., Litowczenko, Jagoda and Tadyszak, Krzysztof (2020). Fabricating versatile cell supports from nano- and micro-sized graphene oxide flakes. *Journal of the Mechanical Behavior of Biomedical Materials*, 103, p. 103594, doi:10.1016/j.jmbbm.2019.103594.
- Xie, Wenqing, Xiao, Wenfeng, Tang, Kun, Zhang, Liyang and Li, Yusheng (2020). Yes-Associated Protein 1: Role and Treatment Prospects in Orthopedic Degenerative Diseases. *Frontiers in Cell and Developmental Biology*, 8, doi:10.3389/fcell.2020.573455.
- Xu, Jian, Lamouille, Samy and Derynck, Rik (2009). TGF- β -induced epithelial to mesenchymal transition. *Cell Research*, 19(2), p. 156–172, doi:10.1038/cr.2009.5.
- Xu, Fan, Zhao, Shichen, Lu, Conghua and Potier-Ferry, Michel (2020). Pattern selection in core-shell spheres. *Journal of the Mechanics and Physics of Solids*, 137, p. 103892, doi:10.1016/j.jmps.2020.103892.
- Yadhuraj, S. R., Babu Gandla, Satheesh, Sudarshan, B. G. and Prasanna Kumar, S. C. (2018). Preparation and Study of PDMS Material. *Materials Today: Proceedings*, 5(10, Part 1), p. 21406–21412, doi:10.1016/j.matpr.2018.06.547.
- Yam, Gary Hin-Fai, Teo, Erica Pei-Wen, Setiawan, Melina, Lovatt, Matthew J., Yusoff, Nur Zahirah Binte M., Fuest, Matthias, Goh, Bee-Tin and Mehta, Jodhbir S. (2018). Postnatal periodontal ligament as a novel adult stem cell source for regenerative corneal cell therapy. *Journal of Cellular and Molecular Medicine*, 22(6), p. 3119–3132, doi:10.1111/jcmm.13589.

- Yan, Xiang-Zhen, van den Beucken, Jeroen J. J. P., Yuan, Chunxue, Jansen, John A. and Yang, Fang (2019). Evaluation of polydimethylsiloxane-based substrates for in vitro culture of human periodontal ligament cells. *Journal of Biomedical Materials Research. Part A*, 107(12), p. 2796–2805, doi:10.1002/jbm.a.36782.
- Yan, Xiaoxiang, Li, Mengyu, Zhao, Mengying, Zhou, Hongwei, Wang, Yufeng and Ba, Miao (2022). Effect of PDMS Viscosity and Additive Amount of Curing Agent Solution on the Mechanical Properties of PDMS Fouling Release Coating. *Journal of Physics: Conference Series*, 2174(1), p. 012036, doi:10.1088/1742-6596/2174/1/012036.
- Yang, Da Hyun, Jung, Sangyong, Kim, Jae Young and Lee, Nae Yoon (2022). Fabrication of a Cell-Friendly Poly(dimethylsiloxane) Culture Surface via Polydopamine Coating. *Micromachines*, 13(7), p. 1122, doi:10.3390/mi13071122.
- Yang, Lingling, Zhang, Songmei, Duan, Haoyun, Dong, Muchen, Hu, Xiaoli, Zhang, Zhaohua, Wang, Yao, Zhang, Xiaoping, Shi, Weiyun and Zhou, Qingjun (2018). Different Effects of Pro-Inflammatory Factors and Hyperosmotic Stress on Corneal Epithelial Stem/Progenitor Cells and Wound Healing in Mice. *Stem Cells Translational Medicine*, 8(1), p. 46–57, doi:10.1002/sctm.18-0005.
- Yeh, Shu-I., Ho, Tsung-Chuan, Chen, Show-Li, Chen, Chie-Pein, Cheng, Huey-Chuan, Lan, Yu-Wen, Hsieh, Jui-Wen, Wang, Chin-Tien and Tsao, Yeou-Ping (2016). Pigment Epithelial-Derived Factor Peptide Regenerated Limbus Serves as Regeneration Source for Limbal Regeneration in Rabbit Limbal Deficiency. *Investigative Ophthalmology & Visual Science*, 57(6), p. 2629–2636, doi:10.1167/iovs.15-17171.
- Yin, Jian, Han, Xue, Cao, Yanping and Lu, Conghua (2014). Surface wrinkling on polydimethylsiloxane microspheres via wet surface chemical oxidation. *Scientific Reports*, 4, p. 5710, doi:10.1038/srep05710.
- Yoon, Jinny J., Ismail, Salim and Sherwin, Trevor (2014). Limbal stem cells: Central concepts of corneal epithelial homeostasis. *World Journal of Stem Cells*, 6(4), p. 391–403, doi:10.4252/wjsc.v6.i4.391.
- Yoshida, Satoru, Shimmura, Shigeto, Kawakita, Tetsuya, Miyashita, Hideyuki, Den, Seika, Shimazaki, Jun and Tsubota, Kazuo (2006). Cytokeratin 15 Can Be Used to Identify the Limbal Phenotype in Normal and Diseased Ocular Surfaces. *Investigative Ophthalmology & Visual Science*, 47(11), p. 4780–4786, doi:10.1167/iovs.06-0574.
- Yu, Min, Bojic, Sanja, Figueiredo, Gustavo S., Rooney, Paul, de Havilland, Julian, Dickinson, Anne, Figueiredo, Francisco C. and Lako, Majlinda (2016). An important role for adenine, cholera toxin, hydrocortisone and triiodothyronine in the proliferation, self-renewal and differentiation of limbal stem cells in vitro. *Experimental Eye Research*, 152, p. 113–122, doi:10.1016/j.exer.2016.09.008.
- Zeisberg, M., Neilson, E.G., 2009. Biomarkers for epithelial-mesenchymal transitions. *The Journal of Clinical Investigation* 119, 1429. <https://doi.org/10.1172/JCI36183>
- Zekušić, Marija, Bujić Mihica, Marina, Skoko, Marija, Vukušić, Kruno, Risteski, Patrik, Martinčić, Jelena, Tolić, Iva M., Bendelja, Krešo, Ramić, Snježana, Dolenc, Tamara, Vrgoč Zimić, Ivana, Puljić, Dominik, Petric Vicković, Ivanka, Iveković, Renata, Batarilo, Ivanka, Prosenc Zmrzljak, Uršula, Hoffmeister, Alan and Vučemilo, Tiha (2023). New characterization and safety evaluation of human limbal stem cells used in clinical application: fidelity of mitotic process and mitotic spindle morphologies. *Stem Cell Research & Therapy*, 14(1), p. 368, doi:10.1186/s13287-023-03586-z.

- Zhang, Duo, Wang, Jinjiang, Li, Chunhui and Huang, Zhihong (2020). Optimal stimulation frequency for vibrational optical coherence elastography. *Journal of Biophotonics*, 13(2), p. e201960066, doi:10.1002/jbio.201960066.
- Zhang, Hong, Brown, Karl David, Lowe, Sue Peng, Liu, Guei-Sheung, Steele, David, Abberton, Keren and Daniell, Mark (2014). Acrylic acid surface-modified contact lens for the culture of limbal stem cells. *Tissue Engineering. Part A*, 20(11–12), p. 1593–1602, doi:10.1089/ten.TEA.2013.0320.
- Zhang, Jingran, Yan, Yongda, Miao, Peng and Cai, Jianxiong (2017). Fabrication of gold-coated PDMS surfaces with arrayed triangular micro/nanopyramids for use as SERS substrates. *Beilstein Journal of Nanotechnology*, 8(1), p. 2271–2282, doi:10.3762/bjnano.8.227.
- Zhang, Shizhen, Xiong, Xiufang and Sun, Yi (2020). Functional characterization of SOX2 as an anticancer target. *Signal Transduction and Targeted Therapy*, 5(1), p. 1–17, doi:10.1038/s41392-020-00242-3.
- Zhang, Xiao, Huo, Tiancheng, Wang, Chengming, Liao, Wenchao, Chen, Tianyuan, Ai, Shengnan, Zhang, Wenxin, Hsieh, Jui-Cheng and Xue, Ping (2016). Optical computing for optical coherence tomography. *Scientific Reports*, 6(1), p. 37286, doi:10.1038/srep37286.
- Zhao, Chen, Cai, Shang, Shin, Kunyoo, Lim, Agnes, Kalisky, Tomer, Lu, Wan-Jin, Clarke, Michael F. and Beachy, Philip A. (2017). Stromal Gli2 activity coordinates a niche signalling program for mammary epithelial stem cells. *Science (New York, N. Y.)*, 356(6335), p. eaal3485, doi:10.1126/science.aal3485.
- Zhao, Y., Feng, B., Lee, J., Lu, N. and Pierce, D. M. (2020). A multi-layered model of human skin elucidates mechanisms of wrinkling in the forehead. *Journal of the Mechanical Behavior of Biomedical Materials*, 105, p. 103694, doi:10.1016/j.jmbbm.2020.103694.
- Zheng, Shaodi, Huang, Shilin, Xiong, Lian, Yang, Wei, Liu, Zhengying, Xie, Banghu and Yang, Mingbo (2018). Tunable wrinkle structure formed on surface of polydimethylsiloxane microspheres. *European Polymer Journal*, 104, p. 99–105, doi:10.1016/j.eurpolymj.2018.05.007.
- Zhou, Wenda, Chen, Ying, Roh, Terrence, Lin, Yinan, Ling, Shengjie, Zhao, Siwei, Lin, James D., Khalil, Noor, Cairns, Dana M., Manousiouthakis, Eleana, Tse, Megan and Kaplan, David L. (2018). Multifunctional Bioreactor System for Human Intestine Tissues. *ACS biomaterials science & engineering*, 4(1), p. 231–239, doi:10.1021/acsbomaterials.7b00794.
- Zhou, Yuheng, Wang, Yuanyuan, Shen, Meixiao, Jin, Zi, Chen, Yihong, Zhou, Yue, Qu, Jia and Zhu, Dexi (2019). In vivo evaluation of corneal biomechanical properties by optical coherence elastography at different cross-linking irradiances. *Journal of Biomedical Optics*, 24(10), p. 105001, doi:10.1117/1.JBO.24.10.105001.
- Zvietcovich, Fernando, Nair, Achuth, Singh, Manmohan, Aglyamov, Salavat R., Twa, Michael D. and Larin, Kirill V. (2020). Dynamic Optical Coherence Elastography of the Anterior Eye: Understanding the Biomechanics of the Limbus. *Investigative Ophthalmology & Visual Science*, 61(13), p. 7, doi:10.1167/iovs.61.13.7.